Carbon Monoxide Poisoning Mechanisms and Mitigation Strategies for Polymer Electrolyte Membrane Fuel Cells

Velia Fabiola Valdés López

A thesis submitted in part fulfilment of the requirements for the degree of Doctor of Philosophy at University College London

Electrochemical Innovation Lab

Department of Chemical Engineering

University College London

2021

Declaration

I, Velia Fabiola Valdés López, confirm that the work presented in this thesis is my own. Where information has been derived from other sources, I confirm that this has been indicated in the thesis.

…………………………….

Signature

…………………………….

Date

Acknowledgements

First, I would like to thank Dan Brett for giving me the opportunity of doing this PhD under his supervision, for all his support and his enthusiasm for science. His work has been very inspiring throughout this time.

I would also like to thank Paul Shearing, my second supervisor, for the questions that made me see deeper into science, and that helped me improve my work.

I would like to acknowledge the National Council of Science and Technology of Mexico (CONACYT) and UCL for the financial support, without which my PhD studies would have not been possible.

I would like to thank Gareth Hinds for supporting the collaboration with NPL and his help to solve any question I had. I would also like to thank Luis Castanheira for hosting me at NPL, and for his support in the lab.

I am thankful for having the chance to work in the EIL, where I was surrounded by so many talented people. I particularly thank Toby, Rhod, Jay and Tom. Their knowledge, experience and willingness to help everybody, make their contribution to the lab unmeasurable. Also, thank you to Albert for his help with the electronic devices.

I would like to thank Jason for his friendship, his support and for always helping me find solutions in the lab. Thank you to Nivedita for keeping me grounded and for motivating me all the time, and to Tan for all for his encouragement and advice. Also thank you to Lara for coding in LabVIEW and for her support.

Thank you to my Mexican family in London, always inspiring and supportive, and through whom I rediscovered my country. Thank you to my family at Goodenough College, for the support, the fun and the entertaining and deep conversations. And, to my friends back in Mexico, as our friendship continues to grow despite the distance.

Last but not least, to my family, simply the most important thing in my life. This is for them.

Abstract

Fuel cells represent a viable option for the diversification of renewable energies, necessary to meet the increasing energy demand and reduce the emissions of greenhouse gases (GHGs). Among the challenges polymer electrolyte membrane fuel cells (PEMFCs) face for their deployment, are the adverse effects that the presence of CO provokes in their performance and durability. A deeper understanding of the mechanisms occurring during the poisoning is needed in order to develop more efficient mitigation strategies that contribute to the competitiveness of PEMFCs. In this work, the spatial variations and temporal dynamics occurring in the presence of CO were studied. As a means of mitigating the effects of CO poisoning, short-circuiting strategies were evaluated.

First, preliminary studies that evaluated the short-term effects of CO under different operating conditions were presented in a single cell. Next, an array of localised reference electrodes measured directly the anodic overpotential in three different locations of an MEA exposed to CO under galvanostatic control, where self-sustained potential oscillations were observed. This information was complemented by the measurement of the concentration of CO_2 in the outlet that followed the evolution of the oxidation of CO. In the following study, a segmented-in-series system combined with different diagnostic techniques including thermal imaging, current interrupt and mass spectrometry was studied in the presence of two different concentrations of CO. The setups studied contributed to show the variations in the coverage of CO throughout the systems, and the effects of the local conditions in the oxidation of CO. These results highlight the importance of the distribution of the poisoning for the design and optimization of mitigation strategies against poisoning. Short-circuiting of the individual cells of a segmented-in-series stack was presented as an alternative, as the different patterns of the shorts (length and frequency) can be adjusted depending on the degree of poisoning, dependant on the location of the cells in the stack.

Impact Statement

The growing demand of energy along with the necessary reduction of the greenhouse emissions provoked by fossil fuels are the main drivers for the development of new clean technologies to generate energy, such as fuel cells. The research presented here aims to contribute to the advance of fuel cells, particularly PEM fuel cells. The main findings should have an impact in different areas, including the contamination of fuel cells by other components present in different parts of the system, apart from CO. Also, increasing the tolerance of the cells to this contaminant could reduce the space and costs of the purification of hydrogen. It is also possible that fuel cells have a double function, as hydrogen purifiers and energy generators.

The studies presented here are focused on the poisoning of PEMFCs by CO, which is one of the most pernicious contaminants present in the hydrogen produced from steam methane reforming. However, it is not the only contaminant that needs to be studied and mitigated. For instance, the sulphur compounds presented in the hydrogen stream, such as H_2S, have also a negative impact in the cells at ppm levels. Other contaminants are present in the air stream, or come from the fuel cell components. Studying the poisoning by CO could be the base for studying these additional components, alone and in mixtures. Some preliminary studies have presented the effects of different mixtures of contaminants coming from the hydrogen stream; however, limited studies have focused on the full range of components present in the system and the mechanisms associated.

Furthermore, the research presented should contribute for a better understanding of the mechanisms involved over the poisoning by CO that could lead to the development of more efficient strategies and hence, more tolerant fuel cells. The development of such techniques would allow the reduction of the purification stages needed to obtain hydrogen of high purity, reducing costs and volume associated, which is of particular interest for portable applications. It is estimated that the clean-up stages require up to one order of magnitude higher volume than the reformer and the fuel cell stack combined. And, the separation and purification of hydrogen can account between 50 and 80% of the total capital investment.

Finally, different strategies have been proposed for the increase of the tolerance of PEM fuel cells to CO. Some of them are technologies that are designed to be applied on board and to reduce the concentration of CO prior to the passage to the cells. These strategies use the structure of the fuel cells itself and operate under different conditions. The electrochemical preferential oxidation (ECPrOx) and the electrochemical hydrogen pumping (EHP) are the main examples. The use of short-circuiting could be used in the same way. It is possible that fuel cells are used to obtain high purity hydrogen in large plants, after the reformation stages, and not just as a source of energy. Several industrial processes where hydrogen is used, such as the ammonia and the methanol production, could benefit from it.

Publications and Conferences

Journal papers

Valdés-López VF, Mason T, Shearing PR, Brett DJL. Carbon monoxide poisoning and mitigation strategies for polymer electrolyte membrane fuel cells – A review. Progress in Energy and Combustion Science. 2020;79:100842.

Conferences attended

H2FC SUPERGEN Researcher Conference 2016, University of Ulster, UK - Poster “Carbon Monoxide Poisoning and Mitigation Strategies for Polymer Electrolyte Membrane Fuel Cells”

H2FC SUPERGEN Research Conference 2017, University of St-Andrews, UK – Presentation “Mapping of spontaneous potential oscillations within a PEMFC exposed to CO/H2 using localised reference electrodes”

Fuel Cells (GRS) Gordon Research Seminar 2018, Bryant University, US – Poster: “Mapping of spontaneous potential oscillations within a PEMFC anode exposed to CO/H2 using localised reference electrodes”

Fuel Cells Gordon Research Conference 2018, Bryant University, US – Poster: “Mapping of spontaneous potential oscillations within a PEMFC anode exposed to CO/H2 using localised reference electrodes”

European Fuel Cell Forum 2019, Lucerne, Switzerland – Poster: “Analysis of the distribution of carbon monoxide poisoning in a segmented-in-series PEMFC system through mass spectrometry and thermal imaging”

Table of Contents

List of Tables

List of Figures

Symbols and Abbreviations

Symbols

A_1	Amplitude in the exponential decay model	V
C	Gas concentration	g L^{-1}
C_{dl}	Capacitance double layer	F
$c*$	Concentration at reaction surface	mol cm^{-2}
c	Concentration	mol m^{-3}
c	Constant describing how mass transport affects concentration losses	V
c	Speed of light in a vacuum	2.998×10^{8} m s^{-1}
D	Diffusivity	cm^{2} s^{-1}
D^{eff}	Effective diffusivity	cm^{2} s^{-1}
d_w	Wien's displacement constant	2897.8 µm K
E	Thermodynamic ideal voltage	V
E^0	Standard thermodynamic voltage	V
E_b	Spectral radiance of the blackbody	W m^{-2} µm^{-1}
F	Faraday constant	96,485 C mol^{-1}
f	Frequency	Hertz
G	Gibbs free energy	J, J mol^{-1}
ΔG_O^0	Standard free energy of adsorption	J, J mol^{-1}
ΔG_r^0	Standard reaction Gibbs free energy	J, J mol^{-1}
H	Henry's law constant for CO solubility	atm L mol^{-1}
H	Planck's constant	6.6×10^{-34} J
I	Current density	A cm^{-2}
I	Radiation beam intensity	lux
I_0	Initial radiation beam intensity	lux
i	Current density	A cm^{-2}
i_0	Amplitude of the current signal (EIS)	A cm^{-2}
j	Current density	A cm^{-2}
j_0	Exchange current density	A cm^{-2}
j_L	Limiting current density	A cm^{-2}

K	Upper limit of the logistic function	V
k	Absorption coefficient	m^2 mol^{-1}
k	Decay rate in the exponential decay model	min^{-1}
k_b	Boltzmann's constant	1.38×10^{-23} J K^{-1}
L	Inductance	H
L	Path length	cm
m/z	Mass-to-charge ratio	kg C^{-1}
n	Number of electrons transferred in the reaction	Dimensionless
p	Pressure	bar, atm, Pa
R	Ideal gas constant	8.1314 J mol^{-1} K^{-1}
R	Resistance	Ω
r	Interaction parameter in the Temkin isotherm	J, J mol^{-1}
T	Temperature	K, °C
t_1	Time constant in the exponential decay model	min
t_m	Midpoint of the logistic function	s
Δt	Growth time in the logistic function	s
V	Voltage	V
V_0	Amplitude of voltage signal (EIS)	V
W	Warburg diffusion element	Ω $s^{1/2}$
Z	Impedance	Ω
Z_0	Impedance magnitude	Ω
Z_{imag}	Imaginary component (EIS)	Ω
Z_{real}	Real component (EIS)	Ω

Greek symbols

α	Charge transfer coefficient	Dimensionless
α	Constant of the logistic function	Dimensionless
β	Growth rate of the logistic function	s^{-1}
Δ	Denotes change in quantity	Dimensionless
δ	Diffusion layer thickness	m, cm
ε	Emissivity	Dimensionless

η	Overpotential	V
η_{act}	Activation overpotential	V
η_{conc}	Concentration overpotential	V
η_{ohmic}	Ohmic overpotential	V
θ_{CO}	CO coverage	Dimensionless
λ	Wavelength of the radiation	µm
μ_{diff}	Diffusion mass flow rate	mol m^{-2} s^{-1}
σ	Stefan-Boltzmann constant	5.67×10^{-8} W m^{-2} K^{-4}
τ	Half-life in the exponential decay model	min
ω	Radial frequency	Radians s^{-1}

Abbreviations

2DS	2°C Scenario
ATR	Auto-thermal reforming
AFC	Alkaline fuel cell
CE	Counter electrode
CPE	Constant phase element
CV	Cyclic voltammetry
COA-MIB	CO adsorption metal hydride intermediate buffer
DHE	Dynamic hydrogen electrode
DMFC	Direct methanol fuel cell
ECPrOx	Electrochemical preferential oxidation
ECSA	Electrochemical surface area
EHP	Electrochemical hydrogen pumping
EIA	U.S. Energy Information Administration
EIS	Electrochemical impedance spectroscopy
EWGS	Electrochemical water gas shift
FCEV	Fuel cell electric vehicle
GDL	Gas diffusion layer
GHG	Greenhouse gases
HAD	Hydrogen adsorption desorption
HOR	Hydrogen oxidation reaction

HT-PEMFC	High temperature PEMFC
IEA	International Energy Agency
ISO	International Organization for Standardization
LC-TS	Lowest conformer to single transition
LHV	Lower heating value
MCFC	Molten carbonate fuel cell
MEA	Membrane electrode assembly
MH	Metal hydride
MOSFET	Metal oxide semiconductor field effect transistor
NDIR	Non-dispersive infrared
OCV	Open circuit voltage
OLMS	Online mass spectrometry
ORR	Oxygen reduction reaction
PAFC	Phosphoric acid fuel cell
PEMFC	Polymer electrolyte membrane fuel cell
PROX	Preferential oxidation
PSA	Pressure swing adsorption
RE	Reference electrode
RHE	Reversible hydrogen electrode
RWGS	Reverse water-gas shift reaction
SMET	Selective methanation
SMR	Steam methane reforming
SOFC	Solid oxide fuel cell
WE	Working electrode
WGS	Water-gas shift
XPS	X-ray photoelectron spectroscopy
Z-HIT	Impedance (Z) – Hilbert - Transformation

Chapter 1

Introduction

1.1 Motivation

The diversification of energy resources is a priority in facing the growing demand of energy, the effects of fossil fuels on the environment and the long-term high world oil prices. According to the U.S. Energy Information Administration (EIA), it is projected that the world energy consumption will grow by 48% (from 549 to 815 quadrillion Btu) between 2012 and 2040. Fossil fuels would account for 78% of energy use by 2040. And over that period, the world energy-related carbon dioxide emissions would rise 34%. The emissions would come from liquid fuels, natural gas and coal, which is the most carbon-intensive fossil fuel [1].

To reduce greenhouse gases (GHG) emissions, the International Energy Agency (IEA) proposed the 2°C Scenario (2DS), an energy system deployment pathway and trajectory that reduces by 60% the carbon dioxide emissions from fuel combustion and process and feedstock in industry. By 2050, increase of the average global temperature could be restricted by 2°C [2]. Hence, the development of renewable sources of energy that could reduce these emissions have gained interest in the last years [1, 3]. According to the EIA, these technologies will be the fastest-growing energy source between 2012 and 2040 with a consumption growth of 2.6%/year [1].

Fuel cells are considered a highly efficient energy source, with the advantage of no carbon dioxide emissions, when operating on hydrogen as a fuel at the point of use. They could contribute to meeting the global energy demands while complying with the environmental constraints. They could potentially replace internal combustion engines, and in some cases energy storage devices such as batteries [4]. Polymer electrolyte membrane fuel cells (PEMFCs) in particular have received much attention as they have high power density and fast start-up and response times [5]. For these reasons, they are the most commonly used fuel cell for automotive applications [6, 7]. In 2017, PEMFCs accounted for 75% of the total industry megawatts [8].

The most important challenges that this technology faces to increase its presence in the market are cost, performance and durability [9]. A range of physical-chemical phenomena can adversely affect performance, including water management issues (membrane humidification, cathode flooding, freezing, drying phenomena), absorption of contaminants, degradation and poisoning of electrocatalysts, etc. Some of these processes are reversible, and others irreversible and lead to long-term degradation [10]. Contaminants such as carbon monoxide (CO), hydrogen sulphide (H_2S) and ammonia (NH_3) [3] are known to be particularly pernicious and affect performance even when present in trace (ppm) amounts [11]. This work focuses on the effect of carbon monoxide on PEMFCs which is usually introduced by the hydrogen fuel supply. The International Organization for Standardization (ISO) state that the limits for vehicle and stationary applications are 0.2 and 10 ppm CO respectively [12, 13] but methods of mitigating CO poisoning can potentially allow practical operation at higher levels.

1.2 Fuel Cells Overview

Fuel cells were developed in the early 1800s by Sir William Grove, who thought about the possibility to generate electricity by reversing the process of electrolysis. The first fuel-operational fuel cell was presented in 1959 by Francis Thomas Bacon, and later the NASA adopted the technology for the Gemini and Apollo space programs. Fuel cells are electrochemical devices that transform in one-step the chemical energy of a fuel into electrical energy [14].

Different fuel cells have been developed, and they have been classified according to the electrolyte used, fuel and operating parameters [15]. Each has its advantages, limitations and potential applications. Table 1.1 presents a comparison of the most deployed, which include the proton exchange membrane fuel cells (PEMFC), the alkaline fuel cells (AFC), the phosphoric acid fuel cells (PAFC), the molten carbonate fuel cells (MCFC) and the solid oxide fuel cells (SOFC) [16]. Between 2008 and 2013, the global market of fuel cells grew up by almost 400% [17].

Table 1.1 Comparison of Fuel Cell Technologies [16].

Fuel Cell Type	**Common Electrolyte**	**Operating Temperature**	**Typical Stack Size**	**Electrical Efficiency (LHV)**	**Applications**	**Advantages**	**Challenges**
Polymer Electrolyte Membrane (PEM)	Perfluorosulfonic acid	<120 °C	<1kW-100 kW	60% direct H_2, 40% reformed fuel	• Backup power • Portable power • Distributed generation • Transportation • Specialty vehicles	• Solid electrolyte reduces corrosion & electrolyte management problems • Low temperature • Quick start-up and load following	• Expensive catalysts • Sensitive to fuel impurities
Alkaline (AFC)	Aqueous potassium hydroxide soaked in porous matrix, or alkaline polymer membrane	<100 °C	1-100 kW	60%	• Military • Space • Backup power • Transportation	• Wider range of stable materials allows lower cost components • Low temperature • Quick start-up	• Sensitive to CO_2 in fuel and air • Electrolyte management (aqueous) • Electrolyte conductivity (polymer)
Phosphoric Acid (PAFC)	Phosphoric acid soaked in a porous matrix or imbibed in a polymer membrane	150-200 °C	5-400 kW, 100 kW module (liquid PAFC); <10 kW (polymer membrane)	40%	• Distributed generation	• Suitable for CHP • Increased tolerance to fuel impurities	• Expensive catalysts • Long start-up time • Sulfur sensitivity
Molten Carbonate (MCFC)	Molten lithium sodium, and/or potassium carbonates, soaked in a porous matrix	600-700 °C	300 kW-3MW, 300 kW module	50%	• Electric utility • Distributed generation	• High efficiency • Fuel flexibility • Suitable for CHP • Hybrid/gas turbine cycle	• High temperature corrosion and breakdown of cell components • Long start-up time • Low power density
Solid Oxide (SOFC)	Yttria stabilized zirconia	500-1000 °C	1 kW-2MW	60%	• Auxiliary power • Electric utility • Distributed generation	• High efficiency • Fuel flexibility • Solid electrolyte • Suitable for CHP • Hybrid/gas turbine cycle	• High temperature corrosion and breakdown of cell components • Long start-up time • Limited number of shutdowns

1.3 Introduction to PEMFC

Polymer electrolyte membrane fuel cells, presented in Figure 1.1, are also known as proton exchange membrane (PEM) fuel cells or polymer electrolyte fuel cells (PEFCs). The electrolyte is a solid proton-conducting polymer electrolyte membrane. Table 1.2 presents the basic components of a PEMFC, and outlines their description and the common materials of construction [18]. The PEMFC only need hydrogen, oxygen from the air and water to maintain membrane hydration to operate [5, 7]. Hydrogen is delivered to the anode, and it is oxidized while the oxygen is reduced into water at the cathode. The only by-product is water. The reactions that take place are [19]:

Anode half-cell reaction: $$\mathbf{H_2 \rightarrow 2H^+ + 2e^-} \quad (1.1)$$

Cathode half-cell reaction: $$\mathbf{\frac{1}{2}O_2 + 2H^+ + 2e^- \rightarrow H_2O} \quad (1.2)$$

Overall cell reaction: $$\mathbf{H_2 + \frac{1}{2}O_2 \rightarrow H_2O + Waste\ Heat} \quad (1.3)$$

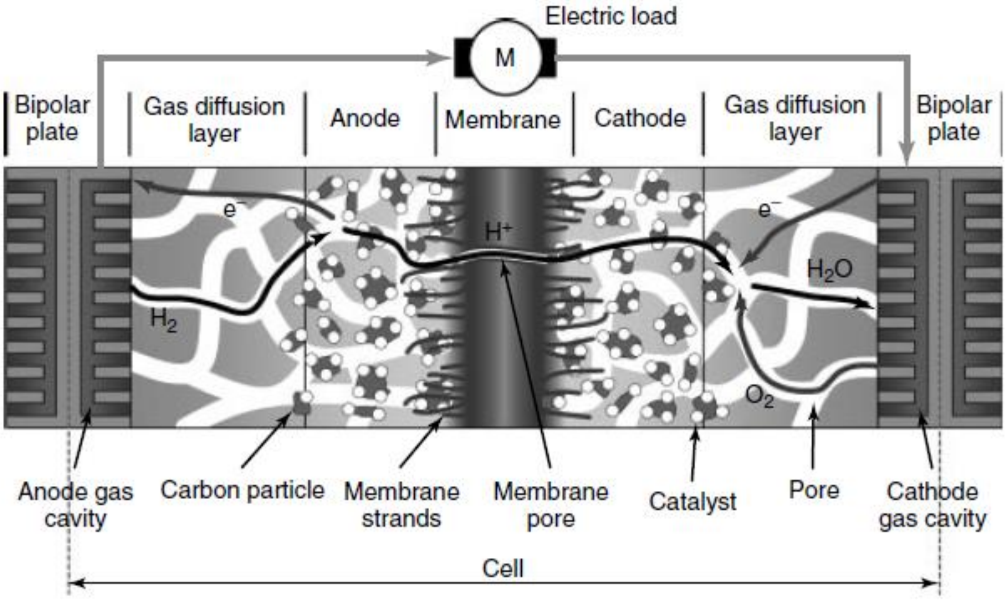

Figure 1.1 Diagram of a PEMFC [20].

Table 1.2 Basic components of a PEM Fuel Cell [18].

Component	Description	Common Types
Proton exchange membrane	Enables hydrogen protons to travel from the anode to the cathode	Persulfonic acid membrane (Nafion 112, 115, 117)
Catalyst layers	Breaks the fuel intro protons and electrons. The protons combine with the oxidant to form water at the fuel cell cathode. The electrons travel to the load.	Platinum/carbon catalyst
Gas diffusion layers	Allows fuel/oxidant to travel through the porous layer, while collecting electrons	Carbon cloth or Toray paper
Flow field plates	Distributes the fuel and oxidant to the gas diffusion layer	Graphite, stainless steel
Gaskets	Prevent fuel leakage, and helps to distribute pressure evenly	Silicon, Teflon
End plates	Holds stack layers in place	Stainless steel, graphite, polyethylene, PVC

PEM fuel cells have received much attention in recent years as they present the highest power density of all fuel cell classes (500-2500 mW cm^{-2}). Other advantages include good start-stop capabilities due to the low-temperature operation below 80 °C [5], and the low weight and volume compared with other fuel cells. They are mostly used for transportation applications, and for some stationary applications [7]. PEM fuel cells are the most common in the automotive industry [6]. The first fuel cell electric vehicle (FCEV) powered by fuel cells was launched in 1993 by Ballard [4]. Nowadays, cars and buses from different companies such are DaimlerChrysler, Toyota, Ford, General Motors are available in the market [21].

1.4 Performance of fuel cells

1.4.1 Polarization curves

In this work, the effects of CO in the performance of PEMFCs will be evaluated through polarization curves under varying operating conditions. The performance of a fuel cell is commonly determined through this electrochemical technique, which shows the variations of the voltage with current or current density (Figure 1.2). Due to irreversible losses, the voltage output of fuel cells is lower than the voltage predicted thermodynamically. The three major losses that give the polarization curve its characteristic shape are the activation, ohmic and concentration losses. Hence, the voltage output is given by [5]:

$$\boldsymbol{V = E - \eta_{act} - \eta_{ohmic} - \eta_{conc}} \tag{1.4}$$

where V is the actual output voltage, E is the thermodynamically predicted voltage output, η_{act} corresponds to the activation losses due to reaction kinetics, η_{ohmic} refers to the ohmic losses due to ionic and electronic conduction and η_{conc} represents the concentration losses due to mass transport. Each one of these losses are affected differently by the presence of CO.

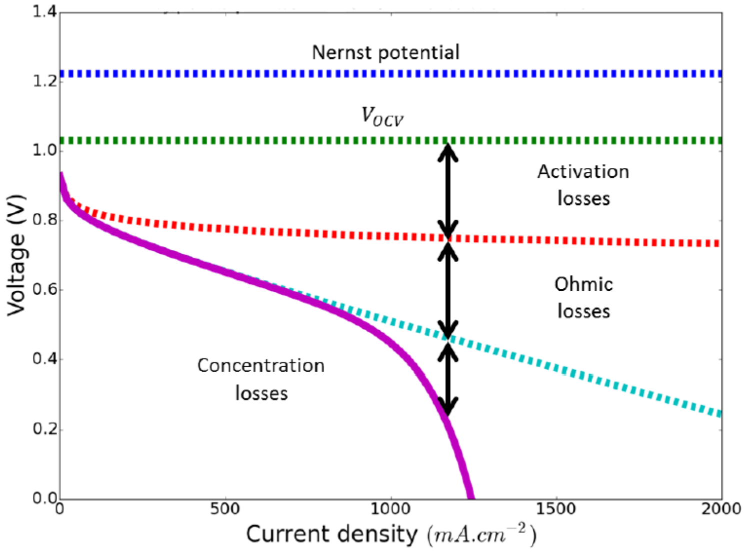

Figure 1.2 Typical polarization curve showing the different performance losses [22].

1.4.2 Reversible potential

Through thermodynamics, the theoretical limits or the ideal performance of fuel cells are established. The reversible voltage of a fuel cell, E, is related to the molar Gibbs free energy, ΔG_r, by the equation

$$\boldsymbol{\Delta G_r = -nFE} \tag{1.5}$$

where n is the electron transfer number in the reaction, F is the Faraday constant and nFE is the electrical work done by the electrochemical reaction. Gibbs free energy is dependent on both temperature and pressure, as shown by the thermodynamic equation for a hydrogen fuel cell:

$$\boldsymbol{\Delta G = \Delta G_r^0 - RT \ln \left[\frac{p_{H_2}(p_{O_2})^{1/2}}{p_{H_2O}}\right]} \tag{1.6}$$

where ΔG_r^0 is the standard reaction Gibbs free energy, R is the gas constant, T is the absolute temperature and p_i corresponds to the partial pressure of the species i. The Nernst equation is thus obtained:

$$\boldsymbol{E = E^0 + \frac{RT}{nF} ln \left[\frac{p_{H_2}(p_{O_2})^{1/2}}{p_{H_2O}}\right]} \tag{1.7}$$

where E^0 is the standard thermodynamic voltage at 25 °C. The value of E^0 is 1.229 V if the pressures of H_2 and O_2 are both 1 atm. The Nernst equation shows that E is dependent on the temperature, where an increase in temperature provokes a decrease in the theoretical voltage [5, 14, 23].

1.4.3 Activation overpotential

The activation overpotential dominates at low current density and corresponds to the voltage loss needed to surmount the activation barrier that impedes the conversion of reactants to products. The Butler-Volmer equation describes the exponential variation of the current density with an increase of the activation overpotential, and constitutes an excellent approximation for most single-step electrochemical reactions:

$$\boldsymbol{j = j_0 \left(\frac{c_R^*}{c_R^0} e^{\alpha n F \eta_{act}/RT} - \frac{c_P^*}{c_P^0} e^{-(1-\alpha) n F \eta_{act}/RT} \right)} \tag{1.8}$$

where j is the current density, j_0 is the exchange current density measured at c_R^0 and c_P^0, which correspond to the reference concentrations of reactant and product, c_R^* and c_P^* represent the surface concentrations of the rate-limiting species in the reaction, η_{act} is the activation overpotential, α is the charge transfer coefficient and n is the number of electrons transferred in the reaction. As the magnitude of η_{act} depends on the reaction kinetic parameters, in particular on the size of j_0, the improvements of the kinetic performance are focused on the increase of j_0.

At high overpotentials (greater than 50-100 mV at room temperature), the second exponential is negligible, and the equation (1.8) is reduced to

$$\boldsymbol{j = j_0 e^{\alpha n F \eta_{act}/(RT)}} \tag{1.9}$$

which can be rearranged as:

$$\boldsymbol{\eta_{act} = a + b \log j} \tag{1.10}$$

This equation is the Tafel equation, where $a = -\left(\frac{2.303\, RT}{\alpha n F}\right) \log j_0$, and the slope $b = \frac{2.303 RT}{\alpha n F}$. η_{act} is linearly dependent on the logarithmic of current density. High current densities are related to high η_{act}. Hence, the interest in this approximation, which describes irreversible reaction processes where the forward-reaction direction dominates [5]. It is expected that the presence of CO has a higher impact in the activation overpotential as the hydrogen oxidation reaction (HOR) occurring in the anode is hindered, as the affinity to Pt is higher for CO than for H_2 (see Section 2.2.2.1).

1.4.4 Ohmic overpotential

The ohmic overpotential is dominant in the intermediate current density range of the polarization curve, where a lineal variation is observed between the working potential and the current density. The ohmic losses are caused by the ionic and the electric contact resistance of the components of the stack. The electrolyte, catalyst layer, GDL, flow field plates, interfacial contacts between components, etc. contribute to the ohmic losses. In PEMFC, the proton resistance of the membrane is predominant in the total ohmic resistance. The ohmic losses follow the Ohm's Law by the equation

$$\boldsymbol{\eta_{ohmic} = jR_{ohmic}} \qquad (1.11)$$

where η_{ohmic} corresponds to the ohmic overpotential and R_{ohmic} is the is the total internal resistance [23]. Previous studies have stated that in the presence of CO, there is a decrease of protons reaching the cathode side, and the amount of water generated [24], increasing the ohmic overpotential.

1.4.5 Mass transport overpotential

At high current densities, the transfer speed of reactants and products is slower than the reaction rate, provoking a rapid decrease of the working voltage. The mass transport of reactants and products is done through convection and diffusion. While diffusion is dominant in fuel cell electrodes, convection prevails in fuel cell flow structures. Considering the reactant is consumed immediately upon arrival to the catalyst layer, the current density depends on the diffusion mass flow rate μ_{diff}, defined by the Fick's diffusion laws as

$$\boldsymbol{\mu_{diff} = -D^{eff}\frac{C_R^* - C_R^0}{\delta}} \qquad (1.12)$$

where D^{eff} refers to the effective diffusivity and δ is the electrode thickness. The current density reaches a maximum value correspondent to the limiting current density j_L when C_R^* decreases to zero:

$$\boldsymbol{j_L = nFD^{eff}\frac{C_R^0}{\delta}} \tag{1.13}$$

The reactant depletion affects the theoretical voltage and the kinetic reaction rate, from which the concentration overpotential can be estimated by

$$\boldsymbol{\eta_{conc} = c\ln\frac{j_L}{j_L - j}} \tag{1.14}$$

where *c* is a constant with an approximate value of $c = \left(1 + \frac{1}{\alpha}\right)\frac{RT}{nF}$, and that depends on the geometry and mass transport properties of the fuel cell. In order to reduce mass transport losses, increasing j_L is necessary [5, 23].

1.4.6 Other polarization losses

In practice, the OCV for PEMFC is around 1.0 V, lower than the thermodynamic predicted value of around 1.2 V. This efficiency loss is mainly due to two phenomena: electrical short-circuits, and crossover of reactants through the membrane which causes mixed-potential reaction at the opposite electrode. The difference between the measured OCV and the theoretical voltage is called the irreversible voltage loss [23, 25].

1.5 Technical Targets for PEMFC

As mentioned, there are three main technical barriers to fuel cell commercialization: cost, performance and durability. The materials and manufacturing components that represent the highest costs are the platinum group metal (PGM) catalyst, the high-membrane performance membranes and lighter, corrosion-resistant bipolar plates. Also, the balance-of-plant (BOP) components and subsystems need further development to achieve cost targets. For a better performance, thermal, water and air management as well as system start-up and shutdown time and energy/transient operation need to be improved. The operating conditions, such as impurities in the fuel and air, starting and stopping, freezing and thawing, and humidity and load cycles affect the durability of cell [10].

Different targets have been proposed to displace more established technologies. For instance, Table 1.3 presents the technical current technical status, and the targets to be obtained by 2020 which are set by the U.S. DRIVE Partnership (United States Driving Research and Innovation for Vehicle efficiency and Energy sustainability) and the U.S. Department of Energy for the automotive industry [26]. Other targets have been established for stationary (combined heat and power), backing power systems and portable power and auxiliary power applications [9].

Table 1.3 Technical targets set for integrated PEMFC power systems, fuel cell stacks and components operating on direct hydrogen for light-duty transportation applications (80 kW net) [10].

Characteristic	**Units**	**2015 Status**	**2020 Targets**	**Ultimate Targets**
Peak energy efficiency @ 25% of rated power	%	60	60	70
Power density	W/L	640	650	850
Specific power	W/kg	659	650	650
Cost	$/kW	51	40	30
Cold start-up time to 50% of rated power				
@ -20 °C ambient temperature	seconds	20	30	30
@ +20 °C ambient temperature	seconds	<10	5	5
Start-up and shutdown energy				
from -20 °C ambient temperature	MJ	7.5	5	5
from +20 °C ambient temperature	MJ	-	1	1
Durability in automotive load cycle	hours	2,500	5,000	8,000
Start-up/shutdown durability	cycles	-	5,000	5,000
Assisted start from low temperatures	°C	-	-40	-40
Unassisted start from	°C	-30	-30	-30

1.6 Research Aims

The overall objective of this thesis is to have a better understanding of the spatial and temporal variations occurring in the CO poisoning of PEMFCs for the design of more effective mitigation strategies that could improve their performance and durability. Different aims are proposed that are in line with this objective:

- Evaluate the anodic overpotentials in three different points in an MEA exposed to CO, through localised reference electrodes.
- Study the CO poisoning in a segmented-in-series PEM fuel cell system composed of five independent cells.
- Evaluate the short-circuiting technique as a mitigation strategy in a segmented-in series stack for different CO concentrations.

1.7 Thesis Overview

Chapter 2 presents an overview of the studies presented in the literature around CO poisoning in PEMFCs, the mechanisms occurring during the contamination are introduced and the mitigation strategies developed so far are described in detail. Chapter 3 describes the materials and the methodology used in the studies presented in this work. An overview of the electrochemical techniques used is also presented for a deeper understanding of the information generated. In Chapter 4 the preliminary tests in a single cell are described. These include the determination of the electrochemical surface area (ECSA) and the short-term effects of CO in the performance under different operating conditions. In Chapter 5 the results obtained from the array of localised reference electrodes are presented. These are divided according to the distinct phases of the experiment. Chapter 6 describes the information generated from the segmented-in-series system. The outcomes are presented according to the diagnostic technique used. Chapter 7 presents the evaluation of the short-circuiting as a mitigation strategy against CO poisoning. Finally, Chapter 8 presents the conclusions and future work recommended.

Chapter 2

Literature Review

2.1 Introduction

This chapter aims to provide a general overview of the studies that have looked at the poisoning of PEMFC by CO. First, the mechanisms of CO poisoning and the effects that it has on the PEMFC performance are considered. The key parameters affecting CO poisoning are identified and methods used to mitigate the effects are discussed. These mitigation strategies are divided into three groups according to how the technologies are applied: pre-treatment of reformate, on-board removal of CO and *in operando* mitigation strategies. The most promising strategies and the future direction that the research in this topic is taking are finally discussed.

2.2 Fundamental understanding

2.2.1 Hydrogen quality for PEMFC

Around 48% of worldwide hydrogen production comes from steam methane reforming (SMR) of natural gas, or other hydrocarbons [27]. This process delivers high conversion to hydrogen at a low cost and high efficiency. Other mature and commercialized technologies are auto-thermal reforming (ATR) of methane and coal gasification. Some predictions expect this to be the most economical path to hydrogen production for decades to come [28]. While this may be a convenient and economical route, the hydrogen produces is not necessarily conducive to direct use in PEMFC. The reformate obtained after a first stage of clean-up through the water-gas-shift (WGS) reaction, has a typical composition of 40 to

70% H_2, 15 to 25% CO_2, 1 to 2% CO, plus small quantities of inert gases such as water vapour and nitrogen, and sulphur impurities. It is also possible to find ammonia in the reformate at ppm levels, if it is used as a gas tracer along the distribution system [29].

Multiple purification stages are needed to reduce the CO concentration to levels conducive to PEMFC operation after the generation of hydrogen from fossil fuels. Typically, the concentration of CO obtained after these processes is of the order of 10 ppm. Purification methods include adsorption, membrane separation, scrubbers, and selective reaction. Pressure swing adsorption (PSA) is the most common technology, accounting for 85% of the hydrogen purified [28]. CO preferential oxidation (PROX) and the CO-selective methanation (SMET) are receiving increasing interest and will be discussed in Section 2.3.1 [30]. These clean-up stages can require an order of magnitude higher plant volume than that for the reformer and fuel cell stack combined [31], increasing the costs and parasitic power demand. It has been estimated that in large-scale chemical plants, separation and purification of hydrogen can account for between 50 and 80% of the total capital investment [32]. The deployment of fuel cells is hindered as a consequence [33].

The reformation of liquid and renewable biomass materials, such as methanol and ethanol, is being studied as an alternative to natural gas, especially due to the advantage of liquid storage and transport compared to gases [29, 34]. Electrolysis of water is being extensively developed as a route to hydrogen from ‘green’ electricity [27]. Other sources include photosynthetic microorganisms, the photoelectrolysis of water, the thermal dissociation of water and thermochemical cycles [35].

2.2.2 Mechanisms of CO poisoning

2.2.2.1 Electrochemical reactions in a PEMFC

Figure 2.1 summarises the key components of a PEMFC along with the action of CO in the fuel stream on a conventional (e.g. Pt) catalyst. The hydrogen oxidation reaction (HOR) takes place at the anode through the Tafel [36], Heyrovsky [37] and Volmer [38] mechanisms. The HOR usually takes place through the Tafel-Volmer, and/or the Heyrovsky-Volmer routes [23], although alternative routes are under study [39].

In the early studies about HOR, it was reported that the reaction was insensitive to surface structure [40]. More recently, it was found that the reaction rate is dependent on the surface structure and the electrolyte [23, 41]. For the most common anode catalyst, platinum, the rate of hydrogen oxidation depends on the crystal orientation following the trend Pt(110)>Pt(100)>Pt(111). The Tafel reaction is the rate-limiting step in the case of Pt(110) [42, 43]:

$\mathbf{2Pt + H_2 \leftrightarrow 2Pt - 2H_{ads}}$ (Tafel reaction) (2.1)

$\mathbf{Pt + H_2 \leftrightarrow Pt - H_{ads} + H^+ + e^-}$ (Heyrovski reaction) (2.2)

$\mathbf{2Pt - H_{ads} \leftrightarrow 2Pt + 2H^+ + 2e^-}$ (Volmer reaction) (2.3)

CO competes with hydrogen for the active sites on the platinum under normal anode operating potentials [44]. CO adsorbs on the Pt surface more easily than H_2 (heat of adsorption of CO on Pt is 134 kJ mol^{-1}, and for H_2 is 87.9 kJ mol^{-1}) [45]. The available surface for the HOR is reduced while the CO accumulates on the platinum surface [46]. The magnitude of the surface covered by CO is determined by the CO adsorption and/or re-adsorption (Reactions 2.4 and 2.5) [47], the electroreduction of CO_2, and the CO removal through oxidation (Reaction 2.6), which occurs through the reactant pair mechanism [48]. These processes compete with each other, depending on conditions [49].

$\mathbf{CO + nPt \leftrightarrow Pt_n - CO_{ads}}$ (2.4)

$\mathbf{2CO + 2(Pt - H_{ads}) \leftrightarrow 2(Pt - CO_{ads}) + H_2}$ (2.5)

$\mathbf{Pt - CO_{ads} + Pt - H_2O_{ads} \leftrightarrow 2Pt + CO_2 + 2H^+ + 2e^-}$ (2.6)

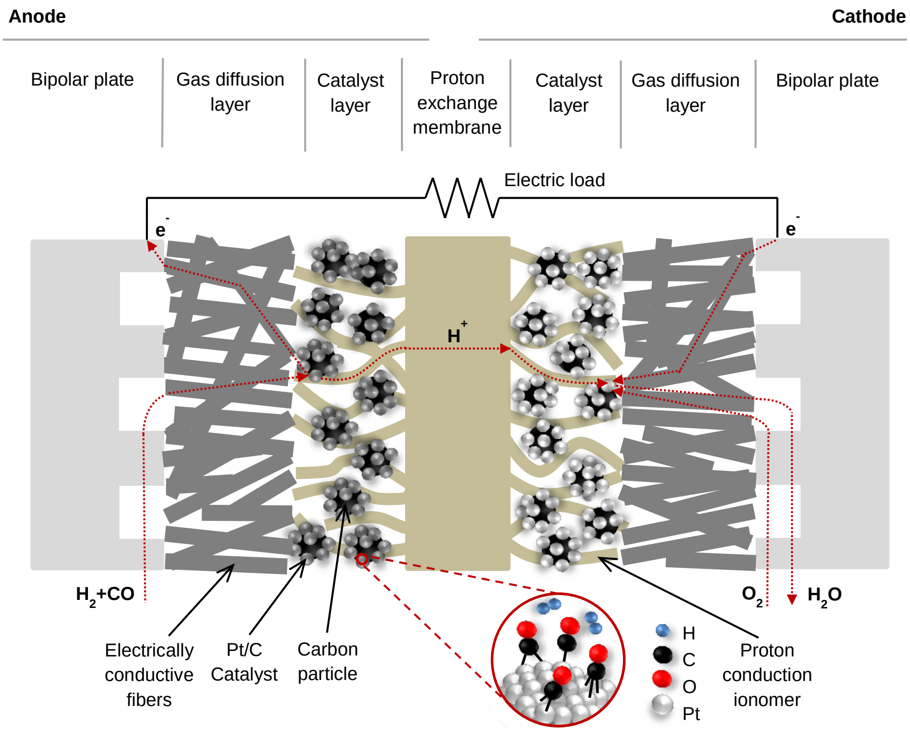

Figure 2.1 Diagram showing the key components of the PEMFC along with the action of CO in the hydrogen feed on the anode catalyst.

Figure 2.1 also shows that different adsorption modes exist for CO on Pt: linear or on-top bonding, bridge or twofold site bonding and hollow or threefold site bonding. The type of CO adsorption site bonding is related to the surface structure at saturation coverage [41]. It has been shown that at less than 50% surface coverage, the bridge-bonded dominates. The linear bonded type is dominant at higher surface coverage (Figure 2.2) [50].

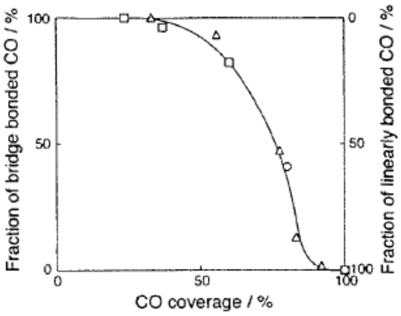

Figure 2.2 Proportion of bridged-bonded or linearly bonded CO sites on Pt at different CO concentrations (O) 10 ppm; (□) 20 ppm; (Δ) 40 ppm; (●) 100 ppm [50].

The increasing coverage of CO on the platinum surface reaches a threshold where the electro-oxidation of CO takes place. For pure platinum electrodes, it takes place above ≈ 0.6 V (vs. RHE) [51]. At 25 °C, the CO contained in 1% CO/hydrogen mixture blocks 98% of the active sites [52]. Figure 2.3 presents the cyclic voltammograms obtained for the CO stripping on a Pt/C catalyst at 23 °C [49].

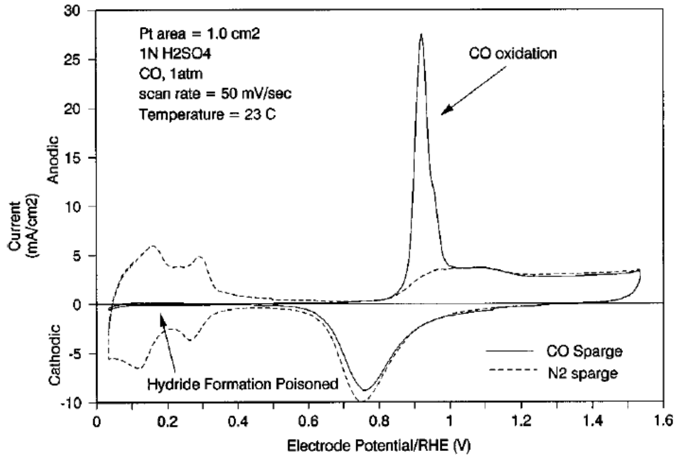

Figure 2.3 Cyclic voltammograms obtained on polycrystalline Pt at 23 °C in the presence and absence of CO [49].

2.2.2.2 "Self-oxidation" or sustained potential oscillations

Murthy *et al.* first reported the oscillatory behaviour of the potential in an operando cell exposed to CO/H_2 at a constant current [53]. Zhang and Datta subsequently reported more details about this behaviour [54, 55]. These oscillations were also presented by Hanke-Rauschenbach *et al* as part of a review of nonlinear dynamics of fuel cells [56]. As the CO accumulates at the surface of the catalyst, the anodic overpotential increases. The higher potential attained allows the oxidation of the CO (as shown in Figure 2.3), and the cell voltage increases (anode overpotential decreases) to the original value [57], with the process of CO build-up occurring again, this cycle leading to anode overpotential oscillations, as shown in Figure 2.4 for different operating conditions.

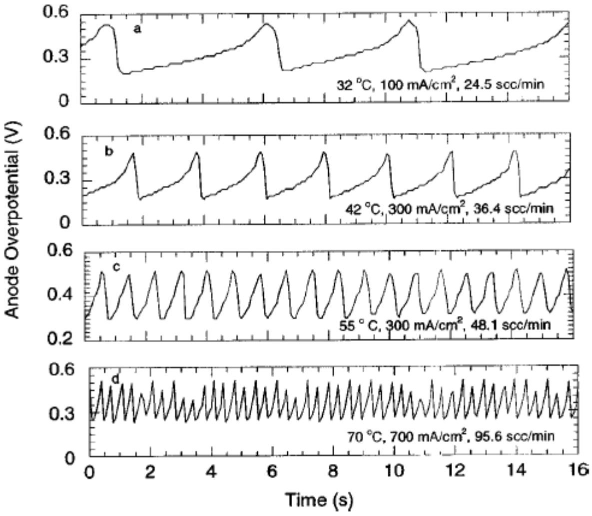

Figure 2.4 Anode overpotential oscillations caused by exposure to CO/H_2 in a PtRu/C anode catalyst. The operating conditions of cell temperature, current density, and anode inlet flow rate are: a) 32°C, 100 mA cm^{-2}, 24.5 sccm; b) 42°C, 300 mA cm^{-2}, 36.4 sccm; c) 55°C, 300 mA cm^{-2}, 48.1 sccm; d) 70°C, 700 mA cm^{-2}, 95.6 sccm [54].

This behaviour was first observed in PtRu/C [53-55], Pd-Pt/C and Pd/C [58] before being studied in Pt/C systems [59]. The nature of the oscillations depends on the temperature, current density, anode CO concentration and flow rate. Generally, the higher the concentration of CO and anodic flow rate are, the shorter the periods are. The period decreases with increasing current density or temperature [54, 60].

The dynamics of the oscillations were studied by Mota *et al.* at different current and anode flow rates, observing periodic and nonperiodic states. The transition from ‘period-1’ to ‘period-2’ and chaotic states occurs with an increase in current at a fixed flow, or over the decrease of the flow rate at a constant current [61]. This behaviour was corroborated in spatio-temporal models [62, 63] and current distribution measurements [64].

Lu *et al.* determined that the time-averaged power density obtained with self-sustained oscillations under galvanostatic operation is higher than when in potentiostatic mode. The measurement of the concentration of CO at the anode outlet under constant current contributed to confirm the electrochemical oxidation of CO, which is responsible for the difference in the power output between the two operation modes [60]. Subsequently, Lopes *et al.* showed the production of CO_2 during the oscillatory behaviour, and presented a model that predicts the coverage of the different species in the electrode surface [65].

2.2.3 Effects of CO on the performance of PEMFCs

2.2.3.1 Effect of operating parameters

CO poisoning affects PEM fuel cell performance in three major ways: the electrode kinetics, conductivity and mass transfer [29]. Blocking of catalyst active sites affects the kinetics of electrocatalysis [45]. Figure 2.5 summarises the effects of concentration, exposure time, temperature, anode flow rate and operating pressure, from a range of experimental investigations.

Early studies show that the effect of CO becomes more severe on Pt electrocatalysts when the CO concentration and time are increased [66-68]. At higher concentrations (typically higher than 100 ppm CO), two slopes are observed in the polarization curves. The slope at lower current densities is due to the adsorption and oxidation of hydrogen and CO at the anode. At higher current densities, the potential at the anode reaches values at which the adsorbed CO is oxidized to CO_2 and the reaction rates for hydrogen adsorption and oxidation are increased [66]. Over time, as the adsorption of CO increases, the performance decreases significantly until it reaches a steady state [66, 69].

Temperature has a strong impact on the effect of CO poisoning. The adsorption of CO is favoured at lower temperatures, blocking the oxidation of H_2 [70]. Zamel *et al.* reported that at higher temperatures the poisoning occurs faster, resulting in a more rapid performance drop towards the steady state [71]. Dhar *et al*. found that the CO coverage follows a Temkin isotherm at a fixed current density, which can be written in the form [70]:

$$\boldsymbol{\theta_{CO} = \frac{-\Delta Go^{\circ}}{r} - \frac{RT}{r}\ln H + \frac{RT}{r}\ln\left(\frac{[CO]}{[H_2]}\right)} \tag{2.7}$$

Where θ_{CO} is the CO coverage, ΔG_o^0 is the standard free energy of adsorption, r is the interaction parameter, and H Henry's law constant for CO solubility (atm L mol^{-1}). This relation shows that the increase in the anodic polarization is due to the replacement of H_2 molecules by CO. The interaction parameter is highly dependent on the catalyst structure [70]. As the anode flow is increased, the voltage of the cell decreases due to the increased total amount of CO that is exposed to the anode. Additionally, the time needed to reach steady-state is diminished as the flow rate is increased.

Another important operating parameter is the cathode pressure. Oxygen permeates through the membrane from the cathode to anode and contributes to the oxidation of the CO into CO_2 [72]. Figure 2.5 (e) shows the combined effect of the concentration of CO and the operating pressure [73].

The influence of the anode feed relative humidity has also been studied. Iorio *et al*. determined that the CO-stripping potential of Pt/C and PtRu/C electrodes decreased at higher water vapor pressure [74]. In high-temperature PEMFCs (HT-PEMFCs), an increase in the humidity reduces the anodic overpotential. This is due to the presence of the OH_{ads} groups, which are consumed in the oxidation of CO (Figure 2.4 (f)) [75-77].

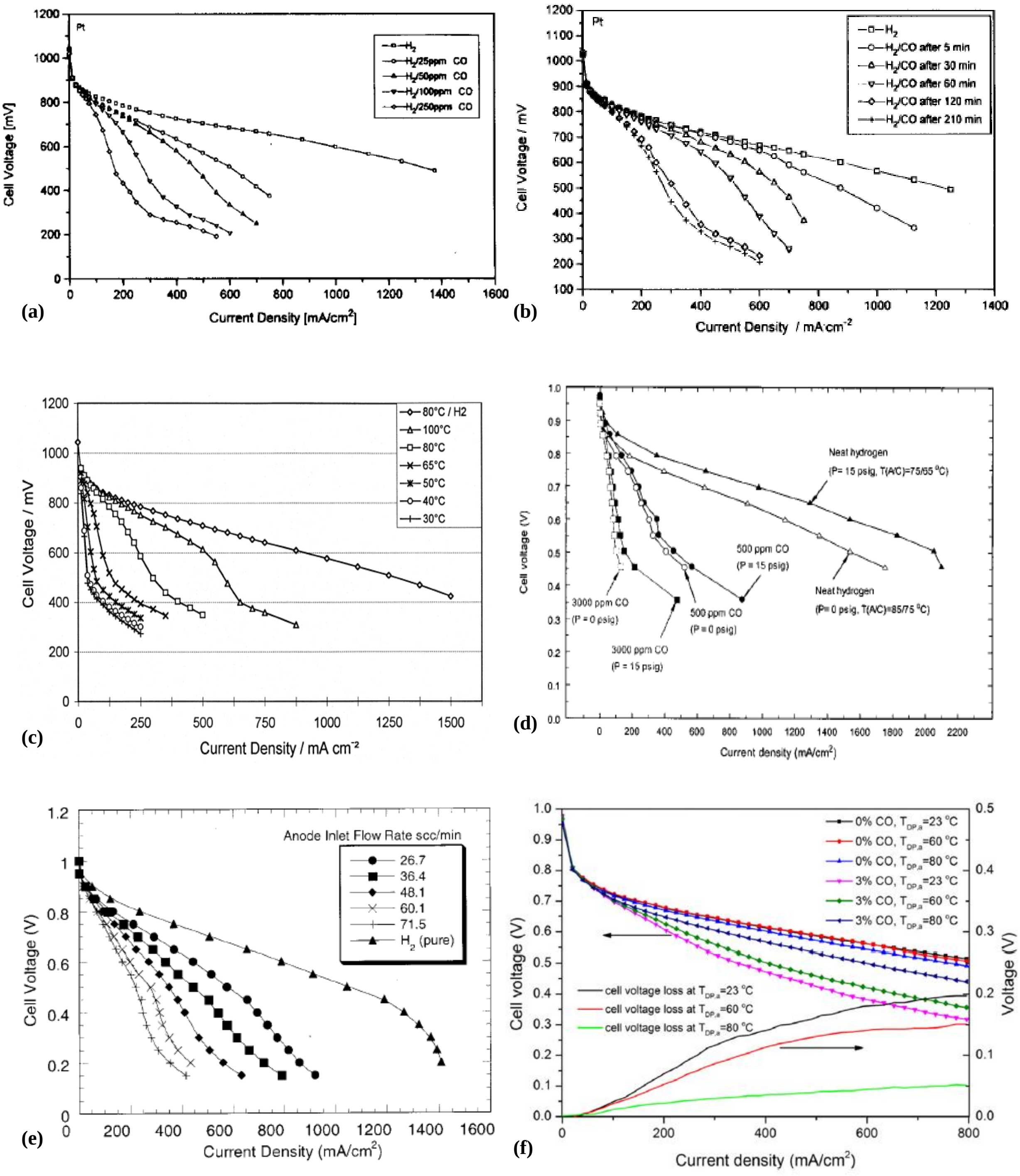

Figure 2.5 Operating parameters that influence the performance of PEMFC in the presence of CO in the anode inlet. (a) Effect of the concentration of CO (ppm) [66], (b) Effect of the exposure time with 100 ppm CO/ H_2//O_2 [66], (c) Effect of the temperature [78], (d) Effect of the pressure and concentration of CO [73], (e) Effect of the anode flow over the exposure to 108 ppm CO/H_2 [72] and (f) Effect of the anode dew point temperatures in HT-PEMFC [75].

2.2.3.2 Influence of additional contaminants

2.2.3.2.1 The combined effect of CO and CO_2

The presence of CO_2 in the anode inlet is closely related to the CO poisoning, as the reverse water-shift reaction (RWGS) produces CO in the presence of platinum [49, 77, 79-82]. 100-200 ppm CO can be reached with a 75% H_2/25% CO_2 feed [49]:

$$\boldsymbol{2Pt + H_2 \rightarrow 2Pt - 2H} \qquad (2.8)$$

$$\boldsymbol{CO_2 + 2Pt - H \rightarrow Pt - CO + H_2O + Pt} \qquad (2.9)$$

Due to the endothermic nature of the RWGS, the production of CO is increased at higher temperatures [75, 79]. As incrementing the temperature also favours the CO electro-oxidation, the degradation of cells is determined by the ratio: $CO_{production}/CO_{electro\text{-}oxidation}$, HT-PEMFCs are particularly sensitive to this [77]. The humidity also has a direct impact on RWGS CO_2 poisoning, as at higher water content the CO produced is oxidised through the water gas shift reaction [75, 77, 79].

The combined effect of CO and CO_2 in the anode inlet has been studied. As the adsorption of CO is much faster than the RWGS, the polarization due to the presence of CO in the anode inlet is higher than for CO_2. This distinction is more evident at high concentrations of CO, as less Pt-H sites are available for the RWGS reaction to take place [49, 79, 83]. Figure 2.6 shows the combined effect of CO and CO_2 on an HT-PEMFC [75].

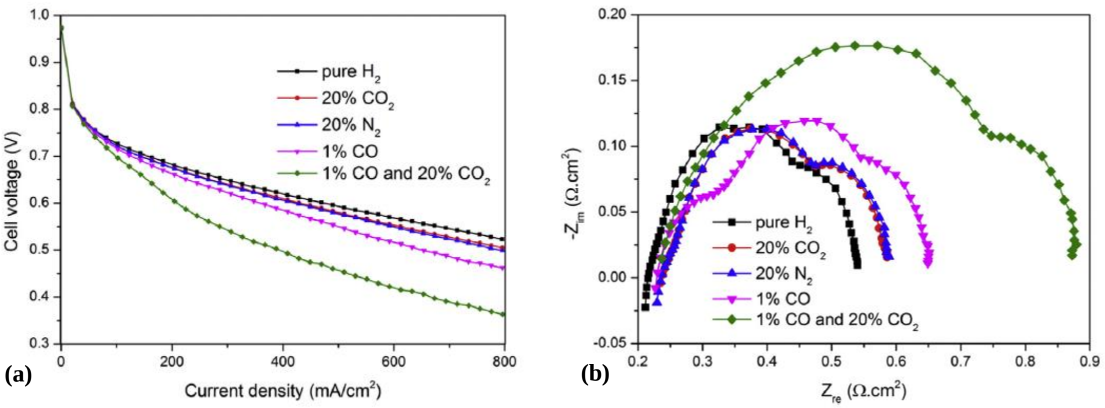

Figure 2.6 Effects of 1% CO, 20% CO_2 and a mixture of both contaminants on the operation of a high-temperature fuel cell, compared with the injection of 20% N_2: (a) polarization curves, and (b) galvanostatic electrochemical impedance spectra [77].

2.2.3.2.2 The combined effect of CO and H_2S

Rockward *et al*. presented the contamination of multiple components in a PEMFC. The combination of H_2S and CO, in particular, was studied through cyclic voltammetry. It was observed that in the presence of both components, the CO is displaced from the surface (Figure 2.7). The longer the exposure time, the more the CO is displaced and the H_2S is adsorbed [84]. This phenomenon could be explained by the H_2S affinity for platinum, which is higher than for CO. S-species are a common component in the reformate, capable of irreversible effects in the cells [85].

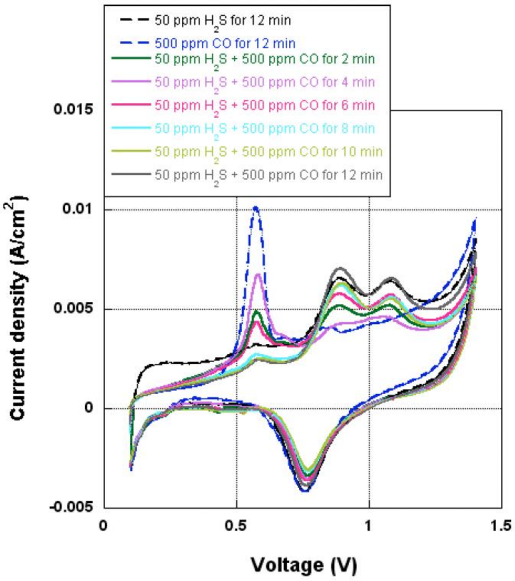

Figure 2.7 Cyclic voltammograms obtained for exposure to 500 ppm CO and 50 ppm H_2S at 2, 4, 5, 8, 10 and 12 minutes, showing the displacement of CO in the presence of H_2S [86].

2.2.3.2.3 The combined effect of CO, *H_2S, formic acid, benzene and ammonia*

Wang *et al*. evaluated the additive effect of other common impurities in hydrogen. The effect of 0.2 ppm CO, 4 ppb H_2S, 0.2 ppm formic acid, 2 ppm benzene and 0.1 ppm ammonia on hydrogen was evaluated individually, without any significant effect on the performance of the cell. The mixture did not have a major impact either. However, when the concentration of the contaminants was increased five times, the effects were discernible (Figure 2.8). Subsequently, cell performance almost fully recovered, but a permanent degradation of the membrane was observed [86].

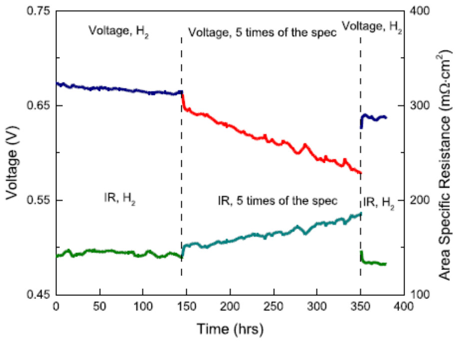

Figure 2.8 Effect of a mixture comprising 1 ppm CO, 20 ppb H_2S, 1 ppm formic acid, 10 ppm benzene and 0.5 ppm ammonia in hydrogen on the voltage of a cell operated galvanostatically at 1000 mA cm^{-2} [86].

2.2.3.2.4 *The combined effect of CO and toluene*

Toluene (C_7H_8) is an aromatic hydrocarbon, also present in the reformate [86-88]. The effects of single-component C_7H_8 and CO, and mixtures thereof, have been studied [88-90]. Concentrations of 2 ppm or 20 ppm C_7H_8 did not have a significant effect on the performance of the cell due to its hydrogenation to methylcyclohexane (C_7H_{14}) [88, 89]. The effects of a mixture of 2 ppm C_7H_8 with 0.2 ppm CO had the same effects than the CO alone [89]. However, when 20 ppm C_7H_8 was mixed with 2 ppm CO, the resultant overpotential increased to higher values than the sum of the individual contributions (Figure 2.9). As the CO is adsorbed on the surface, the HOR and C_7H_8 hydrogenation compete for the active sites, hampering the fuel cell performance [88]. Angelo *et al*. subsequently evaluated the effects of a mixture containing 0.2 ppm CO and 2 ppm C_7H_{14}. It was found that the effects on the performance were similar to the exposure of CO alone [89].

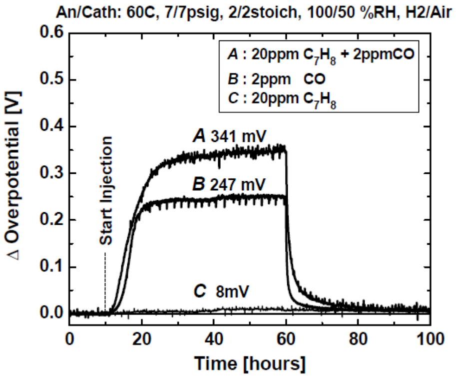

Figure 2.9 Comparison of the cell overpotentials resulting from exposure to 20 ppm C_7H_8, 2 ppm CO and a mixture containing 20 ppm C_7H_8 and 2 ppm CO under galvanostatic control at 1 A cm^{-2} (60 °C) [88].

2.2.4 Contamination of the cathode

In the presence of CO at the anode, it can pass through the membrane and be absorbed on the cathode catalyst, especially on the sites closer to the membrane. Cyclic voltammetry was used to prove the presence of CO on the cathode. The potentials of both electrodes are affected simultaneously (Figure 2.10). Different parameters affect the CO crossover, including the porosity, levels of humidification and the thickness of the membrane, and the pressure difference between anode and cathode. A fully hydrated membrane reduces CO crossover [91, 92].

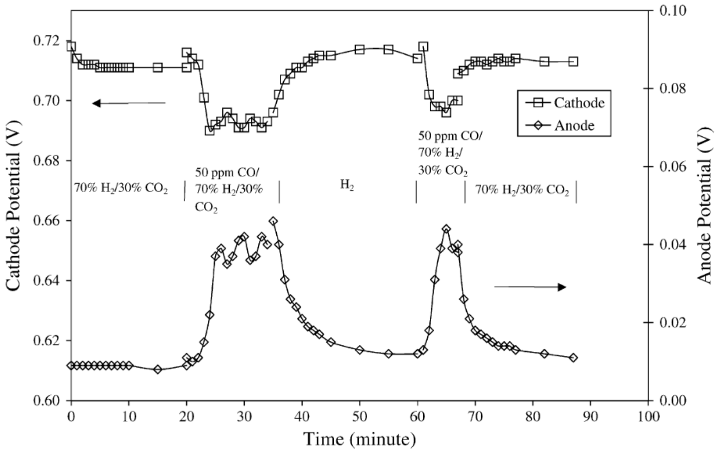

Figure 2.10 Evolution of the anode and cathode potentials over time in a PEMFC operated at 300 mA cm^{-2} with different compositions of anode fuel. Anode: Pt-Ru (0.62 mg cm^{-2}), and cathode: Pt (1.8 mg cm^{-2}) [94].

Reshetenko *et al.* presented the study of a segmented cell exposed to 2 ppm CO/H_2 in H_2/O_2, H_2/air and H_2/H_2 systems under galvanostatic mode at various current densities up to 1.4 A cm^{-2}. Both electrodes showed a drop in the ECSA [93, 94]. The active area loss in both electrodes has been confirmed in long-term (about 1000 hour) experiments under cyclic exposure to CO [95], and under different load cycling protocols [96].

Wagner *et al.* studied the poisoning of CO through electrochemical impedance spectroscopy, and showed an increase on both electrodes at constant cell voltage. At constant current, the increase on the impedance resulted mainly by the anode contribution [97]. This information was complemented by the spatial electrochemical impedance spectroscopy results, where the increase on both electrodes was observed at constant current in the presence of 2 ppm CO (Section 2.2.6.3) [93, 94].

Other studies have focused on the effect of CO in the anode, on the corrosion of carbon supports in the cathode. Parry *et el.* shown through XPS a decrease in the corrosion of the carbon catalyst-support in the cathode in the presence of 5 ppm CO in the anode. This effect was explained by the reduction of the reverse proton pumping from the cathode to the anode [45, 98]. In an HT-PEMFC, CO in the range of 0.1-1.3% was added directly to the cathode to evaluate the corrosion rate of carbon-supports. A competition between CO, O_2 and H_3PO_4 at the three-phase boundaries was shown. The H_3PO_4 molecules that hamper the performance of the cell are replaced by CO. Hence, a low CO content in the cathode side increases the cell potential. Higher concentrations of CO are detrimental due to extensive blockage of the active sites [99].

2.2.5 Long-term studies

Fewer studies have considered the long-term degradation of PEM fuel cells when exposed to CO. Angelo *et al.* reported the loss in the active area of both electrodes over 1000 hours with repetitive exposure to 2 ppm CO, showing the negative impacts of CO in the performance and durability of the cell (Figure 2.11) [95]. Profatilova *et al.* studied load cycling protocols in the presence of CO for about 1000 hours, and confirmed the irreversible losses in the active surface of the electrodes. The main accelerating aging parameters were also identified, which include the CO concentration, the amplitude and frequency of current load cycling, and the application of intermediate electrochemical in situ characterizations [96].

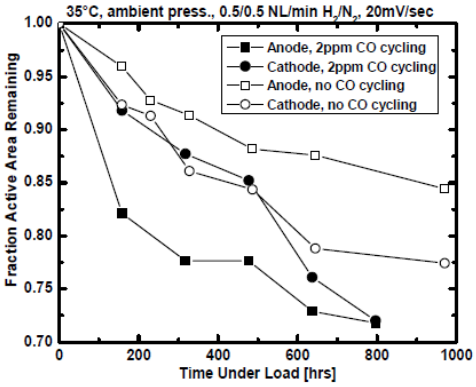

Figure 2.11 Evolution of active area loss in the anode and cathode over long term operation under repetitive exposure to 2 ppm CO [95].

Franco *et al*. examined the effects of 5 ppm CO on an MEA after 600 h under two different current-cycle protocols, representative of transport applications:

- Protocol $0/I_{max}$: alternation of 30 min at 0 A cm^{-2} and 30 min at 0.54 A cm^{-2}
- Protocol I_{min}/I_{max}: alternation of 30 min at 0.108 A cm^{-2} and 30 min at 0.54 A cm^{-2}

Figure 2.12 presents the results of both tests. It was found that the current-cycle operating conditions are strongly related to the effects of CO on the cell potential degradation rate. Under the $0/I_{max}$ protocol, the performance of the cell is degraded in the presence of CO in the short and long-term, mainly because of the contamination of CO that blocked the anode catalytic sites. It is not the case for the long-term degradation under I_{min}/I_{max}, where it is lower under H_2+CO than with pure H_2. As the fuel starvation is higher under the I_{min}/I_{max} protocol, the concentration of the permeated O_2 in the anode is accumulated. The O_2 reacts with the CO, reducing both the poisoning and the carbon-support corrosion on the cathode.

The corrosion decreases the cathode thickness and the catalyst active surface area, degrading the performance of the cell. Thus, the CO poisoning in the anode can be used as a tool to mitigate the cathode catalyst-support corrosion and increase the durability of the MEA [100]. The finding was confirmed through XPS quantitative characterizations by Parry *et al*. that observed the decrease of the reverse proton pumping effect between the cathode and the anode in the presence of CO [98].

More recently, Chandesris *et al*. studied the degradation heterogeneities in a stack exposed to reformate. It was found that the cathode outlet aged more severely than the inlet, and that the anode outlet would lose more CO tolerance [101].

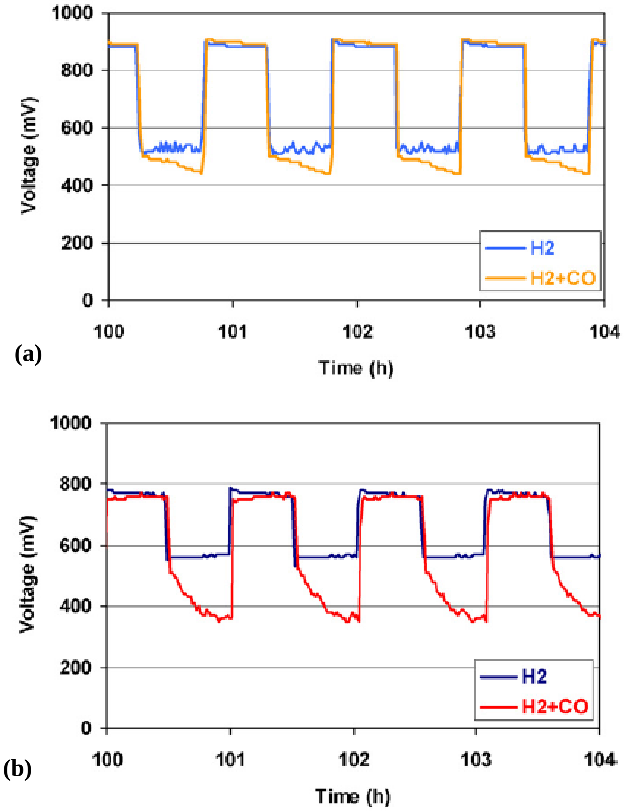

Figure 2.12 Long-term effect of H_2 and 5 ppm CO/H_2 for 0/I_{max} (a) and I_{min}/I_{max} (b) current-cycle protocols after 100 hours of operation [100].

2.2.6 Spatial distribution of the CO adsorption

2.2.6.1 Distribution in a single channel

The distribution ‘pattern’ of CO poisoning across the extent of the anode was studied by Brett *et al.* Localised CO stripping and adsorption transients were used to determine the distribution of CO to either side of a single linear flow channel (Figure 2.13). Low flow rates result in anisotropic distributions of CO away from the channel, and higher flows present a more uniform distribution. The advection along the channel and the lateral diffusion compete between each other. The dispersion of CO is a result of these two mechanisms [102]. The results obtained in this study helped to develop a model able to predict the effects of transient poisoning, which are present, in particular, during the system start-up, in the distribution of the CO adsorption. A good agreement with the experimental results was observed [103].

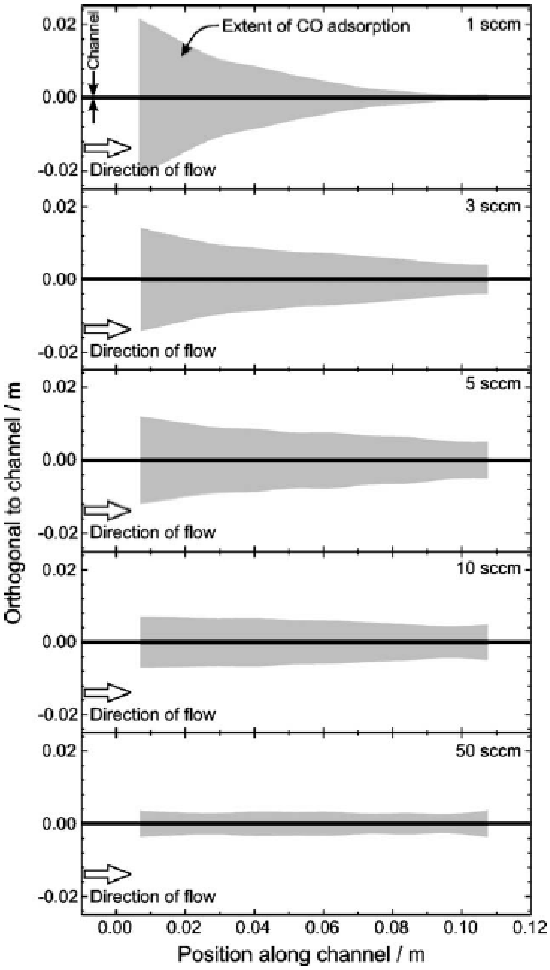

Figure 2.13 Distribution of the CO adsorption in a single cell at different flow rates of N_2, and a constant CO dose of 0.2 cm^3 [102].

2.2.6.2 Current density distribution

Different authors proposed the use of segmented cells to evaluate the current distribution across a cell and assess the effect of CO poisoning [82, 93, 94, 104, 105]. It was found that under galvanostatic control and in the absence of self-sustained potential oscillations (usually low concentrations of CO), the distribution of the surface coverage by CO was uneven as the adsorption of CO is faster at the inlet than at the outlet (Figure 2.14 (a)) [93, 94, 104, 105]. In the presence of potential oscillations, where the hydroxides formed at the surface of the catalyst assist the CO oxidation, the effects of the otherwise uneven distribution are diminished (Figure 2.14 (b)) [82]. In potentiostatic mode, the anodic potential is maintained below the CO oxidation potential so that no substantial CO removal takes place [82]. More research is needed to understand the mechanisms occurring under potentiostatic control as Tingelof *et al.* reported an uneven distribution of the poisoning [82], contrary to Boaventura *et al.* that described an even distribution [105].

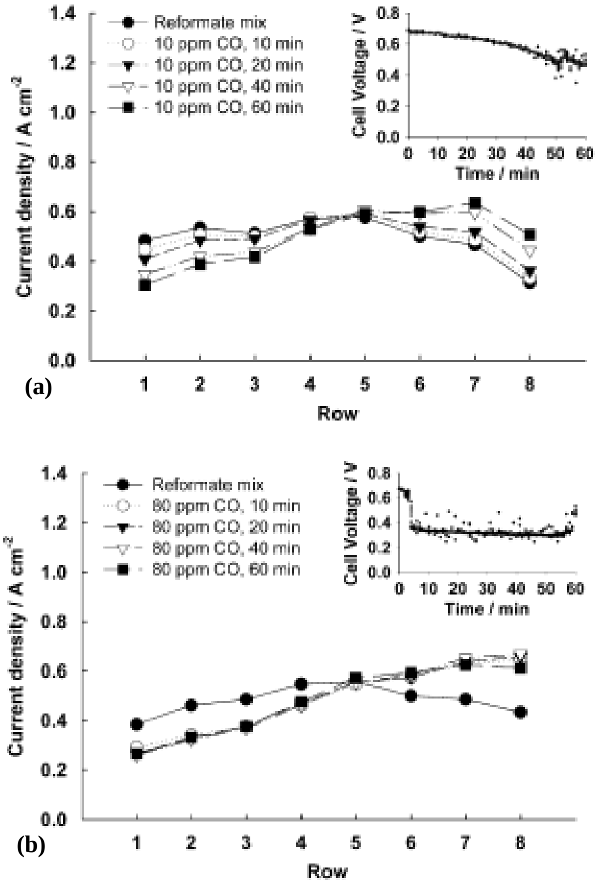

Figure 2.14. Current distribution transient behaviour of a cell (Pt/C) operating under galvanostatic control (0.5 A cm^{-2}) exposed to a simulated reformate gas mixture containing (a) 10 ppm CO, 50% H_2, 40% CO_2 and 10% N_2 and (b) 80 ppm CO, 50% H_2, 40% CO_2 and 10% N_2 [82].

2.2.6.3 Segmented electrochemical impedance spectroscopy (EIS)

Electrochemical impedance spectroscopy (EIS) has been used to evaluate the progress of the CO poisoning. It constitutes an effective diagnostic technique to identify the contamination and to study the mechanisms involved in it [106, 107]. Considering the changing nature of the contamination over time, new methods for the interpretation have been developed. These techniques include real-time drift compensation, time course interpolation and Z-HIT refinement [97, 108]. During the contamination, an increase in the total impedance of the fuel cell is observed. In the case of galvanostatic operation, a pseudo-inductive behaviour is observed in the low frequencies region (< 3 Hz) [97, 108, 109]. And, under potentiostatic control this behaviour is observed at a critical potential, which is coincident with the ignition potential and is dependent on the catalyst in use [110].

The segmented spatial electrochemical impedance spectroscopy (EIS) studies presented by Reshetenko *et al.* evaluated the dynamic response of a cell exposed to 2 ppm CO/H_2 in H_2/O_2, H_2/air and H_2/H_2 systems. Figure 2.15 presents the case of a H_2/air system. In previous studies, it was assumed that under galvanostatic control the changes in the EIS spectra were due exclusively to anode contributions [97, 108]. In this study, it was found that there is an increase of charge transfer resistance for both, the anode and the cathode, confirming that the CO also impacts the electrochemical processes in the cathode. Additionally, the pseudo-inductive behaviour at low frequency was observed in the first segments of the cell (more severely contaminated) for H_2/air and H_2/H_2 systems, which was attributed to the surface relaxation of the anode, related to the competitive electrochemical oxidation of H_2 and CO. The electric equivalent circuit was adapted to include this contribution. For this concentration, the H_2/O_2 operation did not present this behaviour due to the predominance of the direct chemical oxidation of CO by the diffused O_2 [93, 94].

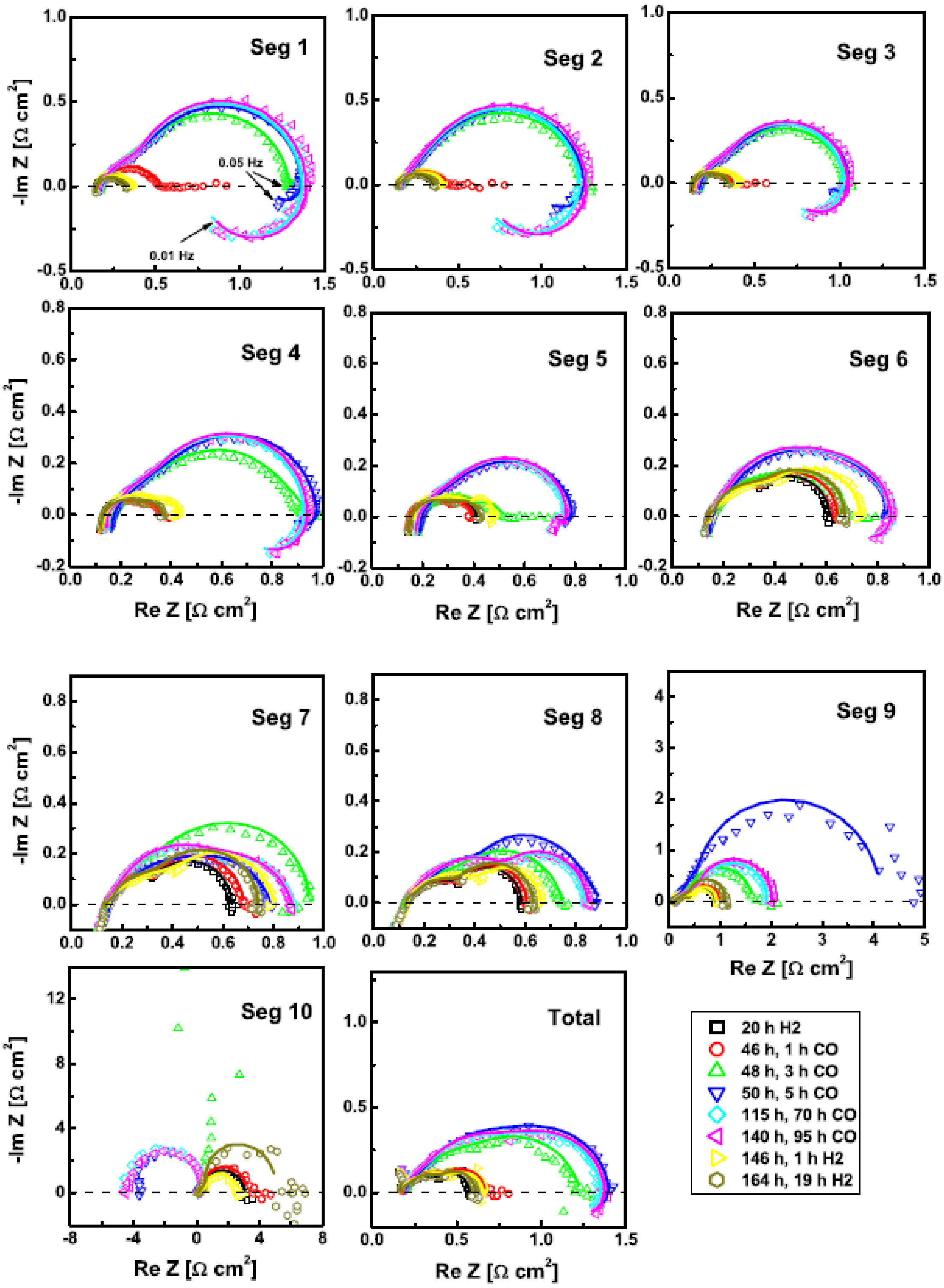

Figure 2.15 Electrochemical impedance spectra evolution obtained for a segmented cell exposed to 2 ppm CO. The ten segments follow a serpentine flow, where segment 1 is closer to the anode inlet. A pseudo-inductive behaviour is observed in the first segments in a H_2/air system. The experimental data is represented by symbols, while the modelling results by solid lines [94].

2.3 Mitigation strategies

The development and optimization of mitigation strategies that could enhance the CO tolerance of fuel cells is a major area of interest. Various mitigation strategies have been proposed in order to reduce the CO content after the first stage of purification is achieved by the WGS reaction. The CO concentration after this process reaches up to 3% [28]. According to the means by which the technologies are applied, these can be divided into three groups: (i) the pre-treatment of reformate; (ii) 'on board' CO removal, and (iii) in-operando strategies (Figure 2.16). Their development follows different approaches that include the development of new materials, the supply of feed gases, variation on the operating conditions, or the modification of the MEA. An overview of the proposed techniques is presented in this section. The choice of the technique will depend on the specific requirements of the system.

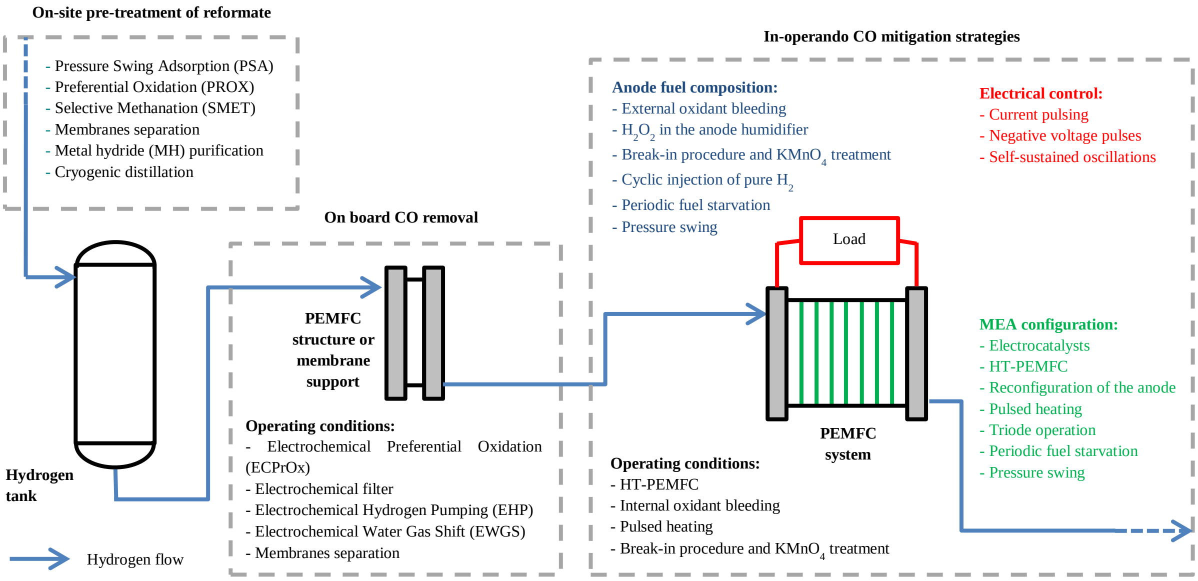

Figure 2.16 Summary of the proposed mitigation strategies for CO poisoning in PEMFCs.

2.3.1 Pre-treatment of reformate

The processes described here are well-established on-site technologies. Although there are more options available for the separation of hydrogen, here the focus is on the removal of

CO and summarised in Table 2.1. The maximum concentration of CO obtained after these processes is 10 ppm CO. There are different categories, including adsorption, membranes, scrubbers, and selective reaction. Around 85% of the hydrogen production units worldwide use the pressure swing adsorption (PSA) as the purification process [28].

Table 2.1. Most deployed pre-treatment technologies for the removal of CO from reformate.

Mitigation strategy	**Subdivision**	**Advantages of the technique**	**Disadvantages of the technique**	**Scale of use**	**Hydrogen output (%)**		**Comments**	**References**
					Purity	**Recovery**		
Pressure Swing Adsorption (PSA)	N.A.	- Fast and continuous without the disruption of the regeneration processes of the adsorbents. - The produced H_2 is at the same pressure as the feed.	- In order to reach high removal efficiencies, a high pressure (between 5 and 10 bar) is needed. - The process requires complex operation.	Large	99-99.999%	70-85%	- 85% of the hydrogen produced worldwide is purified through this technique.	[3, 111-113]
Preferential Oxidation (PROX)	N.A.	- Small amounts of CO react in the presence of large quantities of H_2. - Continuous operation. - Low energy is necessary for the provision of oxygen as it comes from air.	- Careful control of the O_2/CO ratio is needed. - The risk of a spontaneous explosion. - Bulky and complex system. - The hydrogen is consumed as a side reaction.	Small	99.999%			[28, 30, 114, 115]
Selective Methanation (SMET)	N.A.	- No other gas is needed for the reaction to take place. - No advanced controls needed.	- High hydrogen waste. - Low performance of the Ni- and Ru- based catalysts used.	Small	99.999%			[30, 114, 115]
Selective Membranes	Pd based membranes	- Separation in one step. - Low energy consumption. - Continuous operation. - Mild conditions of separation. - High selectivity of H_2. - Capability of scaling.	- Fouling tendency. - Low membrane lifetime. - High costs. - Other contaminants, such as N_2.and CH_4, are not removed.	Small to large	99.9999%	< 99%	- Other types of membrane are available. However, the dense metallic membranes, especially the Pd alloys are more suitable for hydrogen separation.	[28, 111-113, 116, 117]
	Two-dimensional membranes	- High selectivity. - High permeability. - Removal of different contaminants, sucha as CH_4 and CO_2.	- Limited or inexistent experimental preparation of the materials. - Lack of experimental studies about the purification of H_2.				- In the case of graphene, controlling the pores size and the homogeneous distribution is a challenge.	[118, 119]
Metal Hydride Separation	AB_5- type alloys	- Simple device. - Low energy consumption. - Simple and safe operation. - High recovery ratio of hydrogen. - Hydrogen is stored at the same time.	- The H_2 alloys used so far for purification have low storage capacity. - Deterioration of the performance in the presence of impurities such as O_2, H_2O, CO, sulphur containing species, etc. - Limited capacity for the purification of CO.	Small to medium	< 99.9999%	75-95%	- The composition of the feed gas has a great impact on the rate of absorption and hydrogen purity obtained.	[111, 113, 117, 120]

Table 2.1. Most deployed pre-treatment technologies for the removal of CO from reformate (Continuation).

Mitigation strategy	Subdivision	Advantages of the technique	Disadvantages of the technique	Scale of use	Hydrogen output (%)		Comments	References
					Purity	Recovery		
Cryogenic Distillation	N.A.	- Possibility to store hydrogen as a liquid.	- High costs. - Energy-intensive. - High consumption of liquid nitrogen.	Large	90-99%	95%	- The purity obtained depends on the operating temperature, pressure and the composition of the stream.	

2.3.1.1 Pressure Swing Adsorption (PSA)

PSA is a non-cryogenic gas separation process that uses adsorbent technology to obtain hydrogen with a purity between 99% and 99.999% [111-113]. The reformate is placed in a packed column at high pressure, where the impurities are selectively adsorbed by highly porous materials. Multiple adsorbents, such as zeolites, activated carbons, and silica and alumina gels are placed in individual layers inside the column. The retention of impurities depends on the affinity between the adsorbent and the gas molecule [3, 28]. Once the impurities have been adsorbed, the pressure is lowered to regenerate and purge the column. Typically, at least three cyclic columns are operated simultaneously [3].

PSA presents several advantages. It is fast and allows the continuous purification of hydrogen without disrupting the regeneration process of the adsorbents, which are used several times before losing their adsorptive capacity. Additionally, the hydrogen produced is at the same pressure as the feed [121]. The drawbacks are the need for high pressure (between 5 and 10 atm) in order to achieve high removal efficiencies, and the process generally requires a complex operation under a series of sequential, non-isothermal, non-isobaric and non-steady-state process steps. The main areas of research for this process are the hydrogen recovery at high purity, the decrease in the amount of adsorbent needed and the hardware costs [28].

2.3.1.2 Preferential Oxidation (PROX)

In this process, air is supplied to the reformate gas in the presence of a catalyst. The main reaction is [30]:

$$\mathbf{2CO + O_2 \rightarrow 2CO_2} \qquad \mathbf{\Delta_r H^{\circ}_{298} = -566\ kJ/mol} \qquad (2.10)$$

An undesirable side-reaction is:

$$\mathbf{2H_2 + O_2 \rightarrow 2H_2O\ (gas)} \qquad \mathbf{\Delta_r H^{\circ}_{298} = -484\ kJ/mol} \qquad (2.11)$$

The process reduces the CO content to 50-100 ppm [114]. The main advantage of this process is that a small amount of CO reacts in the presence of large quantities of H_2. The process can operate on a continuous basis. Additionally, as the oxygen necessary for the reaction comes from air, low energy is required for its provision and the process can operate at atmospheric pressure [28]. However, this process presents several challenges: the need to control the concentration ratio O_2/CO and the risk of spontaneous explosion due to the gas mixture. The system is bulky and complex as a consequence [30]. Another problem is the consumption of hydrogen by the reaction (2.11) [114].

The catalysts developed are mainly supported Ru and Pt-based alloy catalysts. The advances have been focused on the development of catalysts able to operate over a broader range of temperature, as well as at low temperature to avoid the reverse water-gas shift reaction [115]. Park *et al.* presented a comprehensive review of the different advances made on this technology [115].

2.3.1.3 Selective Methanation (SMET)

The target reaction for the selective methanation (SMET) is [30]:

$$\mathbf{CO + 3H_2 \rightarrow CH_4 + H_2O} \qquad \mathbf{\Delta_r H^{\circ}_{298} = -206\ kJ/mol} \qquad (2.12)$$

The side-reactions are CO_2 methanation and reverse WGS:

$$\mathbf{CO_2 + 4H_2 \rightarrow CH_4 + 2H_2O} \qquad \mathbf{\Delta_r H^{\circ}_{298} = -165\ kJ/mol} \qquad (2.13)$$

$$\mathbf{CO_2 + H_2 \rightarrow CO + H_2O} \qquad \mathbf{\Delta_r H^{\circ}_{298} = +41\ kJ/mol} \qquad (2.14)$$

SMET is a promising technology as there is no need for another gas for the reaction to take place [115]. Additionally, the process is free of nitrogen dilution, avoiding the danger of explosion and the need for advanced controls that PROX requires. The primary challenge that this process presents is the low performance of the Ni- and Ru- based catalysts [30]. Park *et al.* presented a comparison of the catalytic performance for the SMET, and emphasised the focus of the research on increasing the catalyst selectivity to remove CO in the presence of an excess of CO_2 and H_2 [115]. Another challenge to overcome is the high hydrogen waste [30].

2.3.1.4 Membranes separation

2.3.1.4.1 Pd-based membranes

Over the past 50 years, membrane separation has received much attention for different applications, including micro-filtration of bacteria to reverse osmosis for water clean-up [112, 122]. There are several membranes for hydrogen separation. Considering the material they are made of, they can be divided into different categories: polymer, metallic, carbon and ceramic [112, 116, 123]. Another classification would be between porous and dense. For the hydrogen separation, porous membranes use the molecular sieving as a primary mechanism, while the dense membranes utilise solution diffusion [112].

Palladium and its alloys have been the most studied membranes for hydrogen separation, due to palladium's high catalytic activity for hydrogen dissociation and its high permeability for diffusion of hydrogen atoms [115, 116]. Considering that palladium membranes are susceptible to embrittlement below 300 °C, and their tendency to suffer sulphur and carbon monoxide poisoning at low temperatures, Pd-based alloy membranes have been developed to overcome these effects and to enhance the hydrogen permeability. Figure 2.17 presents the processes involved using this class of membrane [112] which can achieve a purity of up to 99.9999% H_2 [111].

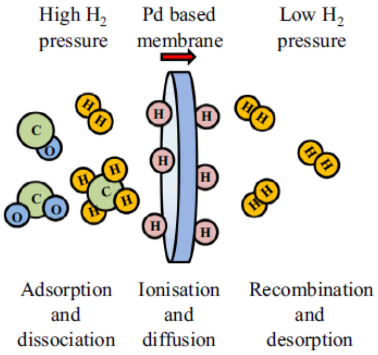

Figure 2.17 Processes involved in the separation of hydrogen from a hot gas mixture through a Pd-based membrane [112].

However, not all the Pd-alloy membranes are resistant to the presence of certain species, in particular, H_2S hinders the permeability of hydrogen [116, 123]. The costs are another disadvantage of Pd-based membranes. Thin metallic membranes have been developed to reduce costs and increase the hydrogen flux [123]. Due to the reduced thickness, membranes are deposited onto substrates to provide mechanical support. Different materials have been proposed, from which porous stainless steel (PSS) has proved to provide strength, robustness, similar thermal expansion and ease of welding and sealing [112]. Most Pd-based membrane research is focused on optimizing the alloys and creating new fabrication methods [116].

2.3.1.4.2 Two-dimensional membranes

Two-dimensional materials have emerged in the development of membranes due to their high selectivity and permeability. Highly specific separations are achieved under high flux rates [118]. In the case of graphene-based membranes, produced from graphene, graphene oxide and chemically converted graphene materials, three main types of membranes exist according to their microstructure (Figure 2.18): porous graphene layer, assembled graphene laminates and graphene-based composite [124]. The three types of membranes have been considered for the purification of H_2 [124], although for the H_2/CO separation the theoretical studies of porous membranes stand out. A few examples are the two-dimensional polyphenylene [125], the PG-ES1 [126] and the nitrogen-substituted porous graphene monolayers 3N-PG and 6N-PG [127].

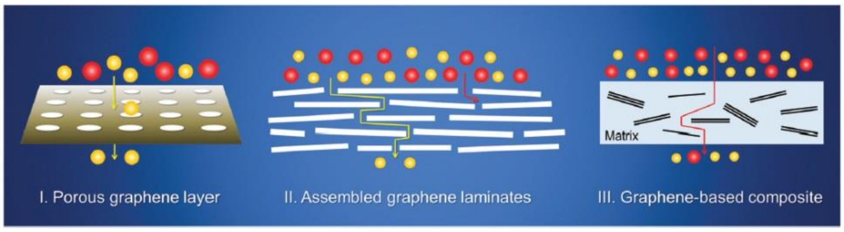

Figure 2.18 Diagram of the microstructures of the main types of graphene-based membranes: porous graphene layer (type I), assembled graphene laminates (type II) and graphene-based composite (type III) [124].

Controlling graphene with specific pore sizes and homogeneous distribution is a challenge, hence the interest in other two-dimensional carbon allotropes with uniformly distributed pores [119]. Among them is graphdiyne [128], whose framework is formed by hexagonal carbon ribs linked by diacetylene [129]. For the separation of CO/H_2, several theoretical studies have evaluated the properties of the elemental graphdiyne [130, 131], while others have modified the structure to enhance the purification capabilities in the cases of nitrogen modified graphdiyne [132] and charge-modulated graphdiyne [133]. Other two-dimensional membranes under study for the CO/H_2 separation include the rhombic graphyne [134], the g-C_3N_3 [119] and C_3N_4 [135] monolayers, the strain-controlled nanoporous graphenylene [136] and the inorganic graphenylene [137], among others. While the predicted properties of these materials are promising for the purification of H_2, their preparation and characterisation is limited. An advantage these membranes would present (depending on the material) compared to other mitigation strategies would be the removal of other species such as CO_2 and CH_4, also present in the reformate [118].

2.3.1.5 Metal hydride (MH) purification

Metal hydrides (MH) are one of the most promising materials for the storage of hydrogen due to their applicability in stationary, mobile and portable applications, their efficiency and safe use [138]. Since the 1970s, the use of metal hydrides has been extended for hydrogen separation and purification [120]. The mechanism is based on the selective adsorption of molecular hydrogen on the metal or alloy surface under certain conditions of temperature and pressure. The hydrogen is decomposed into atoms, forming a solid solution MH_x, followed by formation of the metal hydride MH_y. The hydrogen is stored, which constitutes one of the main advantages of the system. When desorbed, the impurity gases are purged first [117]. The most deployed MH for separation and purification of hydrogen are the AB_5-type [120].

Among the advantages that these devices present are their simplicity, low energy consumption, relatively safe use and straightforward operation, as well as the high purity reached (up to 99.999%) [117]. Major challenges include the impact of the composition of the fed gas on the final composition, the rate of absorption and the long-term stability. The most severe contaminants are CO, O_2, H_2O and sulphur-containing compounds [117, 120]. Hence, MHs have a serious limitation regarding removal of CO. However, Modibane *et al*. reported substrates La(Ni, Co, Mn, Al)$_5$ with stable performances over gas mixtures containing 10% CO_2 and 100 ppm CO [120]. Concurrently, Miura *et al*. proposed a system for start and stop operations, composed by several units connected in series. In the first one, the CO is removed by an adsorbent, while the hydrogen was stored in the following units. The process is called CO adsorption metal hydride intermediate buffer (COA-MIB), and 83% of hydrogen recovery was achieved after one month of operation. Figure 2.19 presents the operation of the COA-MIB [139, 140], and common AB_5-type alloys [120].

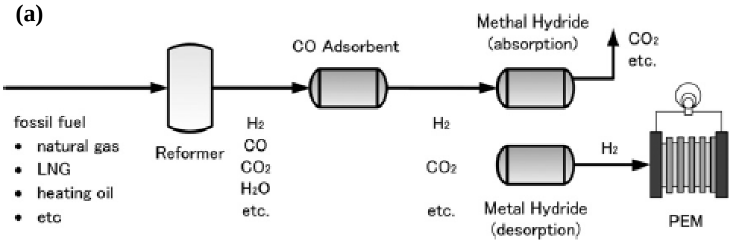

(b)

Alloy	Absolute [H/AB_5]		Reversible	
	Absorption (80 °C / 2.5 bar)	Desorption (200 °C / 1 bar)	[H/AB_5]	[cm^3/g STP]
$LaNi_4Mn$	5.205	1.252	3.953	104
$LaNi_4Mn_{0.5}Co_{0.3}Cu_{0.2}$	3.306	0.092	3.214	85
$La_{0.34}Ce_{0.50}(Pr,Nd)_{0.16}$ $Ni_{3.15}Co_{0.65}Mn_{0.6}Al_{0.6}$	3.937	0.192	3.745	99
$LaNi_{3.55}Co_{0.75}Mn_{0.3}Al_{0.4}$	5.035	0.368	4.667	124

Figure 2.19 Metal hydride reactor for hydrogen separation and purification. (a) operation of the CO-MIB system [139], (b) Hydrogen sorption capacities of common AB_5- type alloys [120].

2.3.1.6 Cryogenic distillation

The cryogenic distillation or partial condensation is based on the difference in volatility of the components on the gas stream [27, 141]. The process is performed at low temperatures at which the impurities condense, while the hydrogen remains in the gaseous phase due to its low boiling point (-252.9 °C). The efficiency of the process depends on the operating temperature and pressure, and the composition of the feed [113]. This process has been used for the separation of the different hydrogen isotopes [27]. The separation is highly energy intensive and costly. An additional disadvantage is the limited purity that is reached compared to other processes, which typically reaches ~99% [112].

2.3.2 On-board removal of CO

In recent years, some on-board hydrogen purification technologies have emerged. Their structure is similar to PEMFCs; however, their operation is focused on the purification of the stream, and not the generation of energy. An external power supply is required, and they are placed in-line before the fuel cell stack. A common advantage is the generation of power, or in particular cases, the consumption of almost null power. Although promising results have been obtained, the optimization of these technologies is vital to be able to compete with the conventional in-site purification processes. A summary of these technologies is presented in Table 2.2.

Table 2.2 On-board removal of CO from hydrogen for its use in PEMFCs.

Mitigation strategy	**Subdivision**	**Stream with the highest reported CO content in the anode**	**Advantages of the technique**	**Disadvantages of the technique**	**Comments**	**References**
Electrochemical Preferential Oxidation (ECPrOx)	N.A.	H_2/24.1% CO_2/9380 ppm CO	- CO is removed without any H_2 or CO waste. - The operation is feasible at room temperature, high anode pressure, atmospheric air pressure, and without external humidification. - Supplemental electrical power is produced. - The use of electrical power as an additional tool to enhance the oxidation of CO. - It is possible to cascade several ECPrOx reactors, depending on the initial CO concentration in the reformate.	- A heat exchanger might be needed in order to reach the optimal operating conditions. - Relatively new, it has not been tested in the industry.		[114]
Electrochemical Filter	N.A.	10,000 ppm CO/H_2	- The size of the filter is scalable according to the concentration of CO.	- The volume of the filter increases as the concentration of CO. To reduce 10,000 ppm to 10 ppm the volume of the filter occupies up to 10 times the one of the cell.	- The combined use of a PrOx reaction and an electrochemical filter can be used to reduce the volume of the filter, over high concentrations of CO.	[31, 33, 142]
Electrochemical Hydrogen Pumping (EHP)	High Temperature (PBI membranes)	74.7% H_2, 1.36% CO, 23.5% CO_2 and 0.36% CH_4	- Removal of other contaminants, such as CO_2 and N_2. - Simultaneous separation and compression of hydrogen. - The power requirements are minimal. - Excellent stability and durability. - Fast dynamic response.	- An increase in the inlet pressure enhances the hydrogen generation, but decreases the purity of it.	- The generation of hydrogen is dependent on the applied current.	[143-145]
	High-temperature EWGS	50 mol% H_2, 50 mol% CO	- Simultaneous generation and separation of H_2 - Mitigation of high concentrations of CO.	- Limited studies about the mechanisms involved.	- The reported concentration is prior to humidification.	[146, 147]
	Periodic current pulsing	80% H_2 with 1000 ppm CO / 20% CO_2	- Low temperature operation. - Removal of other contaminants, such as CO_2 and N_2. - Simultaneous separation and compression of hydrogen.	- Under short-circuit conditions, the anode potential might reach values above the thermodynamic stability limit, decreasing its catalytic activity.	- So far little research and optimisation of the system have been made.	[148]

Table 2.2 On-board removal of CO from hydrogen for its use in PEMFCs (Continuation).

Mitigation strategy	Subdivision	Stream with the highest reported CO content in the anode	Advantages of the technique	Disadvantages of the technique	Comments	References
Electrochemical Hydrogen Pumping (EHP)	EWGS at ambient temperature	100 ppm CO/H_2	- High efficiency, as CO is used to generate H_2. - Low energy consumption. - Removal of other contaminants such as NO, H_2S, CS and CO_2. - Safe to use.	- Limited studies of the mechanisms.	- The use of a liquid electrolyte is proposed in order to increase the CO adsorption.	[149]
Hydrogen purification membranes	Al_2O_3-supported Si_3N_4 membrane	1% CO/H_2	- Continuous separation of CO. - Low energy consumption. - High tolerance. - Low cost and ease of fabrication of Si_3N_4. - Capability of scaling.	- Limited understanding of the separation mechanisms. - The need of a converter for the disposal of CO.		[150]

2.3.2.1 Electrochemical Preferential Oxidation (ECPrOx)

Electrochemical preferential oxidation (ECPrOx) has been proposed as an alternative to conventional PrOx [117]. The structure of the ECPrOx units is similar to that of the PEMFC. The difference is the operation, which is based on the spontaneous potential oscillations the cells exhibit due to the exposure to CO under galvanostatic control (Section 2.2.2.2). The objective is to enhance the adsorption of CO and its oxidation to CO_2, so the concentration of CO in the stream is reduced before entering the fuel cell. Figure 2.20 shows how the system integrates the ECPrOx and PEMFC [114].

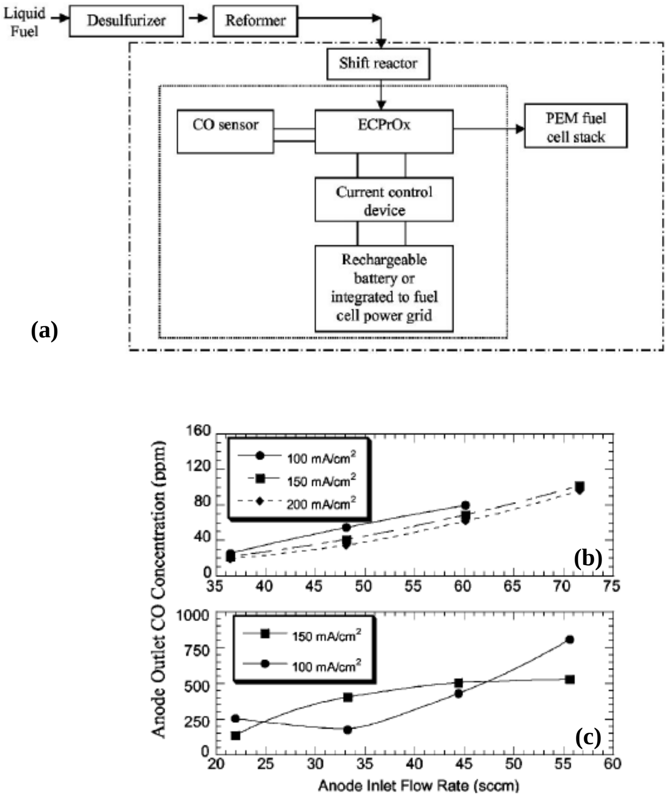

Figure 2.20 (a) Integration of the ECPrOx unit into a reformer-fuel cell system, (b) and (c) anode outlet concentration of CO as a function of inlet flow rates at different current densities over the exposure to 1000 ppm CO/H_2 and 9380 ppm CO/24% CO_2 /75% H_2 respectively [114].

The advantages of the ECPrOx compared to PrOx are the CO removal without H_2 waste and the supplemental electrical power produced. The ECPrOx can take place at room temperature, atmospheric air pressure, and with no external humidification. A high anode pressure facilitates the CO adsorption, lowering the concentration of CO at the anode outlet. Moreover, the use of electrical potential is used to enhance the electro-oxidation of CO. As the efficiency is increased at lower temperatures, a heat exchanger might be needed prior to the ECPrOx unit [114].

Hanke-Rauschenbach studied the oscillatory behaviour of potential using the model presented by Zhang *et* Datta as a base, and compared the behaviour of two ECPrOx reactors with electrical connections in series and in parallel [54, 151]. It was concluded that the CO conversion is improved in the series system due to the independent oscillations of each unit. The units connected in parallel oscillate simultaneously, affecting the performance of the system [151]. This comparison is supported by the experimental results obtained by Lu *et al.* [152], and also by Heidebrecht *et al.*, who presented a design approach for cascades of ECPrOx, using a degrees-of-freedom analysis [153].

2.3.2.2 Electrochemical filter

Lakshmanan *et al.* were the first to show how a PEMFC operating under pulse potential control could be used as a filter to remove CO from reformate [31]. In order to ensure constant operation, the system involves the use of two PEM fuel cells that alternately cycle between CO adsorption and CO oxidation [142]. Figure 2.21 shows how reformate enters the anode of the first cell (F1), which is operated at open-circuit. The CO is adsorbed on the catalyst surface, effectively filtering the CO from the stream, the remaining ‘purified’ hydrogen-rich gas entering the second fuel cell. After a switching time, when most of the catalyst surface is covered by CO, the reformate enters into the second cell (F2 in the diagram). A potential pulse is then applied to F1 that allows the oxidation of CO [33, 142, 154].

A fixed-bed adsorber model was used to optimise the switching time and different operating conditions. It was possible to reduce the concentration of CO from 10,000 ppm to 10 ppm at 25 °C, using a flow 100 cm^3 min^{-1}, a catalyst charge of 4 mg Pt cm^{-2} and a switching time of 20 s. The potential for the CO oxidation was 0.7 V. A primary consideration to take into account is the volume of the ‘filter’ to remove high concentrations of CO. For instance, reducing the concentration of CO from 10,000 ppm to 10 ppm to feed a cell operating at 1 A cm^{-2}, requires a filter cell almost ten times the area of the fuel cell [33].

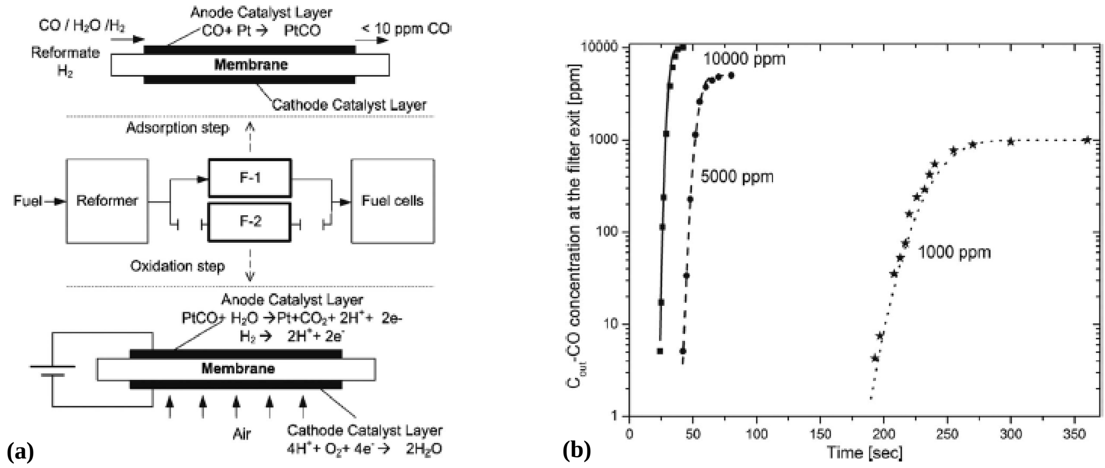

Figure 2.21 Electrochemical filter: (a) diagram showing the two PEMFCs operating over the adsorption and oxidation steps, (b) experimental (symbols) and model fit (lines) for different CO/H_2 concentrations at 25 °C, 100 $cm^3\ min^{-1}$ and 4 mg Pt cm^{-2} [33].

2.3.2.3 Electrochemical hydrogen pumping (EHP)

Electrochemical hydrogen pumping is a technology originally presented in the 1960s, with the main objective of purifying and compressing hydrogen [155, 156]. As shown in Figure 2.22, the mixed stream enters the anode, where the hydrogen is oxidized. The protons 'pumped' to the cathode where pure and pressurized hydrogen is collected [157].

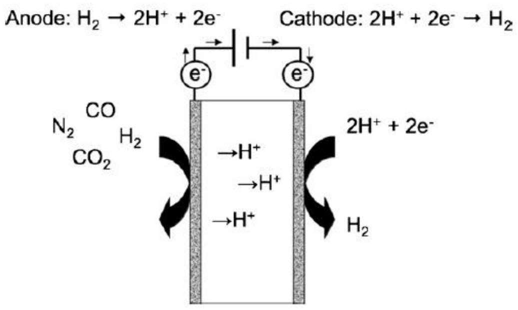

Figure 2.22 Diagram illustrating the operation of an electrochemical hydrogen pump, separating hydrogen from a mixture of gases in the anode [143].

The EHP can separate the hydrogen as long as the components of the stream do not poison the catalyst, so that the technology was not considered for the separation of CO [158]. The introduction of EHP at high temperature PEMFC with phosphoric acid-doped PBI membranes (Section 2.3.3.2) [143], and EHP combined with other techniques such as the current pulsing operation (Section 2.3.3.10) [148] and the enhancement of the

Electrochemical Water Gas Shift (EWGS) [146, 147] offered the possibility of CO mitigation at high levels.

2.3.2.3.1 *High-temperature EHP*

Studies have reported the separation of CO through EHP at high temperatures using phosphoric acid-doped PBI membranes. Perry *et al.* evaluated a non-humidified stream containing 35.8% H_2, 11.9% CO_2, 1906 ppm CO and N_2 balance at 160 °C. At 0.4 A cm^{-2}, the outlet stream had a concentration of 11 ± 1 ppm CO and 0.37 ± 0.09 % CO_2. Higher hydrogen purity was obtained by increasing the current to 0.8 A cm^{-2}, obtaining 13 ± 3 ppm CO and 0.19 ± 0.02 % CO_2. It was also demonstrated that the long-term durability could reach up to 4000 hrs [143]. Thomassen *et al*. evaluated a different range of temperatures for the separation of CO (Figure 2.23), and demonstrated the fast dynamic response and the stability of the system [144].

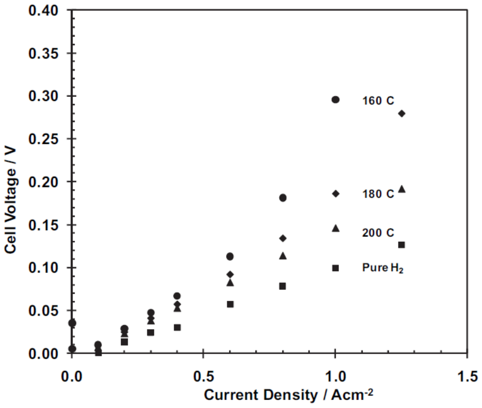

Figure 2.23 Polarisation curves at different temperatures of a PBI-based EHP unit, fed with a reformate mixture containing 74.7% H_2, 1.36% CO, 23.5% CO_2 and 0.36% CH_4 [144].

2.3.2.3.2 *Electrochemical water gas shift (EWGS)*

The Electrochemical Water Gas Shift (EWGS) combines the separation of H_2 through the EHP, and the electrochemical CO oxidation. In the case of the EWGS at high temperatures (between 130 and 150 °C), PBI membranes were used as the electrolyte. Both the EHP and the electrochemical CO oxidation occur simultaneously at high current densities, and with a feed containing high concentrations of CO and H_2O. A diagram of the processes involved, and a typical polarization curve, are presented in Figure 2.24. Oettel *et al*. tested concentrations up to 50 mol% H_2 and 50 mol% CO (prior to humidification) achieving exergy efficiencies as high as 43.3% [146, 147].

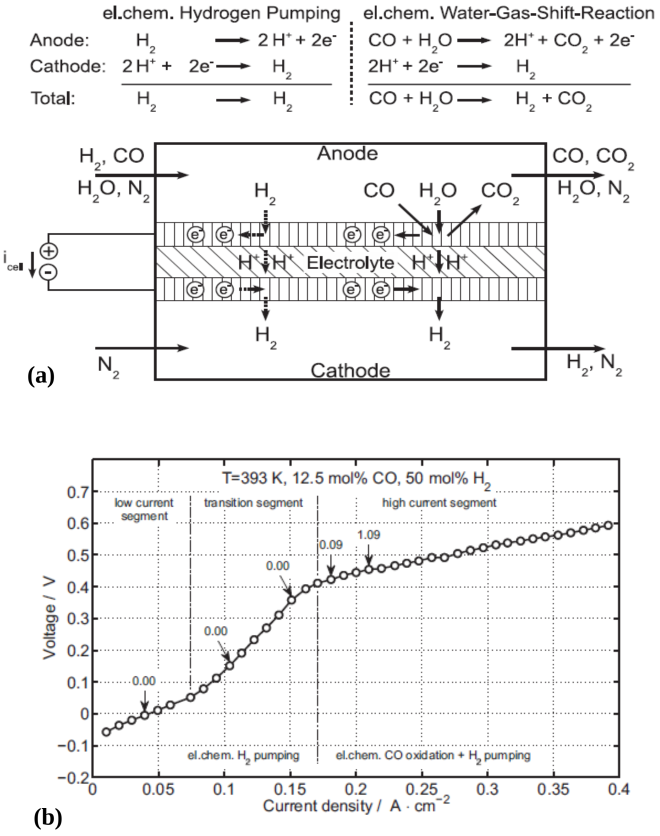

Figure 2.24 Electrochemical water gas shift reactor (EWGSR): (a) diagram showing the simultaneous generation and separation of hydrogen; (b) typical polarization curve obtained at 393 K, showing the operation of the EHP (transition current segment) and the EWGS (high current segment). The anode feed contained 12.5 mol % CO and 50 mol% CO (subsequently humidified). The concentration of CO_2 in the anode outlet was determined for five points, through GC analysis [146].

2.3.2.3.3 *Current pulsing in EHP*

At room temperature and atmospheric pressure, Gardner *et al*. tested the application of anodic current pulses in an EHP unit, for the separation of CO from a stream containing a mixture of 80% H_2 with 1000 ppm CO/20% CO_2. The cell pulsing substantially reduced the separation efficiency, even though the performance of the unit is better with no CO (Figure 2.25). A model representing the separation of hydrogen was also presented, taking the model from Zhang as a basis [148, 159].

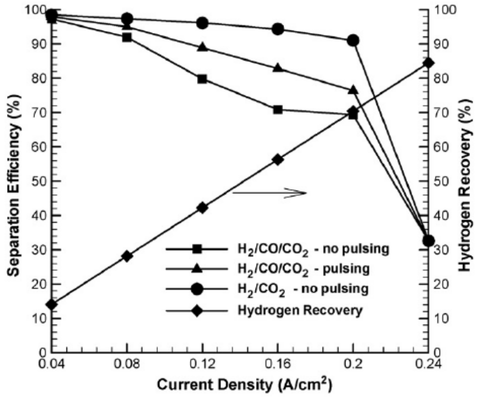

Figure 2.25 Effect of the current pulsing technique in the anode of a EHP unit over the exposure to different compositions of gases: ● no pulsing, 80% H_2 and 20% CO_2; ▲ pulsing, 80% H_2 with 1000 ppm CO/20% CO_2; ■ no pulsing, 80% H_2 with 1000 ppm CO/20% CO_2; ♦ hydrogen recovery [148].

2.3.2.3.4 EWGS at ambient temperature

A study on the separation of H_2 in combination with the electro-oxidation of CO was presented by Huang *et al*. The EHP operation was done at ambient temperature, until the complete coverage of the catalyst by CO. The operation was then interrupted, and a fraction of the power generated by the subsequent fuel cell was applied into the reactor to operate as an electrolyser. The OH^- molecules generated in the anode contributed to the electro-oxidation of CO. The system response showed that it could mitigate a stream containing 100 ppm CO/H_2. The process has the advantage of using the CO as a reducing reagent to produce additional H_2 from water. Other advantages are the removal of other contaminants, that include hydrogen sulphide (H_2S), carbonyl monosulfide (CS), carbon dioxide (CO_2), and nitrogen oxide (NO); and inherently safe use compared to other technologies [149]. A diagram showing the processes involved is presented in Figure 2.26, as well as the evolution of the voltage over its operation. Additionally, the use of a liquid electrolyte in order to increase the CO adsorption capacity of the reactor was reported [149].

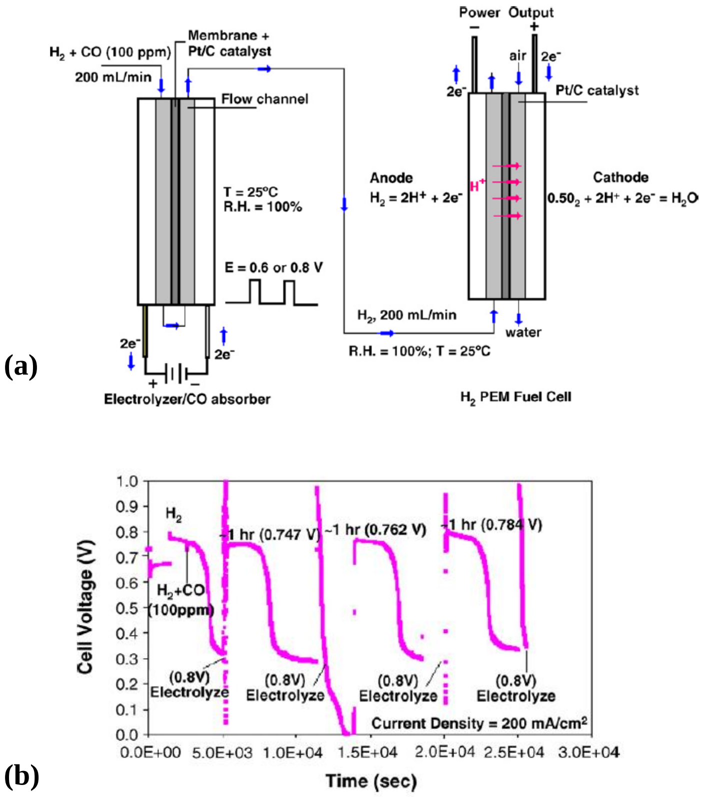

Figure 2.26 Electrochemical water gas shift (EWGS): (a) Diagram of the process, (b) performance of the fuel cell fed with the stream coming from the EWGS unit. The fuel entering the unit contained 100 ppm CO/H_2 [149].

2.3.2.4 Membranes separation

In recent years, the use of membranes has broadened to the on-board purification of hydrogen. Liu *et al.* presented an Al_2O_3-supported Si_3N_4 membrane capable of removing CO from a stream containing 1%CO/H_2. The separation occurred through a combination of chemisorption and physisorption processes, and the resultant hydrogen fed the fuel cell operating on-line. The CO was disposed through a bypass needle valve. With the membrane in place and in the presence of CO, the decrease in power density was less than 0.01 W cm^{-2}. An advantage of this technique is the low cost and ease of fabrication of Si_3N_4, although more research is needed for the understanding of the mechanisms in place, and to determine the efficiency of the membrane in the case of long exposures to CO [150]. Another consideration is the need of a converter for CO, as in this study it is directed to the exhaust.

2.3.3 In-operando mitigation strategies

Several *in operando* techniques have been developed to mitigate CO poisoning in PEMFCs; these follow a range of approaches including the development of new materials, the variation of the conditions of operation, the change of fuel cell design and/or the addition of new components. In general, the objectives are to allow operation of cells at a high concentration of CO (up to that delivered at the exit of a reformer), be of simple design and economically feasible. Of these approaches, the development of CO tolerant catalysts is the most examined, followed by air-bleeding and high-temperature operation. Table 2.3 presents the advantages and disadvantages of each approach.

Table 2.3 In-operando mitigation strategies for CO poisoning in PEMFCs.

Mitigation strategy	**Subdivision**	**Stream with the highest reported CO content in the anode**	**Advantages**	**Disadvantages**	**Comments**	**References**
Electrocatalysts	Platinum-based catalysts	2000 ppm CO/H_2	- Different structures and compositions are available. - No alteration of the configuration of the cell.	- Scarcity and high costs of platinum - The stability of Pt alloys in the long term is limited.	- Pt-Ru catalysts are the most effective against CO poisoning in the market and the most durable, although they are less stable than Pt.	[29, 160-166]
	Non-platinum catalysts	1% CO/H_2	- Different structures and compositions are available. - Lower costs compared to Pt-based catalysts	- Low activity for HOR in most cases. - Limited studies about the durability of the catalysts.	- The tests performed in the presence of 1% H_2/CO were done in half-cell tests. This concentration has not been tested in real fuel cell conditions.	[167-169]
High-temperature fuel cells	N.A.	5% CO/H_2	-The use of direct reformate is possible, simplifying the balance-of-plant. - Simplification of water management and heat rejection. - The contamination by H_2S can also be mitigated.	- Most membranes are susceptible to dehydration at high temperature, resulting in low conductivity. - The phosphoric acid blocks the surface of the Pt, limiting the oxygen reduction reaction (ORR) in the cathode. - Fast-start capabilities are limited compared to conventional PEMFC. - A corrosion mechanism can be activated due to the elevated temperatures.	- Jiao *et al*. presented numerical simulations with various flow channel designs, considering a CO concentration to up to 20%.	[170-177]
Oxidant bleeding	External bleeding	10,000 ppm CO/H_2	- High efficiency against CO poisoning. - Limited concentrations of H_2S can also be mitigated	- Fuel utilization rate is diminished. - Increased temperature reduces the anode lifetime due to sintering of the catalyst. - Can promote the formation of pin-holes in the membrane after extended operation due to the formation of H_2O_2. - Careful control is needed over air supply. - High concentrations of CO are not mitigated in the long run. - Fuel efficiency limited due to the production of water in the anode	- Oxygen bleeding is less effective for lower CO concentration, lower catalyst loading and thin electrodes.	[178-181]
	H_2O_2 in the anode humidifier	100 ppm CO/H_2	- High efficiency. - Safer than the external bleeding.	- The concentration of CO that can be mitigated is limited. - The presence of H_2O_2 provokes degradation of the membrane in the long-term.		[78, 162, 180, 182]

Table 2.3 In-operando mitigation strategies for CO poisoning in PEMFCs (Continuation).

Mitigation strategy	Subdivision	Stream with the highest reported CO content in the anode	Advantages	Disadvantages	Comments	References
Oxidant bleeding	Internal bleeding	0.24% CO/12.82% CO_2/ 12.84% H_2/12.18% N_2/ 61.92% He	- Simple application. - Effective in mitigating CO poisoning.	- Reduced thickness of the membrane enhances CO crossover to the cathode and the decrease of the membrane conductivity. - Crossover of oxygen can produce H_2O_2, which can degrade the membrane.		[46, 158, 180, 183]
Reconfiguration of the anode	Bilayer anode structure	5000 ppm CO/H_2	- In most cases the amount of catalyst is reduced without affecting the performance. - Lifetime of the cells is extended if it is combined with oxidant bleeding. - Can also be used to mitigate CO_2 contamination.	- Careful control for the oxidant bleed is required. - High consumption of platinum in the case of the PtMo/PtRu bilayer.	- The method of preparation of the layers has an important influence on the concentration of CO that can be tolerated.	[161, 184-189]
	Refined diffusion layer	100 ppm CO/H_2	- The heating effects of the oxidant bleeding are not observed, and the lifetime of the cell is extended if combined with oxidant bleeding.	Careful control for the oxidant bleed is required. - Limited studies about the distribution of the particles in the GDL.	- The catalytic activity of Au particles depends mostly by the size and the distribution of the particles, even though its high activity for WGS reaction.	[190, 191]
	Complementary composite film coating	100 ppm CO/H_2	- The composite film is prepared with transition metal oxides (e.g. Fe_2O_3 or CuO) - less expensive than Pt. - In combination with an air bleed, it is possible to raise the CO tolerance of a Pt/C to the same level as a PtRu/C alloy. - The design is simple and there is no need for additional hardware.	- Careful control for the oxidant bleed is required. - Limited studies about the stability of the catalysts.	- The cells can tolerate up 500 ppm CO/H_2, if the air-bleed limit is increased to 6%.	[192, 193]
	Catalyst sheet in front of the anode	5000 ppm CO/H_2	- The catalyst-sheet does not significantly hinder the gas transport to the anode or cause additional Ohmic losses. - The reformate can be directly introduced into the cells.	- Careful control for the oxidant bleed is required.		[194]
Pulsed heating	N.A.	1000 ppm CO/H_2	- The temperature of the membrane is not affected, maintaining its conductive properties. - The performance was four times higher. - The removal of CO is done in short periods of time.	The implementation of the technique affects the structure of each of the cells.		[164]

Table 2.3 In-operando mitigation strategies for CO poisoning in PEMFCs (Continuation).

Mitigation strategy	**Subdivision**	**Stream with the highest reported CO content in the anode**	**Advantages**	**Disadvantages**	**Comments**	**References**
Pressure swing	N.A.	1000 ppm CO/H_2	- The amount of oxidant is significantly reduced in comparison with conventional external oxidant bleeding. - High efficiency.	- Extensive control needed.		[164]
Break-in procedure and $KMnO_4$ treatment	N.A.	100 ppm CO/H_2	- Highly efficient, simple and applicable to larger stacks.	- Interrupted operation of fuel cell.	- The break-in procedure is predominant at higher operating temperatures. - The combined procedure of break-in and $KMnO_4$ solution regenerates 90% of the performance of the cells.	[179]
Triode operation	N.A.	760 ppm CO / 4.05% CO_2 / 4.6% H_2 / 3.8% N_2 / He	- Operation allows potential differences not accessible in normal operation.	- The three electrodes work in corrosion mode. - Some power is compromised in the operation of the auxiliary electrode.	- Triode operation has been used in SOFC to improve their performance in the presence of H_2S. - Also used in electrolysers and batteries.	[195-199]
Periodic variation in the fuel supply	Cyclic injection of pure H_2	72 ppm CO/H_2	- The endurance of the membrane is maintained as there are no major voltage excursions.	- Exhaustive control of CO content needed. - Not effective against irreversibly adsorbed contaminants. - The recovery time can be very long.	- The cell was completely recovered after 15 min of pure H_2, after the exposure to 100 ppm CO/H_2.	[200, 201]
	Periodic fuel starvation	75% H_2 /25% CO_2/100 ppm CO	- The application of different fuel-free fluid, from nitrogen, to water, a cooler or the recirculation from the cathode outlet.	- Careful cell monitoring required to ensure fuel starvation effects do not become extreme and affect the durability of the fuel cell.		[201]
Pulsed oxidation or pulsing technique	Current pulses	3% CO/H_2	- As the removal of CO is done in a short period of time, the anode potential is maintained in the hydrogen oxidation region rather than at the CO oxidation potential. - The frequency of the pulses can be adjusted to different concentrations of CO. - No additional energy needed apart from the trigger device.	- Under short-circuit conditions, the anode potential might reach values above the thermodynamic stability limit, degrading its catalyst activity. - The use in stacks requires rigorous control of each of the cell's potentials. - The operation of the cells is interrupted during the operation.	- The use of a power converter to modulate the application of the pulses can increase the power of the cell by 50% in the presence of 500 ppm CO/H_2 and extend the fuel cell lifetime without reducing the output power.	[57, 163, 202-205]

Table 2.3 In-operando mitigation strategies for CO poisoning in PEMFCs (Continuation).

Mitigation strategy	**Subdivision**	**Stream with the highest reported CO content in the anode**	**Advantages**	**Disadvantages**	**Comments**	**References**
Pulsed oxidation or pulsing technique	Negative potential pulses	50 ppm CO/H_2	- Rapid and with less experimental requirements than under the conventional oxidant bleeding. - Increase of up to 500% of the voltage output.	- Takes a significant amount of power to apply negative pulses.		[206, 207]
Potential oscillations or self-oscillations	N.A.	1000 ppm CO/H_2	- No control system or any additional equipment needed. - Can be used as a back-up solution.	- Takes place under limited operating conditions (e.g. concentrations higher than 50 ppm CO/H_2).	- Current pulsing technique is more effective than "self-oxidation" in increasing CO tolerance.	[57, 208]

2.3.3.1 CO tolerant electrocatalysts

The development of electrocatalysts is an area of significant research for CO poisoning mitigation. Suitable catalysts for CO tolerance must exhibit high activity for the HOR and the lowest possible overpotential in the presence of CO [209]. It is necessary to maximize the oxidation of CO, and reduce the adsorption processes for the improvement of the CO tolerance [209]. This has been achieved by alloying Pt with Ru, for example. PtRu/C is considered as one of the most promising CO-tolerant electrocatalysts, and is the most commercially available [210].

The bifunctional and the electronic mechanisms are well-accepted pathways that explain the increased tolerance to CO. These were first proposed from studies performed on PtRu catalysts and then expanded to other systems. The electronic or ligand effect considers the decrease of the Pt-CO bond strength by the addition of the additional alloying element. The platinum properties are modified by the electron donation or back-donation of ruthenium. The CO adsorption energy decreases reducing the CO coverage [211, 212]. The electronic modifications also affect the CO oxidation reaction rate. At lower potentials, the electronic mechanism predominates due to the diminishment of CO adsorption, and at higher overpotentials, the bifunctional mechanism takes place [209].

The bifunctional mechanism was first referred to PtRu alloys [213], and occurs over the formation of oxygen-containing species, such as OH, on oxophilic sites present on the second element at lower potentials than for Pt, allowing electro-oxidation of CO to CO_2 [211]. The mechanism between the adsorption of CO and the formation OH follows the Langmuir-Hinshelwood (L-H) mechanism [209]:

$$\mathbf{Pt + CO \rightarrow Pt - (CO)_{ads}} \tag{2.15}$$

$$\mathbf{M + H_2O \rightarrow M - OH + e^- + H^+} \tag{2.16}$$

$$\mathbf{M - OH + Pt - CO \rightarrow Pt + M + CO_2 + e^- + H^+} \tag{2.17}$$

Different electrocatalysts have been developed since. The structures are covered in several reviews [81, 160, 161, 209, 214-217]. Figure 2.27 presents the different classes of Pt-based catalysts for fuel cells [217], although the non-platinum structures are of great interest due to the scarcity and the high costs of platinum [218]. Some representative examples from the vaste array of electro-catalysts are presented next.

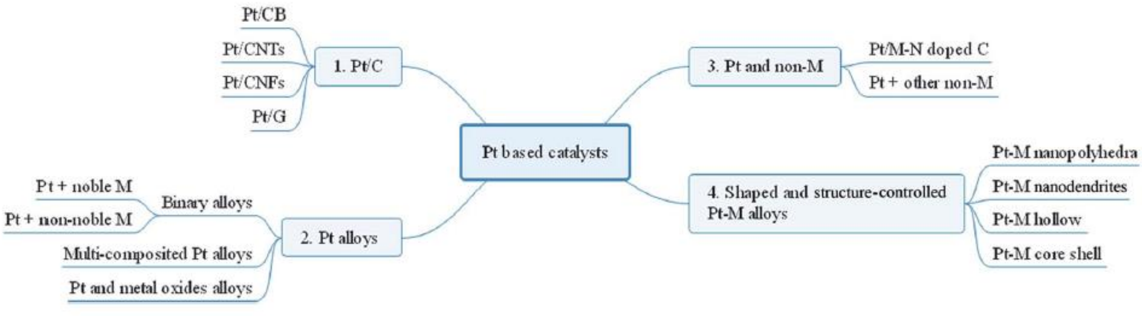

Figure 2.27 Representative classes of Pt-based catalysts for fuel cells [217].

Ehteshami *et al.* compared the performance of a series of binary and ternary Pt-based catalysts (Figure 2.28) and studied the relationship between the electronic properties of the catalysts and their tolerance to CO and CO_2. PtMo/C presented the highest CO tolerance due to the formation of well-dispersed oxy-hydroxides on the surface and to the turn-over of the Mo (IV/VI) redox couple, followed by PtCoMo/C, PtRuMo/C, PtRuPb/C, PtRu/C, PtCo/C, PtFe/C, PtNi/C and Pt/C. Although PtCoMo/C presented a higher CO oxidation onset potential than PtMo/C, this ternary electro-catalyst presented a higher tolerance to CO_2 by the added ligand effect due to the presence of Co, making it more suitable for the operation with reformate [218].

Some features have a direct impact on the catalyst efficiency and CO tolerance, including the type, composition and atomic ratios of the added elements. The synthesis method is also an important research area as the structure, morphology and size distribution of the catalysts rely on the process chosen [160]. For instance, Narischat *et al.* evaluated the effect of different porous structures of carbon support for Pt_2Ru_3 catalysts. The supports were prepared from resorcinol-formaldehyde carbon gels, varying the resorcinol to catalyst ratio (R/C). The highest tolerance was found to be related to the largest volume of mesoporous, due to a higher diffusivity. A cell using Pt_2Ru_3/RC1000ac58 (R/C=1000) presented a voltage decrease of 0.132 V at 0.2 A cm^{-2} in the presence of 2000 ppm CO/H_2 [166].

A catalyst class of interest is the core-shell structures due to the reduction of platinum utilisation. Some reports have also shown them to be more stable and catalytically more active than the alloy structures [160]. Most recent studies on the CO tolerance of core-shell catalysts include the synthesis of PtRu/PtNi/C with PtRu alloy surface and PtNi alloy core. The PtRu/PtNi/C catalyst presented a higher CO tolerance when compared to PtNi/C and PtNi-Ru/C in a PEMFC cell test in the presence of 30 ppm CO/H_2 [219].

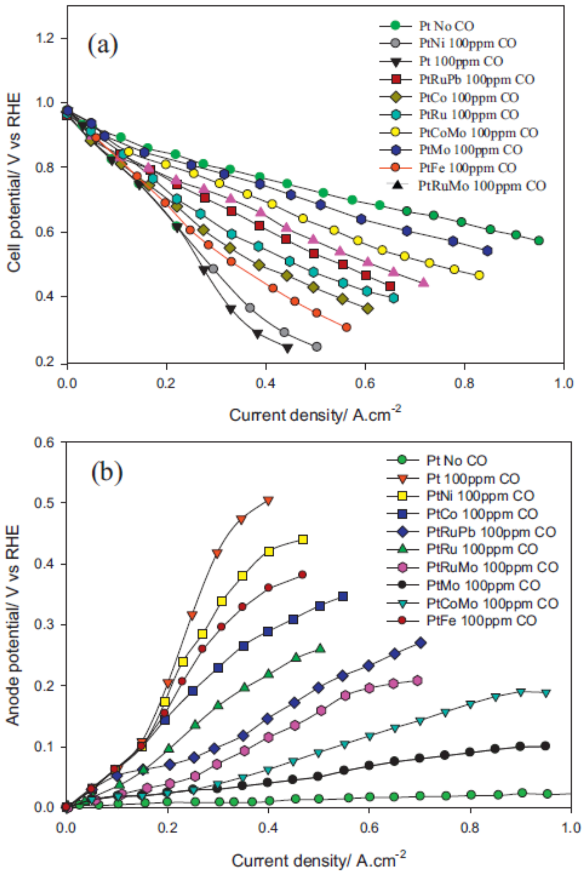

Figure 2.28 Comparison of the performance of different catalysts (Pt-M (M=Ru, Mo, Fe, Co, Ni), PtRuMo/C, PtCoMo/C, PtRuPb/C) in a H_2/O_2 PEM fuel cell system operating in the presence of 100 ppm CO/H_2. (a) polarization curves and (b) anodic overpotentials [218].

Another novel catalyst studied is AuPt-prGO, a partially reduced graphene oxide sheet, incorporated with gold and platinum nanoparticles, presented by Isseroff *et al*. This material was applied to the electrodes and the membrane of a cell, showing a complete tolerance to 1000 ppm CO/H_2 [220].

As for the development of non-platinum electro-catalysts, a variety of tungsten carbide (WC) produced from different routes were tested in the presence of 1% CO/H_2 carbon catalyst in half-cell tests. The reduction in the current density due to the presence of CO was less than 6%, showing the weak adsorption of CO in catalyst sites [167]. Although these materials have shown a high CO tolerance, they present a low activity for HOR and are not convenient for commercial use [168]. More recently, Li *et al.* reported the synthesis of Ir-V-Mo/C catalysts. The ternary 40%Ir-10%V-10%Mo/C (in weight) presented a 26.4% higher power density than a conventional 40%Pt/C catalyst in a H_2/air system, and a superior tolerance to 10 ppm CO/H_2, due presumably to the bifunctional mechanism [168].

Despite the progress made in the electro-catalysts area, there is room for improvement. At present, the research is concentrated in the development of CO-tolerant electrocatalysts more active and stable. For instance, the anode materials synthetized so far degrade under fuel cell operating conditions, due to leach out of the incorporated ions [160]. In the case of PtRu alloys, the anodic dissolution of ruthenium is favourable at potentials of 0.5 V vs RHE, leading to the loss of catalytic activity. Moreover, the dissolved ruthenium provokes the poisoning of the cathode due to its crossover, and the deterioration of the membrane properties [163].

2.3.3.2 High-temperature fuel cells

As mentioned, CO poisoning is very temperature dependent. At higher temperatures, the hydrogen adsorption is less exothermic than the CO adsorption, the H_2 adsorption is favoured at higher temperatures, diminishing the coverage by CO and increasing the H_2 oxidation rate. The development of polymer membranes capable of operating at elevated temperatures opened up the possibility of high-temperature PEM fuel cells (HT-PEMFC) [170]. HT-PEMFCs operate between 150 °C and 200 °C and are much more resistant to CO poisoning than conventional PEMFCs operating <80 °C. Figure 2.29 presents the effects of the operation of HT-PEMFC at different concentrations of CO.

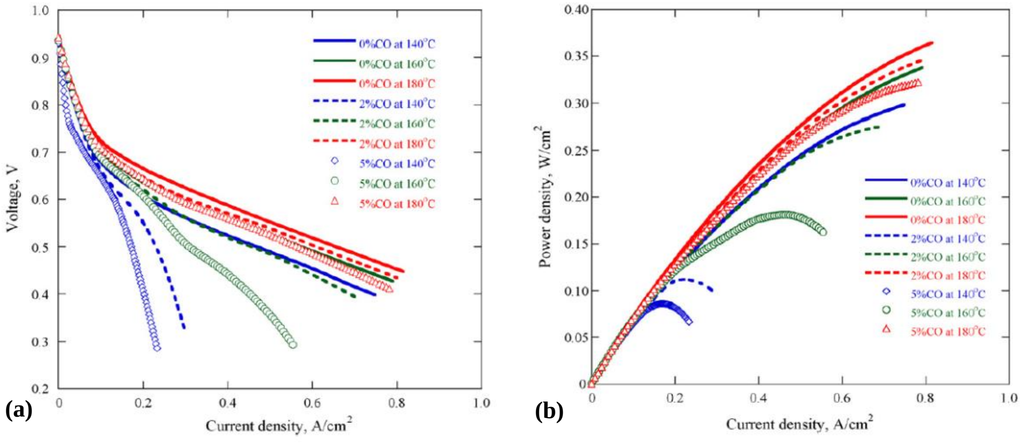

Figure 2.29 Effects of the temperature with a PBI-based PEMFC with different concentrations of CO: (a) polarization curves, (b) power density curves [170].

Another characteristic of this operation is the simplification of the water management problems that conventional PEMFC present. As the water is present only as vapour above 100 °C, flooding is not an issue. Nevertheless, the membrane is susceptible to lose ion conductivity due to dehydration [170, 171]. Additionally, a corrosion mechanism can be activated due to the high operating temperatures [177].

Different membranes have been developed for high-temperature operation, such as inorganic-organic composite membranes, sulfonated hydrocarbon polymers and acid-base polymer membranes. The acid-base polymer membrane polybenzimidazole (PBI) doped with phosphoric acid (PA) has received much attention [171]. This membrane alone possesses a very low proton conductivity; however, the addition of PA increases it from 10^{-9} mS cm^{-1} to 0.1 S cm^{-1} at 150 °C [221]. At the same time, the addition of PA entails the blockage of the catalyst, especially on the cathode, limiting the oxygen reduction [171].

HT-PEMFCs allow the use of direct reformate, containing 3% of CO [172], and up to 5% of CO [170]. There is no need for other processes such as PSA, PROX or SMET, obtaining a simpler and more economical system (Figure 2.30) [171]. Additionally, it is possible to integrate HT-PEMFCs into the fuel processing unit by recovering the heat from the cells and using it to service system requirements [171, 221, 222]. Moreover, it is also possible to mitigate the contamination by H_2S through this technique [176]. Liu *et al*. presented a comprehensive review of HT-PEMFCs for their use in auxiliary power units (APU) [223].

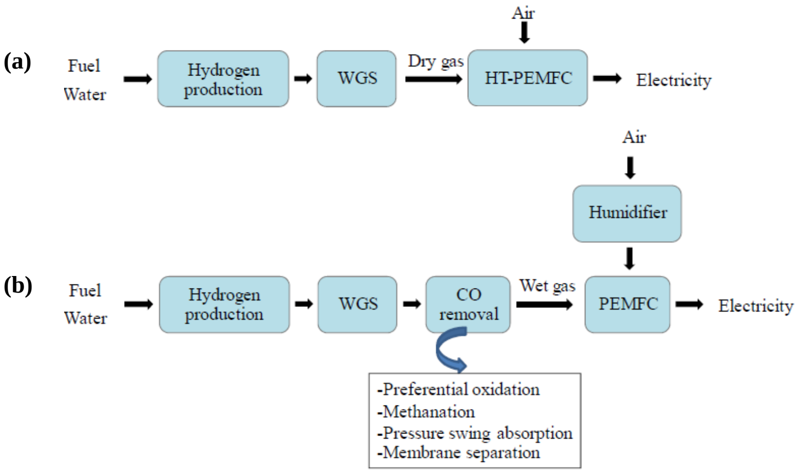

Figure 2.30 Comparison between (a) a conventional PEMFC system and (b) a HT-PEMF [171].

2.3.3.3 Oxidant bleeding

Oxidant bleeding leads to the enhancement of the oxidation of CO to CO_2 through low levels of oxygen or oxygen-evolving/containing species, such as air or hydrogen peroxide. Sugiyama *et al.* deducted the energy profile of the CO oxidation by O_2 on Pt(111) surface, presented in Figure 2.31, where two pathways for the CO_2 formation are shown: (i) via O_2 dissociation, and (ii) via the OC-COO complex. The rate determining step via the O_2 dissociation corresponds to the generation and desorption of CO_2 (second step), while via the OC-COO complex the formation of this species is the rate determining step (first step) [224].

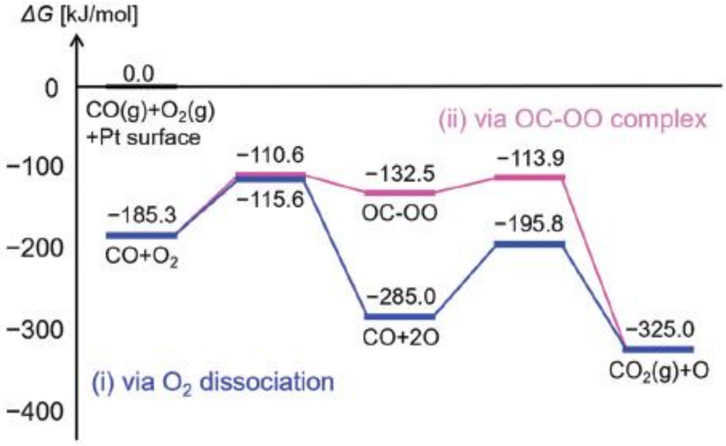

Figure 2.31 Energy profile of the CO oxidation by O_2 on Pt (111) obtained by the lowest conformer to single transition state (LC-TS) model at T = 300 K. The values of energy are relative free energies to the total energy of CO(g), O_2(g) and the Pt(111) surface [224].

This strategy was first introduced by Gottesfeld and Pafford who demonstrated that a concentration of 2-5% O_2/H_2 in the anode stream was enough to completely mitigate the effects of a concentration of 100 ppm CO at 80 °C [67]. The technique was quickly deployed and became one of the most studied. The variations over the introduction of the oxidant in the anode are presented next.

2.3.3.3.1 External bleeding

The external oxidant bleeding technique involves introducing the oxidant, usually air, into the fuel stream. The oxygen is adsorbed onto CO-free Pt catalyst sites, and then the surface reaction between Pt-CO and Pt-O takes place to form CO_2. This gas-phase catalytic oxidation reduces the CO coverage on the catalyst surface and increases the hydrogen electro-oxidation activity [161]. Roughly one out of every 400 O_2 molecules participates in the oxidation of CO [225]. The remaining oxygen chemically combusts with hydrogen [226]. Studies have summarized the different experimental conditions under which the CO poisoning has been evaluated [178, 181]. Figure 2.32 shows how current density is affected by cell exposure to different levels of air bleeding [178].

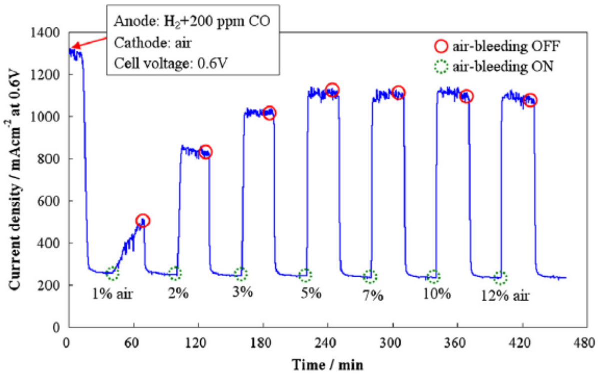

Figure 2.32 Evaluation of various levels of air bleeding on the current density of a fuel cell exposed to 200 ppm CO, operated at 0.6 V / 65 °C [178].

Cell potential losses due to CO poisoning can be mitigated by this technique, and recently it has been proven that low concentrations of H_2S can be mitigated through air bleeding [169]. However, there are significant drawbacks regarding anode lifetime due to the temperature increase caused by internal hydrogen combustion with oxygen, which is highly exothermic (Reaction 2.18). The temperature provokes the sintering of the catalyst that reduces the number of active sites [161].

$$\mathbf{H_2 + \frac{1}{2}O_2 \leftrightarrow H_2O} \qquad \mathbf{\Delta H = -251\ kJ\ mol^{-1}} \qquad (2.18)$$

An additional drawback is the degradation of the membrane after extended periods of operation, due to the formation of hydrogen peroxide (H_2O_2) [180]. Ralph *et al.* reported the appearance of pin-holes, leading to cell failure, although the anode lifetime can be increased by reconfiguring the anode (Section 2.3.3.4) [161]. Other disadvantages of this technique are the inefficiency associated with consumption of hydrogen and the need for careful control of the air feed [202].

Recent studies evaluated the effect of temperature in the effect of air bleeding, showing a slower process at higher temperature [227]. Another study includes the proposition of a methodology to optimize the amount of air bleed through the evaluation of the distribution of the contamination over a novel segmented cell, and the analysis of the CO conversion to CO_2 [181]. Hafttananian *et al*. developed a model that apart from predicting the operation and the poisoning of the cell, could enhance the oxygen bleed and diminish oxygen / hydrogen consumption by 63% [228]. Another study checked the long-term effects of this technique [229].

2.3.3.3.2 H_2O_2 in the anode humidifier

The use of hydrogen peroxide in the humidification of water was also evaluated [78, 162, 182]. The H_2O_2 is heterogeneously decomposed into active oxygen that contributes to the oxidation of the adsorbed CO in the catalyst, having the same effect as an air bleed [182]. Bellows *et al*. found that a certain amount of H_2O_2 is catalytically decomposed by interaction with the metallic surfaces of the humidifier [162]. The approach has certain safety advantages over air bleed; however, it presents other disadvantages inherent to oxidant bleeding (Section 2.3.3.3.1), in particular the degradation of the membrane in the long term due to the formation of H_2O_2 [180]. In short-time operation the technique has been found to perform effectively, with 5% H_2O_2 in the deionized water of a humidifier completely avoiding the detrimental effects of 100 ppm CO in the anode hydrogen feed [78].

2.3.3.3.3 Internal air bled

The carbon monoxide poisoning can also be mitigated by permeated oxygen coming from the cathode, which allows the heterogeneous oxidation of CO at the anode. This process is known as internal air bleed [183]. Wang *et al*. studied its effects on a Pt-Ru/C anode by increasing the cathode backpressure and the use of ultra-thin membranes ($\leq 25\ \mu m$) for a CO concentration of 50 ppm [183]. Sapountzi *et al*. also reported an increase in the Faradaic efficiency by 2.5 in the presence of 2400 ppm CO (0.24% CO/12.82% CO_2/ 12.84% H_2/12.18% N_2/ 61.92% He) [158]. The main disadvantage of this approach is that use of a thin membrane can also lead to CO crossover from the anode to the cathode, which can degrade the cathode electrocatalyst and decrease membrane proton conductivity [46]. The formation of H_2O_2 from the diffused O_2 to the anode is also pernicious, as it provokes the degradation of the membrane in the extended hours of operation [180].

2.3.3.4 Reconfiguration of the anode

The modification of the anode structure has also been evaluated. The different approaches followed are presented next. These comprehend the inclusion of additional layers of different composition to the catalyst or diffusion layer, and/or the spread of new particles in the diffusion layer. The research about these methods is limited and certain concerns about their applicability, such as durability and costs, remain unsolved. However, when these structures are used in conjunction with an oxidant bleeding, these avoid the heating problems that degrade the performance of the cells in the long term.

2.3.3.4.1 Bilayer anode structure

Composite electrodes with different layers have been proposed by Johnson Matthey and Ballard Power Systems [230]. As hydrogen diffuses faster than CO, the inner catalyst layers of the composite electrodes have a higher loading of platinum to sustain the hydrogen oxidation reaction (HOR). The CO reacts in the outer layers, where bespoke CO oxidation catalysts are used. The layers can be designed with different electrocatalyst components, contents and pore distribution. This method allows the total amount of catalyst used to be reduced without any loss of performance [184, 185]. The decrease in the anodic overpotential was confirmed by a modeling study presented by Janssen *et al.*, where single layers and bilayer structures were compared [187].

Different catalysts layers prepared by different methods have been studied. Yu *et al.* proposed two layers of catalysts; a hydrophilic Pt/C inner-layer (0.02 mg cm^{-2} Pt) prepared by the transfer method [231], and a PtRu/C (0.28 mg cm^{-2} Pt/Ru) outer-layer composed by a thin carbon cloth [232], to mitigate 50 ppm CO [184]. Another proposition was to use an outer layer composed of two nano-Ru layers prepared by magnetron sputtering deposition, followed by a Pt_{50}-Ru_{50} layer by screen-printing. A third layer (the inner layer) is composed of pure Pt and is prepared by direct-printing on the membrane. This structure presents a better performance in the presence of 50 ppm CO than a conventional Pt_{50}-Ru_{50} screen printed on GDL [225].

The method of preparation was shown to affect the performance. The sputter deposition technique in the outer layer was found to double the CO tolerance (200 ppm CO vs 100 ppm CO) compared to conventional ink-based filters. It creates more sites upon which CO can be oxidized, using 40% less of Ru (0.080 vs 0.21 mg cm^{-2}). The different structures studied are presented in Figure 2.33 [186]. The most efficient structure corresponds to a sputter-deposited Ru filter placed beside a Pt:Ru alloy (Figure 2.34) [186].

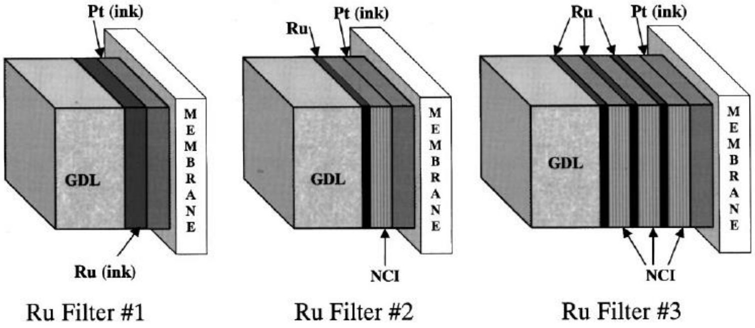

Figure 2.33 Structures of the Pt + Ru anodes studied. Filter 1: 0.08 mg cm^{-2} ink-based 20% Ru/C, Filter 2: Nafion-carbon ink (NCI) + 25 min (0.08 mg cm^{-2}) of sputter-deposited Ru, and Filter 3: NCI + 3 × (8.33 min of sputter-deposited Ru + NCI). The total Ru loading was 0.08 mg cm^{-2} [186].

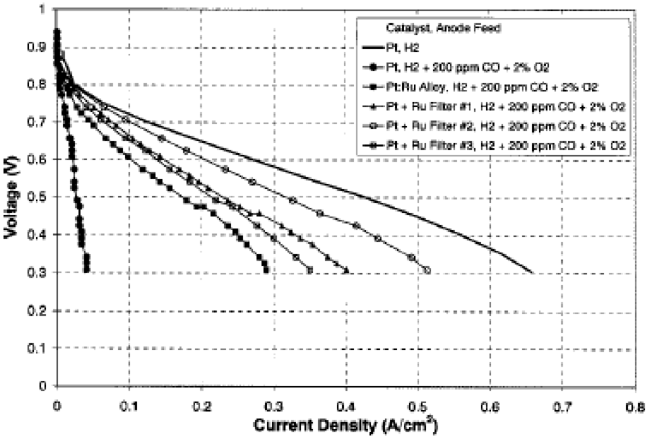

Figure 2.34 Performance comparison of the configurations of MEAs presented in Figure 2.33, under H_2 + 200 ppm CO + 2% O_2. P = 1 atm, T = 70 °C [186].

An additional advantage of the bilayer structure is that it can be used to mitigate CO_2 contamination[187] and the combined use with air bleeding extends the lifetime of the cell, as shown in Figure 2.35, where a reformate containing 70% H_2, 5% N_2, 25% CO_2 and 40 ppm CO was evaluated. 3% of air bleed was necessary to maintain the cell performance [161].

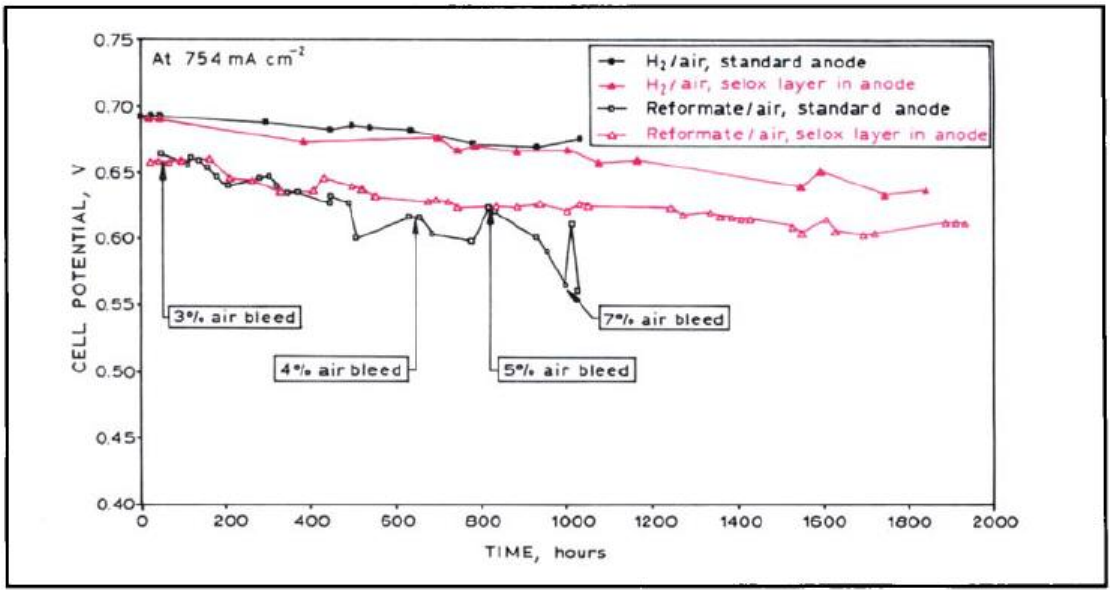

Figure 2.35 Durability study of a standard anode and a bilayer anode structure for hydrogen/air and reformate (70% hydrogen, 5% nitrogen, 25% CO_2, 40 ppm CO)/air operation at 754 mA cm^{-2} with an air bleed. The standard anode is composed of 20% Pt, 10%Ru/Vulcan XC72R at a loading of 0.25% mg Pt cm^{-2}. The bilayer structure includes an additional catalytic oxidation layer (selox layer) containing 20% Pt/Shawinigan carbon black at a loading of 0.1 mg Pt cm^{-2} [161].

A bilayer structure conformed of an exterior layer of PtMo and an interior layer of PtRu was studied by Ball *et al.* The PtMo/PtRu electrode was tested in the presence of concentrations of CO as high as 5000 ppm CO/H_2, obtaining a good performance, even in the absence of an air bleed. In spite of the quantity of platinum used, the results obtained opened up the possibility of reducing the system required for the purification of the reformate.

2.3.3.4.2 Refined diffusion layer

Shi *et al*. placed Pt or Au particles in the diffusion layer by impregnation, to enhance the oxidation of CO with oxygen before the gas reaches the catalyst layer of the anode. This structure can mitigate 100 ppm CO together with 2% of oxygen bleed [190]. Santiago *et al*. studied the modification of the diffusion layer, by applying filtering layers (Ru/C or

RuO_xH_y/C) on the diffusion layer and evaluated their performance in the presence of 100 ppm CO/H_2 [191].

2.3.3.4.3 *Complementary composite film coating*

Uribe *et al*. placed a thin film composite layer in addition to the gas diffusion layer (GDL), containing an inexpensive non-noble metal based materials. The MEA is prepared by brush painting an ink containing the non-noble metal on the anode carbon cloth, which is subsequently dried and sintered. As with the previous anode reconfigurations, the CO is oxidized with oxygen before entering the anode catalyst layer [192].

A variety of metals were tested, from which the most effective in promoting the CO oxidation correspond to metals (or their oxides), that present at least two predominant low stable oxidation states (1 to 4) [192]. Adcock *et al.* studied Fe, Co and Cu, from which the primary components in the composite were Fe_3O_4, Co_3O_4 and CuO, respectively. Figure 2.36 presents the voltage losses presented by these different complementary composite film coatings prepared and tested at 80 °C. The combined use of a complementary composite film coating and an air bleed (6%) enhance the tolerance of the cells to a concentration up to 500 ppm CO/H_2 [193].

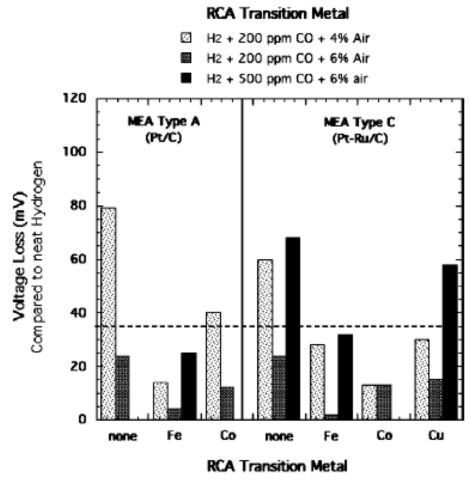

Figure 2.36 Voltage loss of the different anodes containing the complementary composite film coating at 0.5 A cm^{-2}. Fe major component: Fe_3O_4, Co major component: Co_3O_4 and Cu major component: CuO. The dotted line indicates maximum voltage loss considered as “full tolerance” [193].

2.3.3.4.4 *Catalyst sheet in front of the anode*

Rohland and Plzak proposed a Ni-foam sheet filled with Au/Fe_2O_3 -catalyst powders. This catalyst sheet is placed in front of the Pt/Ru-C anode of a PEMFC, separated by carbon paper that provides the necessary electrical contact without compromising the gas transport (Figure 2.37 (a)). The CO bonds created with Au are weaker than with Pt at 80 °C. Their strength is comparable to the CO bonds with Pt at 200 °C. The selective oxidation of CO is consequently increased in the Au-catalyst, providing a higher CO tolerance to the system. The catalyst sheet was tested simultaneously with an oxygen bleed, being able to mitigate 1000 ppm CO with 1% oxygen (Figure 2.37 (b)) [194].

(a)

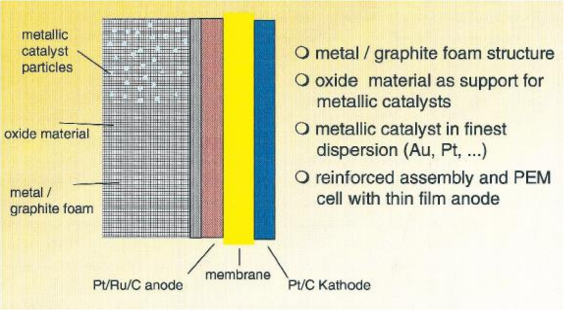

(b)

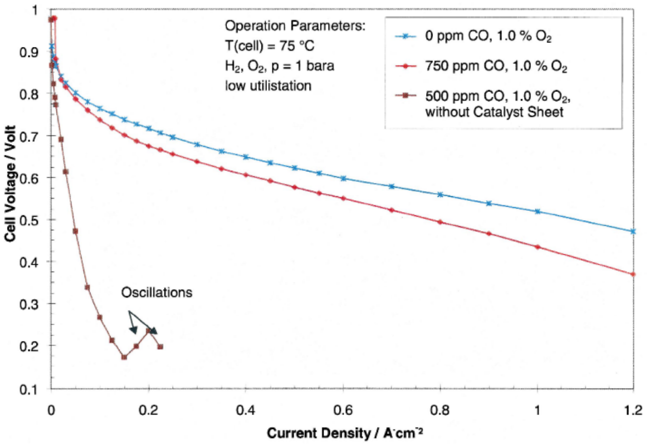

Figure 2.37 PEMFC with a catalyst sheet: (a) diagram of the components, (b) evaluation of the performance of the catalyst sheet together with an oxidant bleed [194].

2.3.3.5 Pulsed heating

A microheater device consisting of a stainless steel mesh was introduced in direct contact with the anode to locally increase the temperature, without affecting the temperature and the conductive properties of the membrane (Figure 2.38). The temperature of the anode was increased through heating pulses to recover the cell performance over-exposure to CO. The use of this recovery process allowed a performance four times higher than the poisoned case over the exposition to 1000 ppm CO/H_2 [164].

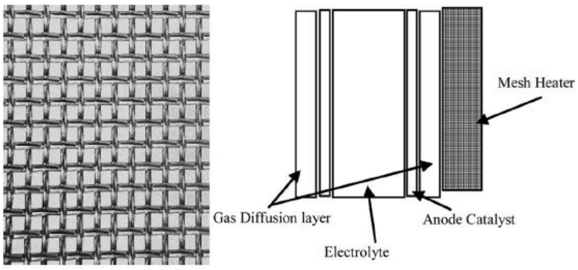

Figure 2.38 Application of heating pulses though the stainless steel mesh [164].

2.3.3.6 Pressure swing

The pressure swing system was proposed by Guo *et al*. As shown in Figure 2.39, a fuel cell was divided into subunits, which were connected to a feed control valve. Through this valve it is possible to pull off the supply of hydrogen to specific units, producing a “vaccum”. Unconsumed hydrogen from the anode outlet mixed with air or oxygen is then introduced to the starved cells.The amount of oxidant used is reduced compared to a typical air bleed, and the performance of the system is improved by a factor of four in the presence of 1000 ppm CO/H_2 [164].

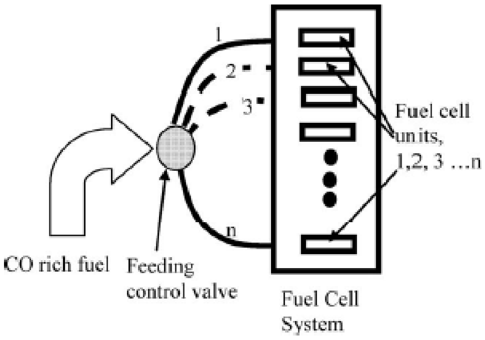

Figure 2.39 Diagram showing the disposition of the cells and the feeding control valve over the application of pressure swing [164].

2.3.3.7 Combined break-in procedure and $KMnO_4$ treatment

Narayanan *et al*. proposed a regeneration process composed of a break-in procedure and the injection of a diluted solution of $KMnO_4$ in the anode. The break-in procedure consists of the application of lower and higher overpotentials for a determined period, where the CO is oxidised to produce CO_2. In the presence of the $KMnO_4$ solution, the CO is also oxidised, this time by the nascent [O]. Figure 2.40 compares the influence of the break-in procedure and the $KMnO_4$ treatment on the catalyst activity at different temperatures. The combination of both treatments allows the regeneration of the catalyst by 90% [179].

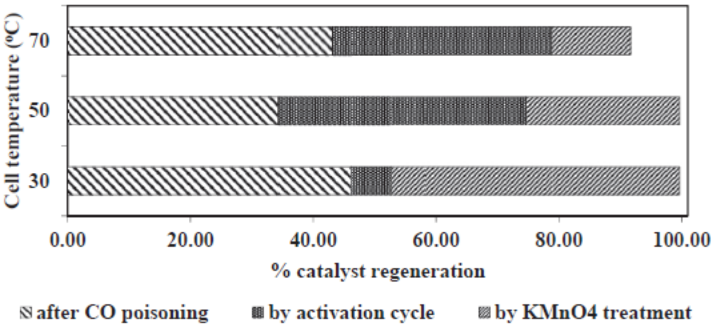

Figure 2.40 Regeneration of the catalyst for different temperatures through the break-in procedure (activation cycle) and the $KMnO_4$ solution treatment [179].

2.3.3.8 Triode operation

The triode operation consists of the addition of an auxiliary electrode to the fuel cell, in addition to the anode and the cathode, and in contact with the membrane (Figure 2.41). Two circuits are formed:

- The conventional fuel cell circuit between the anode and the cathode.
- An auxiliary circuit, between the auxiliary electrode and the cathode, working in parallel to the fuel cell and in electrolytic mode (I_{aux}<0 and ΔV_{aux}<0).

Over the operation, the potential difference between the auxiliary electrode and the cathode increases simultaneously the potential difference between the anode and the cathode. This allows the fuel cell to operate at potentials not accessible under normal operation (higher than 1.23 V), and thus, enhance its performance [196, 197, 199]. Figure 2.42 presents the performance of a cell exposed to 90 ppm CO/H_2 under triode operation [199]. In the presence of CO, the transport of protons from the auxiliary electrodes enhances the oxidation of CO, favouring the self-sustained potential oscillations [196, 197]. Katsaounis *et* *al.* explained the improvement of the performance of the cells under triode operation by the proton tunnelling mechanism, which increases the membrane conductivity [233, 234].

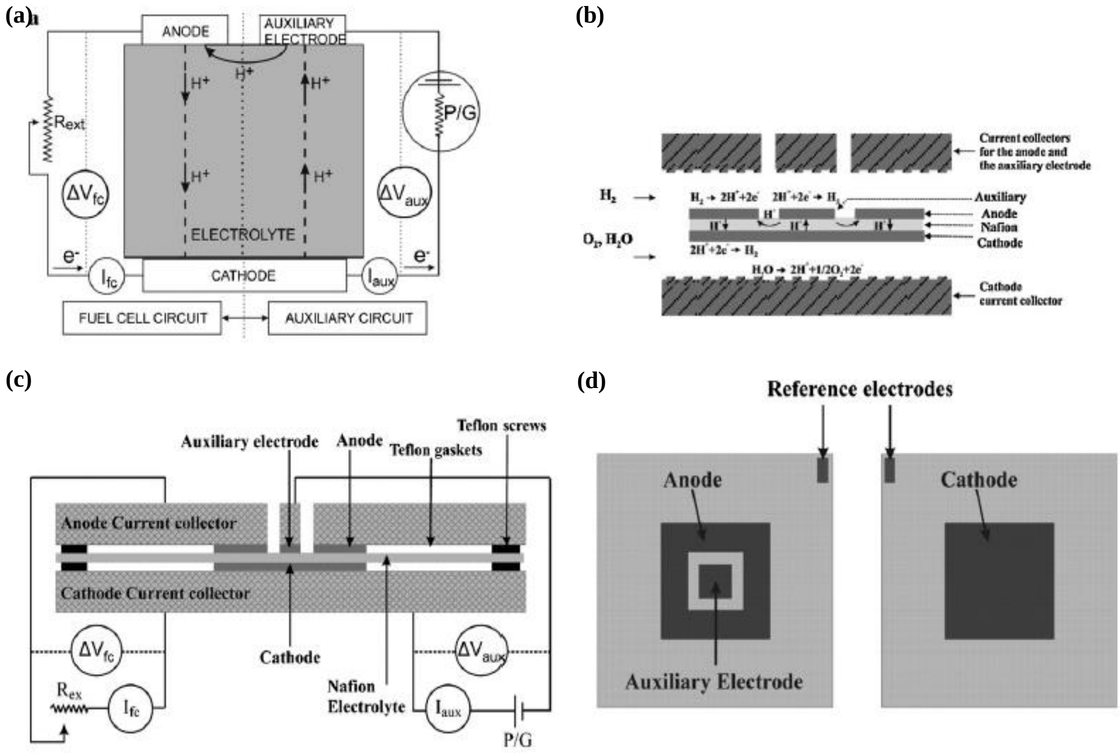

Figure 2.41 Triode operation system: a) Circuits involved and different current flow direction, b) reactions taking place, c) side-view of the system and d) electrodes layout as part of MEA. P/G: potentiostat-galvanostat [196].

.

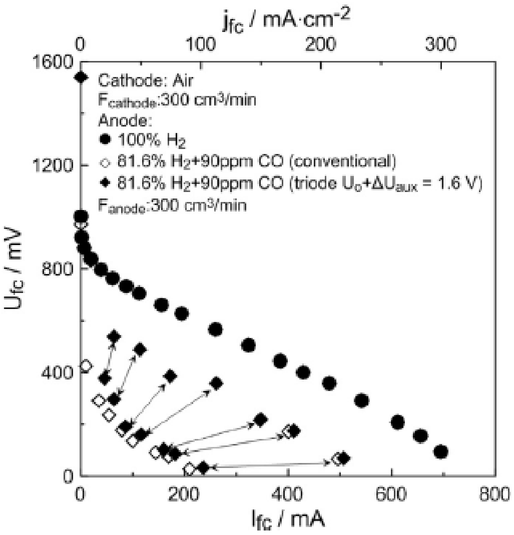

Figure 2.42 Polarization curves of a fuel cell exposed to pure H_2 and to 81.6% H_2 and 90 ppm CO /H_2. These are compared with the triode operation over the exposition to 81.6% H_2 and 90 ppm CO /H_2. The arrows over the triode operation represent self-sustained current or potential oscillations [199].

Another advantage is the use of less expensive materials [195, 233] and practical adaptation into stacks [196, 197, 199]. Among the disadvantages is the power consumption in the auxiliary circuit, and the corrosion-type mode under which the three electrodes, as reduction and oxidation reactions take place on their surface at the same time [196, 197, 199].

Martino *et al*. developed a model based on the laws of Kirchhoff and the Nernst-Planck equation, and proposed a comb-type electrode geometry that reduced the resistance between the auxiliary electrode and anode or cathode. The new design was exposed to up to 120 ppm CO/H_2, increasing by 500% the power output compared to a fuel cell operation under the same concentration of CO [199].

2.3.3.9 Periodic variation in the fuel supply

2.3.3.9.1 Cyclic injection of pure H_2

The reversibility of CO poisoning has been examined by different authors [77, 81, 92, 106]. Zhang *et al*. showed that the adsorption of CO on Pt at 80 °C is reversible with a pure hydrogen purge, even when the Pt is exposed to high concentrations of CO [235, 236]. As such, the poisoning can be considered a transient phenomenon [81].

Taking into account this property, Jimenez *et al*. proposed the cyclic feeding of hydrogen-containing CO, with the injection of pure H_2 streams. This operation allowed the desired cell voltage range to be maintained during operation on 72 ppm CO/H_2 (Figure 2.43). An advantage of this operation is that due to the relatively stable voltage, the lifetime of the cells is extended. However, careful monitoring and control of the feed gasses is required [200].

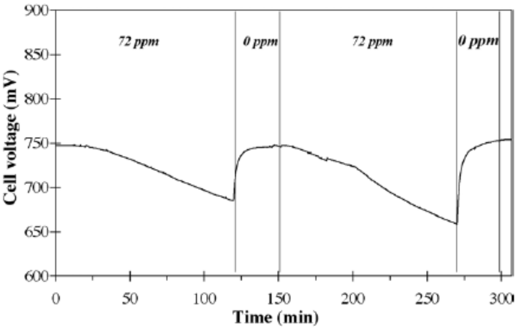

Figure 2.43 Cyclic injection of 72 ppm CO/H_2 and pure hydrogen [200].

2.3.3.9.2 Periodic fuel starvation

Hydrogen starvation occurs under extreme operating conditions (high currents, failure to supply adequate hydrogen to the anode), and results in an increase of the anode potential. The electric potential difference is consequently narrowed and even reversed [237, 238]. Wilkinson *et al.* presented the application of periodic starvation of fuel as a mitigation strategy against CO. In the presence of the contaminant, the increase of the anodic potential due to starvation is added to the rise due to the accumulation of CO in the catalyst, resulting in the oxidation of CO [201].

Different set-ups presented, such as the periodic interruption of the fuel, or the periodic introduction of a fuel-free fluid, such as nitrogen, argon, helium and hydrocarbons into the anode. Other possible fuel-free fluids are liquid water or the cathode exhaust from the fuel cell. Another setup involves the application of a higher transient load, without the respective increase of the fuel flow. It was proposed that the starvation is applied in a portion of the anode while maintaining continuity in power supplied by the rest of the fuel cell [201].

An important consideration is the parameters used to define the periods of fuel starvation and supply, as cell reversal is undesirable. A controller is used to vary the frequency and length of the pulses following a specific time set, or by monitoring the performance of the cell [201]. The reversal of the cell implies the consumption and not the supply of energy, the production of oxygen in the anode and of hydrogen in the cathode, and irreversible damage in the cell materials that affects the durability of the cell [237]. The technique has been evaluated in the presence of 75% H_2, 25% CO_2 and 10 ppm or 100 ppm CO [201].

2.3.3.10 Pulsed oxidation or pulsing technique

2.3.3.10.1 Current pulsing

The current pulsing technique involves introducing periods of high load (high current) so that the anode potential increases and CO on the catalyst is oxidised to CO_2 (Figure 2.44) [202]. The removal of CO from the Pt surface occurs in a short period (tens of milliseconds); thereby the anode potential is mostly in the hydrogen oxidation region rather than in the CO oxidation potential [44].

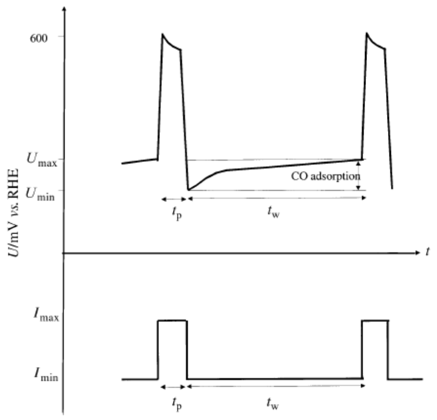

Figure 2.44 Pulsing technique description. The current is pulsed over the period t_P. t_W corresponds to the waiting time as CO builds up on the catalyst surface again [202].

The pulse amplitude can be adjusted depending on the specific MEA, as the potential at which the CO oxidation occurs depends on the catalyst used. This can be determined through cyclic voltammetry. As for the pulse duration, some reports recommend keeping this constant regardless of the CO concentration in the feed [202]. Extending the pulse time unnecessarily long will reduce the fuel cell efficiency [205]. Rather, it is the frequency of the pulse that should be used as the key parameter to tune depending on the size of the electrode, flow rate and CO concentration of the anode feed [202].

Studies with different CO concentrations have been performed, from 50 ppm to 3% CO/H_2 [44, 57, 202, 205, 239], with good results compared to the operation with pure H_2. In the case of 3% CO/H_2, a feedback control algorithm was used, using the current pulsing and the flow rate as control variables. 54% of the power obtained with pure H_2 was reached (Figure 2.45) [239]. Another advance for the application of this technique is the model proposed by Ozdemir *et al*. that predicts the CO coverage and the CO-free surface over the application of the current pulsing technique in the presence of 10,000 ppm CO/H_2 [240].

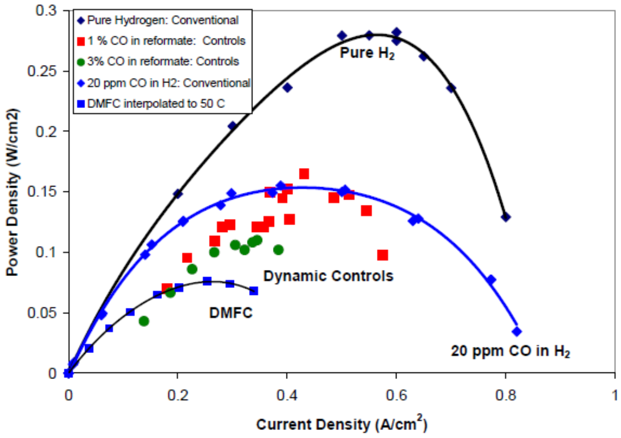

Figure 2.45 Power density obtained for a PEMFC with pure H_2 and 20 ppm CO/H_2 over a conventional operation, and with 1 and 3% CO/H_2 using a feedback control algorithm [239].

The pulsing technique presents several advantages as it allows the direct use of reformate gas without a significant loss of performance. Additionally, to carry out this technique, no external source of energy is necessary, apart from that required to trigger the pulsing event. As for the losses, these arise due to the low voltage (inefficient operation) during the pulse [202].

On the other hand, long-term stability tests are needed for the catalysts used in this method [202], such as the Pt dissolution and the loss of ECSA (electrochemical surface area). This constitutes the main reasons for the optimization of the pulses to reach a sufficiently high anode overpotential to oxidise CO, but not so much as to stress the electrode materials into degradation by dissolution, for example [240].

While execution of this method with single cells is quite straight-forward, applying it to a stack is much more challenging as the balance of reactant distribution and resistances in the stack means that each cell is likely to behave differently during the pulse period. Therefore, the approach can only be relied upon in a conventional bipolar stack if rigorous control of the voltage of each cell in the stack can be achieved [205]. Adams *et al*. proposed a new device that allows each cell in the stack to be pulsed independently under controlled conditions. The Fuel Cell Health Manager (FCHM) is a microprocessor-based controller that has proved to be effective with 10,000 ppm CO [44, 241, 242].

Another strategy to optimize the application of current pulses is the use of a power converter. For instance, a two-stage dc/dc power converter with a supercapacitor module was proposed by Choi *et al*. to perform in a clean, fast and reliable manner the pulsing technique. It was possible to increase the power of the fuel cell by 50% in the presence of hydrogen fuel with 500 ppm CO. The diagram of the device and the performance studies are shown in Figure 2.46 [203].

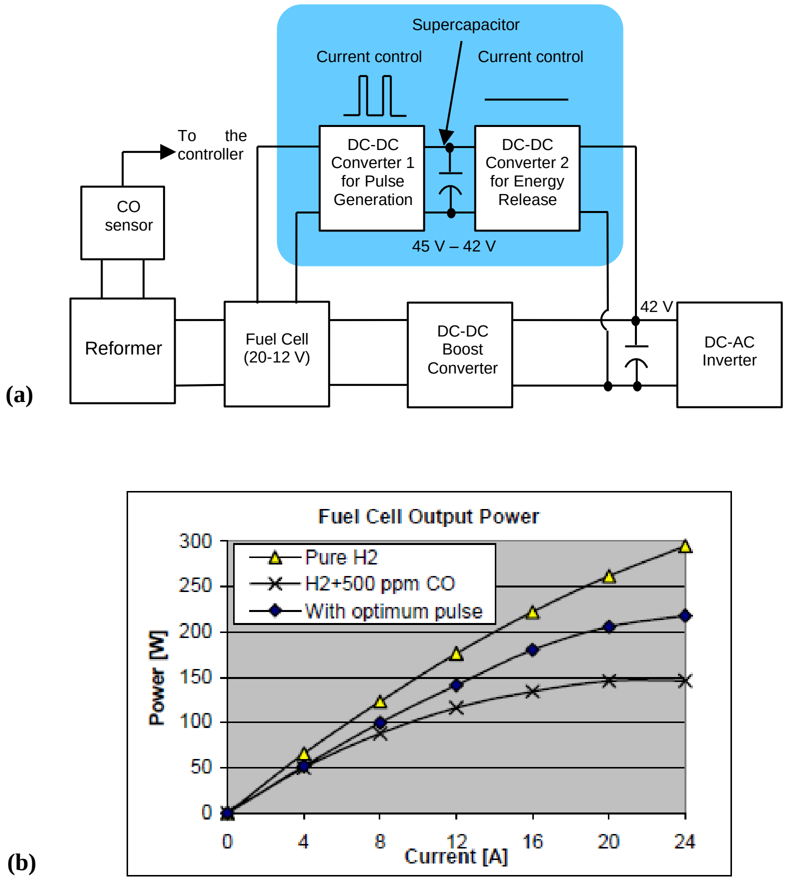

Figure 2.46 Optimization of the current pulsing through a power converter: (a) Diagram of the two-stage dc/dc power converter with a supercapacitor module, (b) comparison of the power output of a cell operating with pure H_2, 500 ppm CO/H_2 and 500 ppm CO/H_2 with current pulses [203].

Palma *et al*. proposed a different power converter able to modulate the current drawn from the stack. As is shown in Figure 2.47, instead of applying pulses of fixed magnitude, as in the conventional current pulsing technique, the pulses vary linearly with load current until full load. Figure 2.47 also presents the system, which has a boost converter in parallel with the reverse blocking diode placed at the output terminals of the fuel cell. It only operates for the duration of the pulses. The use of this device leads to reduced losses when operating at light loads. It also extends the lifetime of the fuel cell without reducing the output power [204, 243].

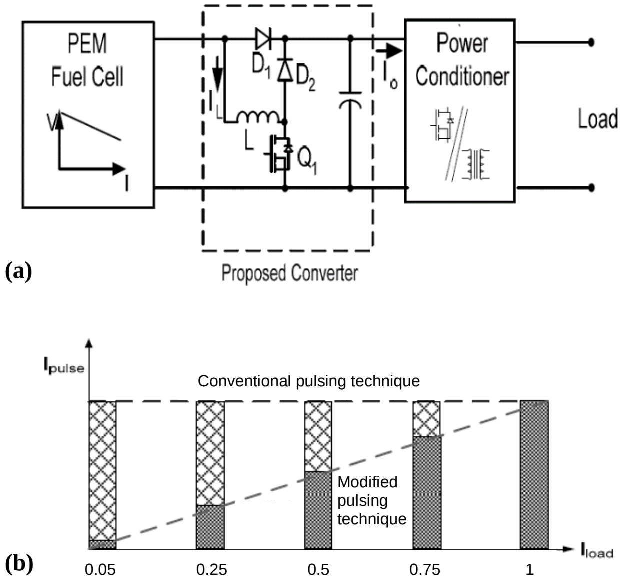

Figure 2.47 Power converter for the optimisation of the current pulsing technique: (a) Diagram of the power converter that includes a boost converter in parallel with the reverse blocking diode placed at the output terminals of the fuel cell, (b) comparison between the conventional pulsing technique and the modified pulsing technique used in the power converter [204].

2.3.3.10.2 *Negative potential pulses*

Mao *et al*. were the first to propose the application of a reverse voltage for the regeneration of a single PEMFC in the presence of CO at the anode. During the negative pulse, water present at the anode is electrolyzed, producing oxygen that oxidises the carbon monoxide on the Pt surface [207]. The electrolysis reactions taking place are [206]

$$\boldsymbol{4H_2O + 4e^- \rightarrow 2H_2 + 4OH^-} \tag{2.19}$$

$$\boldsymbol{2H_2O \rightarrow O_2 + 4H^+ + 4e^-} \tag{2.20}$$

Wingelaar *et al*. studied the application of periodic negative voltages to regenerate a system composed of four cells fed in series, but electrically connected in pairs (the first two and the last two in parallel) [206]. Although the application of negative voltage pulses requires a significant amount of power, it was possible to increase to up to 500% the voltage output of the system when exposed to 50 ppm CO/H_2. The electrical position of the individual cells in the stack determined their CO-tolerance and regeneration [206]. Other advantages found by

Mao *et al*. were the rapid and more controllable application of this pulsing technique compared to oxidant bleeding [207].

2.3.3.11 Potential oscillations or self-oscillations

The spontaneous potential oscillations over the CO poisoning mentioned in Section 2.2.2.2 can also be used as a mitigation strategy. As there is no need for any active control system or any additional equipment, the self-oxidation can be considered a passive back-up solution [57]. As previously mentioned, the oscillations occur under determined conditions. For instance, the concentration of CO has to be high enough for the self-oxidation to take place [57], and a minimum current density is required [208].

Figure 2.48 shows the effect of the self-oxidation in a CO-poisoned cell with 496 ppm CO. The catalyst used was Pt/Ru. The cell voltage drops until it reaches ~ 0.2 V, at which point the anode overpotential is large enough to cause oxidation of CO. Thomason *et al*. compared this method to the current pulsing technique. Both presented a similar efficiency in terms of the voltage produced and the CO tolerance (496 ppm). However, the voltage cell was above 0.60 V about 50% of the time, compared to 80% in the case of the pulsing technique. The pulsing technique also produced 13% more energy, and 13% more average power. Figure 2.48 presents a comparison of the two techniques in terms of the voltage [57].

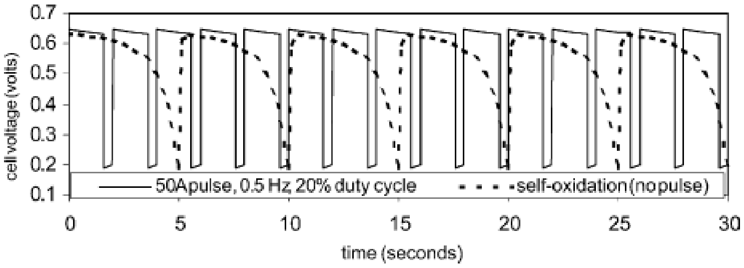

Figure 2.48 Variation of voltage over time of a cell exposed to 496 ppm CO/H_2. The constant cell current applied was at 20 A (0.4 A cm^{-2}). The pulse was 1.0 A cm^{-2} (50 A), 0.5 Hz, with a 20% duty cycle [57].

2.4 Critical discussion on mitigation strategies

An array of the mitigation strategies developed to counteract the pernicious effects of CO in PEMFC has been presented. Comparing the different technologies, it is possible to observe certain trends and elucidate the most promising techniques to be used in the future for each one of the categories where the strategies were divided.

Currently, 95% of the hydrogen generated worldwide is produced and used in the same location, as part of large industrial processes [244]. However, some expect hydrogen to be generated and purified on-board. This requires reformate pre-treatment technologies, that at present are part of large industrial processes, to evolve into more compact designs. An indication of this trend is the development of an ultrathin reformer incorporated to a high temperature PEMFC, presented by Avgouropoulos *et al.* [245]. Another example would be the use of the Al_2O_3-supported Si_3N_4 membranes, which are already being used on-board [150].

Membranes, in particular made of two-dimensional materials, are the most promising technology of the pre-treatment technologies presented. This is due in large part to the possibility of separating additional pernicious contaminants to the operation of PEMFC, such as CH_4 and CO_2. Membrane-based technologies also offer additional benefits such as low investment cost, facile operation, small footprint and easy maintenance [122]. Hence, this technology is also promising if adapted to on-board applications.

As mentioned, additional contaminants are present in the fuel, which depend on the nature of the generation of hydrogen. In the case of reformate, H_2S and NH_3 are also present apart from CO and cause degradation of the cells. Thus, the importance of the study of mixtures of contaminants and the development of mitigation strategies able to neutralize their combined effect. Examples of these mitigation strategies are the air bleed and the HT-PEMFC, able to mitigate both CO and H_2S [169, 176]. The deployment of these two strategies is expected to rise, in spite of their operational challenges.

Another area of interest is the development of electrocatalysts, as the scarcity and high costs of platinum represent one of the impediments for the commercialization of fuel cells [160]. Important progress has been reported in terms of CO tolerance and the reduction of platinum use. However, the stability of the catalyst structures, in particular of alloys, continues to be a challenge. Although the catalyst tolerance to other contaminants such as H_2S has been explored [246], the combined mitigation of CO, H_2S and other species has not been reported, showing a promising field of research.

Due to the catalyst limitations, other engineering and operational approaches have emerged from which, pulsed oxidation through current pulses presents the highest tolerance to CO. Cells have been tested in the presence of 3% CO/H_2 [239]. Considering the CO content of the reformate after the WGS reaction of 1-2% [29], this is a mitigation strategy that could contribute to the total reduction of the more complex purification stages. Moreover, no changes in the operating conditions, such as an increase in the temperature are needed, and no other reactant is added as in the oxidant bleeding technique. However, limitations still exist, such as the degradation of the catalyst and further development is needed.

2.5 Future research on CO poisoning

The research on CO poisoning in PEMFC is taking different directions. Firstly, new techniques are being developed to obtain more accurate measurements for a better understanding of the mechanisms of CO poisoning. For instance, Kaserer *et al*. took as a reference the localised reference electrode technology presented by Hinds *et al*. to study the poisoning in HT-PEMC [24, 247]. Another improvement is the rapid detection of the CO by in-line [248-250] and in-situ [251] sensors allowing the application of a mitigation strategy before the performance of the cell is degraded.

An increasing array of analytical techniques is being applied to understand the CO poisoning mechanism. Caldwell *et al*. applied $\Delta\mu$ adsorption near-edge spectroscopy (XANES) to reveal details of the binding-site for H, CO and biphosphate on the platinum anode catalyst that contributes to the better performance of HT-PEMFC in the presence of CO [252]. Another example is the use of the H_2-D_2 switch with Ar purge (HDSAP) method to study the effect of humidity on contamination [235, 236].

Computational and modelling methods, often combined with experimental validation, are being more extensively applied to derive new insights and optimise mitigation techniques. For example, new methods for the interpretation of how the EIS response evolves over time due to the exposure of CO have been proposed. These include techniques such as real-time drift compensation, time course interpolation and Z-HIT refinement [97, 108].

In the modelling of the poisoning process, models proposed present specific limitations, such as accounting for the homogeneity of contamination over the anode [240]. However, good agreement with experimental results is obtained over different stages of CO poisoning, which include an initial decrease in performance, pseudo-steady behaviour, and regeneration when exposed to pure hydrogen. These modelling studies have been reviewed and critically compared in the literature [46, 240, 253].

The studies evaluating the effects of CO poisoning on the anode are extensive, with little research on the effects on other components of the cell. It is expected that the research on the impact on the cathode and the membrane, for instance, is extended, covering short and long-term effects. These studies could also be executed under the normal operation of the cell, and under harsh conditions prone to occur, such as cold-freezing conditions.

Another area of research concerns mixtures of contaminants, which corresponds to more plausible conditions of operation than a single contaminant. The nature of the contaminants depends on the hydrogen generation process and on the purification step. As new technologies are developed for the production of hydrogen, new contaminants are expected to emerge. The effects of many mixture combinations in operational fuel cell are unknown. For instance, it is known that methane (CH_4) is a contaminant produced from steam methane reforming and the purification by PSA [254]. Although its presence is rare, the combined effects with CO has not been studied.

As mentioned, the development of mitigation strategies against CO is a key factor for the deployment of PEMFCs, as the increase in the CO tolerance represents a reduction in the costs and volume of the hydrogen purification stages. The research for techniques that compel with these requirements without compromising the power generated by the fuel cells continues. Additional issues are their durability and complexity. CO tolerant electrocatalysts are the most researched area; however, a variety of new mitigation strategies has been proposed recently for their application over the hydrogen purification and separation in site and on board, and during the operation of the cells. Different approaches have been explored, from the variation of operating conditions, to the addition of new reactants in the fuel and the modification of the design of the cell.

Another approach towards the mitigation of CO poisoning is the application of dual-purpose redox processes. Designed for direct methanol fuel cells (DMFCs), the removal of CO is done by the injection of hexavalent chromium (Cr(VI)), a toxic and carcinogenic substance. The CO is used as a reducing agent for the Cr(VI) that is converted into Cr(III). The removal of CO and the conversion of Cr(VI) are done simultaneously [255].

2.6 Conclusions

CO poisoning is an important area of research in PEM fuel cells as the performance and durability of these cells are significantly affected by it. A review of the mechanisms of contamination and its effects on the performance of the cells shows the complexity of the process as evidenced by the short and long-term degradation on the anode side, impact on the cathode side, and the heterogeneous spatial distribution of the contamination. In recent years, the development of more accurate techniques and advanced computational and modelling methods has contributed towards the discovery of new information about the phenomena. More research would elucidate a comprehensive profile of the poisoning and tolerance to CO.

Advancement in mitigation strategies that allow the reduction of the space and costs that the actual H_2 separation and purification processes represent is needed for the deployment of PEMFC. Over the last decade, an array of varied techniques has emerged at the ‘on site’ (pre-treatment of reformate) and ‘on board’ H_2 purification stages, and particularly over the operation of the cells. The development of CO-tolerant electro-catalysts continues to be the most studied; nevertheless, other approaches have been explored and shown to operate effectively with high CO tolerance.

Chapter 3

Experimental Setup and Methodology

3.1 Introduction

The studies presented in this work required the preparation of different systems and the execution of individual sets of experiments. In this chapter these are described in detail, from the preparatory experiments carried out in a single cell, to a more complex setup that comprises the placement of localised reference electrodes on the anode side of a single cell. The following setup concerns a segmented-in-series system that could be considered a segmented cell. The study of the short-circuiting as a possible mitigation strategy was evaluated in this last system. The main objectives of the experiments were the study of the mechanisms involved in the poisoning of CO, and the proposition of a technique that could potentially alleviate the adverse effects of the contamination.

3.2 Single-cell studies

Different experiments were carried out in a single PEM fuel cell to evaluate the catalyst activity and to observe the short-term effects of CO. These results were compared with studies presented in the literature and contributed for a better understanding of the system. The configuration of this cell and the execution of these tests were also the base for the following phase of the research.

3.2.1 Configuration of the single-cell

The membrane electrode assembly (MEA) was prepared with Pt/C catalyst from Johnson Matthey with a loading of 0.4 mg cm^{-2} in the anode and the cathode. The surface area was 5.29 cm^{2} and the cation exchange membrane used was Nafion HP membrane (20.3 μm) from Dupont. These components were not hot-pressed, and were directly placed in a built-in-house cell. Figure 3.1 (a) presents the components of the cell in a transversal view. The bipolar plates are made of graphite and have a serpentine configuration. Gas-tight sealing was achieved using three layers of Tygaflor on each side of the MEA. All the components were assembled in the order shown, and compressed with a torque of 2 Nm. Figure 3.1 (b) presents a picture of the cell, with the fuel and electrical connections.

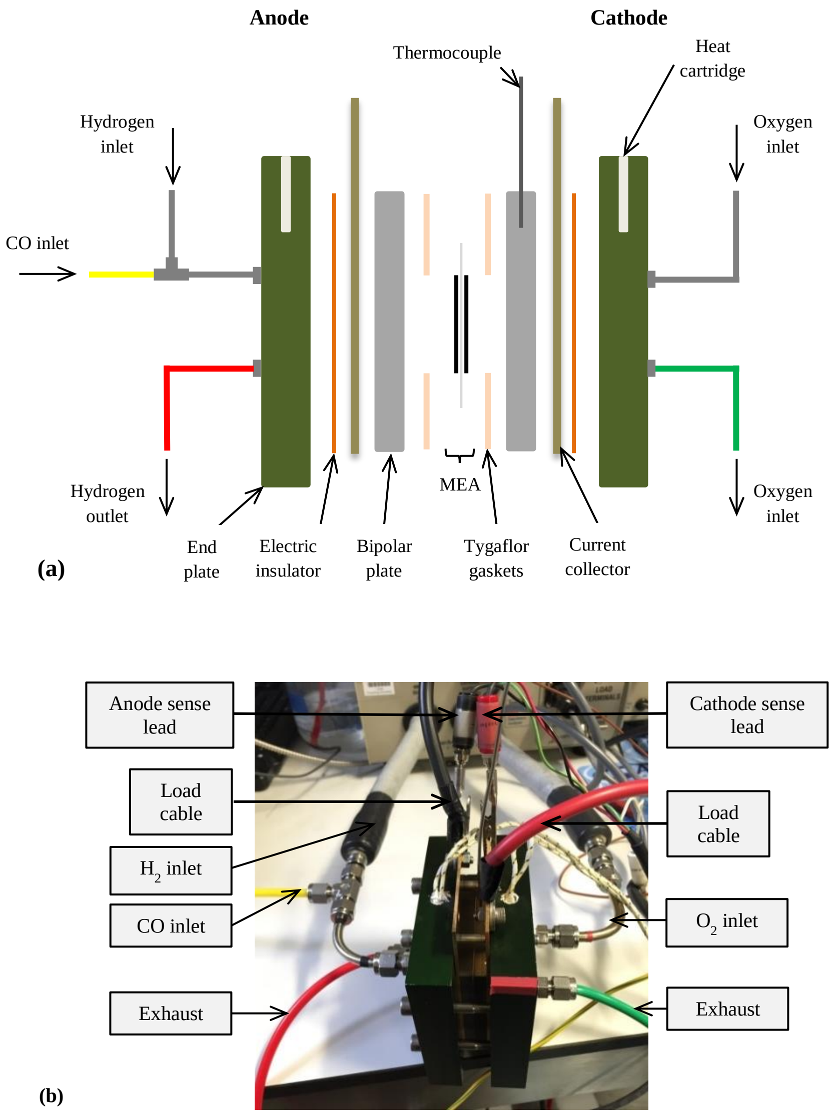

Figure 3.1 Configuration of the single-cell: (a) transversal view showing its components, (b) picture of the cell.

3.2.2 Fuel cell testing

The cell was operated using a Fuel Cell Test System 850e (Scribner Associates Incorporated). The gases that were used were hydrogen, oxygen and argon (zero grade from BOC). A mixture of CO/H_2 was supplied to the cell through a flowmeter (Bronkhorst (UK) Ltd). Two concentrations were used: 200 ppm and pure CO. In most of the experiments, the total flow entering the anode was 100 mL min^{-1}, combining the flow of H_2 and the mixture of CO/H_2. The total flow in the cathode was 100 mL min^{-1} of O_2. It is worth mentioning that the flow coming from the test system was not exact, as there was a variation of about 5%. The gases provided by this equipment were humidified. The load was provided by the 885 Fuel Cell Potentiostat, which is integrated into the Fuel Cell Test System. The Interface 5000E potentiostat (Gamry Instruments) was also used for certain measurements. The outlet of the anode and the cathode were connected to two ‘bubble bottles’ that directed the gases to the exhaust and avoided suck-back from the atmosphere.

3.2.2.1 Determination of the ECSA

The evaluation of the catalyst activity of the MEA was carried out through the measurement of the ECSA that was done through two techniques: adsorption/desorption of H_2 and CO stripping. The adsorption/desorption of H_2 was done in one step, while CO stripping in two. For both techniques cyclic voltammetry was performed, as detailed in Table 3.1.

Table 3.1 Evaluation of the ECSA.

Characterization technique	**Anode side**	**Cathode side**	**Equipment**	**Test conditions**
Adsorption / desorption of H_2	H_2 at 100 mL min^{-1} (DHE)	Ar at 300 mL min^{-1} (WE)	Interface 5000E	Cyclic voltammetry: Scan rate: 10 mV s^{-1} Range: 0-1.4 V Number of cycles: 3
CO Stripping	H_2 at 100 mL min^{-1} (DHE)	Pure CO at 10 mL min^{-1} + Ar at 100 mL min^{-1} (WE) for 10 min	Interface 5000E	Constant 0.1 V
	H_2 at 100 mL min^{-1} (DHE)	Ar at 300 mL min^{-1} (WE)	Interface 5000E	Cyclic voltammetry: Scan rate: 10 mV s^{-1} Range: 0-1.4 V Number of cycles: 3

3.2.2.2 Effect of CO in the performance of the cell

As for the study of the short-term effects of CO, the time exposure, the concentration, the temperature, and the flow on the anode inlet were varied. For all the experiments, except for the time of exposure, 210 min in the presence of CO were considered before the measurements. At this stage, the system was considered stable. The main characterization techniques used were polarization curves and EIS. The performance of the cell in the presence of CO was compared with the results obtained under the conditions indicated in Table 3.2, and the summary of the tests completed is presented in Table 3.3.

Table 3.2 Standard operation of the cell.

Parameter	Reference value
Temperature	70 °C
Flow rate in the anode (H_2)	100 mL min^{-1}
Flow rate in the cathode (O_2)	100 mL min^{-1}
Humidity of H_2 and O_2	100% RH

Table 3.3 Experiments for the evaluation of the short-term effects of CO.

Parameter	Range studied	Characterization technique	Equipment	Test conditions
Exposure time	0, 5, 60, 210 min	Polarization curve	885 Fuel Cell Potentiostat	0-9.25 A 30 sec/Pt
		Galvanostatic EIS	Interface 5000E	250 mA cm^{-2} 100,000 - 1.0 Hz 30 Pt/decade
Concentration of CO	20, 40, 60, 80, 100 ppm	Polarization curve	885 Fuel Cell Potentiostat	0-9.25 A 30 sec/Pt
		Potentiostatic EIS	Interface 5000E	0.7 V 20,000 – 0.1 Hz 12 Pt/decade
Temperature	40, 50, 60, 70, 80 °C	Polarization curve	885 Fuel Cell Potentiostat	0-9.25 A 30 sec/Pt
		Hybrid EIS	Interface 5000E	250 mA cm^{-2} 100,000 – 0.1 Hz 30 Pt/decade
Flow rate in the anode inlet	100, 200 mL min^{-1}	Polarization curve	885 Fuel Cell Potentiostat	0-9.25 A 30 sec/Pt
		Potentiostatic EIS	Interface 5000E	0.7 V 20,000 – 0.05 Hz 12 Pt/decade

3.3 Localised reference electrodes

The following experiment consisted of the placement of three localised reference electrodes throughout the anode side of a single cell, as detailed next. These electrodes allowed the direct measurement of the anode potential in the presence of CO at different time and space.

3.3.1 Configuration of the cell

A 50 cm^2 single PEMFC with a six-channel serpentine geometry was used. The MEA was composed of two identical Pt/C electrodes (Johnson Matthey, SA), 0.4 mg cm^{-2} Pt loading, and a membrane electrolyte (Nafion HP, 22 µm thickness). The cell assembly was hydraulically compressed at 7 barg, and the variation of the anode potentials was monitored through an array of three localised reference electrodes, numbered following the hydrogen path. The structure and location of the reference electrodes is shown in Figure 3.2.

The localised reference electrodes used were previously developed by Hinds *et al.* [247]. These include the use of salt bridges composed by Nafion tubing inserted in a polytetrafluoroethylene (PTFE) sheath, filled with a solution of 0.5 M H_2SO_4. The end-plate and the flow-field were drilled to allow the passage of the salt bridges that were in direct contact with the GDL through a polyether ether ketone (PEEK) filament. To allow ion conductivity, the GDL was impregnated with Nafion using a solution previously heated at 70 °C, composed by 50:50 by volume of a 10% dispersion of Nafion in water (Sigma Aldrich) and 2,2,3,3-tetrafluoro-1-propanol (Sigma Aldrich). O-ring seals were used to prevent any gas leakage from the flow-field. On the other end of the salt bridges, glass chambers containing Gaskatel GmbH hydrogen reference electrodes were located. Each one of these electrodes was previously calibrated using a saturated calomel electrode. The measurement and data acquisition of the anode potentials were done through a NI-9205 32-channel analogue input module in a compact DAQ chassis (National Instruments, USA), controlled by a LabVIEW program.

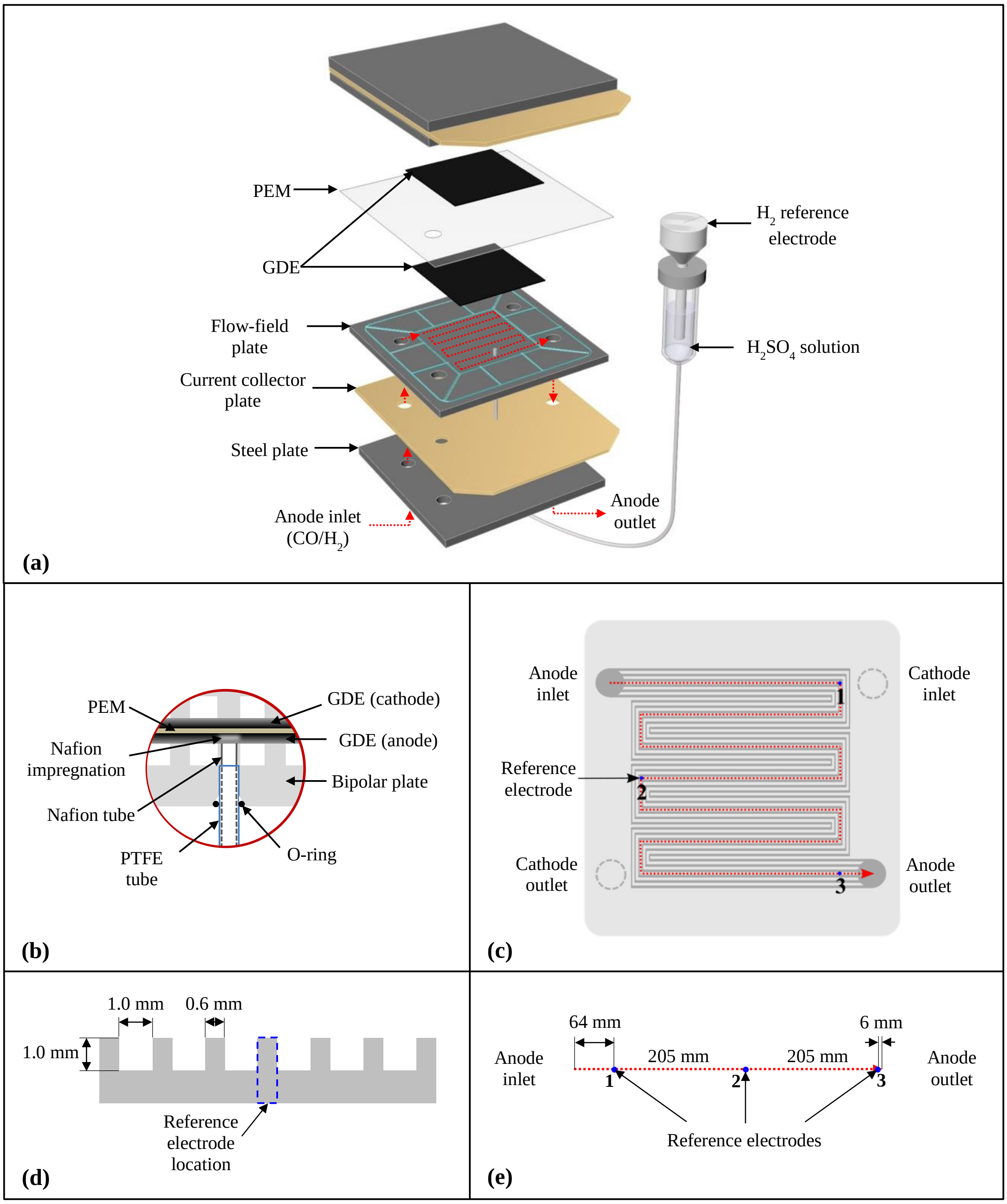

Figure 3.2 Placement of the reference electrodes in the 50 cm^2 PEMFC with a six-channel serpentine geometry: (a) Configuration of the system in the presence of one reference electrode; (b) insertion of the reference electrode into the MEA; (c) location of the reference electrodes in the MEA for the study of the anode overpotentials; (d) transversal view of the channels, and (e) approximate distance between the reference electrodes following the channels trajectory within the MEA. The numeration follows the hydrogen path, where the reference electrode 1 is closer to the anode inlet, 2 is half way along the anode path and 3 is at the anode exit.

3.3.2 Fuel cell testing

The cell was operated through a G050 unit from Green Light Power Technologies Inc. The current was maintained constant during the experiment at an average current density of 0.3 A cm^{-2}, which corresponds to a typical operation, and the temperature of the cell was 70 °C. A humidified stream of pure H_2 and humidified stream of air were introduced to the anode and the cathode respectively at a stoichiometry of 2 on both electrodes. A second G50 unit was used for the heating of the humidified CO/H_2 mixture, and the alternation with the pure H_2 stream was carried out through a three-way valve. The concentration of CO_2 in the exit gas was monitored over time using an infrared CO_2 detector (GMP343 from Vaisala), which was connected in the anode outlet. Previous to the detector, a filter using a PTFE membrane of 1.2 µm porosity was connected in the anode outlet, followed by two cooling traps to remove the water vapour from the stream.

The experiment consisted of three phases: (i) an initial period of 30 minutes where the cell was operated with high purity H_2 (>99.99%), (ii) the operation with a mixture of 100 ppm CO/H_2 for ~16 hours, and (iii) a one-hour recovery stage with pure H_2. 100 ppm CO/H_2 were chosen as CO concentration with the objective of observing self-sustained potential oscillations. Previous studies that considered Pt as catalyst reported this oscillatory behaviour with this fuel composition and similar operating conditions [59].

3.4 Segmented-in-series system

The segmented-in-series system allowed the use of different characterisation techniques that include thermal imaging, mass spectrometry and current interrupt. Combined with the information generated from the measurement of the individual cell voltages, it is possible to observe the effects of the poisoning beyond the coverage of the catalyst surface in the anode.

3.4.1 Configuration of the stack

A modified printed circuit board (PCB) stack from Bramble Energy was used. The stack was composed of five cells fueled and connected electrically in series, with a four-channel serpentine flowfield, and covered with a metal passivation technology that prevented chemical degradation. Each cell had a surface area of 14.77 cm^2. Considering the disposition of the cells in series, each cell can be considered a segment of a larger cell.

The MEAs were prepared with catalyst from Hyplat with a loading of 0.4 mg cm^{-2} of platinum in carbon support in the anode and the cathode, and a GORE Select membrane (20 µm thickness) as a cation exchange membrane. The stack was assembled using intermediate layers of A47 prepreg, and the ensemble was hot-pressed at 140 °C for one hour at 2 bar pressure. Stainless steel connections were subsequently added in the outlet of each one of the cells on the anodic side as sampling ports for mass spectrometry measurements, and the PCB surface on the anode side was painted in matt black to reduce the infrared reflections and ensure a uniform emissivity for thermal images. Figure 3.3 presents the assembled stack, the serial distribution of the cells and the location of the points where the transient temperature was measured through thermal imaging.

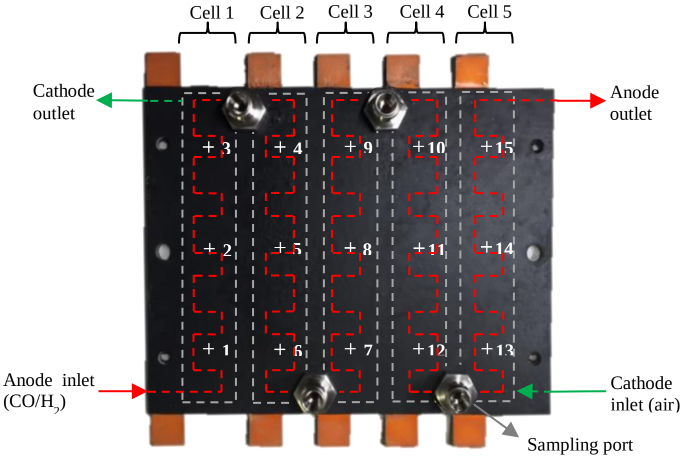

Figure 3.3 Assembled stack observed from the anode side, showing the serial flow of the fuel and the points where the transient temperature was measured.

3.4.2 Stack testing

The stack was operated through a Fuel Cell Test System 850e from Scribner Associates Incorporated. Zero grade H_2 was supplied to the cell through a flowmeter (Bronkhorst (UK) Ltd), while a humidified mixture of O_2/Ar was introduced in the cathode in counter-flow through the Fuel Cell Test System unit. It is important to mention the presence of a few ppm of CO in the H_2 zero grade stream. The H_2 was switched to a mixture of CO/H_2 and vice versa through a 4-way valve. The stoichiometries used were 2 in the anode and 3 in the cathode.

The experiments carried out were divided into three phases: (i) an initial period of 30 minutes where the cell was operated with H_2 zero grade; (ii) the operation with a mixture of CO/H_2 for three or four hours; and (iii) a one-hour recovery stage with H_2. Throughout the tests, the operation was maintained a constant current density of 0.3 A cm^{-2}. Two concentrations were evaluated: 100 ppm CO/H_2 for four hours and a mixture of 200 ppm CO/H_2 for three hours. In the case of 200 ppm CO/H_2 the experiment was repeated five times, where each time a different sampling port was used for the measurement of the concentration of gases in the outlet of cells.

A record was maintained of the voltage drop of the stack and the individual cells as well as the ohmic resistance by the Fuel Cell Test System unit which was captured through current interrupt (five times per second). During the measurement of the concentration of gases in the outlet of Cell 5, a thermal image was taken every 10 minutes during the exposition to CO and during the recovery with H_2 through a FLIR SC5000MB camera (FLIR Systems France).

For the mass spectrometry measurements, around 40 mL min^{-1} of the stream was deviated through the sampling port to a coalescing filter made of borosilicate glass fibre (0.3µm pore size) in order to remove the liquid water. A T-piece followed, connecting on one side the exhaust and on the other the quadrupole mass spectrometer (QGA, Hiden Analytical) through a quartz inert capillary (QIC). A flow of 16 mL min^{-1} entered the mass spectrometer that detected the concentration of H_2, H_2O, CO, O_2, Ar and CO_2 (predominant *m/z* equal to 2, 18, 28, 32, 40 and 44 correspondingly) on the stream. The O_2/Ar mixture was used in the cathode instead of air to avoid the presence of N_2, whose predominant *m/z* is 28 and overlaps with the CO peak. The total pressure in the mass spectrometer chamber was maintained at 2.0×10^{-6} Torr (around 2.0×10^{-6} mbar), and the ions were detected through two detectors: Faraday (H_2, H_2O and Ar) and Secondary Electron Multiplier (SEM) (CO, O_2 and CO_2).

Prior to the measurements, the mass spectrometer was calibrated following a sequence of steps. First, the background was determined passing He through the system until the measurements were stable. A mixture of CO_2/Ar was introduced to determine the contribution of CO_2 to the different *m/z* peaks, in particular of 44, where CO also presents a secondary peak. This step allowed the more accurate differentiation between CO and CO_2 in the spectrum. Two mixtures were then used for the final step of calibration: 100 ppm CO/200 ppm CO_2/1500 ppm Ar/H_2 and 200 ppm CO_2/40 ppm O_2/Ar, where a calibration factor was determined for each one of the species. During each one of these steps and during the experiments, the scroll pump was purged with a stream of around 500 mL min^{-1} of Ar to avoid the accumulation of H_2 in the system.

3.5 Localised reference electrodes and segmented-in-series system comparison

Despite the similarities in the experiments carried out in the single-cell and the segmented-in-series stack, these systems present some fundamental differences in their configuration and operation beyond their materials fabrication. The comparison between them is useful to understand the information provided by each one of them.

The array of reference electrodes and the segmented-in-series system monitor different parameters and consequently the electrochemical technique differs between them. In the first study, a localised reference electrode measures the electrode potential (anode potential in this case) directly in a specific point of the MEA. The area covered by this point is defined by the Nafion impregnation and the Nafion tubing presented in Figure 3.2 (b), which has an inner diameter of 0.64 mm and an outer diameter of 0.84 mm. Furthermore, the electrode potential was measured through the hydrogen reference electrode placed at the end of the Nafion tubing. In the case of the stack, the voltage of the five individual cells is measured, where each cell represents an area of 14.77 cm^2. The cell voltage is monitored through the Fuel Cell Test System that measures the electrical potential difference between these two electrodes.

Both systems also present a distinct configuration of the MEA, provoking different operating conditions and performance. An example is the humidification and protons conductivity of the membrane, which is continuous in the single-cell (reference electrodes setup), and interrupted in the stack due to the segmentation of the cells. The division of the cells in the stacks also affects the transport of gases through the GDL, as the only possible pathway for the gases to reach the following cell is through connections placed at the end of each cell, where the flow fields lead to. In the single-cell, the transport through the GDL is continuous throughout all the area and is added to the flow of gases passing through the channels.

Although each cell in the stack can be considered a segment of a larger cell, there is another consequence of the segmentation, as the cells are electrically isolated. These are connected in series; hence the current loaded to the stack is reflected in all the cells, where the same current is applied to each one of them. In the case of the voltage provided by the stack, this is calculated by adding the individual cell voltages. These dynamics occur independently of the galvanostatic or potentiostatic operation. Both, the segmented-in-series stack and the array of reference electrodes contribute to the study of the spatial distribution of the CO poisoning; however, no segmentation was carried in the preparation of the reference electrodes setup.

Finally, it is also worth mentioning the different operating conditions of both systems, in particular of the temperature. The operation of the single-cell was done at 70 °C, while the operation of the stack was at ambient temperature. The design of the stack setup did not consider the integration of any heating system, although it was possible to determine the heat waste energy more easily due to this configuration through thermal imaging. No spatial distribution of the temperature was monitored in the single cell.

3.6 Short-circuiting in a segmented-in-series stack

3.6.1 Configuration of the stacks

Two stacks similar to the presented in 3.3.1 were prepared. The difference with those segmented-in-series stacks relies in the absence of sampling ports, as in this study mass spectrometry was not used. Figure 3.4 presents one of the stacks observed from the anode side, where the location of the individual cells and the flow through them is marked. Considering the serial disposition of the cells, each cell could be considered a segment of a larger cell of 73.85 cm^2.

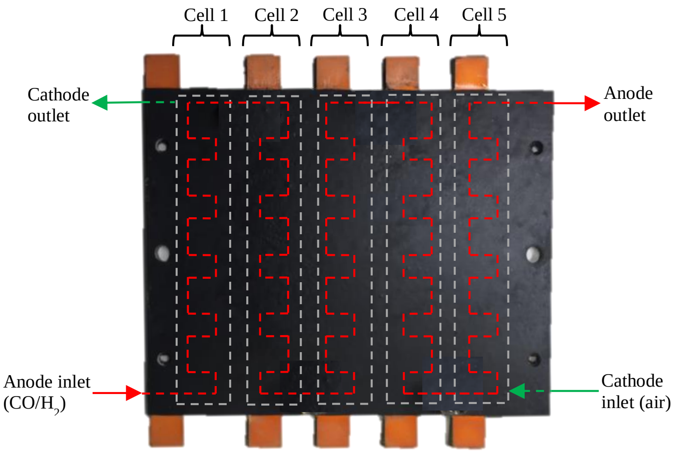

Figure 3.4 Stack observed from the anode side, showing the location of the individual cells and the serial flow of the fuel.

3.6.2 Application of short-circuiting

Figure 3.5 presents a diagram of the electrical arrangement for simultaneous operation of one cell and the application of the shorts. The load was applied to the cell through a Fuel Cell Test System 850e (Scribner Associates Incorporated). For the application of the shorting, a MOSFET and a DAQ board (NI Corp.) named 'controller' in the diagram were electrically coupled with the cell. The shorting time and the frequency of the shorts were controlled through LabVIEW. Three additional MOSFETs were connected in parallel to the first MOSFET in case of a peak of current. The recording of the voltage was equally done by the DAQ board and monitored via LabVIEW. The same system comes into play for the rest of the cells, where the same current traverses every cell due to the serial configuration of the stack.

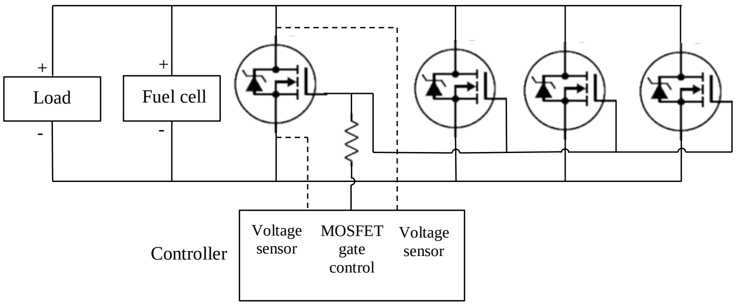

Figure 3.5 Electrical setup for the application of short-circuiting in a cell. The load was controlled by a Fuel Cell Test System 850e unit (Scribner Associates Incorporated), and a MOSFET and a DAQ board (NI Corp.) named 'controller' were electrically coupled with the cell for the application of the shorting. Additional MOSFETs were included in parallel to the cell and the first MOSFET in case of a peak of current.

3.6.3 Test of short-circuiting

Two experiments were carried out. For the first experiment, the first stack was maintained at a constant current density of 0.2 A cm^{-2}. For the operation, dry H_2 (stoichiometry of 2) was supplied to the anode through a flowmeter (Bronkhorst Ltd), while a mixture of humidified O_2/Ar (stoichiometry of 3) was introduced in the cathode through the Fuel Cell Test System 850e that also controlled the load. After 15 minutes of operation with pure H_2, all the cells started to be shorted simultaneously using a short length of 100 ms at a frequency of 0.1 Hz for 15 minutes. The shorting continued and the pure H_2 was switched to a dry mixture containing 200 ppm CO/H_2 by a 4-way valve for 3 hrs before reinserting pure H_2 for the recovery of the cell.

For the second experiment, the stack 2 was operated at a constant current of 0.3 A cm^{-2}, using dry H_2 at a stoichiometry 2 in the anode and humidified air stream at a stoichiometry of 3 in the cathode. The pure H_2 stream was maintained for 30 minutes before introducing a dry mixture of 100 ppm CO/H_2 in the anode. Different short-lengths were tested after one hour exposure, and various frequencies were evaluated after two hours of exposure. The patterns studied are described in Table 3.4. The shorting was removed after three hours of exposure to CO and pure H_2 was reintroduced for one hour.

Table 3.4 Short lengths and frequencies evaluated in the five different cells of a PEMFC stack exposed to 100 ppm CO/H_2.

Cell	**1**	**2**	**3**	**4**	**5**
Short length (ms)					
Frequency of 0.2 Hz	200, 300, 500	200, 500, 1000	200, 500, 1000	200, 300, 500	-
Frequency (Hz)					
Short length of 100 ms	1, 2, 3	1, 2, 3	-	-	0.1, 1
Short length of 200 ms	-	-	1, 2.5, 2	-	-

3.7 Methodology

Different techniques were used apart from the measurement of the anodic overpotential through localised reference electrodes and of the individual cell voltages in the stack. These techniques are described next for further understanding of the information generated.

3.7.1 Polarization curve

The polarization curve is the standard electrochemical technique to evaluate the performance of fuel cells under operating conditions. It shows the variations of the voltage with current or current density. The curve and the major losses that confer its characteristic shape were presented in Section 1.4. The disadvantages of this technique are that it is not possible to obtain information of the performance of individual components within the cell; different mechanisms cannot be differentiated from each other; it is not possible to obtain during the operation of the cell, and it takes time to measure it [23].

3.7.2 Cyclic voltammetry

The cyclic voltammetry (CV) is a dynamic technique that provides information about the catalyst activity, such as relative reaction and diffusion rates [256]. It is also useful to detect reaction intermediates, and for obtaining stability in reaction products [23]. The potential is swept linearly back and forth across a voltage range of interest (Figure 3.6 (a)), while the current is measured as a function of time [5]. The cyclic voltammogram plots the current versus the voltage as shown in Figure 3.6 (b)). The current peaks are related to an active electrochemical reaction. The reverse electrochemical reaction is shown on the reverse voltage scan [256].

Cyclic voltammetry can be performed ex situ and in situ. While ex situ measurements provide information about relative activities of a series of electrocatalysts toward a reaction or the activity of one electrocatalyst toward several reactions, they are not suitable for an operating cell. In situ voltammetry, on the other hand, is commonly used to determine the ECSA and the catalyst utilization of PEM fuel cells [23]. In this study, two methods were used to determine the ECSA through in situ cyclic voltammetry: the hydrogen-adsorption and CO Stripping. The ECSA is useful to evaluate the catalyst layers, as not all the catalyst is in contact with the membrane and participate in the electrochemical reaction, some particles are isolated. The changes of ECSA through time are also used to evaluate the durability of the cell [23].

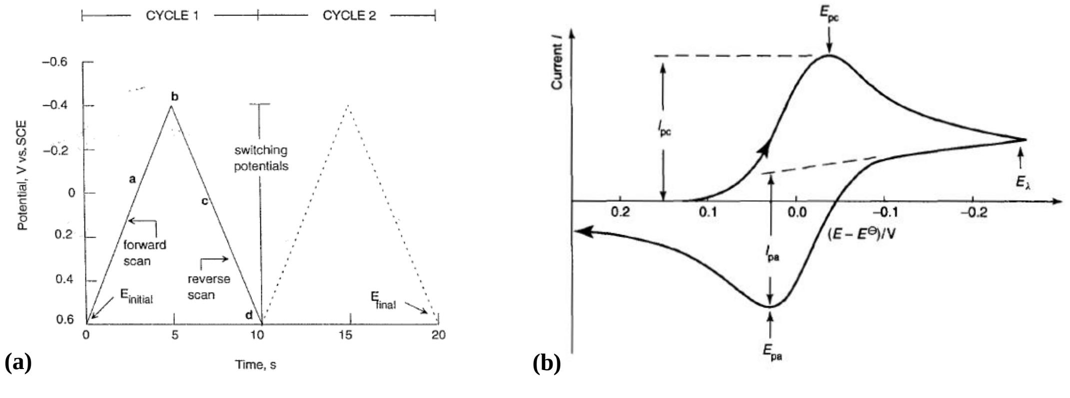

Figure 3.6 Cyclic voltammetry depiction: (a) Potential applied as a function of time [257], (b) Cyclic voltammogram for the reduction reaction of a solid electrode [258].

3.7.2.1 Hydrogen Adsorption/Desorption

A two-electrode configuration is used. The working electrode (WE) is the electrode of interest, and is flushed with an inert gas (N_2 or Ar). The other electrode is fed with H_2, and represents the counter electrode (CE) and reference electrode (RE). It is a dynamic hydrogen electrode (DHE). The reaction that takes place in this process is [259]:

$$\mathbf{Pt - H_{ads}} \underset{\text{Reverse}}{\overset{\text{Forward}}{\longleftrightarrow}} \mathbf{Pt + H^{+} + e^{-}} \tag{3.1}$$

The impedance losses in the porous electrodes are avoided by using a lower sweep rate [256]. Figure 3.7 shows the cyclic voltammogram after the hydrogen adsorption/desorption process. The ECSA is calculated with the H_2 adsorption charge on the electrode, the surface area and the H_2 adsorption charge on a smooth Pt electrode, which value is estimated in 210 µC cm^{-2} [256]:

$$\mathbf{ECSA}\left(\frac{\mathbf{cm^2\,Pt}}{\mathbf{g\,Pt}}\right) = \frac{\mathbf{charge}\left(\frac{\mathbf{\mu C}}{\mathbf{cm^2}}\right)}{\mathbf{210}\left(\frac{\mathbf{\mu C}}{\mathbf{cm^2}}\right)\times\mathbf{catalyst\ loading}\left(\frac{\mathbf{g\,Pt}}{\mathbf{cm^2}}\right)} \tag{3.2}$$

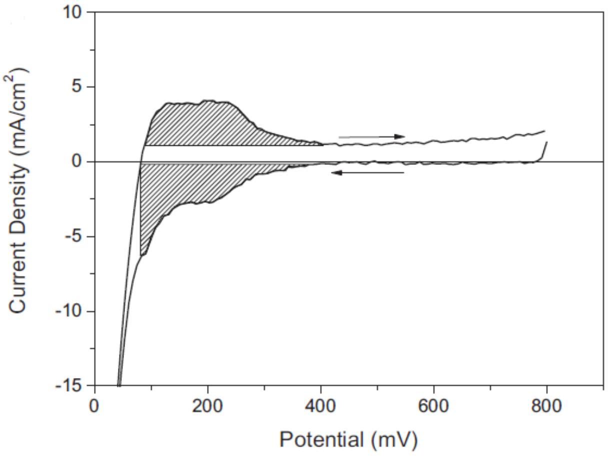

Figure 3.7 Hydrogen adsorption/desorption method showing the charge exchanged during the process [260].

3.7.2.2 CO Stripping voltammetry

The ability of CO to strongly adsorb on Pt is used to determine the ECSA. This is through the oxidation of adsorbed CO at room temperature under the same principle than H_2

adsorption/desorption. One side of the cell is fuelled with CO plus inert gas (Ar or N_2), while the other is fed with H_2 and works as the DHE. The electrode potential is kept at about 0.1 V. The supply of CO is then changed to high purity of Ar to remove the non-adsorbed molecules of CO before the scan. Subsequent cycles help to verify that the process is completed [261]. The oxidative stripping of adsorbed CO reaction is as follows [259]:

$$\mathbf{Pt - CO_{ads} + H_2O \rightarrow Pt + CO_2 + 2H^+ + 2e^-} \tag{3.3}$$

Figure 3.8 presents an example of a cyclic voltammogram obtained through this method for Pt/C. The filled area emphasises the charge related to the CO oxidation reaction. The ECSA can be calculated using Equation (3.2) using the value 424 µC cm^{-2} which corresponds to polycrystalline Pt [256]. One limitation of CO stripping voltammetry is the uncertainty of the types of CO bonding in the surface of the catalyst [23].

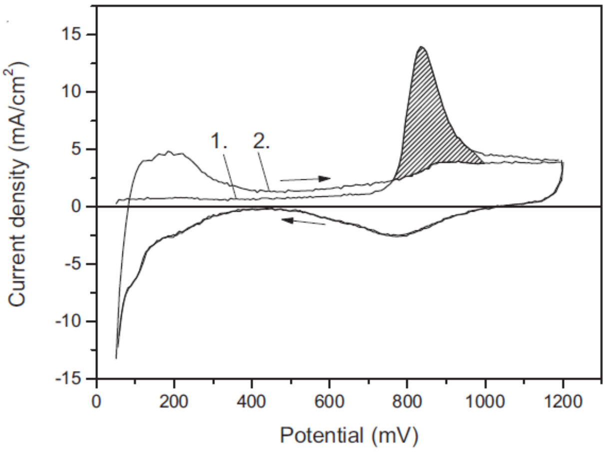

Figure 3.8 CO Stripping voltammetry on a Pt/C electrode. Cycle 1: CO stripping process. Cycle 2: baseline [260].

3.7.3 Electrochemical Impedance Spectroscopy (EIS)

EIS is one of the most widely used characterization technique for distinguishing the major losses in a fuel cell [5]. Different processes can be distinguished through this technique, especially multi-step or parallel reactions or additional processes [262]. The impedance *Z* measures the ability of a system to impede the flow of an electrical current, and is given by the ratio between a time-dependent voltage and a time-dependent current:

$$\boldsymbol{Z = \frac{V(t)}{i(t)}} \tag{3.4}$$

The technique consists on applying a sinusoidal AC current (or potential) perturbation and measuring the amplitude and phase shift of the potential (or current) response. In situ analysis can be performed for single cells or stacks, while ex situ analysis can be performed for material or component characterization [262]. When a voltage perturbation is applied to the system, the input and response signals are given by the expressions:

$$\boldsymbol{V(t) = V_0 \cos(\omega t)} \tag{3.5}$$

$$\boldsymbol{i(t) = i_0 \cos(\omega t - \phi)} \tag{3.6}$$

Where V_0 and i_0 are the amplitudes of the voltage and current signals respectively, *V(t)* and *i(t)* are the potential and current at time *t*; ω is the radial frequency, and φ is the phase shift. The relationship between the radial frequency ω (radians per second) and frequency *f* (Hertz) is given by:

$$\boldsymbol{\omega = 2\pi f} \tag{3.7}$$

According to Equation (3.4), the sinusoidal impedance response of a system can be written as:

$$\boldsymbol{Z = \frac{V_0 \cos(\omega t)}{i_0 \cos(\omega t - \phi)} = Z_0 \frac{\cos(\omega t)}{\cos(\omega t - \phi)}} \tag{3.8}$$

The impedance response of a system can alternatively be expressed using complex notation, in terms of a real and an imaginary component:

$$\boldsymbol{Z} = \frac{\boldsymbol{V_0 e^{j\omega t}}}{\boldsymbol{i_0 e^{(j\omega t - j\phi)}}} = \boldsymbol{Z_0 e^{j\phi}} = \boldsymbol{Z_0}(\mathbf{cos}\,\boldsymbol{\phi} + \boldsymbol{j}\,\mathbf{sin}\,\boldsymbol{\phi}) \tag{3.9}$$

where j is the imaginary unit. The impedance of a system can be expressed in a Bode plot in terms of an impedance magnitude Z_0 and a phase shift $\boldsymbol{\varphi}$, or in an Nyquist plot in terms of a real component ($Z_{real} = Z_0 \cos\phi$) and an imaginary component ($Z_{imag} = Z_0 \sin\phi j$) [5].

Different information can be obtained by fitting the spectra to equivalent circuits [262]. Figure 3.9 presents the standard representation of the processes involved in a single cell, and how a Nyquist plot can be interpreted through the equivalent circuits. The ohmic losses are represented by the ohmic resistance R_Ω, the anodic and cathodic activation losses are simulated by two parallel RC elements. A Warburg element was also considered for the cathode mass transfer effects [5].

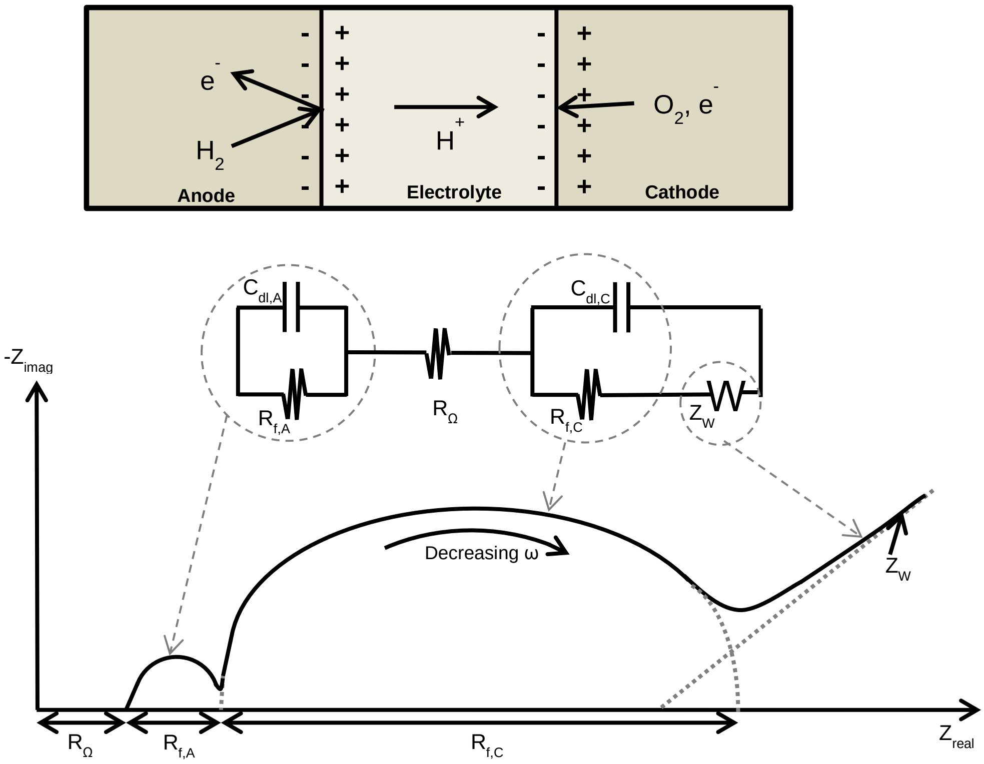

Figure 3.9 Interpretation of the EIS, considering the electrochemical, the equivalent circuit and the Nyquist plot for a single cell [5].

For the study of CO poisoning, the EIS experiments are usually done in situ and offer the possibility of studying the oxidation processes on the anodic catalyst [110]. In Section 2.2.6.3 the characterization of CO poisoning in PEMFC is revised, particularly the spatial distribution of the CO coverage through segmented EIS [94]. The most recent representation of the EIS spectra through electrical equivalent circuits of a cell under different operating conditions with and without CO was proposed by Reshetenko *et al.*, shown in Figure 3.10.

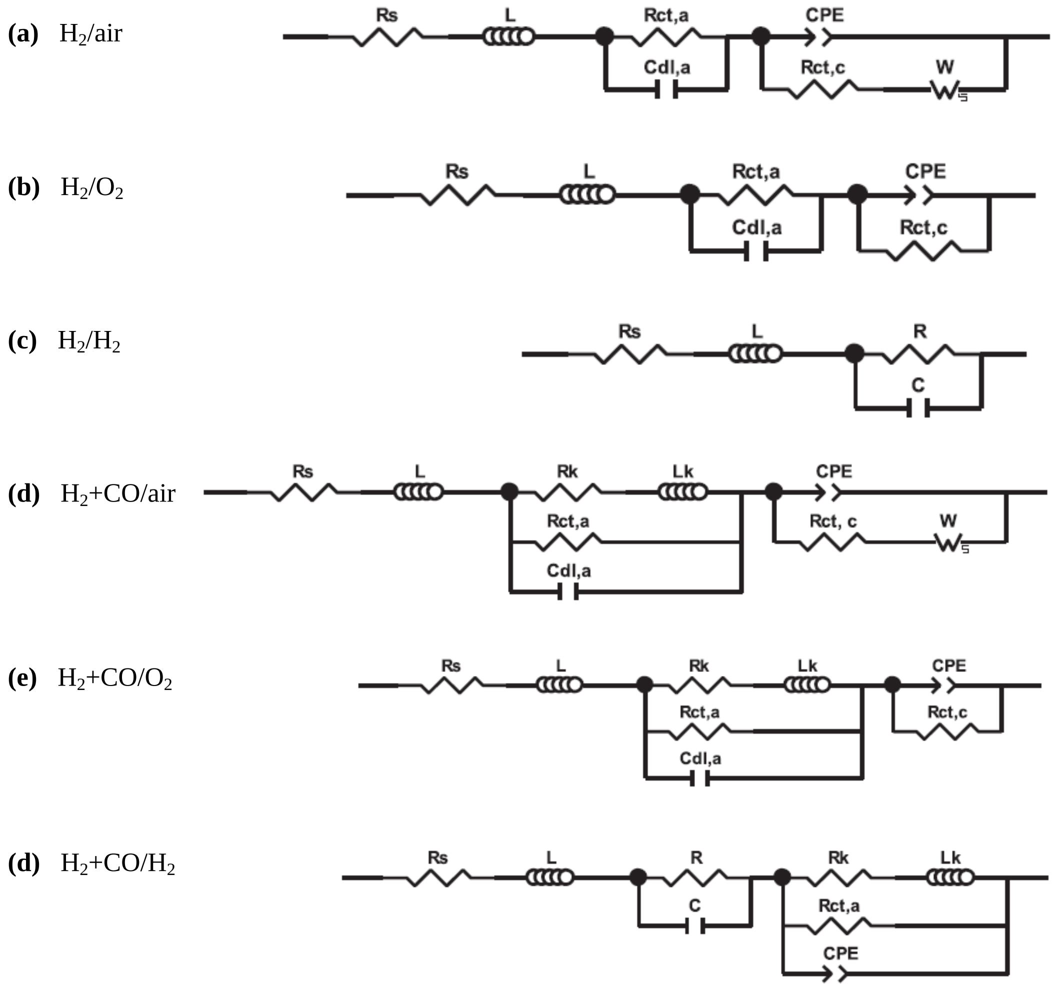

Figure 3.10 Representation of EIS spectra through electrical equivalent circuits of a PEMFC operating under different conditions: (a) H_2/air, (b) H_2/O_2, (c) H_2/H_2, (d) H_2+CO/air, (e) H_2+CO/O_2 and (d) H_2+CO/H_2. R_S: serial resistance, L: high-frequency cable inductance, $R_{ct,a}$: charge-transfer resistance of HOR in the anode, $C_{dl,a}$: capacitance in the anode, $R_{ct,c}$: charge transfer of the ORR in the cathode, CPE: constant phase element and W: finite length Warburg diffusion element. The inductance L_K represents the voltage perturbation with a phase delay due to the slowness of the CO adsorbed coverage relaxation and R_K modifies the phase-delay [94].

3.7.4 Nondispersive infrared (NDIR) gas sensors

Infrared spectroscopy is based on the vibrations of the atoms of a molecule. An infrared spectrum is obtained by passing infrared radiation through a sample and quantifying what fraction of the incident radiation is absorbed at a particular energy [263]. The non-dispersive infrared (NDIR) gas measurement is an application of the infrared spectroscopy that focuses on the wavelength absorption for the identification of gases [264]. Different gases can be identified through this technique. It is the most common technique used to detect CO_2, for example [265]. The main components of a NDIR gas sensor are the light source, the measurement chamber or gas chamber and the IR detector as shown in Figure 3.11.

The operation of NDIR gas sensors is based on the Beer-Lambert Law:

$$\boldsymbol{I = I_0 e^{-kCL}} \tag{3.10}$$

where I_0 refers to the initial radiation beam intensity, I is the beam intensity after passing the gas through the detector, k is the absorption coefficient, C is the gas concentration and L is the sample optical path length, defined by the effective sample chamber length of the sensor [264]

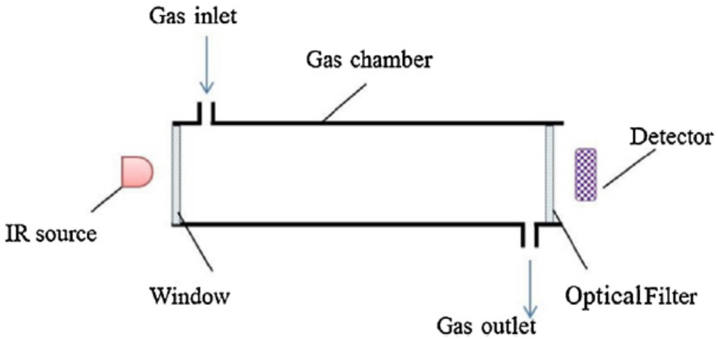

Figure 3.11 Structure of a typical NDIR gas sensor [264].

The advantages of the NDIR gas sensors compared to other techniques is the low energy consumption and the operation of sources with 1-15 µm wavelength can take place at lower temperatures. However, this technique presents two major disadvantages: interference and detection limit [264].

3.7.5 Thermal imaging

Infrared (IR) thermal imaging is a non-contact method that allows temperature measurements on operational fuel cells without disturbing the behaviour of the fuel cell. It provides high spatial resolution (<1 mm) useful for model input and fast acquisition time that allows the study of dynamic phenomena [266]. The basic principles of thermography are presented next, although the reader is referred to further literature for a deeper understanding.

Every object with a temperature higher than 0 K (-273.15 °C) emits infrared radiation, which is related to the temperature of its surface. Max Planck derived the law of radiation that describes the spectral distribution of the radiation from a blackbody [267]:

$$\boldsymbol{E_b = \frac{2\pi hc^2}{\lambda^5\left(e^{\frac{hc}{\lambda k_b T}}-1\right)}} \tag{3.11}$$

where E_b is the spectral radiance of the blackbody, h = 6.6×10^{-34} J s is Planck's constant, c = 2.998×10^{8} m s^{-1} is the speed of light in a vacuum, k_b = 1.38×10^{-23} J K^{-1} is the Boltzmann's constant, λ is the wavelength of the radiation and T is the absolute temperature of the blackbody given in Kelvin.

As shown in Figure 3.12, a trend is observed when the spectral radiance is plotted for numerous absolute temperatures, as the temperature is increased, the wavelength at which the maximum occurs decreases. The Wien's displacement law describes this shift and states the maximum radiation intensity:

$$\boldsymbol{\lambda_{max} = \frac{d_w}{T}} \tag{3.12}$$

where d_w = 2897.8 µm K is denominated as Wien's displacement constant.

By integrating Planck's law over the entire spectrum (from zero to infinity) gives the excitance (emissive power) or the blackbody, which depends entirely on its temperature [267, 268]:

$$\boldsymbol{E_b = \sigma T^4} \tag{3.13}$$

where $\sigma = 5.67\times10^{-8}$ W m^{-2} K^{-4} refers to the Stefan-Boltzmann constant.

The above laws refer to black bodies, which are only an idealized model of real bodies. In reality, these bodies are not perfect absorbers of incident radiation and are called gray bodies. Therefore, the concept of emissivity is introduced, which recognises the error and uncertainty in infrared thermographic measurements. The emissivity ε of a body is the ratio of full-range radiant exitance E_λ of that body to full-range radiant exitance $E_{\lambda b}$ of a black body at the same temperature [269]:

$$\boldsymbol{\varepsilon_\lambda = \frac{E_\lambda}{E_{\lambda b}}} \tag{3.14}$$

Equations (3.6) and (3.8) can be rewritten for real bodied by multiplying their second term by the spectral emissivity coefficient ε_λ [267].

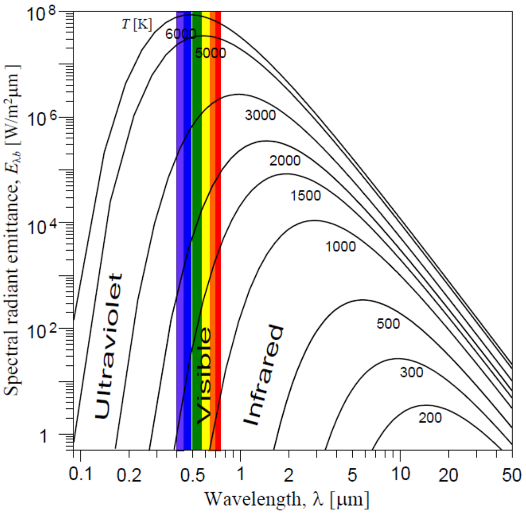

Figure 3.12 Representation of Planck's law for the radiation of a blackbody at several absolute temperatures [267].

3.7.6 Current interrupt

The current interrupt or current interruption is generally used to measure ohmic losses due to transport resistance of protons and anions in batteries, fuel cells, and other electrochemical devices [270]. The principle relies on the rapid fading of the ohmic losses compared to the electrochemical overpotentials when the current is interrupted [271]. Figure 3.13 (a) presents the evolution of the voltage during the operation under galvanostatic control, followed by the interruption of the current I, and Figure 3.13 (b) presents the equivalent circuit of a fuel cell for the measurement of the current interrupt, which consists of two resistors and a capacitor. The R_{cell} represents cell resistance, including the electronic resistance and ionic resistance. R_{t} is in a loop with a capacitor of the MEA, and represents the charge transfer resistance related to the activation losses. When the current is interrupted, no current flows through the first resistor provoking an instantaneous increase of the voltage is observed at first. The voltage increases very slowly afterwards due to the discharge of the capacitor. Once the capacitor is completely discharged, the system reaches the open-circuit voltage (OCV) [256, 270, 272].

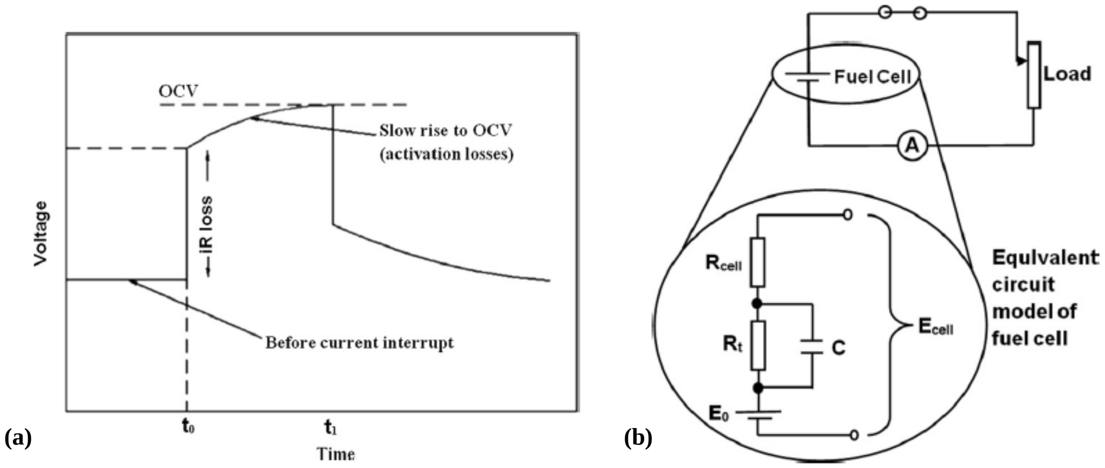

Figure 3.13 Current interrupt measurement (a) Cell voltage evolution during the interruption of the current [273], (b) equivalent circuit model representing a fuel cell [272].

When the current is set to zero, the voltage drop ΔV induced by the resistance disappears immediatly and can be expressed by Equation 3.15, from which the resistance can be obtained [270]:

$$\boldsymbol{\Delta V = iR} \tag{3.15}$$

3.7.7 Mass spectrometry

Mass spectrometry measures the molecular masses of individual compounds and atoms and their relative abundance. Figure 3.14 presents the three basic steps involved in the analysis. The ionization converts the molecular and atomic species into gas-phase ions and is followed by the fragmentation, which consists on the separation and analysis of the species in terms of the mass-to-charge ratios (m / z) by electromagnetism. These two steps are effectuated under high vacuum to allow the movement of ions without collisions or interaction between the species. In the final step, the current generated by the ions is measured, amplified and displayed in a mass spectrum [274, 275].

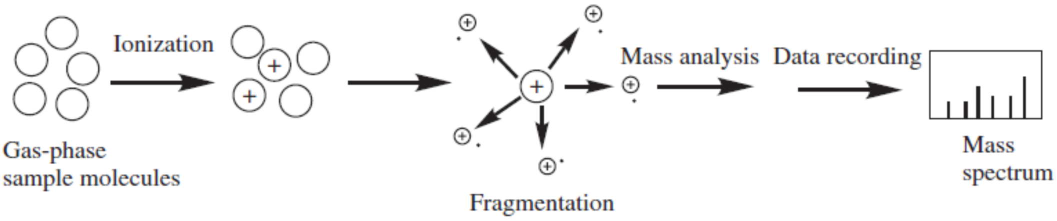

Figure 3.14 Basic steps involved in mass spectrometry analysis [274].

3.8 Conclusions

A description of the systems studied in this work was presented. The single-cell experiments aim to evaluate the short-term effects of CO under different operating conditions. The information obtained from these experiments will contribute to a better understanding of the spatial variation and temporal dynamics occurring during the poisoning, which will be evaluated in the following chapters.

The placement of localised reference electrodes will allow the direct measurement of the anodic overpotential in three different locations of the MEA in the presence of CO and under galvanostatic control, where self-sustained potential oscillations are commonly observed. These have been associated to the adsorption and oxidation of CO, however their variations in space have not been reported. It is expected that local operating conditions such as temperature and humidity, have a direct impact in the poisoning and in the dynamics of the oscillations.

The study of the segmented-in-series system will evaluate the effects of CO beyond the anode surface through the combination of different techniques that include the measurement of individual cell voltages, thermal imaging, current interrupt and mass spectrometry. The size of the stack is more representative of real operating conditions and although it is representative of a segmented-cell, it will allow the observation of the poisoning in a electrode surface where there is no electrical connection as in the localised reference electrodes system.

Finally, the integration of the short-circuiting into the segmented-in-series system will be evaluated as a possible mitigation strategy against the pernicious effects of CO poisoning. It is expected that the information from previous chapters about the spatial variations of the CO coverage will contribute to the optimization of the system.

Chapter 4

Single-Cell CO Poisoning Characterisation

4.1 Introduction

CO poisoning in PEMFCs is a complex process. Before introducing the results from elaborated systems, such as the localised reference electrodes setup and the segmented-in-series system, it is essential to examine and understand the effects of CO in a single cell through the most standardised characterisation techniques. This is the aim of the chapter. A single cell was used to evaluate the catalyst activity in the anode, and the short-term effects of CO under different operating conditions. Although some of the conclusions have already been reported in the literature, the comprehension of these results represents the base for a deeper understanding of the information generated in the following chapters.

4.2 Evaluation of the ECSA

The ECSA is a critical performance metric for the catalyst and the MEA, as it determines the catalyst area that is available for the reactions to take place [259]. Two in situ methods were used to obtain it: adsorption/desorption of hydrogen, and CO stripping voltammetry. Figure 4.1 (a) presents the cyclic voltammograms obtained for the CO stripping of the adsorbed CO on Pt/C. Three curves are presented: the curve obtained with H_2 (no CO), and the first and second scan after the exposure to CO. Gamry Echem Analyst was used to find the peak voltage on the first cycle, which was 0.78 V. This is the value at which the CO adsorbed in the surface is oxidised more intensively under these operating conditions. The charge related to the oxidation of CO was obtained by integrating the area. The standard norm is to integrate the area between the curves from the first cycle and the second cycle; however, it is seen that the second cycle presents an oxidation peak that partially overlaps with the CO oxidation from the first cycle. This is an indication that the CO was not completely removed from the surface. Hence, the curve obtained with H_2 will give a more accurate approximation of the ECSA through this method. In Figure 4.1 (b), the charges associated with the H_2 adsorption and desorption are indicated. The curve where no CO was used was taken as a baseline.

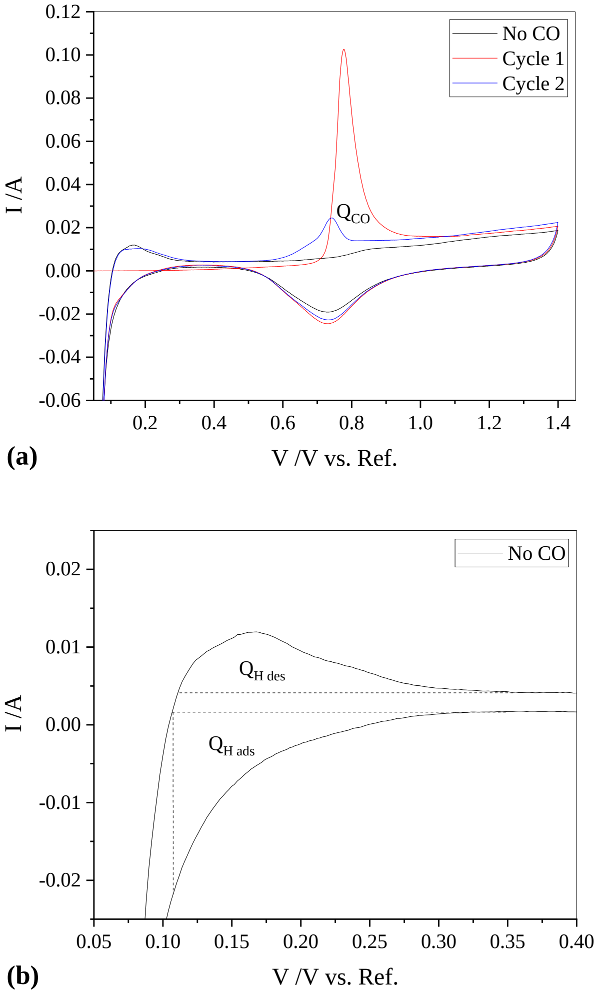

Figure 4.1 Cyclic voltammogram for the determination of the ECSA in Pt/C (Johnson Matthey) at ambient temperature showing (a) the charge associated to the CO oxidation, (b) the charges associated to H_2 adsorption and desorption.

The average from the ECSA obtained through H_2 adsorption and desorption (HAD) was used to avoid the tilting effects from the ohmic shorting and carbon support [276]. Table 4.1 presents the ECSA obtained through both methods. It is noticed that the ECSA obtained through CO stripping is 2.5 higher than the HAD. It is commonly observed that the ECSA obtained through CO stripping is higher when compared to the HAD method. CO stripping has been recognised as a more accurate measurement of the ECSA, as the HAD technique entails limitations that include the underestimation of small Pt nanoparticles (1.5-2 nm) by up to a factor of two, and in some surfaces the full monolayer is completed only at negative potentials where the hydrogen evolution potential takes place [276, 277]. To these limitations, the uncertainty in the extrapolation of the baseline could be added [260], particularly in the case of the CO stripping where the second cycle curve was not used.

Table 4.1 ECSA of a Pt/C electrode (Johnson Matthey), obtained through CO stripping and hydrogen adsorption-desorption (HAD).

ECSA ($m^2\ g^{-1}$)		**$ECSA_{CO}/ECSA_{HAD}$**
HAD	**CO stripping**	
26.0	66.1	2.5

4.3 Effect of CO in the performance of the cell

The short-term effects of CO in the performance of the cell are presented next, starting with the variation of the current density and the voltage over time. Then, the effects of the concentration, the temperature, the time of exposure and the flow at the anode are shown. These parameters have proven to vary throughout the cell and to have a direct impact in the performance during the operation with pure H_2 and in the presence of CO. The prediction of the performance of the cell under different conditions allows the optimization of the system, hence its importance.

4.3.1 Variation of the current density and the voltage over time

Current and voltage are interdependent in the functioning of fuel cells. When the voltage is controlled, the electrochemistry of the system determines the current, and concurrently, when the current is set, the electrochemistry of the system defines the voltage. As both operations are common in fuel cells, it is important to understand the effects of CO under the two regimes. Hence, one of the first steps was the observation of the evolution of the performance in the presence of CO over time.

The effects of CO are observed under potentiostatic control (0.7 V) when a CO in H_2 at the level of 20 ppm is introduced into the cell, as shown in Figure 4.2 (a). It is observed a diminishment of the current density from 366 mA cm^{-2} to 241 mA cm^{-2} after three hours of exposure. In Figure 4.2 (b) the evolution of the cell voltage over time is observed when 100 ppm CO/H_2 are injected under galvanostatic control (250 mA cm^{-2}). A voltage drop from 0.754 to 0.315 occurs in 40 minutes of exposure to CO. The decrease in the performance observed in both operation modes is confirmed and is related to the adsorption of CO in the catalyst surface that hinders the occurrence of the HOR. Although the adverse effects of CO are shown, limited information is obtained from these tests. More sophisticated tools are needed in order to elucidate the mechanisms involved during the contamination, and differentiate the effects under the distinct operation modes.

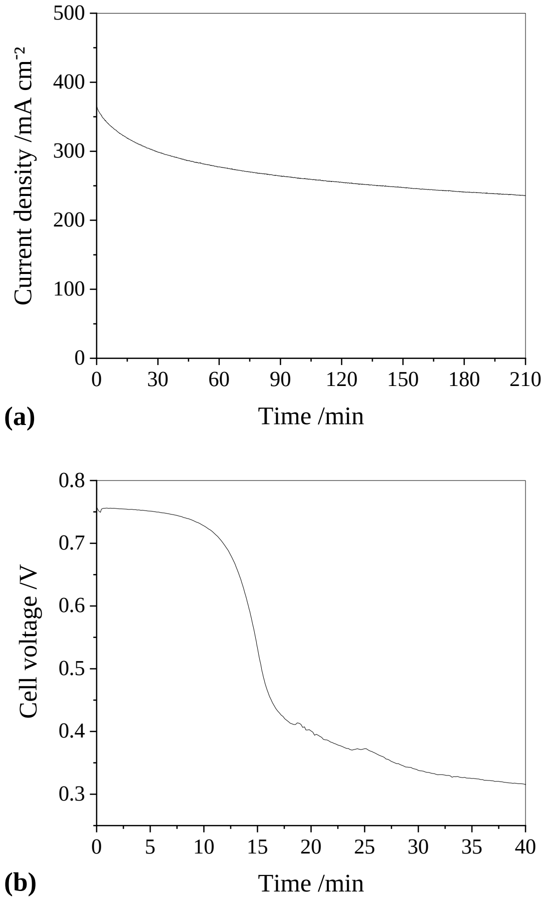

Figure 4.2 (a) Variation of the current density over time over the exposure to 20 ppm CO under potentiostatic control (0.7 V), (b) variation of the voltage over the exposure to 100 ppm CO under galvanostatic control (250 mA cm^{-2}). The 5.29 cm^2 PEMFC uses Pt/C as catalyst in both electrodes and is operated at 70 °C with O_2 in the cathode.

4.3.2 Effect of the concentration

The first parameter that was evaluated was the concentration of CO in the anode inlet of the cell. The range studied was between 20 and 100 ppm CO/H_2. In Figure 4.3, it can be observed that the performance of the cell is significantly diminished at the ppm-level. For instance, at 350 mA cm^{-2}, a concentration of 20 ppm CO/H_2 provoked a decrease of the cell voltage from 0.71 to 0.41 V, which represents a decrease in the performance of approximately 43%.

For all the concentrations of CO, the OCV was approximately 0.97 V, and the degradation occurred in two steps. At low current densities the decrease of the voltage is much higher than at higher current densities, where the voltage was low and almost stable. This is comparable with the results found in the literature [66]. From the CO stripping experiment, it was determined that at 0.7 V the oxidation of CO to CO_2 occurred. This can explain the decrease in the performance at higher current densities, where the voltage is below this value. The CO covers the surface, hindering the oxidation of H_2. The increase of the coverage increases with the concentration of CO. The curves of 20, 40 and 60 ppm CO might present a partial coverage of the surface.

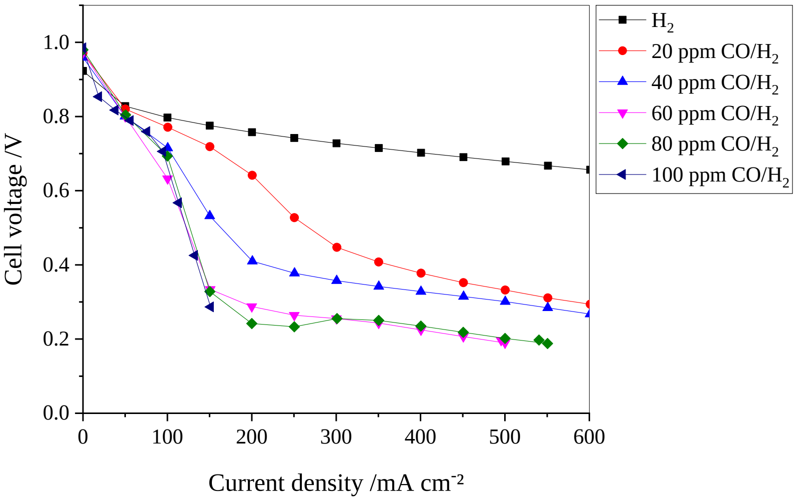

Figure 4.3 Polarization curves showing the effect of different concentrations of CO in the anode inlet of a 5.29 cm^2 PEMFC using Pt/C as catalyst in both electrodes at 70 °C, and using O_2 in the cathode. *Note:* in the case of 100 ppm CO/H_2, it was not possible to hold a current density higher than 150 mA cm^{-2}.

The effect of the concentration was also evaluated through potentiostatic EIS at 0.7 V (Figure 4.4). The ohmic resistance is approximately 0.1 Ω cm^{-2} for all the cases except for 100 ppm CO, where is slightly higher. It is important to mention the change of MEA for each experiment that could explain this variation. As for the effects of the concentration, the increase of CO is translated in higher activation losses in the EIS spectra due to a higher coverage of CO in the catalyst surface. This is also reported in the literature [97]. For a better understanding of the processes involved, it is advisable to compare the curves through electric circuit modelling. The different losses could be quantified and compared more accurately.

The measurement of the potentiostatic EIS is difficult due to the changes in the anode and cathode impedances over time [97]. However, additional information can be obtained through potentiostatic EIS. Leng *et al.* evaluated different catalyst at different temperatures over a wider range of potentials (0.30 to 0.7 V) to obtain more accurately the critical or ignition potential for the oxidation of CO to CO_2. This value was determined by the appearance of the pseudo-inductive behaviour [110].

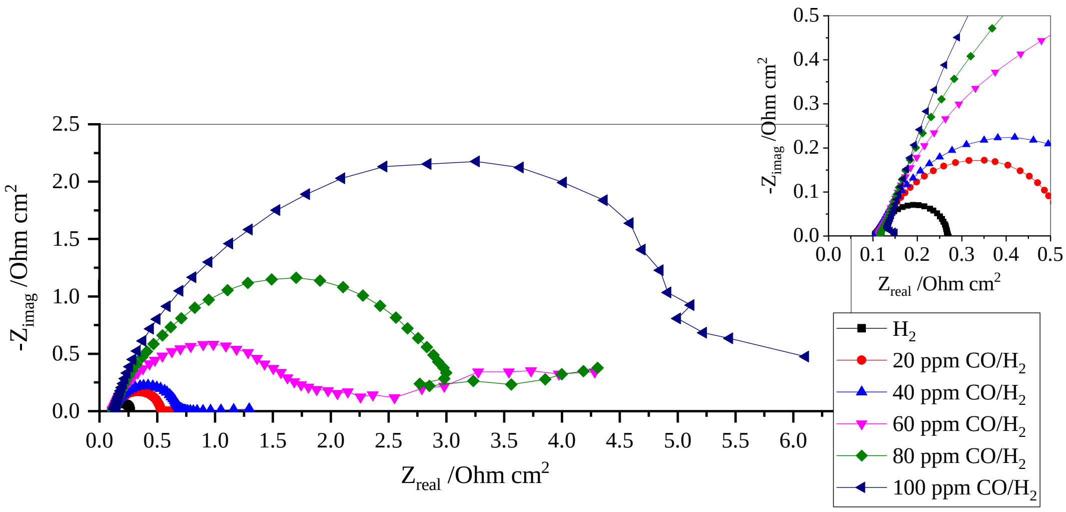

Figure 4.4 Potentiostatic EIS (0.7 V) showing the effects of different concentrations of CO after 210 minutes of exposure in the anode inlet of a 5.29 cm^2 PEMFC using Pt/C as catalyst in both electrodes at 70 °C, and using O_2 in the cathode. Frequency range: 0.1-20,000 Hz.

Finally, it is also important to mention the changes that the system suffers due to the poisoning of the catalyst, and how this has an influence on the EIS measurement. Not just between the measurements, but also during their recording. This is the case for both galvanostatic and potentiostatic EIS. Three main mathematical methods have been proposed to explain this effect: real-time drift compensation, the time course interpolation and Z-HIT refinement [108].

4.3.3 Effect of the temperature

The temperature also affects the performance of the cell. The range that was evaluated was between 40 and 80 °C. Figure 4.5 presents the polarization curves obtained. It is observed that at higher current densities (>100 mA cm^{-2}), as the temperature decreases the voltage losses increase. This is related to three phenomena that are favoured at higher temperatures: the thermal desorption of CO, the reduction of the CO oxidation potential, and the O_2 crossover through the membrane. All of them are responsible for the enhanced tolerance of the cell [212].

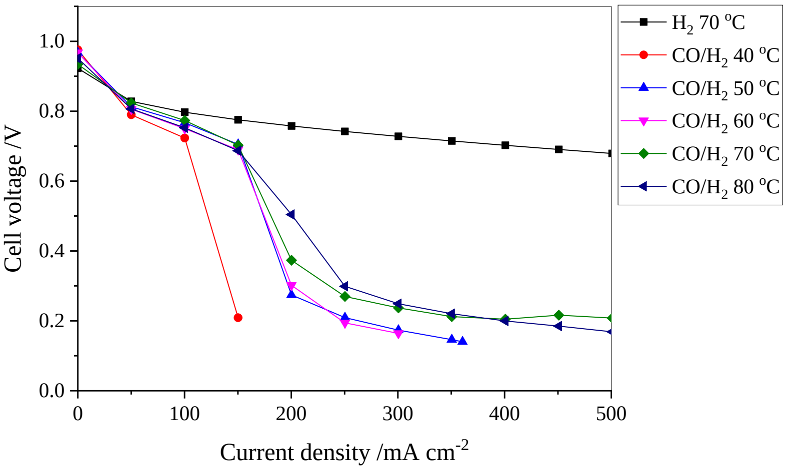

Figure 4.5 Polarization curves showing the effect of the exposure to the anode to 100 ppm CO at different temperatures. The 5.29 cm^2 PEMFC uses Pt/C as catalyst in both electrodes and is operated at 70 °C with O_2 in the cathode. *Note:* at 40 °C it was not possible to hold a current density higher than 150 mA cm^{-2}.

Hybrid EIS experiments were also used for the study of the CO tolerance, at 250 mA cm^{-2}. The hybrid EIS is a variation of the galvanostatic EIS, present in the Interface 5000E station. The AC current applied is constantly adjusted to optimize the measured potential. It avoids surpassing the limits of the potential that could damage the MEA [278]. An estimation of the AC voltage and the expected impedance are proposed before the measurement. The galvanostatic EIS is more accurate than the hybrid one, but the hybrid mode is still useful for this study.

Observing the curves obtained in Figure 4.6, it is possible to see how the ohmic resistance is lower for the 70 and 80 °C cases, with and without CO, confirming the rise on the O_2 crossover previously mentioned. Also, an increase in the real and imaginary part is noticed as the temperature diminishes. As under this mode the cathodic and membrane resistance are considered constant, the contribution of the anodic activation losses is responsible for it. At 50 °C the losses are the highest, showing the poorest tolerance to CO.

Finally, a pseudo-inductive behaviour is present at low frequencies, as the temperature diminishes. This behaviour is observed at 70, 60 and 50 °C, and it is related to a competition between the oxidation of H_2 and CO in the anode. This competition is known as relaxation. The pseudo-inductive behaviour was not observed in the potentiostatic mode for the study of different concentrations of CO, which is comparable with results in the literature at 0.7 V [97]. However, it is expected to be seen at the ignition potential [110].

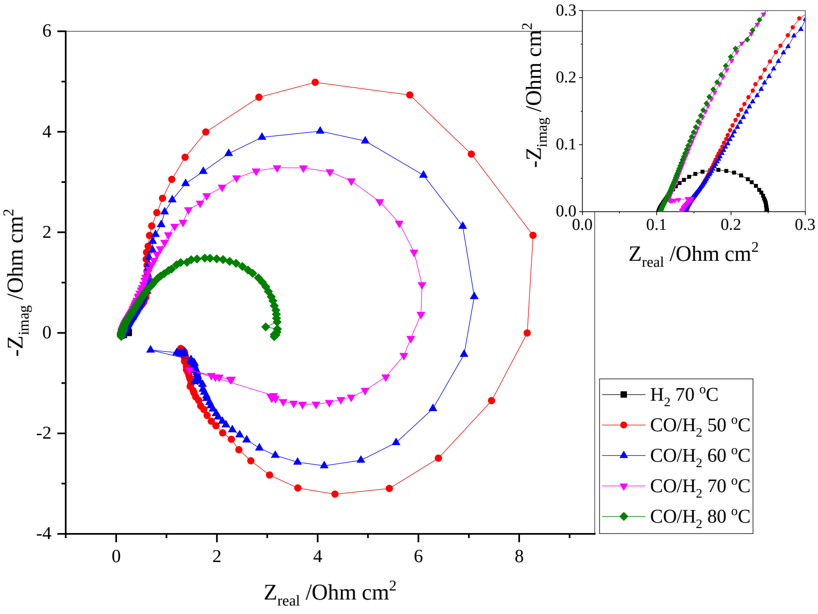

Figure 4.6 Hydrid EIS (250 mA cm^{-2}) showing the effect of 210 minutes of exposure to 100 ppm of CO in the anode inlet at different temperatures. The 5.29 cm^2 PEMFC uses Pt/C as catalyst in both electrodes and is operated at 70 °C with O_2 in the cathode. Initial frequency: 100,000 Hz, final frequency: 0.1 Hz.

In this study, it was also possible to observe potential oscillations after the exposure of CO at the steady behaviour for 70 and 80 °C (Figure 4.7). No oscillations were observed at lower temperatures. These oscillations are related to the adsorption and desorption of CO, and have been used as a mitigation strategy (see Section 2.3.3.11). There are irregularities in the oscillations in both cases due to the variable flow of H_2 coming from the fuel cell test system. However, it is noticed that at 80 °C, the amplitude of the oscillations is higher and the period shorter than at 70 °C. As the period is related to the velocity of the catalyst poisoning [60], it is inferred that the rate of the oxidation of CO at 80 °C is higher. This is confirmed by the higher performance obtained by the polarization curves and the EIS.

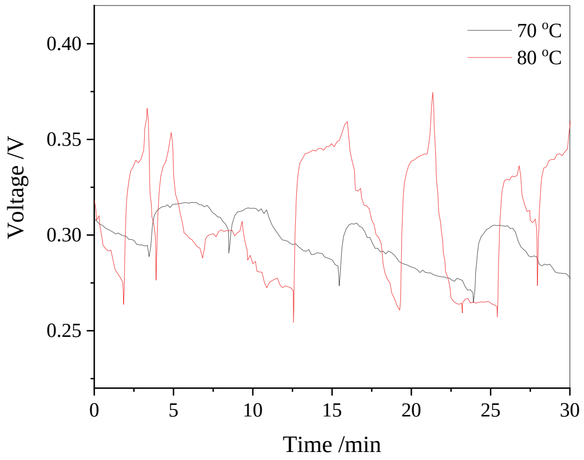

Figure 4.7 Potential oscillations at constant current (250 mA cm^{-2}) in the presence of 100 ppm CO in the anode inlet at 70 °C and 80 °C in a 5.29 cm^2 PEMFC using Pt/C as catalyst in both electrodes, and using O_2 in the cathode.

4.3.4 Effect of the time of exposure

The time of exposure is another parameter that affects the performance of PEMFCs exposed to CO. In Figure 4.8, the polarization curves obtained for 5, 60 and 210 minutes of exposure to 100 ppm CO are presented. At 5 min of exposure, the performance is very similar to the operation with pure H_2. Only after 600 mA cm^{-2}, the losses due to the presence of CO are evident. After 60 minutes, the drop in the performance is very similar to the cases observed at different temperatures. An important voltage decrease from 0.8 V to 0.3 between 100 and 200 mA cm^{-2} and a moderate decrease at higher currents were observed.

The variation in the performance could be explained by the partial coverage of the MEA by the CO. As the time increases, the CO is adsorbed on the Pt catalyst as it passes across the MEA. The amount of CO adsorbed increases with the time of exposure. The partial coverage explanation can be supported by previous studies that evaluated the current density distribution in segmented cells. In the first segments, the current diminishes due to the adsorption of the CO on the catalyst, while it increases in the rest [93, 94].

Galvanostatic EIS at 250 mA cm^{-2} was also measured for these experiments (Figure 4.9). As the time of exposure increases, the activation losses due to the adsorption of CO on the anode increase as well. There is a significant difference with only 5 minutes of exposure, even if the difference in the polarization curves is minimal at this current density. This shows the effects of ppm levels of CO on the performance of the cell in a very short period and the need for more advanced tools for the diagnostic of this phenomenon. At 5 and at 60 minutes, a pseudo-inductive behaviour was observed at low frequencies, due to the relaxation of the surface.

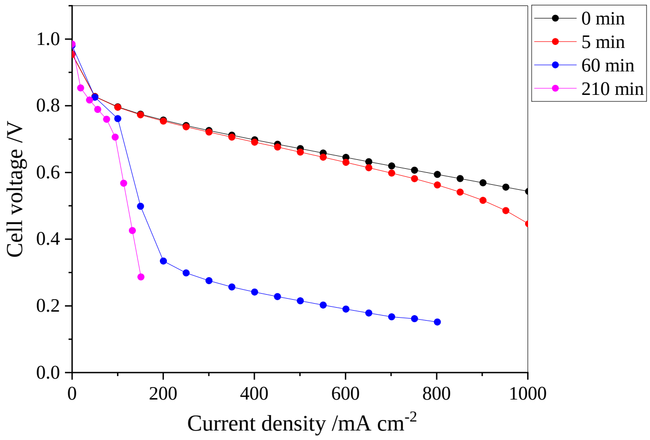

Figure 4.8 Polarization curves showing the effect of 100 ppm CO in the anode inlet after different times of exposure in a 5.29 cm^2 PEMFC using Pt/C as catalyst in both electrodes and operated and using O_2 in the cathode at 70 °C. *Note:* in the case of 210 min of exposure to CO, it was not possible to hold a current density higher than 150 mA cm^{-2}.

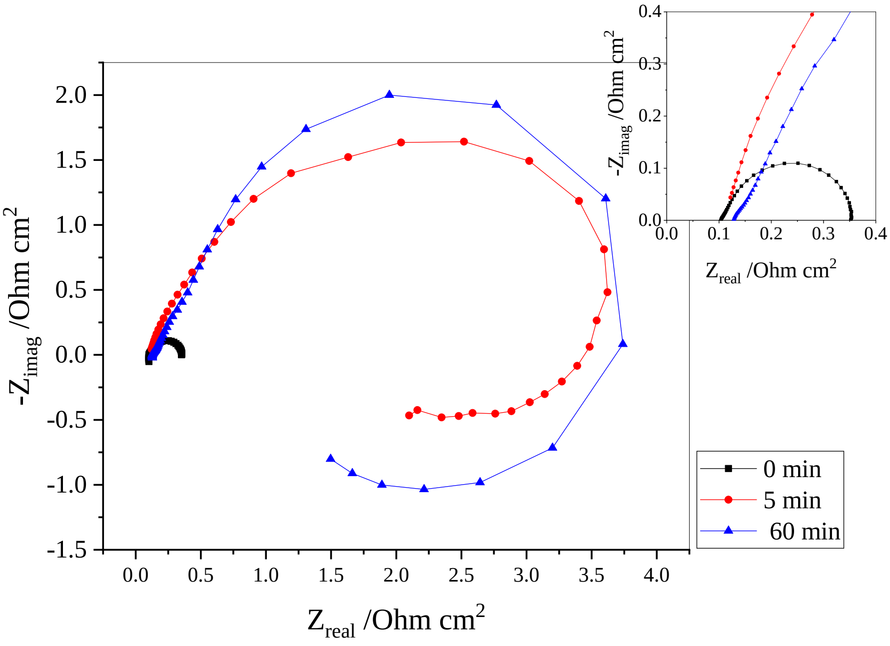

Figure 4.9 Galvanostatic EIS (250 mA cm^{-2}) showing the effect of the exposure time to 100 ppm of CO in the anode inlet of a 5.29 cm^2 PEMFC using Pt/C as catalyst in both electrodes at 70 °C, and using O_2 in the cathode. Initial frequency: 100,000 Hz, final frequency: 1.0 Hz.

4.3.5 Effect of the anode flow rate

Two different flows in the anode inlet (100 and 200 mL min^{-1}) were also studied for the same concentration. Polarization curves and potentiostatic EIS measurements were obtained to evaluate the effects (Figure 4.10 and Figure 4.11). In the polarization curves, it is observed that at 200 mL min^{-1} the degradation of the performance occurs at lower current densities (between 50 and 100 mA m^{-2}) than at 100 mL min^{-1} (between 100 and 150 mA m^{-2}). The drop of the voltage at 200 mL min^{-1} is due to the presence of the CO that blocks the catalyst surface, but also to the stripping of the molecules due to the high flow.

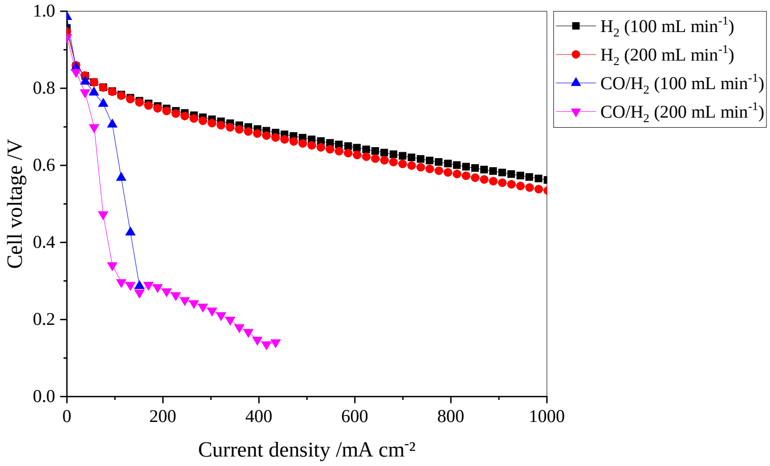

Figure 4.10 Polarization curves showing the effects of 100 ppm CO in the anode inlet at different flow rates. The 5.29 cm^2 PEMFC uses Pt/C as catalyst in both electrodes and is operated at 70 °C with O_2 in the cathode. *Note:* in the case of the exposure to CO at a flow of 100 mL min^{-1}, it was not possible to hold a current density higher than 150 mA cm^{-2}.

For the potentiostatic EIS measured, the cases with and without CO are presented in Figure 4.11. Higher activation losses are observed in the case of 100 mL min^{-1} with CO than in the case for 200 mL min^{-1}.. More CO enters into the cell when the flow rate is increased at a given concentration. However, a higher flow rate also implies a shorter residence time of the gas in the cell, hindering the penetration of CO into the active sites.

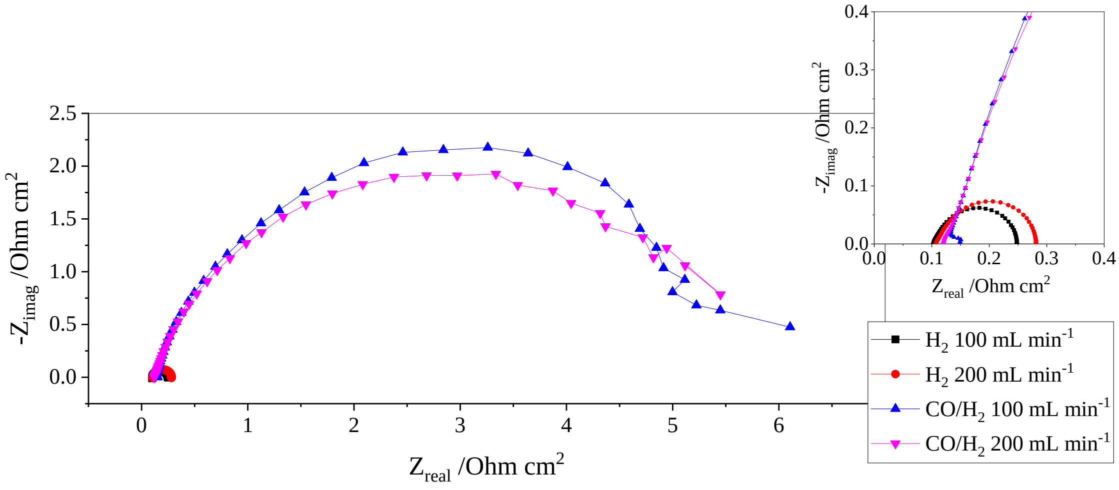

Figure 4.11 Potentiostatic EIS (0.7 V) showing the effects of 100 ppm CO in the anode inlet at different flow rates. The 5.29 cm^2 PEMFC uses Pt/C as catalyst in both electrodes and is operated at 70 °C with O_2 in the cathode. Frequency range: 0.05 to 200,000 Hz.

4.4 Conclusions

CO poisoning was experimentally studied in a single PEMFC. It was observed that the performance of the cell is affected over time in the presence of CO at ppm levels. The ECSA was determined through the H_2 adsorption/desorption and the CO stripping methods. CO stripping was also useful for the determination of the ignition potential for the oxidation of CO.

The short term effects of the poisoning were also confirmed. The performance of the cell is affected by the exposure of time, the concentration of CO and the temperature. The degradation increases with the exposure of time and the concentration of CO. The adsorption of CO is favoured compared to the H_2, blocking the surface of the catalyst preventing the HOR to occur. On the contrary, the performance is enhanced at higher temperatures by different phenomena, such as the thermal desorption of CO, the reduction of the CO oxidation potential and the O_2 crossover through the membrane. The study of these parameters is useful for the prediction of the performance of the cell over the exposure of CO.

The cyclic voltammetry, the polarization curves and the EIS represent useful tools for the diagnostic of the cell. However, more information can be obtained through the EIS. In particular, if equivalent circuit models are used, as well as H_2/H_2 systems are used for the study of the impedance in the anode alone. Also, variations of the galvanostatic and potentiostatic EIS provide additional information about the activation losses in the anode and the ignition potential respectively. In the case of the potentiostatic EIS, a wider range of voltage should be evaluated. Finally, mathematical tools that consider the variations on the system over time due to the poisoning should be used.

The experiments presented in this section contributed to understanding the bases of the CO poisoning in PEMFC, already in the literature. The generation of new information about phenomena involved in the process and its interpretation is consequently more accessible. In this work the research focus was on the distribution of the poisoning over time throughout a cell and a stack, and the evaluation of short-circuiting as a mitigation strategy. The results are presented in the following sections.

Chapter 5

Evolution and Distribution of the Anodic Overpotential Using Localised Reference Electrodes

5.1 Introduction

In section 2.2.2 the mechanisms occurring during the CO poisoning in PEMFC were reviewed. It has been shown that the dynamics of CO adsorption and the effect on the performance are complex and often results in the voltage of cells oscillating when operated under galvanostatic control [53-55]. Single-cell studies on CO poisoning have revealed the effect of different parameters on the frequency of the oscillations. As a general rule, the period decreases with an increase of the CO concentration or the anodic flow rate. The period is equally shorter with increasing current density or temperature [54, 60]. Other studies have focused on the patterns of the oscillations. Mota *et al.* observed periodic and non-periodic states at different conditions of flow and current density. The transition from period-1 to period-2 and chaotic states occurs over an increase in the current density at a fixed hydrogen (CO) flow, or over the decrease of the flow rate at a constant current [61].

The measurement of current and voltage across a range of electrical loads (the polarisation plot) is the most commonly used means of assessing fuel cell performance. While it represents the ultimate output of a cell or stack, a crude bulk measurement withholds the complexity of what is occurring across the extent of the electrodes. In fact, there will be a distribution of performance such that local current density, temperature, water composition and reaction conditions will vary across the electrodes in space and time. Localised measurement of these parameters is now extensively performed [279-283] and such measurements have been responsible for many new insights that have led to advanced hardware design and operating protocols. In this section, the aim is to uncover new information about the nature of CO poisoning by taking account of the spatial variations and temporal dynamics that occur during CO poisoning; in particular, the spatially varying characteristics that accompany potential oscillations. This is achieved using an array of reference electrodes to probe local electrode potential. In addition, the exit gas composition (CO_2) is used to corroborate the true existence of the oscillatory mode and link the electrical response to the chemical reaction.

Bulk voltage measurements of cells poisoned with CO have shown that the process is a function of many factors, including temperature [70], water content / gas humidification [74-77], CO concentration [66], anode gas flow rate [72], pressure [73], etc. Taking this into account and adopting a local view (individual location on an electrode) of fuel cell operation, it is clear that the process of CO poisoning is highly complex, as each of these factors will vary across the extent of a cell. What is more, local variations in one parameter can affect the situation elsewhere in the cell. For example, in the absence of self-sustained oscillations (typically low concentrations of CO), an uneven current distribution is observed as a result of the rapid adsorption of CO at the inlet compared to the outlet under galvanostatic control [93, 94, 104, 105]. Moreover, a pseudo-inductive behaviour at low frequencies has also been observed in the first segments (anode entrance) of cells using segmented electrochemical impedance spectroscopy (EIS) [93, 94]. A more complex response is therefore anticipated in the local electrode potential measurements under oscillatory behaviour. As precedent, different patterns experimentally observed were predicted by spatiotemporal models based on a one-channel cell that proposed the visualisation of the system as a series of individual oscillators with additional interactions, including CO oxidation throughout the channel and two main interactions occurring between them: the mean-field (global) coupling and the migration (local) coupling [62, 63]. The pattern observed will depend on the dominant interaction. A dominant mean-field coupling, where all the catalyst sites are electrically connected, combined with a high flow rate results in a homogeneous system where the oscillations are in phase and present a sole frequency. A reduction in the flow rate provokes a period-doubling bifurcation of the homogeneous oscillation. As for the dominant migration coupling, the interaction is related to the appearance of spatiotemporal turbulence, reflected by phase or defect turbulence. Small disturbances in the phase relation between adjacent oscillators is present in the phase turbulence, while local aperiodic breakdown of the oscillation amplitude, so-called phase slips, are part of the defect turbulence. Spatial current density measurements in six parallel channels validated the appearance of these patterns, although no turbulence was found under galvanostatic control [64].

This study explores how cells enter the oscillation mode from a localised perspective and answer questions like: is the extent of the cell poisoned evenly and at the same rate? Do the oscillations start in one part and are extended to the entire cell? Do different parts of a cell oscillate at different frequencies, with different amplitude or phase? Do rational trends exist across the extent of a cell? Are the existing models useful to understand the mechanisms occurring throughout a standard cell? These issues are important for developing mitigation strategies for CO poisoning [284], spatially distributing catalyst type and composition across electrodes and understanding if and how one cell oscillating can affect another cell in a stack.

5.2 Results and discussion

The results obtained through the localised reference electrodes are presented according to the evolution of the system, where different phases are identified: transition phase, pseudo-steady state and recovery phase. The transition phase comprises the time from the introduction of CO until a pseudo-steady state is reached. During the pseudo-steady state complex self-sustained potential oscillations are observed in this experiment. Although oscillations are present, the average cell potential over time remains almost constant during this phase. Finally, the recovery phase evaluates the behaviour of the system when the CO is removed and pure H_2 is reinstated.

5.2.1 Transition phase

Figure 5.1 (a) presents the evolution of the cell voltage and the changes in the anodic overpotential, $\Delta\eta$, measured by the three reference electrodes, RE1, RE2 and RE3, during operation with pure H_2 and during the first 90 minutes of exposure to 100 ppm CO/H_2 at constant current density (0.3 A cm^{-2}). The decrease in overall cell potential is attributed to the evolving increase in anode overpotential, starting from the inlet and progressing along the anode flow-field. During the first minutes of exposure to CO, $\Delta\eta$ remains close to zero before an increase is observed in the reference electrodes. This time period is dependent on the diffusion rate of CO to the catalyst surface, the rate of CO adsorption [285] and on the distance from the anode inlet, as the catalyst sites closer to the inlet are first exposed to CO. As these areas become saturated, more CO is available to poison downstream locations. Hence, the increasing order of this ‘induction’ time observed in the three reference electrodes, where RE1 is the first to be affected, followed by RE2 at ~15 mins. The induction time for RE3 is shown in Figure 5.1 (b) where the evolution of the cell voltage and the $\Delta\eta$ for the three reference electrodes is shown exclusively for the ~16 hrs of exposure to CO in a logarithmic graph. For this electrode located closer to the anode outlet, the induction time is at ~75 min.

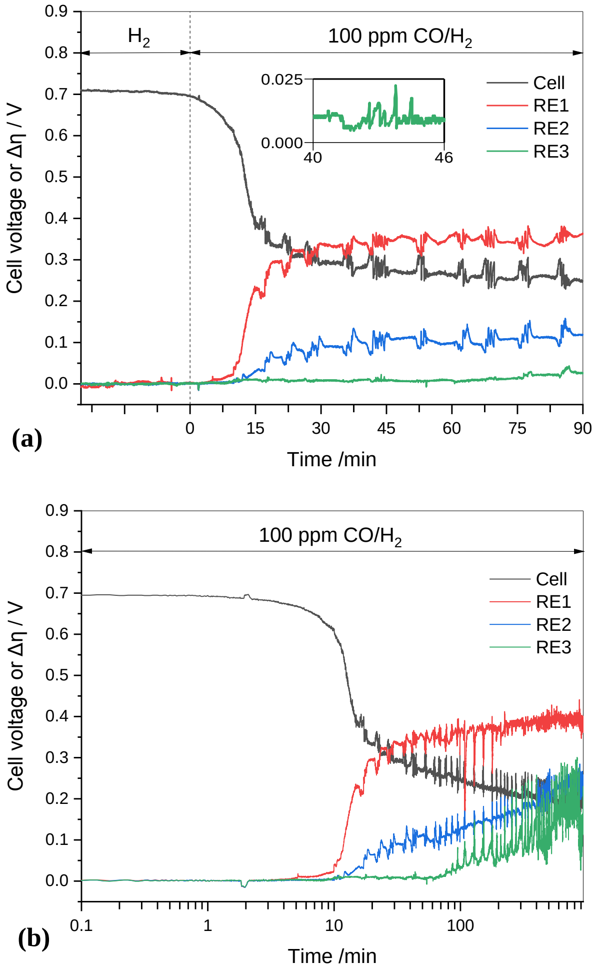

Figure 5.1 Evolution of the cell voltage and the anodic overpotential change ($\Delta\eta$) measured through the three reference electrodes (RE) in a PEMFC exposed to 100 ppm CO/H_2 under galvanostatic control (0.3 A cm^{-2}) during (a) the operation with pure H_2 and the first 90 min of exposure to CO, (b) the operation with CO/H_2 for 15 hours approximatively (logarithmic graph). The numeration follows the hydrogen path, where RE1 is closer to the anode inlet.

In Figure 5.1 (a) it is observed that the induction period is followed by an increase in *$\Delta\eta$*, confirming the poisoning of the catalyst which impedes the hydrogen oxidation reaction (HOR). Throughout this transition phase, $\Delta\eta$ follows a characteristic S-shape (sigmoidal) over time, which can be described by the logistic function which is commonly used to describe transition phenomena in various fields, including the kinetics of autocatalytic and biomolecular reactions [286], crystallization [287], wetting [288] and dewetting [289] processes, among others. Through the logistic function, it is possible to estimate the time needed to advance from 10% to 90% of the $\Delta\eta$ at the pseudo-steady-state for the different reference electrode locations, as detailed in the Appendix A1. The approximate transition times calculated are shown in Figure 5.2(a) and confirm the more rapid poisoning closer to the anode inlet and decreasing towards the outlet. At RE1, the approximate transition time was 22 min, while for RE2 and R3 it was 51 min and 181 min, respectively. The transition time for the entire cell to reach the pseudo steady-state is consequently higher than 181 min. Bender *et al.* presented a different methodology for the determination of the transition time in cases where the cells are contaminated by low concentrations of CO (1-2 ppm CO/H_2), no self-sustained oscillations were observed and a linear fit of the $\Delta\eta$ over time was possible [253]. Although the logistic model provides a broad estimation of the transition time, it is still considered more adequate in this case due to the presence of the oscillations during the pseudo-steady state that impedes the depiction of the variation of $\Delta\eta$ as a straight line.

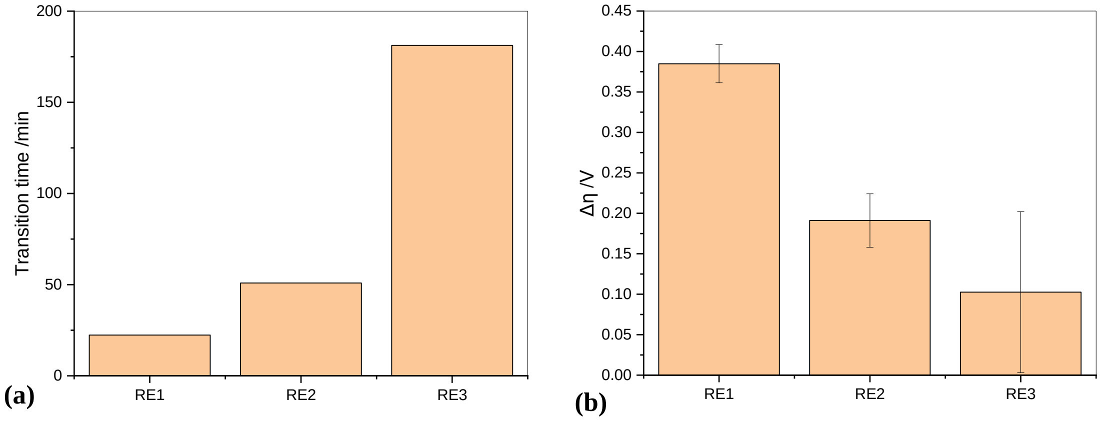

Figure 5.2 (a) Estimated transition time needed to reach from 10% to 90% of the maximum anodic overpotential change, obtained through the logistic model, and (b) average anodic overpotential change ($\Delta\eta$) at the pseudo-steady-state at the different locations of the reference electrodes (RE) in a PEMFC exposed to 100 ppm CO/H_2 and controlled galvanostatically at 0.3 A cm^{-2}. The numeration follows the hydrogen path, where RE1 is closer to the anode inlet.

The more rapid contamination closer to the anode inlet is due in part to the progressive adsorption of CO along the flow-field that provokes different induction times in the electrodes, as mentioned, but also to the varying concentration of CO throughout the cell.

The area closer to the anode inlet adsorbs and partially oxidises CO from the stream, reducing the CO concentration travelling downstream. As a result, the $\Delta\eta$ growth rate once the induction has passed for the different electrodes decreases towards the end of the channel, delaying the transition to the pseudo-steady-state. As such, areas of the catalyst upstream are both abstracting CO from the feed by absorbing it onto the catalyst active sites and also converting the CO to CO_2, effectively ‘purifying’ the stream to the advantage of downstream catalyst sites.

Another aspect to take into consideration to explain the progressive increase of the transition time towards the end of the anode is the local operating conditions throughout the cell. The effects of local humidity are of particular interest, as the CO stripping potential of Pt/C decreases with increasing water vapour pressure [74]. According to in situ measurements of relative humidity in a cell with a similar counter-flow configuration and operating with pure H_2, it is assumed that the relative humidity in the anode increases towards the outlet due to back diffusion of water from the cathode [290]. Moreover, it is also assumed that this variance is deepened by the presence of CO, as previous studies have shown a redistribution of the current density under galvanostatic control in the presence of CO. The anode inlet tends to present a diminishment of the current, while the current increases in the outlet [93, 94]. The production of water closer to the anode outlet is consequently intensified, contributing to the oxidation of CO in this region.

In this transition phase, complex self-sustained potential oscillations begin to occur. Previous studies have depicted the oscillations exclusively in the pseudo-steady-state. In this study, it is shown that these can breakthrough in the transition phase in all the extension of the cell. The $\Delta\eta$ oscillations are observed in the three reference electrodes, including RE3, where very small oscillations are present in the induction phase where the major effects of the poisoning have not occurred in the first 75 min of exposure to CO (Figure 5.1 (a)). As the CO reaches the area of RE3, the amplitude of the oscillations gradually increases until the pseudo-steady-state is reached, as observed in Figure 5.1 (b).

The appearance of the oscillations in all the reference electrodes despite the variation of the CO concentration and humidity is explained by the electrical coupling throughout the cell, as described by the models presented by Hanke-Rauschenbach and co-workers [62-64]. It is inferred that the process starts with the adsorption of CO in the area closer to the anode, which is more severely contaminated due to the proximity to the entrance. It is deduced that it is in this area that anode overpotential threshold for the occurrence of CO oxidation and the consequent self-sustained potential oscillations is reached. Due to mean-field and migration coupling interactions, oscillations are observed throughout the cell even if the local anodic overpotential is lower towards the anode outlet (RE3) and during the induction phase where the CO content is very low. The complex pattern observed is examined in detail next.

5.2.2 Pseudo-steady-state

In Figure 5.2 (b), the average $\Delta\eta$ is presented for the different locations at pseudo-steady-state, over the space of one hour between 420 and 480 min of exposure to CO, once the pseudo-steady-state has been reached and the overall cell has a very low potential indicative of almost complete deactivation of performance. It is confirmed that the average $\Delta\eta$ varies significantly across the active area of the cell. The area closer to the anode inlet, represented by the measurements of $\Delta\eta$ at RE1, is more affected due to the exposure to a higher concentration of CO and lower relative humidity. As the concentration of CO decreases along the cell and the relative humidity increases towards the anode outlet, at RE2 the $\Delta\eta$ measured is lower than at RE1, but higher than at RE3. The area towards the exit of the cell is less poisoned by the CO entering the cell.

Figure 5.3 (a) presents the cell voltage and $\Delta\eta$ profiles in the three locations for one hour after ~420 min of exposure to CO, where the sequence of various periods of oscillations is observed. A detailed view of one oscillation period is presented in Figure 5.3 (b) in the space of five minutes. The complex behaviour of the cell voltage during the oscillations is confirmed, where a cascade of up to six maxima period-doubling bifurcation is shown. Similar behaviour was experimentally observed at low flow rates and high current densities by Mota *et al.* that correlated the different spikes to a series of oxidation steps [61]. Following the model presented by Hanke-Rauschenbach *et al.*, it could also be inferred that the complex pattern of the oscillations is related to a low flow rate, where the time for CO transport in the channel (or cell in this case) is higher than the time needed for the adsorption of CO. The cycle starts with the partial coverage of the active area by CO, the anode double layer potential increases and provokes a first oxidation step in this part of the cell. The remaining CO continues to be adsorbed in the rest of the catalyst surface, leading to a second oxidation peak. This sequence is repeated until practically all the area is covered and a final oxidation step occurs that liberates the cell surface from CO and sets out the beginning of a new cycle [62]. The simplification of this model presented by Kirsch *et al.* states further about the dominant interactions occurring throughout the cell, as the pattern observed is associated to a dominant mean-field coupling in combination with a low flow rate [63, 64].

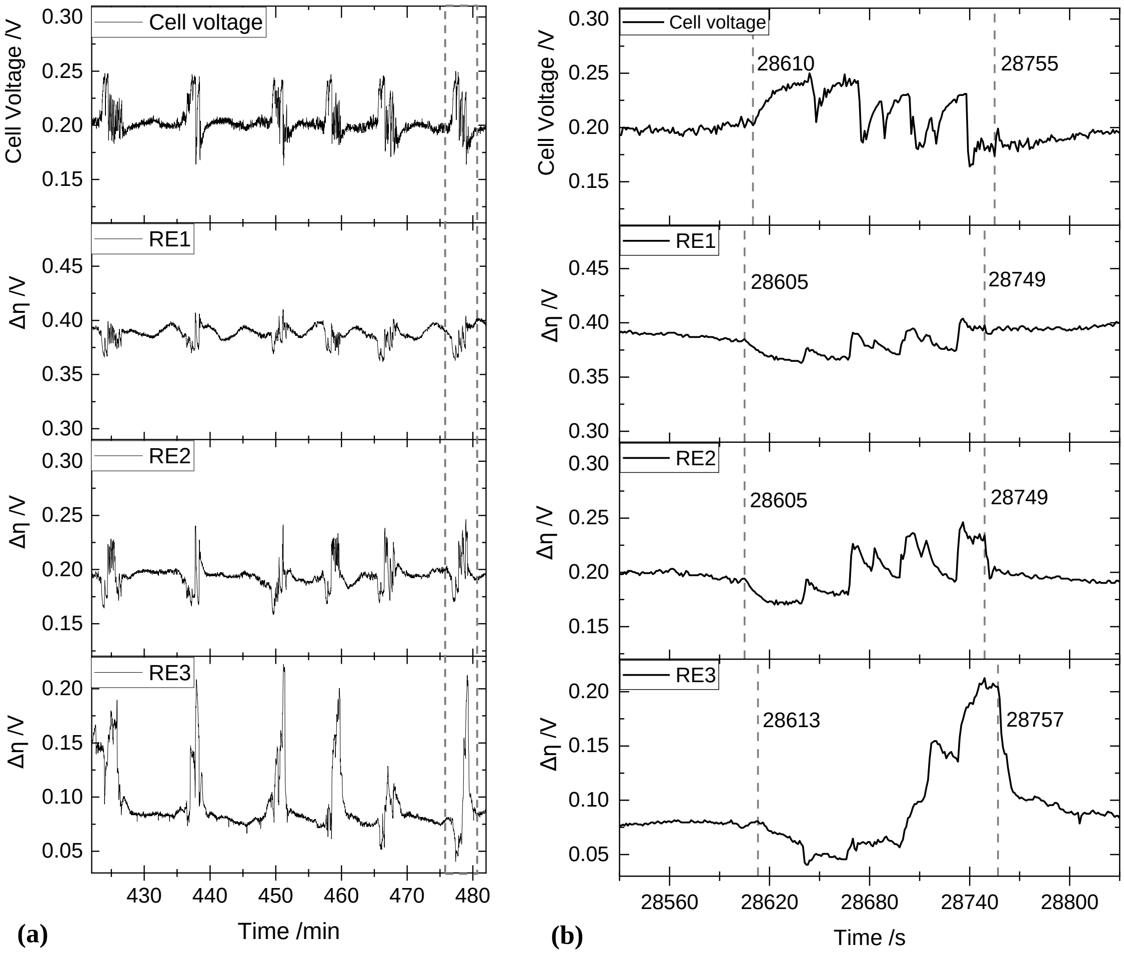

Figure 5.3 Self-sustained oscillations of the cell voltage and the anodic overpotential change ($\Delta\eta$) in the three localised reference electrodes, in a PEMFC exposed to 100 ppm CO/H_2 under galvanostatic control (0.3 A cm^{-2}), in the space of (a) one hour after 422 minutes (~7 hours) of exposure, (b) 5 minutes after 475 and a half minutes of exposure.

The simultaneous measurement of the cell voltage and the $\Delta\eta$ profiles allows studying the dynamics of these parameters during the occurrence of the oscillations. It is shown in Figure 5.3 (b) that the evolution of $\Delta\eta$ in RE1 and RE2 is in opposite direction to the cell voltage. The $\Delta\eta$ decreases over an increase in the CO oxidation rate, decreasing the coverage of the surface by CO, provoking a rise in the cell voltage. Similarly, when the CO adsorption is enhanced, the cell potential drops due to the diminishment of the H_2 oxidation rate. The sequence of the period-doubling bifurcation is well defined in these two locations. In RE3 however, the evolution of $\Delta\eta$ differs from RE1 and RE2, as a lower number of bifurcation periods is observed. In some cases, $\Delta\eta$ in RE3 decreases while an increase is observed in RE1 and RE2, and vice versa. There is not a defined trend in the ascension of $\Delta\eta$ to the highest peak of the oscillation in RE3. Moreover, the oscillations are not simultaneous in all the extent of the cell. Two points at the start and at the end of the period-doubling bifurcation series were chosen in the evolution of the cell potential and the $\Delta\eta$ of the three reference electrodes to elucidate the sequence of the events. These are indicated by dotted lines and include the time in seconds from the injection of CO in the system. It is observed that while the $\Delta\eta$ variations are simultaneous in RE1 and RE2, there is a delay of approximately eight seconds in RE3. The oscillations in the cell voltage start occurring after RE1 and RE2, but before RE3.

While the observation of the evolution of the cell potential implies a global dominant mean-field coupling in combination with a low flow rate, as mentioned, the study of the $\Delta\eta$ variations in the extent of the cells provides new information about an area where the migration coupling is dominant. The well-defined $\Delta\eta$ profiles in RE1 and RE2 in anti-phase to the cell voltage imply that in the area closer to the anode inlet (RE1) and the central area (RE2) the dominant interaction between the individual oscillators is mean-field coupling. However, the differences observed in the RE3 indicate phase and defect turbulence, characteristic of a dominant migration coupling. As a larger area of the cell is dominated by mean-field coupling, this behaviour is reflected in the cell potential profile. This result agrees with the case presented by Kirsch *et al.*, where the coexistence of a dominant mean-field coupling inlet area and a dominant migration-field coupling outlet region was predicted in a straight channel under the operation of an intermediate conductivity. The membrane conductivity and the system dimensions were identified as determinative for the dominance of one of these interactions [63].

As for the turbulence occurring in the outlet region of the anode, previous studies have presented evidence of phase and defect turbulence in a PEMFC exposed to CO under potentiostatic control [64], although this behaviour had not been reported experimentally under galvanostatic control. Considering the dominant migration-field-coupling, this area is more influenced by the local operating conditions where the CO coverage is limited and the relative humidity is higher. It is inferred that these conditions contributed to the reduction of the number of the oxidation steps that compose the cascade or doubling-bifurcation periods. It is also important mentioning that the model was originally proposed for the extent of one channel and not a six-channel serpentine flow field, as is more technologically relevant and used in this work.

The variations in the CO oxidation rate during the self-sustained oscillations are reflected in the variation of the concentration of CO_2 in the anode outlet, as shown in Figure 5.4, where oscillations are observed. In each cycle, the concentration of CO_2 increases as a result of the oxidation of CO in the cell. Over this increase, several spikes are observed confirming the multiple oxidation steps related to the period-doubling bifurcation cascade evidenced in the cell voltage and the $\Delta\eta$ variations oscillations shown in Figure 5.3 (b). A maximum concentration of CO_2 is reached before a uniform decrease is observed during the increasing adsorption of CO in the surface.

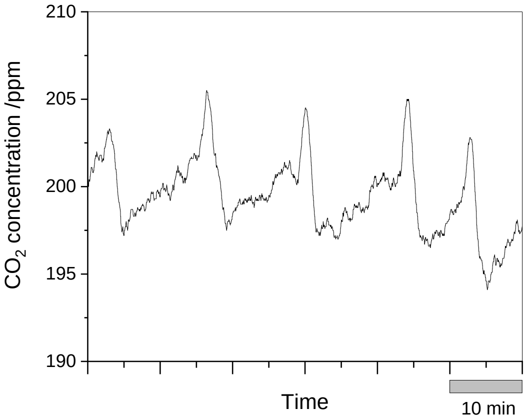

Figure 5.4 Oscillations of the concentration of CO_2 measured at the outlet of a PEMFC exposed to 100 ppm CO/H_2 operated at a constant current density of 0.3 A cm^{-2}.

The periodicity of the oscillations observed in the evolution of the cell voltage, the $\Delta\eta$ in the three reference electrodes and in the concentration of CO_2 in the anode outlet was measured in the pseudo-steady-state after 420 minutes of exposure to CO and is compared in Figure 5.5. Even though there is a difference in the starting points of the oscillations in the $\Delta\eta$ throughout the cell and the cell voltage, each cycle occurs every ~11 min for each one of the parameters studied. The period of a cycle is determined by the time the CO takes to propagate throughout the cell [62].

The comparison of the peak-to-peak amplitude (i.e. the difference between minimum and maximum) for the cell voltage and the $\Delta\eta$ in the three reference electrodes oscillations is presented in Figure 5.5 (b), where an increasing the peak-to-peak amplitude of the $\Delta\eta$ towards the area closer to the anode outlet is noticed. This variation is a result of the mentioned redistribution of the current density in the presence of CO under galvanostatic control. As Kadyk *et al.* related an increasing current to an increase in the amplitude of the self-sustained potential oscillations [59], it is expected to observe lower amplitudes in the area closer to the anode inlet where a decrease in current is presented, and higher amplitudes closer to the outlet where an increase in the current density is sustained. This trend is reinforced by the local conditions of CO coverage and humidity. Considering the surface coverage by CO is higher closer to the anode inlet and decreases towards the outlet, the CO oxidation steps that occur during the self-sustained oscillations are consequently more effective in the areas where the CO coverage is lower, which is a result of the CO concentration and the relative humidity.

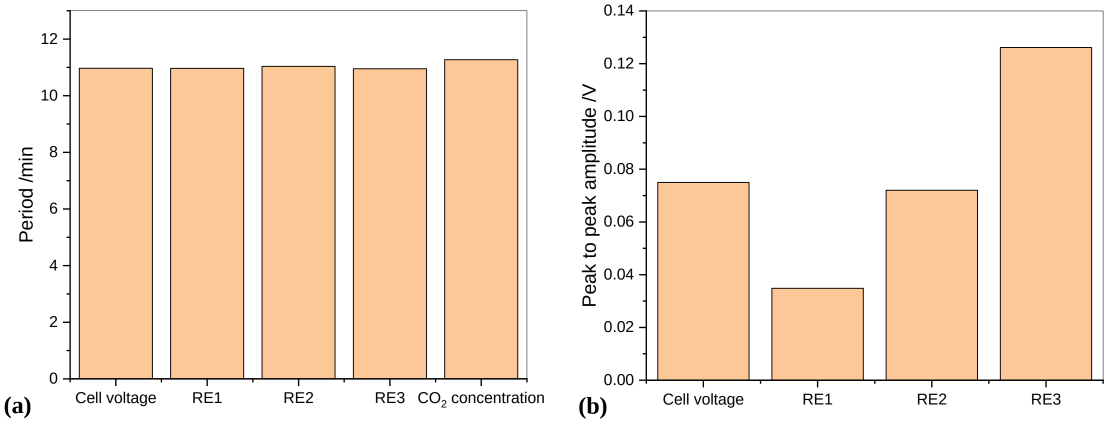

Figure 5.5 (a) Prominent period and (b) average peak to peak amplitude of the oscillations observed in a PEMFC at pseudo-steady-state between 420 and 480 minutes of exposure to 100 ppm CO/H_2 under galvanostatic control (0.3 A cm^{-2}). The peak to peak amplitude of the oscillations observed in the CO_2 concentration in the anode outlet is of 7 ppm.

Finally, another trend examined in this phase is observed in Figure 5.1 (b), where each reference electrode presents a gradual increase of the average $\Delta\eta$ over time. This variation is presumably due to the degradation of the electrode, as previous studies have demonstrated an increased loss of the electrochemical surface area in the short and long term in the presence of CO [96]. No studies have evaluated the effects of self-sustained potential oscillations in the degradation of the active area, in particular the spatial deterioration of the electrodes in the long term. In this relatively short experiment, it is possible to observe a higher increase in the average $\Delta\eta$ closer to the anode inlet (RE3) than in the inlet (RE1). Considering the differences in the amplitude of the oscillations studied in Figure 5.5 (b), it is deduced that the higher fluctuations in $\Delta\eta$ entail an increase in the loss of the catalyst surface area. As the amplitude of the oscillations increase towards the outlet of the anode, the degradation of the electrode is also intensified towards the anode outlet.

5.2.3 Recovery phase

Figure 5.6 shows how the cell responds when CO is removed from the hydrogen feed. A decrease in $\Delta\eta$ is observed in the three reference electrodes and the increase of the cell voltage is observed to start to occur as soon as the gas is switched to pure hydrogen and is complete in less than 1 min. Compared to the initial phase of poisoning, the recovery is a fast process in all the locations of the REs. In order to compare the time required for the reestablishment of the anodic overpotential, the time scale was adapted so the reintroduction of pure H_2 starts at zero, and an exponential model was used, as described in the Appendix A2. Figure 5.7 presents the decay rate and the half-life for each one of the reference electrodes. It is observed that the decay rate increases towards the anode outlet, which is explained by the coverage of CO. As the area closer to the anode inlet is more covered by the contaminant, the time required to clean the surface is longer. The opposite occurs near the outlet, where less adsorbed CO molecules are found, and less H_2 is needed for the recovery of the area.

The high coverage of CO, related to high $\Delta\eta$ levels, also has an influence on the half-life. The area closer to the inlet, where RE1 is placed, presents the highest $\Delta\eta$ from the reference electrodes, and considering the low decay rate compared to RE2 and RE3, the half-life is consequently higher. The opposite occurs near the outlet, where less adsorbed CO molecules are found. The half-life is lower closer to RE3.

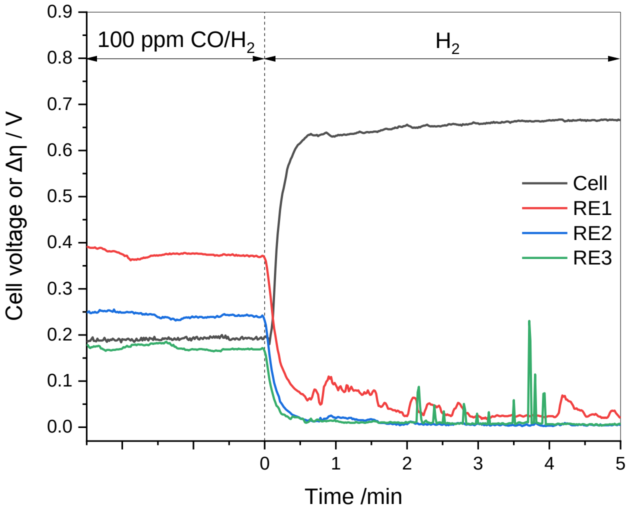

Figure 5.6 Exponential decay of the anodic overpotential change ($\Delta\eta$) during the recovery with pure H_2 at the three reference electrodes, and increase of the cell voltage after the exposure to 100 ppm CO/H_2. The operation of the cell is at constant current (0.3 A cm^{-2}).

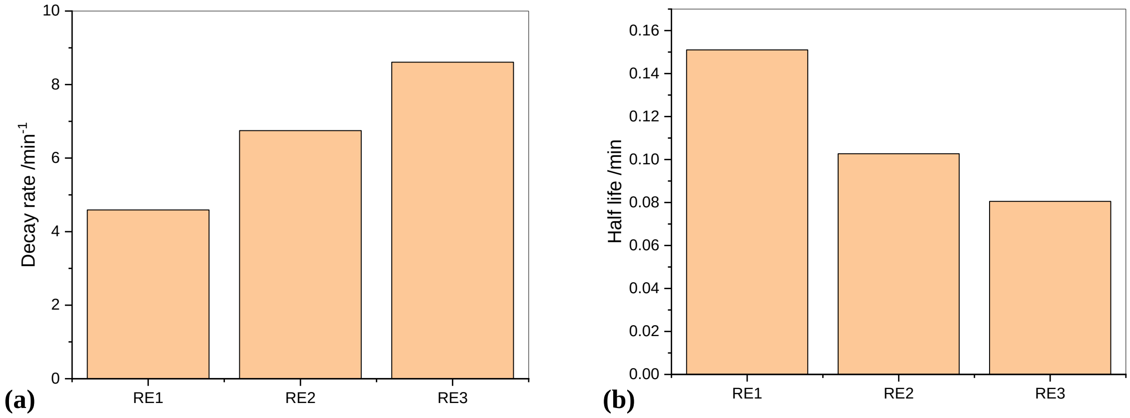

Figure 5.7 Exponential decay of the anodic overpotential change $\Delta\eta$ due to the reintroduction of H_2 instead of CO/H_2 mixtures and measured at the three reference electrodes, (a) decay rate and (b) half-life.

5.3 Conclusions

Localised reference electrodes were used to measure the anode potential of a cell exposed to 100 ppm CO/H_2 under galvanostatic control. The location of the reference electrodes over the MEA provided information of the distribution and dynamics of the poisoning process. The poisoning process, as indicated by the anode overpotential, follows a sigmoidal function with time during the transition phase. This is notionally split into three phases, an initial slow induction period, a rapid transition period and a pseudo-steady-state period. It was observed that the sites closer to the anode inlet reached the pseudo-steady-state faster and presented a higher $\Delta\eta$ than the sites closer to the outlet due to the exposure to a higher concentration of CO and due to lower relative humidity in the area.

Complex self-sustained oscillations composed by a cascade of doubling bifurcation periods were observed in the cell voltage and the anodic overpotential throughout the cell during the transition phase and at the pseudo-steady-state. Following the models presented by Hanke-Rauschenbach *et al.*, the system was analysed as a series of individual oscillators and the coexistence of a dominant mean-field-coupling area in the anode inlet and the centre, and a dominant migrant-field-coupling region closer to the anode outlet was demonstrated. The dominant mean-field-coupling area was characterised by defined and simultaneous oscillations in the $\Delta\eta$ profiles in RE1 and RE2, while phase and defect turbulence were observed in the $\Delta\eta$ evolution in RE3 where the migration-coupling field is dominant. This result is in agreement with the case predicted in one straight channel at intermediate conductivity by Kirsch *et al.* Moreover, the turbulence observed closer to the anode outlet was experimentally reported for the first time under galvanostatic control. In this work, the size of the cell was also related to the delay in the start of the cell observed in RE3 for the start of the oscillations, and the lower CO coverage and higher humidity were associated to the decrease in the doubling period bifurcation in $\Delta\eta$ observed in RE3. The variation in the CO oxidation rate was demonstrated by the oscillatory evolution of the concentration CO_2 in the anode outlet, where the doubling bifurcation periods were also denoted. The period of the oscillations was also measured and was found similar for the cell voltage, each one of the $\Delta\eta$ profiles and the CO_2 concentration at the anode outlet despite the variable start of the oscillations. The amplitude of the oscillations was nonetheless found to increase towards the anode outlet, which was explained by the uneven current density distribution, and the variant CO coverage and humidity. Additionally, the areas where the highest amplitudes are observed (the anode outlet in this case) were related to a more rapid degradation of the catalyst, most probably by the loss of electrochemical surface area.

As for the recovery of the cell by the injection of high purity H_2, it was proved to be a more rapid process than the transition phase. The exponential model was used to compare the differences in the $\Delta\eta$ in the reference electrodes. It was found that the recovery velocity is related to the CO coverage, as the area closer to the anode inlet (RE1) where the coverage is higher, presents a lower decay rate and a higher half-life compared to RE2 and RE3.

Finally, the study of the poisoning dynamics in the extent of the cell during the different phases of the poisoning provides valuable information for the design and optimization of more efficient mitigation strategies. For instance, a sacrificial area with a more active catalyst that enhances the oxidation of CO can be considered closer to the anode inlet where the contamination is more severe.

Chapter 6

Distribution of CO Poisoning in a Segmented-in-Series Fuel Cell System through Thermal Imaging and Mass Spectrometry

6.1 Introduction

Most of the research on CO poisoning has been carried out in single cells. Limited studies have evaluated larger systems. Lu *et al.* compared the CO removal through potential oscillations (self-sustained potential oscillations) in two cells connected in series and in parallel operated under galvanostatic control. The CO removal and the power output were higher in a serial configuration as the potential was operated independently in the cells. It was not the case of the parallel system where the cells were operated in an equipotential mode [152]. Perez *et al.* used an arrangement of single cells similar to a segmented cell and evaluated the performance distribution of the stack as well as the concentration of CO_2 in the anode outlet. A methodology for the optimization of the air bleeding was developed [181]. As for the possibility of a cascade of reactors operating under ECPrOx, Heidebrecht *et al.* proposed a methodology for the sequence design considering an economic objective function [153].

In Chapter 5 localised reference electrodes in an MEA were used to evaluate the distribution of the anodic overpotential over time in the presence of CO under galvanostatic control. Self-sustained potential oscillations were observed and studied as a series of individual oscillators. Two dominant interactions coexisted: a dominant mean-field-coupling in the anode inlet and centre characterised by the electrical connection of the catalyst sites, and a dominant migrant-field-coupling region closer to the anode inlet where the oscillations were decoupled from the rest of the cell and responded to the local operating conditions. In this chapter, the CO poisoning was evaluated through a segmented-in-series system, where each cell is electrically isolated. Hence, it was possible to study the poisoning in adjacent areas where the dominant mean-field-coupling is considered negligible.

The segmented-in-series system also allows the study of an industrial size cell. And, numerous small stacks consider the series configuration in their design. It is consequently possible to study a PEMFC system commercially in use. Moreover, the planar configuration of the stack and the disposition of the cells in series allowed the use of thermal imaging as a probe of the location of poisoning due to increased heat generation associated with increased kinetic overpotentials. Combined with the measurement of the individual cell voltages and the estimation of the concentration of gases in the outlet of each cell through mass spectrometry, it was possible to examine the effects of the poisoning beyond the adsorption of the CO molecules in the catalyst surface of the anode.

6.2 Results and discussion

The results presented in this section are divided according to the information obtained from the measurement technique: the evolution of the individual voltages, thermal imaging, current interrupt and mass spectrometry.

6.2.1 Voltage evolution

The effects of CO in the performance of the stack were evaluated through time. Figure 6.1 presents the evolution of the voltage of the stack and the individual cells during the measurement of the concentration of the gases in the outlet of Cell 5, where no gas was deviated from the stack to the mass spectrometer. The measurements cover the galvanostatic operation (0.3 A cm^{-2}) with high purity H_2, the presence of 100 ppm CO/H_2, and the recovery with H_2. It is observed that over the period of exposure to the CO/H_2 mixture, the voltage of the stack decreases due to the adsorption of CO on the catalyst sites (Figure 6.1 (a)). The coverage of the surface continues until a steady-state is reached. When the mixture of CO/H_2 is removed and substituted by high purity H_2, the performance of the cell is recovered.

In Figure 6.1 (b), the contribution of the individual cells into the stack voltage is presented. It is observed that the cells are consecutively affected by the presence of CO. Each one of the cells presents a different transition time to a pseudo-transition state, where the cell closer to the inlet (Cell 1) is the first one to be affected. The difference in the transition time is due to the concentration of CO entering the cells. As the CO is adsorbed onto the catalyst surface in one cell, the concentration of CO in the fuel decreases, increasing the time needed to reach the equilibrium in the following cell.

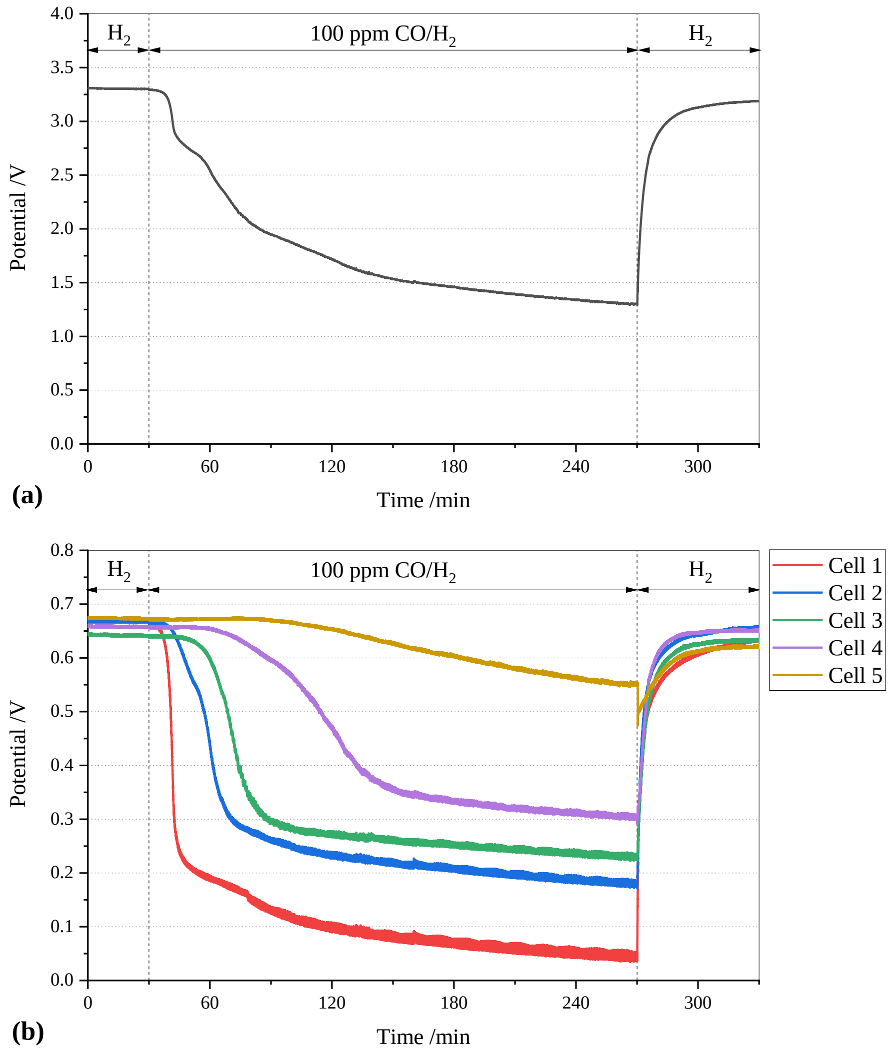

Figure 6.1 Evolution of (a) the stack voltage and (b) the individual cell voltages during the galvanostatic operation (0.3 A cm^{-2}) with high purity H_2, in the presence of 100 ppm CO/H_2 and during the reinjection of high purity H_2.

The content of CO also has an impact on the voltage drop of the cells. Table 6.1 presents the voltages of the stack and the individual cells throughout the experiment, and Table 6.2 shows the voltage drops compared to the operation with high purity H_2. After three hours of exposure to 100 ppm CO/H_2, Cells 1 to 4 have reached the equilibrium voltage and Cell 5 still presents a continued decrease in performance. At this moment in time, the voltage losses were approximately 92, 71, 61, 51 and 14% for Cells 1, 2, 3, 4 and 5 respectively, while the overall performance of the stack decreased by 58% on average. As observed, as the amount of CO increases, the cells present a higher voltage drop. The exposure to CO continued for an additional hour, and the losses increased to 94, 74, 65, 53 and 18% for Cells 1, 2, 3, 4 and 5 and a loss of approximately 61% for the stack. It is noticeable that while the stack voltage represents the overall performance of the cell, the performance varies throughout the stack.

As for the recovery phase, it constitutes a faster process than for the CO poisoning. According to Table 6.1 and Table 6.2, just 10 minutes are enough to restore the stack voltage from 60.7 to 13.2% of voltage drop compared to the initial operation with H_2. The recovery continued for one hour in total, and the performance of the stack improved up to an overall voltage drop of 3.7%. Cell 1, which was more severely affected by CO, presented the highest voltage increase, although it was further away from the initial performance with H_2 than Cell 2, Cell 3 and Cell 4 with a voltage drop of 5.4%. Cell 2, Cell 3 and Cell 4 followed with a voltage drop of 1.8, 1.8 and 1.2% respectively. Although Cell 5 also presented an increase in its performance, it only reached 7.7% of voltage drop. Further studies are needed in order to elucidate if a longer period of recovery would contribute to a full recovery of the performance, as except for Cell 5, the areas with the highest coverage of CO, presented the lowest recovery. Another mechanism that could explain the partial recovery of the stack would be the degradation of the components, as previous studies have confirmed irreversible losses in the active surface of the electrodes at lower concentrations of CO (up to 50 ppm) under load cycling protocols [96]. A more severe degradation could occur in the presence of 100 ppm CO/H_2.

The lower recovery of Cell 5 compared to the rest of the cells could be due to the diminishment in its performance during the transition from the mixture CO/H_2 to H_2. A pressure drop could have been provoked by the 4-way valve that was used to alternate these two gases. As Cell 5 is the last one to receive the fuel, it is possible that a lower flow of H_2 reached this cell, or even starvation occurred for a short period of time. This defect in the experiment is not reflected in the stack voltage presented in Figure 6.1 (a), emphasising the need for localised measurements for the optimization of the system. Another reason could be related to a higher degradation compared to the middle cells, in part due to the uneven distribution of the current density during the poisoning. Previous studies have reported a decrease in the current in the area closer to the anode inlet, and an increase in the area closer to the anode outlet in the presence of CO under galvanostatic control [93, 94]. And, local high current densities in a cell have been associated with higher irreversible degradation rates in the cathode side due to Pt dissolution and Pt band formation [291]. Cell 5 could be consequently more affected by the high operating current density in the cell than by the CO content reaching the area.

Table 6.1 Evolution of the stack and individual cell voltages during the galvanostatic operation (0.3 A cm^{-2}) with high purity H_2, in the presence of 100 ppm CO/H_2 and during the recovery with H_2.

Time of exposure	Cell 1	Cell 2	Cell 3	Cell 4	Cell 5	Stack
Operation with H_2						
N.A.	0.6666	0.6671	0.6424	0.6574	0.6745	3.3087
Exposure to 100 ppm CO/H_2						
10 min	0.5512	0.6556	0.6384	0.6572	0.6728	3.1734
20 min	0.2083	0.5701	0.632	0.6555	0.6701	2.74
30 min	0.1917	0.442	0.596	0.652	0.6706	2.5454
1 hr	0.1244	0.258	0.2949	0.5967	0.6715	1.9454
2 hrs	0.0902	0.2146	0.2554	0.3514	0.6249	1.5325
3 hrs	0.0557	0.1958	0.2495	0.3212	0.5782	1.3935
4 hrs	0.037	0.175	0.2279	0.3063	0.5537	1.3004
Recovery with H_2						
10 min	0.5431	0.5934	0.5682	0.6095	0.562	2.8723
30 min	0.6044	0.6437	0.623	0.6451	0.6103	3.1275
1 hr	0.6308	0.6548	0.6306	0.6496	0.6229	3.1868

Table 6.2 Evolution of the stack and individual cell voltages drop (%) compared with the operation with high purity H_2 under galvanostatic control (0.3 A cm^{-2}) in the presence of 100 ppm CO/H_2 and during the recovery with H_2.

Time of exposure	Cell 1	Cell 2	Cell 3	Cell 4	Cell 5	Stack
Exposure to 100 ppm CO/H_2						
10 min	17.3	1.7	0.6	0.0	0.3	4.1
20 min	68.8	14.5	1.6	0.3	0.7	17.2
30 min	71.2	33.7	7.2	0.8	0.6	23.1
1 hr	81.3	61.3	54.1	9.2	0.4	41.2
2 hrs	86.5	67.8	60.2	46.5	7.4	53.7
3 hrs	91.6	70.6	61.2	51.1	14.3	57.9
4 hrs	94.4	73.8	64.5	53.4	17.9	60.7
Recovery with H_2						
10 min	18.5	11.0	11.6	7.3	16.7	13.2
30 min	9.3	3.5	3.0	1.9	9.5	5.5
1 hr	5.4	1.8	1.8	1.2	7.7	3.7

Figure 6.2 (a) presents the evolution of the stack voltage and Figure 6.2 (b) of the individual cell voltages throughout the exposure to 200 ppm CO/H_2 during three hours. Similar behaviour is observed compared to the 100 ppm CO/H_2 case, as Cell 1 presented faster and more severe contamination, followed by Cell 2, Cell 3, Cell 4 and Cell 5. However, it is noticeable that the voltage decrease of each one of the cells is higher in the presence of 200 ppm CO/H_2 for three hours than with 100 ppm CO/H_2 during four hours. In Table 6.3 the stack and cell voltages during the operation with high purity H_2, in the presence of 200 ppm CO/H_2 and during the recovery with H_2 are presented. Table 6.4 shows the respective voltage drops compared to the initial operation with high purity H_2. After 10 minutes of exposure to 200 ppm $CO/H_{2,}$ the voltage decrease in Cells 1, 2, 3, 4 and 5 is 76, 18, 2, 0.9 and 0.7% respectively, and a stack voltage decrease of 19% compared to the initial operation with H_2. Compared to the 100 ppm CO/H_2 case, this voltage drop was attained after between 20 and 30 minutes of exposure. Moreover, after three hours of exposure to 200 ppm CO/H_2, the individual cell voltage drop was of 111, 82, 71, 59 and 51% for Cells 1, 2, 3, 4 and 5 respectively, and an overall decrease of 75%, which is 17% higher than in the case of 100 ppm CO/H_2 during the same period of time. The major difference is presented in Cell 5 that is explained by the increase in the concentration of CO entering the stack, which entails an increase in the concentration of CO reaching each one of the cells. As the first four cells are close to the saturation of CO in their surface, it is assumed that the difference in the concentration of CO reaching Cell 5 between the 100 and 200 ppm CO/H_2 is the largest. Considering Cell 5 is the less poisoned cell due to its location, it is consequently the cell most affected by this specific increase in the concentration of CO.

In Figure 6.2 (b) it is also observed that after approximately one hour of exposure, Cell 1 is reversed and the voltage continues to decrease until the mixture of 200 ppm CO/H_2 is switched to H_2. The reversal of Cell 1 occurs due to the increase of the anodic potential produced by the CO adsorption. The anode potential surpasses the cathode potential and the cell shifts into electrolytic operation. This operating mode causes several detrimental consequences, including the consumption of energy instead of the supply; the presence of H_2 and O_2 in the cathode and anode respectively provoking a potential change; and irreversible material damage, such as carbon corrosion and a subsequent ECSA loss [237]. However, the presence of O_2 in the anode provokes the chemical oxidation of the adsorbed CO. Considering the irreversible effects of this operating mode, mitigation strategies against CO poisoning should consequently consider not just the enhancement of the CO oxidation for a better performance of the cell, but also abate the pernicious effects of a possible reversal.

These techniques should be applied more intensively closer to the anode inlet where the poisoning is more severe.

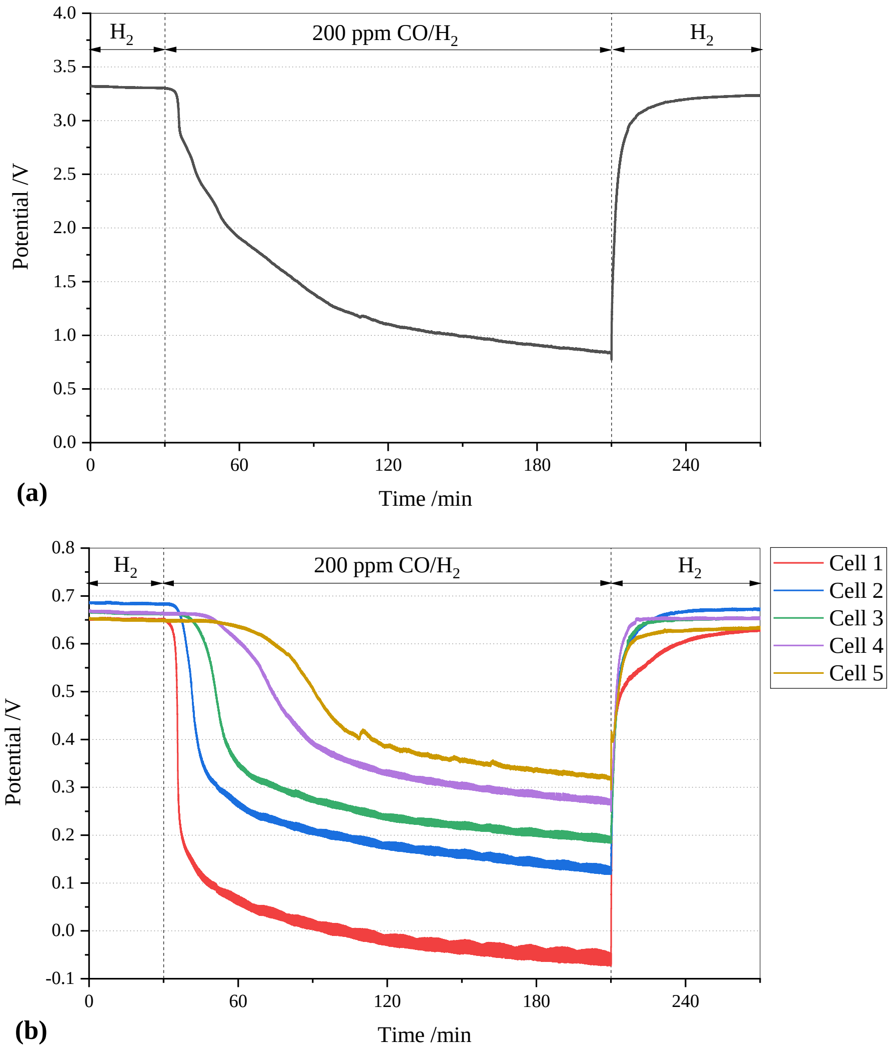

Figure 6.2 Evolution of (a) the stack voltage and (b) the five individual cell voltages during the galvanostatic operation (0.3 A cm^{-2}) with high purity H_2, in the presence of 200 ppm CO/H_2 and during the reinjection of high purity H_2.

The recovery of the cell with H_2 was also effective in the case of 200 ppm CO/H_2. After one hour the overall voltage loss compared to the initial operation with H_2 was 2.7%. Moreover, the trends observed in the case of 100 ppm CO/H_2 are also valid in this concentration, where Cells 1, 2, 3, 4, and 5 presented a voltage drop of 3.5, 1.5, 2.2, 1.7 and 2.9% respectively. It is conveyed that the recovery of the cells depends not just on the desorption of CO, where the cells with higher coverage of CO require more time to recover their performance. A full recovery of the cell also depends on the degradation provoked by the uneven distribution of the performance of the cell, which could be irreversible in some cases.

Table 6.3 Evolution of the stack and individual cell voltages during the galvanostatic operation (0.3 A cm^{-2}) with high purity H_2, in the presence of 200 ppm CO/H_2 and during the recovery with H_2.

Time of exposure	Cell 1	Cell 2	Cell 3	Cell 4	Cell 5	Stack
Operation with H_2						
N.A.	0.6504	0.6847	0.6671	0.6673	0.6513	3.3236
Exposure to 100 ppm CO/H_2						
10 min	0.1546	0.5642	0.6537	0.6611	0.6466	2.6859
20 min	0.1021	0.3079	0.5267	0.6489	0.6446	2.226
30 min	0.0553	0.2654	0.3528	0.6047	0.638	1.9076
1 hr	0.0094	0.2019	0.2703	0.391	0.508	1.3858
2 hrs	-0.0462	0.1533	0.218	0.3102	0.3544	0.99293
3 hrs	-0.0728	0.1206	0.1952	0.2737	0.3208	0.83301
Recovery with H_2						
10 min	0.5377	0.6251	0.6269	0.6469	0.608	3.0409
30 min	0.6033	0.6657	0.6493	0.6509	0.6293	3.1977
1 hr	0.6278	0.6742	0.6526	0.6558	0.6322	3.2333

Table 6.4 Evolution of the stack and individual cell voltages drop (%) compared with the operation with high purity H_2 under galvanostatic control (0.3 A cm^{-2}) in the presence of 200 ppm CO/H_2 and during the recovery with H_2.

Time of exposure	Cell 1	Cell 2	Cell 3	Cell 4	Cell 5	Stack
Exposure to 100 ppm CO/H_2						
10 min	76.2	17.6	2.0	0.9	0.7	19.2
20 min	84.3	55.0	21.0	2.8	1.0	33.0
30 min	91.5	61.2	47.1	9.4	2.0	42.6
1 hr	98.6	70.5	59.5	41.4	22.0	58.3
2 hrs	107.1	77.6	67.3	53.5	45.6	70.1
3 hrs	111.2	82.4	70.7	59.0	50.7	74.9
Recovery with H_2						
10 min	17.3	8.7	6.0	3.1	6.6	8.5
30 min	7.2	2.8	2.7	2.5	3.4	3.8
1 hr	3.5	1.5	2.2	1.7	2.9	2.7

6.2.2 Thermal imaging

The waste energy resulting from the operation of PEMFCs is predominantly dissipated in the form of thermal mechanisms [292]. The caption of thermal images in the planar structure of the stack allowed the measurement of the temperature distribution of the anode side during the contamination and the recovery of the system. The images obtained during the initial operation with H_2, the exposure to 100 ppm CO/H_2 at different stages of the contamination and the recovery with H_2 after 10 minutes and 1 hour are presented in Figure 6.3. During the operation with H_2 (Figure 6.3 (a)), the middle region that covers the Cells 2, 3 and 4, presents a higher temperature than the two extremes that correspond to Cells 1 and 5. Considering the counterflow configuration of the stack, it is assumed that this difference is due to a variation in the current density due to the depletion of H_2 in Cell 5 and of air in Cell 1. It is presumed that the middle region operates at a higher current density than the extremes, provoking an increase of the temperature in this region. This difference is enhanced by the feed of H_2 at ambient temperature entering Cell 1, and by the air coming into Cell 5. Both cold streams offset the heat generated by the losses that carry the operation of these cells. The gases heat as these pass through the stack.

When the 100 ppm CO/H_2 stream is injected in the stack, the major losses associated with the poisoning occur closer to the anode inlet, where the CO concentration is higher. The surface is more covered by CO and the occurrence of the HOR is hindered, provoking an increase in temperature (Figure 6.3 (b)-(g)). The losses in Cell 1 increase significantly, although the entrance of the CO/H_2 mixture at ambient temperature counteracts an abrupt increase of the temperature at the inlet of the cell. In the following cells, a rise in the temperature is observed, which increases with a higher exposure time to CO. Cell 5 presents the lowest temperature due to the lower adsorption of CO and to the volume of air entering the stack in this cell. It is important to mention that although an increase of the temperature is observed in the presence of CO, a decrease in the current occurs in the cells closer to the anode. In fact, the highest current density takes place in Cell 5. It is inferred that the losses due to CO are higher than the losses due to the operating current density.

Over the injection of H_2 for the recovery of the stack, presented in Figure 6.3 (h)-(i), redistribution of the temperature occurs. The temperature profile is similar to the one observed during the initial operation with H_2. It is assumed that the current distribution is also reconstructed, and the losses after 1 hr of recovery are mostly due to the losses associated with the operating current density.

The case of 200 ppm CO/H_2 is presented in Figure 6.4. Similar trends are observed compared to the 100 ppm CO/H_2 case, although the increase of the temperature in the presence of CO in each one of the cells is higher. This rise also occurs in a shorter period of time (3 hrs), and is not just due to the adsorption of CO, which is more intensive due to the higher content of CO that provokes a decrease in the voltage, but also to the presence of O_2 produced in Cell 1 that enters electrolytic mode, as the reaction between H_2 and O_2 is highly exothermic.

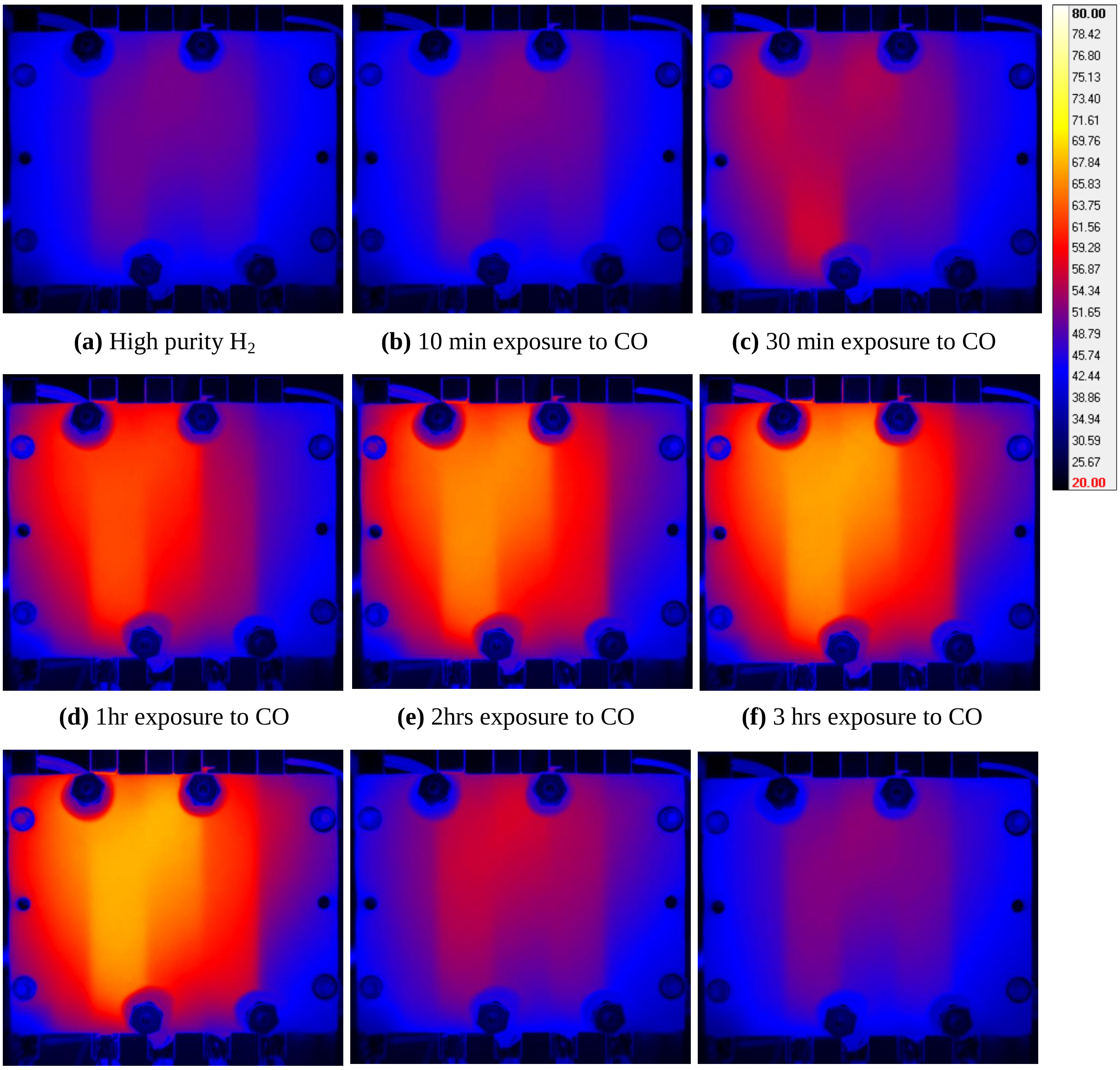

(a) High purity H_2 **(b)** 10 min exposure to CO **(c)** 30 min exposure to CO

(d) 1hr exposure to CO **(e)** 2hrs exposure to CO **(f)** 3 hrs exposure to CO

(g) 4hrs exposure to CO **(h)** 10 min recovery **(i)** 1 hr recovery

Figure 6.3 Temperature profiles over the operation at 0.3 A cm^{-2} with (a) high purity H_2, with 100 ppm CO/H_2 for (b) 10 min, (c) 30 min, (d) 1 hr, (e) 2 hrs, (f) 3 hrs and (g) 4 hrs, and with H_2 as recovery for (h) 10 min and (i) 1 hr.

It is important to mention in both cases the effect of an increase of the temperature in the poisoning by CO, as the adsorption of CO is favoured at lower temperature [70]. An increase in the temperature results in the diminishment of the CO coverage and the rise on the H_2 oxidation rate. Observing the increase in the temperature in the thermal images combined with the voltage losses in the system, it is possible to infer the CO coverage is still predominant over the H_2 oxidation in the cells closer to the anode inlet.

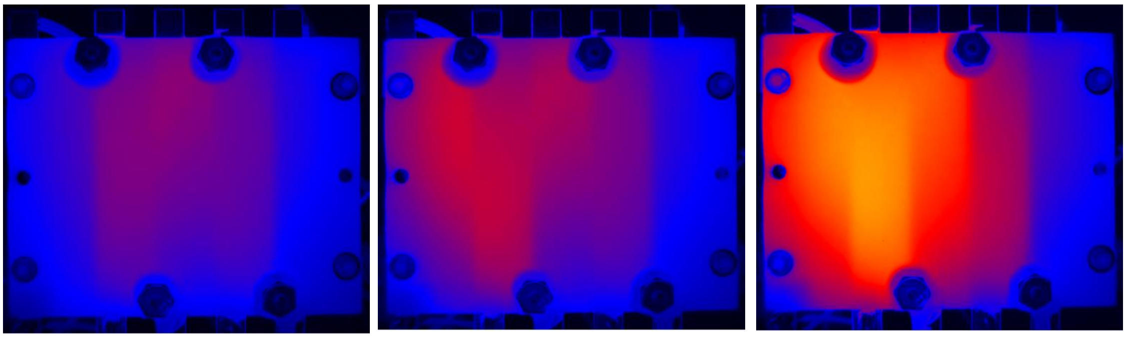

(a) High purity H_2 **(b)** 10 min exposure to CO **(c)** 30 min exposure to CO

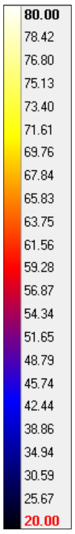

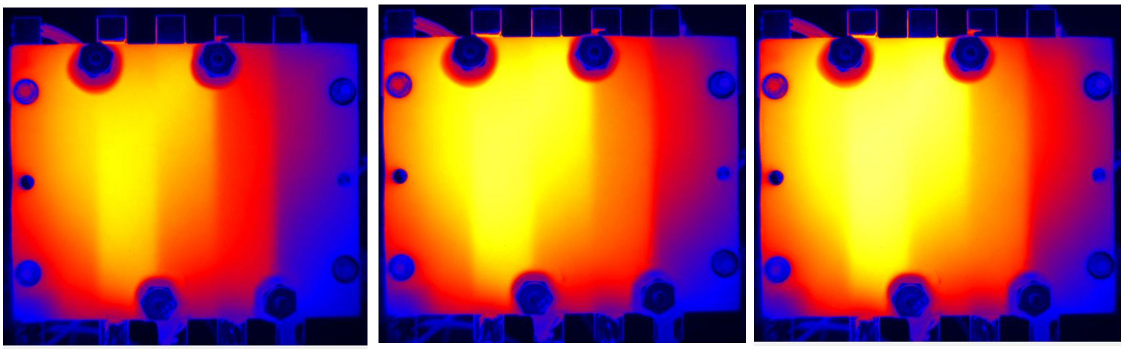

(d) 1hr exposure to CO **(e)** 2hrs exposure to CO **(f)** 3 hrs exposure to CO

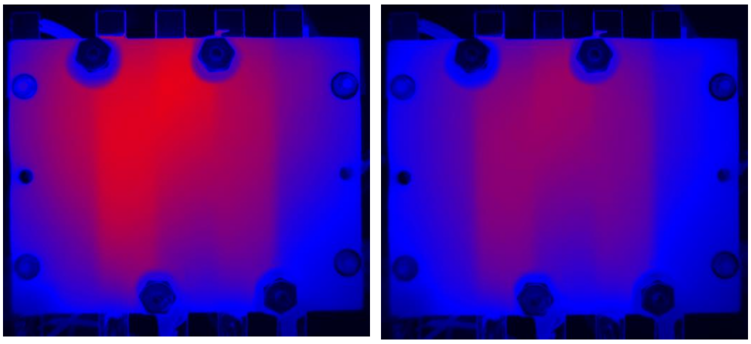

(g) 10 min recovery **(h)** 1 hr recovery

Figure 6.4 Temperature profiles over the operation at 0.3 A cm^{-2} with (a) high purity H_2, with 200 ppm CO/H_2 for (b) 10 min, (c) 30 min, (d) 1 hr, (e) 2 hrs and (f) 3 hrs, and with H_2 as recovery for (g) 10 min and (h) 1 hr.

Figure 6.5 presents the transient temperature in 15 points throughout the stack during the poisoning with 100 and 200 ppm CO/H_2, and the temperature difference ΔT between both cases for their comparison. The location of these points is illustrated in Figure 3.3 (Section 3.4.1). More information about the uneven distribution is obtained, as, besides the temperature gradient between the external cells and the middle region mentioned, additional gradients are observed within the cells.

It is observed that there is a temperature gradient between the bottom and the upper regions of the cells, which is attributed to a great extent to the counterflow configuration of the stack and to the ambient temperature at which the fuel in the anode and the air in the cathode are introduced. During the operation with H_2, prior to the injection of 100 ppm CO/H_2 (Figure 6.3 (a)), the temperature in the points 1 and 13, which are closer to the anode and cathode inlet respectively, are the lowest of the stack at 45 and 42°C respectively. Heat transfer between the proximities provokes the points situated in the bottom part in Cells 2, 3 and 4 are also low compared to the upper region with a temperature of 50, 47 and 47 °C respectively.

After 30 minutes of exposure, it occurs that the temperature is higher in the outlet region of Cell 1. It is assumed that this gradient is in part due to the temperature difference between the CO/H_2 mixture that counteracts the heat produced by the losses due to CO. The temperature of the stream increases as it passes through the cell, hence the temperature is higher in the outlet of the cell.

As the exposure time to CO increases, more CO is adsorbed in the surface, increasing the kinetic overpotential and provoking a rise in the temperature. Considering the disposition of the cells, where the outlet of Cells 1 and 3 are in the upper region of the stack, it is assumed that the heat generated in the outlet of these cells is dissipated to the proximities, i.e. inlet of Cells 2 and 4. Moreover, as the CO/H_2 mixture and the air enter at the bottom section of the stack, as shown, the increase in the temperature due to CO is counteracted by this cooling effect in the bottom section. The temperature gradients between the bottom and upper regions are consequently enlarged as the exposure time rises. After 4 hrs of exposure, the temperature gradients between the bottom and upper points in Cells 1, 2, 3, 4 and 5 are 6.9, 1.4, 7.2, 3.9 and 8.8 °C respectively. And, the highest temperatures, usually located in the upper region of the cells expect for Cell 2, are 64.2, 67.5, 67.6, 61.9 and 55.3°C. The increase of the temperature is minimal after 3 hrs and 4 hrs of exposure to 100 ppm CO/H_2, indicating the stack is in equilibrium.

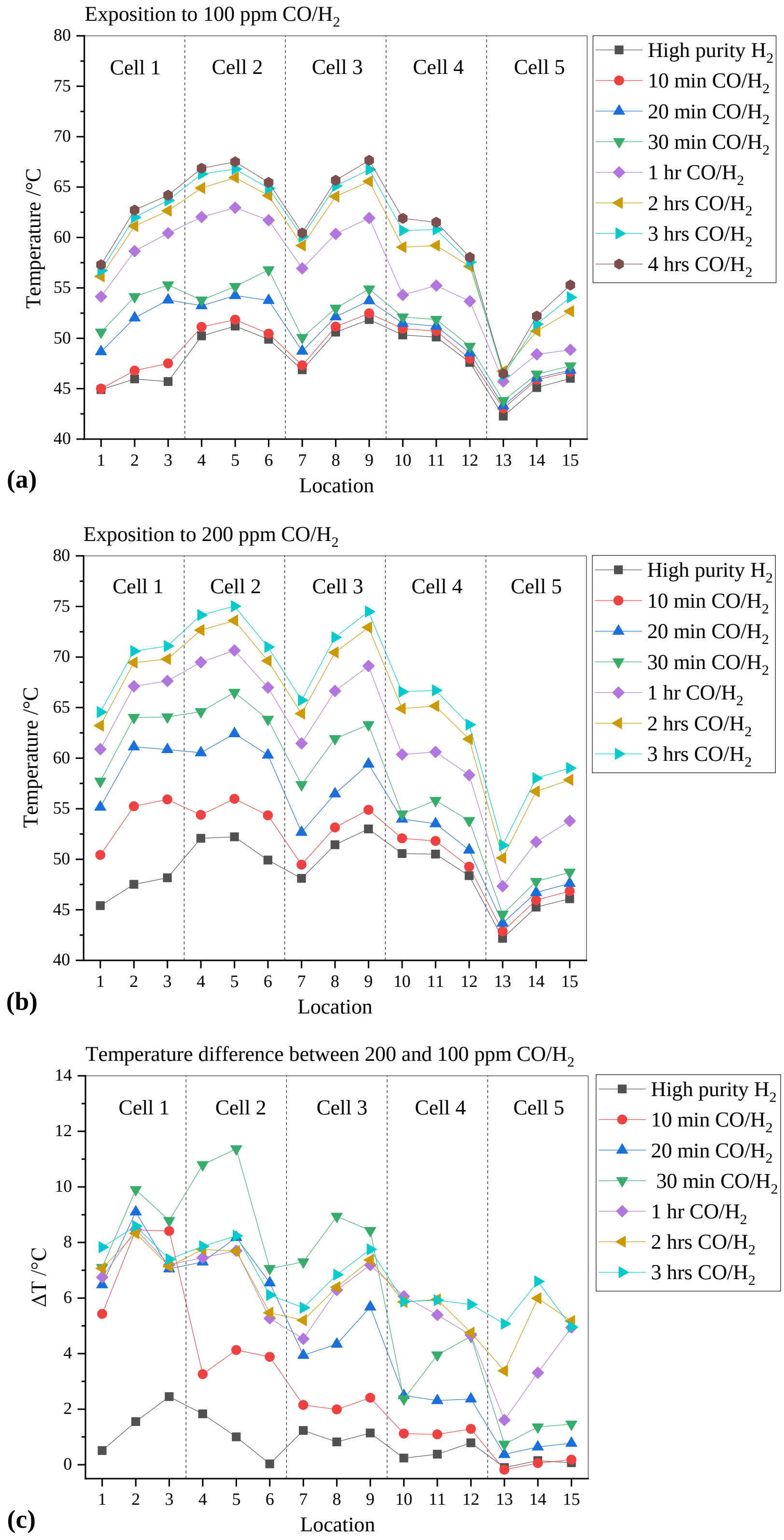

Figure 6.5 Evolution of the temperature in the different locations of the stack (see Figure 3.3) during the galvanostatic operation at 0.3 A cm^{-2} at different exposure times to (a) 100 ppm CO/H_2 and (b) 200 ppm CO/H_2. The temperature differences between 200 ppm CO/H_2 and 100 ppm CO/H_2 are presented in (c).

Similar behaviour is observed in the case of 200 ppm CO/H_2 presented in Figure 6.3 (b), although the overall temperature of the stack is higher than over the exposure to 100 ppm CO/H_2. After 3 hours of exposure to CO, the highest temperatures in Cells 1, 2, 3, 4 and 5 are 71.1, 74.2, 74.5, 66.7 and 59 °C respectively, and the temperature gradients between the bottom and the upper points are 6.5 °C in Cell 1, 3.2 °C in Cell 2, 8.8 °C in Cell 3, 3.3 in Cell 4 and 7.6 °C in Cell 5. In this case the highest gradient is not in Cell 5 due to a higher coverage of CO compared to the exposition to 100 ppm CO/H_2. It is important to mention that Cell 3 presents the highest gradient in both cases due to the combination of mechanisms occurring during the poisoning: the counterflow of CO/H_2 and air at ambient temperature that counteract the heat generated by the CO losses, and the heat transfer between the proximities.

In Figure 6.5 (c) the temperature differences $\varDelta$T due to the variance in the CO content is presented. Considering the higher temperatures presented during the exposure to 200 ppm CO/H_2, these were subtracted from the profiles obtained in the case of 100 ppm CO/H_2. Comparing the initial operation with H_2, it is observed that although the operating conditions are the same, higher temperatures are observed in the case of 200 ppm CO/H_2, which are due to a higher coverage of the catalyst by CO, and to the degradation of the stack occurring during the operation with 100 ppm CO/H_2, as it was the first experiment to take place. The major differences are observed in the first cells, where the poisoning of CO occurs first and is more severe.

Comparing the ΔT at the different times of exposure, it is seen that after 10 minutes of exposure the first cells present the highest ΔT, which is due to the more rapid and severe poisoning in this area. ΔT increases in the rest of the cells after 20 minutes and reaches a maximum in Cells 2 and 3 after 30 minutes of exposure. The stack reaches the equilibrium faster when it is exposed to 200 ppm CO/H_2 than to 100 ppm CO/H_2. As the stack reaches the equilibrium after the exposure to 100 ppm CO/H_2, ΔT is reduced. After one hour of exposure, there is no significant increase in ΔT in Cells 1, 2 and 3, as the poisoning has reached the equilibrium in these cells, which is in agreement with the individual cell voltage curves (Figure 6.1 and Figure 6.2). And, a $\varDelta T$ increase is observed in Cells 4 and 5 after 1 hr of exposure, as these cells are the last to be poisoned. In this graph, it is also seen that the overall temperature of the stack is higher in the presence of 200 ppm CO/H_2 than in the case of 100 ppm CO/H_2, and it is also observed that the major differences correspond to the cells closer to the anode inlet, where the poisoning is more severe.

Figure 6.6 presents the transient temperature in the same 15 points throughout the stack during the recovery from the exposure to 100 and 200 ppm CO/H_2, and the temperature difference ΔT between both cases. It is seen that decrease in the temperature due to the desorption of CO in the catalyst surface and the increase in the HOR is a fast process, as reflected by the individual cell voltage curves (Figure 6.1 and Figure 6.2). As for the comparison of both cases in Figure 6.6 (c), it is observed that after 30 minutes of recovery, the major ΔT is observed in Cell 1. Although this cell did not present the highest temperature during the poisoning, due to the severity of the poisoning, it is the cell that takes the longest period of time to recover. Additionally, the negative ΔT in Cell 5 indicates that the temperature in the recovery of 100 ppm CO/H_2 is higher than during the recovery from 200 ppm CO/H_2. It is assumed that this difference is due to the decrease in the performance of the cell during the transition from 100 ppm CO/H_2 to the H_2 stream. These losses are also reflected in the temperature profile of the stack, indicating thermal imaging could be used as a diagnostic tool.

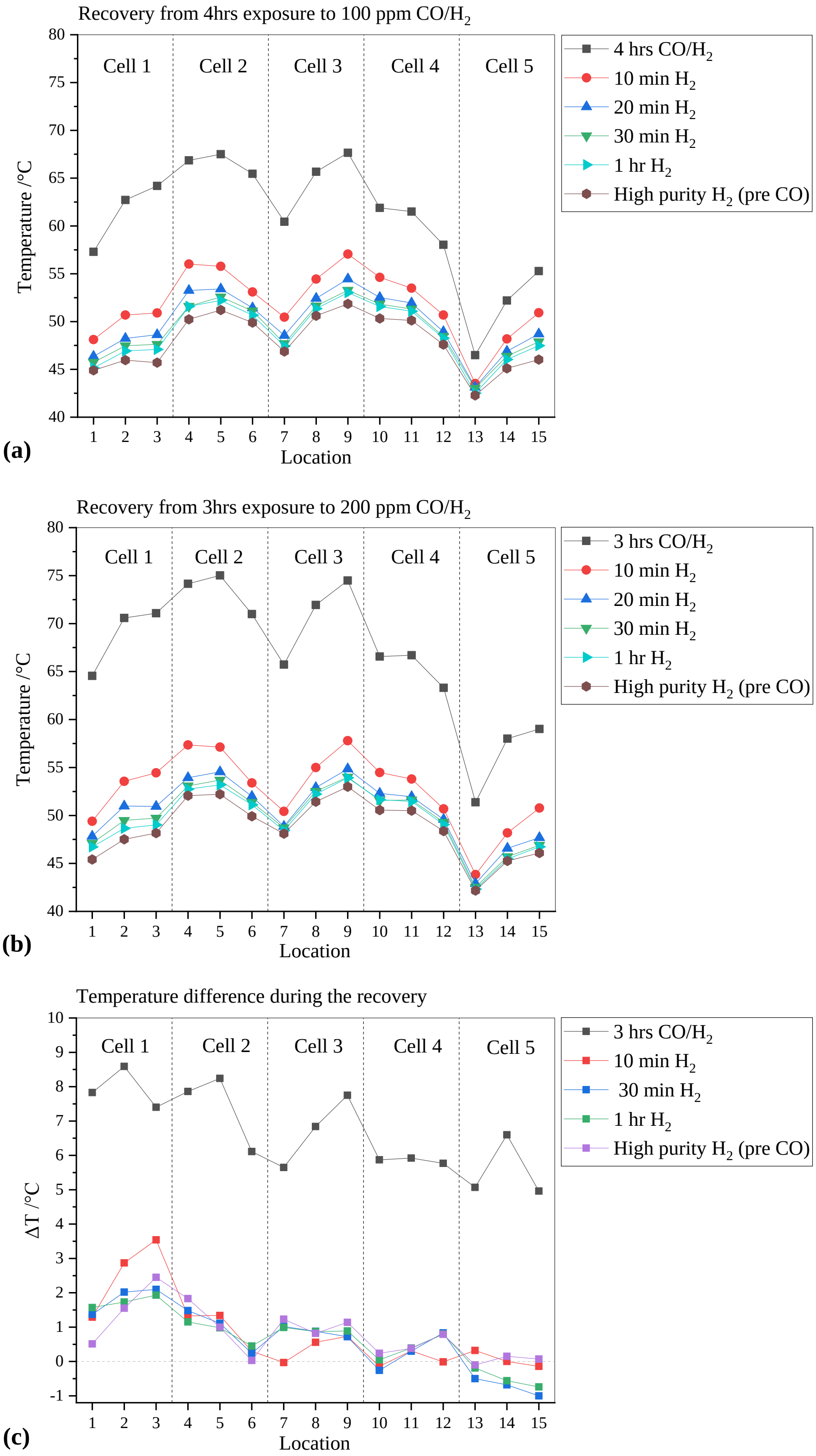

Recovery from 4hrs exposure to 100 ppm CO/H_2

Recovery from 3hrs exposure to 200 ppm CO/H_2

Temperature difference during the recovery

Figure 6.6 Evolution of the temperature in the different locations of the stack (see Figure 3.3) during the recovery with high purity H_2 after the exposure to (a) 4 hrs to 100 ppm CO/H_2 and (b) 3 hrs to 200 ppm CO/H_2 under galvanostatic control (0.3 A cm^{-2}). The temperature differences between 200 ppm CO/H_2 and 100 ppm CO/H_2 are presented in (c). Note in (c) that although ΔT after 3 hrs of exposure to 100 and 200 ppm CO/H_2 is shown, in the case of 100 ppm CO/H_2 the stack was exposed an extra hour to CO/H_2.

6.2.3 Current interrupt (ohmic impedance variation)

Another phenomenon occurring during the poisoning is the increase of the ohmic resistance during the exposure to CO. Figure 6.7 (a) presents the evolution of the ohmic resistance during the different phases of the experiment in the case of the exposure to 100 ppm CO/H_2, while Figure 6.7 (b) describes the case of 200 ppm CO/H_2. This increase is due to the water required for the electro-oxidation of CO, and on the other hand, due to the increase in the temperature of the system as illustrated in the thermal imaging analysis (Section 6.2.2). Both contribute to the dehydration of the membrane. The increase of the ohmic resistance exhibits a deeper impact of CO beyond the coverage of the catalyst on the anode side and is in agreement with previous studies that reported the decrease of protons reaching the cathode side, and the amount of water generated [24]. During the recovery, the production of water increases and the temperature of the stack decreases, contributing to the hydration of the membrane. It is noticeable in Figure 6.7 (a) that the ohmic resistance is affected by the sudden decrease in the performance of Cell 5 during the transition from the 100 ppm CO/H_2 mixture to the H_2 stream. The decrease of the ohmic resistance during the recovery is not complete during the hour of recovery, as is the case of 200 ppm CO/H_2.

In Table 6.5 the measurements of the ohmic resistance at different times of exposure to CO/H_2 and during the recovery with H_2 are presented. It is possible to compare the effects of a different concentration of CO in the dehydration of the membrane. While a concentration of 100 ppm CO/H_2 provoked an increase in the ohmic resistance of 21.5 % after four hours of exposure, 200 ppm CO/H_2 caused a rise of 46.5% after three hours of operation in the presence of CO. The dehydration of the membrane and its effects and consequently intensified when there is an increase in the content of CO. The potential negative effects of the dehydration of the membrane include power loss, membrane thinning, delamination, and the formation of holes and voids in some cases, which provokes the direct mixing of hydrogen and oxygen [293, 294].

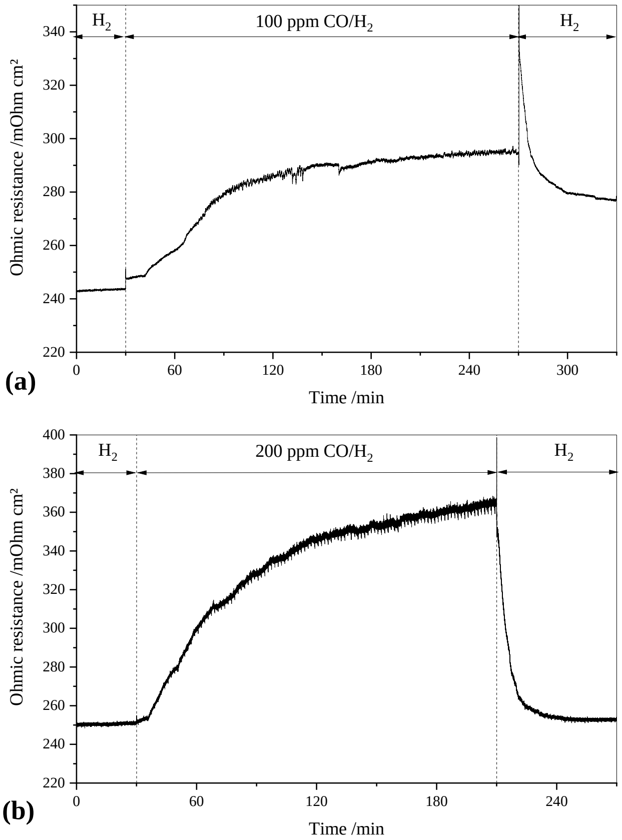

Figure 6.7 Variation of the ohmic resistance in the presence of (a) 100 ppm CO/H_2 and (b) 200 ppm CO/H_2 under galvanostatic control (0.3 A cm^{-2}).

Table 6.5 Evolution of the ohmic resistance during the galvanostatic operation (0.3 A cm^{-2}) with high purity H_2, in the presence of 100 and 200 ppm CO/H_2 and during the recovery with H_2.

Time of exposure	**100 ppm CO/H_2**		**200 ppm CO/H_2**	
	Ohmic resistance (mOhm cm^2)	**Increase (%)**	**Ohmic resistance (mOhm cm^2)**	**Increase (%)**
Operation with H_2				
N.A.	242.65	N.A.	250.31	N.A.
Exposure to CO/H_2				
10 min	248.45	2.4	262.2	4.8
20 min	254.05	4.7	278.84	11.4
30 min	257.77	6.2	299.26	19.6
1 hr	279.19	15.1	328.44	31.2
2 hrs	290.11	19.6	351.34	40.4
3 hrs	292.91	20.7	366.65	46.5
4 hrs	294.85	21.5	N.A.	N.A.
Recovery with H_2				
10 min	290.1	19.6	268.2	7.1
30 min	279.61	15.2	253.76	1.4
1 hr	277.89	14.5	252.64	0.9

6.2.4 Mass spectrometry

Evaluating the effects of the CO poisoning in the increase of the temperature and the dehydration of the membrane, the exposition to 200 ppm CO/H_2 during three hours was repeated five times in order to obtain measurements of the composition of the gases in the anode outlet of each one of the cells. It is important to mention that the system in the presence of CO is perturbed easily, and the norms of reproducibility are not standard. Phenomena that need to take into consideration from one test to the other are the degradation of the catalyst layer and the membrane, the presence of self-sustained potential oscillations, among others. For these reasons, a mass balance was not considered. Moreover, it was only possible to measure the concentration of gases in the outlet of Cells 1, 2, 3 and 4. However, additional phenomena occurring throughout the stack are elucidated.

Figure 6.8 (a) shows the variation of the concentration of CO. During the operation with zero grade H_2, the presence of a low ppm of CO is observed. The origin of CO in this case comes from the production of H_2 from fossil fuels (e.g. stream reforming of methane). When the 200 ppm CO/H_2 mixture is introduced into the system, the CO is adsorbed on the catalyst surface of Cell 1, increasing until it reaches an equilibrium surface composition. Not all is CO is adsorbed and passes to Cell 2, where the content of CO is also reduced due to the adsorption of the contaminant in this cell. The CO concentration in Cell 1 is consequently higher than in Cell 2, and this trend continues throughout the stack, as the CO concentration in Cell 3 is lower than in Cell 2, but higher than in Cell 4.

The electro-oxidation of CO is confirmed by the measurements of CO_2 obtained (Figure 6.8 (b)), as there is a significant difference between the concentration of CO_2 over the operation with zero grade H_2 and in the presence of 200 ppm CO/H_2. The amount of CO_2 increases as the active surface of the catalyst increases. For this reason, in the outlet of Cell 1, the lowest concentration of CO_2 is observed, and Cell 4 presents the highest with over 400 ppm CO_2. It is important to mention that in addition to the CO_2 produced by the CO oxidation, some CO_2 is expelled as a result of the carbon oxidation occurring during the electrolytic mode in Cell 1. These processes are well-identified in the literature [237, 295].

The variations in the concentration of O_2 and Ar were also observed and presented in Figure 6.8 (c) and (d) respectively. The effects of the membrane dehydration are observed as the crossover of gases coming from the cathode increases over the injection of CO/H_2 in the anode side. The crossover increases with an increase in the area covered, consequently Cell 1 presents the lowest and Cell 4 presents the highest crossover. In Cell 4, the concentration of O_2 reaches around 800 ppm and around 0.35% of Ar during the steady-state. This assumption is reinforced by previous studies where the crossover is attributed to a temperature increase, which entails an increase in the crossover of H_2 [296] and O_2 [297] in polytetrafluoroethylene (PTFE)-reinforced composite membranes, which were used in this study. These membranes are composed of expanded PTFE porous sheet and a perfluorinated ionomer [298]. The same trend is observed in the case of perfluorosulfonic acid (PFSA) membranes (Nafion), which are more commonly used. The permeability of O_2 and H_2 rises with an increase of the temperature, and of the relative humidity [299, 300]. In general, PTFE-reinforced composite membranes present a lower crossover of species than PFSA membranes due to the incorporation of PTFE which increases the gas tortuosity [296].

The crossover of gases affects the operation of the cells in the short and long term. The most significant effects are fuel inefficiency, the degradation of the membrane due to the formation of peroxide and hydroperoxide radicals over the mixture of H_2 and O_2; mixed potentials at the electrodes, and the starvation of the cells in some cases [23]. Additional effects should be considered in the presence of CO. For instance, an increasing O_2 crossover implies the chemical oxidation of adsorbed CO on the anode side, known as internal air bleed [183]. Wang *et al.* suggested the increase of the cathode backpressure to increase the internal air bleed and apply it as a mitigation strategy against CO poisoning [183]. Another effect is the CO crossover to the cathode side and the subsequent adsorption of CO in the catalyst sites of this electrode. The contamination of the cathode by the injection of CO in the anode fuel has been proved by the simultaneous effects on both of the electrode potentials [91, 92], the loss of the active area on both of the electrodes over a long term exposure to CO [96], and an increase of both electrodes contributions over the measurement of the electrochemical impedance spectroscopy in the presence of CO [93, 94].

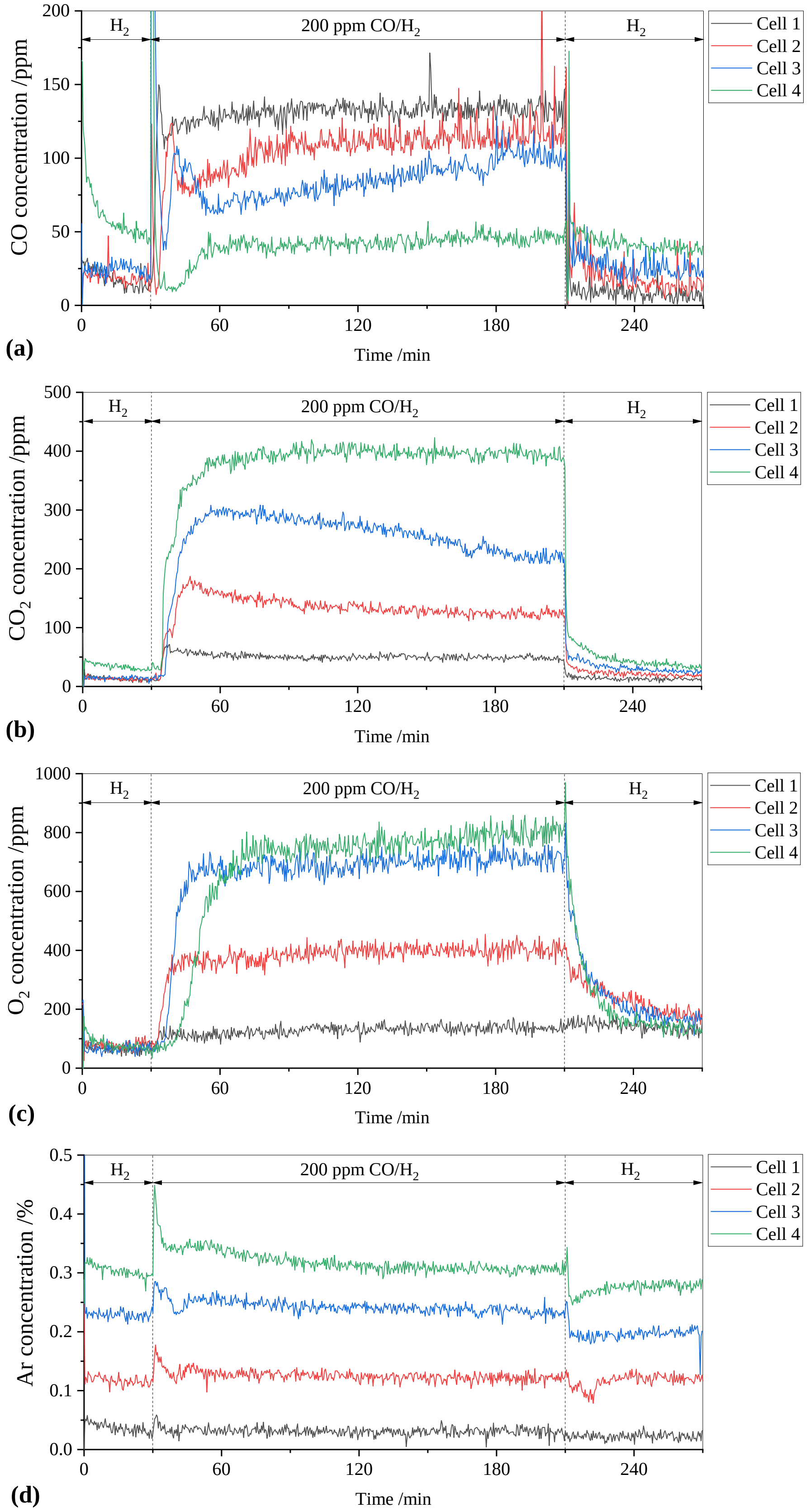

Figure 6.8 Variation of the concentration of (a) CO, (b) CO_2, (c) O_2 and (d) Ar in the outlet of cells 1, 2, 3 and 4 of the stack, during the operation with pure H_2 and in the presence of 200 ppm CO/H_2 under galvanostatic control (0.3 A cm^{-2}).

6.3 Conclusions

The effects of 100 and 200 ppm CO/H_2 were evaluated in a segmented-in-series PEMFC operating under galvanostatic control (0.3 A cm^{-2}). The configuration of the system allowed the study of the distribution of the contamination by tracking the individual cell voltages, the estimation of the variations of the temperature due to the presence of CO through thermal imaging, and the measurement of the concentration of gases (CO, CO_2, O_2 and Ar) in the outlet of the cells through mass spectrometry. The information obtained provided an insight into different mechanisms occurring during the poisoning and unveils the effects of CO in different components of the cell.

The poisoning occurred more rapidly in the cells closer to the anode inlet than to the outlet due to the difference in CO concentration. The region closer to the inlet was also more severely affected by the presence of CO. Moreover, an increase in the concentration of CO entering the stack entailed a decrease in the stack voltage and the individual cell voltages. A higher CO content also increases the risk of a localised reversal. As for the recovery, this process proved to be fast compared to the poisoning by CO, irrespective of the concentration of CO entering the stack.

Uneven distribution of the temperature is observed during the operation of the stack with H_2 due to different processes taking place simultaneously, such as the variation in the current density which is higher in the middle region, the entrance of gases in counterflow, and heat transfer between the proximities. The presence of CO entailed an increase in the waste energy (as heat) that was reflected by an increase in the overall temperature of the stack that raised with the exposure time to CO until the steady-state is reached. Although Cell 1 presented the highest voltage decrease, the increase in the temperature was counteracted by the ambient temperature of the fuel. The highest temperature increases were observed in the upper region of Cells 2 and 3. Temperature gradients were also observed between the upper and the bottom region. Moreover, although an increase of the temperature is observed in the presence of CO, a decrease in the current occurs in the cells closer to the anode, and an increase occurs in the cells closer to the anode outlet.

The temperature increase combined with the consumption of water by the CO oxidation provoked the increase in the ohmic resistance, exhibiting the dehydration of the membrane and a reduction in the transfer of protons to the cathode during the poisoning. An increase in the CO entering the stack entailed an increase in the ohmic resistance.

Finally, through mass spectrometry, it was shown that the CO content decreases towards the anode outlet. The oxidation of CO was also confirmed by the measurement of the concentration of CO_2 in the outlet of each one of the cells. The content of CO_2 increased towards the end of the stack (anode outlet), as more catalyst area was covered. Additionally, the increase in the temperature contributed to an increase in the crossover of gases from the cathode to the anode (O_2 and Ar in this case) which resulted in the reduction of the performance of the stack in the short term despite the presence of O_2, which enhances the oxidation of CO (internal air bleed). The concentration of O_2 and Ar increased towards the anode outlet as more surface membrane was covered, although the highest crossover rate should occur closer to the anode inlet, where the CO poisoning and the highest increase in the temperature are seen. It is presumed that an increase to the crossover of CO and H_2 to the cathode occurs simultaneously, contaminating the catalyst area of this electrode.

More studies are needed to determine the irreversible degradation in the cells due to the side effects of the operation in the presence of CO. The cell reversal, the degradation of the cathode in the regions operating at a higher current density, and the membrane dehydration are phenomena with recognised irreversible degradation in the materials of the cells.

Chapter 7

Pulsed Oxidation of CO by Short-Circuiting

7.1 Introduction

Short-circuiting during the operation of the cells has been recognized as an effective strategy to improve the performance of the cells. A recurrent explanation is the improvement of the humidification and conductivity of the membrane by a higher water production [301, 302] and a higher flow of air in the cathode due to an increase in the temperature and evaporation of the water [303]. An alternative theory is the elimination of oxide layers formed in the cathode side as intermediates of the oxygen reduction reaction (ORR), such as H_2O_2, that constitute contaminants and limit the current density at a given potential [304, 305]. Although the mechanisms responsible for the performance enhancement are not clear, short-circuiting controllers have been developed for the application in hybrid systems for unmanned aerial vehicles [301] and uninterrupted power supply (UPS) systems [303]. Others have been successfully commercialised by Ballard and Horizon fuel cell [304]. Recent studies on the operation with short-circuiting include the development of a strategy to optimise the application of the shorts at different current densities by Gupta *et al.* [304] and the control of the humidification of the fuel cell through shorts and the quantification of the respective increase in the hydrogen consumption by Kim *et al.* [301].

The current pulsing technique and the negative potential pulses presented in sections 2.3.3.10.1 and 2.3.3.10.2 respectively have been proposed against CO poisoning in PEMFC, and constitute two techniques similar to short-circuiting in their application. The short-circuiting implies the electrical contact between the two electrodes, while in the current pulsing technique the pulses are applied under a controlled current range, adjusted according to the MEA in use. The negative voltage pulses refer to the operation of the cell in electrolytic mode. The application of the pulses in the three techniques is done for short periods (milliseconds) so the cell operates mostly in the hydrogen oxidation potential rather than in the CO oxidation region.

In this chapter, two similar segmented-in-series systems described in Section 3.4 were used to evaluate the efficacy of the short-circuiting as a mitigation strategy against CO poisoning, using Pt as the catalyst. As shown in Chapter 5, each one of the cells or segments of a stack is affected differently by the poisoning by CO, hence the need of a mitigation strategy attending the variations in the distribution of the poisoning.

7.2 Results and discussion

7.2.1 Simultaneous shorting in a segmented-in-series system

In the first experiment, one of the stacks was operated with H_2 for 15 minutes. All the cells were then shorted simultaneously for 15 minutes at a frequency of 1 Hz and a short length of 100 ms. The H_2 stream was switched to 200 ppm CO/H_2 for 3 hours while the shorts continued. A recovery phase with H_2 followed for 15 minutes. Considering the segmented-in-series stack can be considered a segmented cell conformed of five segments, it is possible to observe the effects of the shorting in the five different segments of a cell.

Figure 7.1 presents a comparison of the voltage evolution of the stack and all the individual cells during the operation with H_2, with and without shorting, and in the presence of 200 ppm CO/H_2, once the system reached a steady state. Due to the variations of the voltage when the shorting is applied, a one-second moving average voltage was included when H_2 and 200 ppm CO/H_2 were used as fuel. This measure allowed the graphical comparison of the voltage of the cells and the stack with and without shorting.

Comparing the performance of the stack and the cells measured through the evolution of the voltage, it is observed that shorting during the operation with H_2 is beneficial for the increase of the voltage in between shorts, which is in agreement with the literature. The increment of voltage in between shorts compared to the voltage using H_2 is presented in Figure 7.2 (a). The voltage increase is of 4.5, 5.0, 4.2, 3.7 and 2.1% for Cells 1, 2, 3, 4 and 5 respectively. The major increment is observed in cell 2, and decreases towards the outlets of hydrogen (Cell 5) and oxygen (Cell 1).

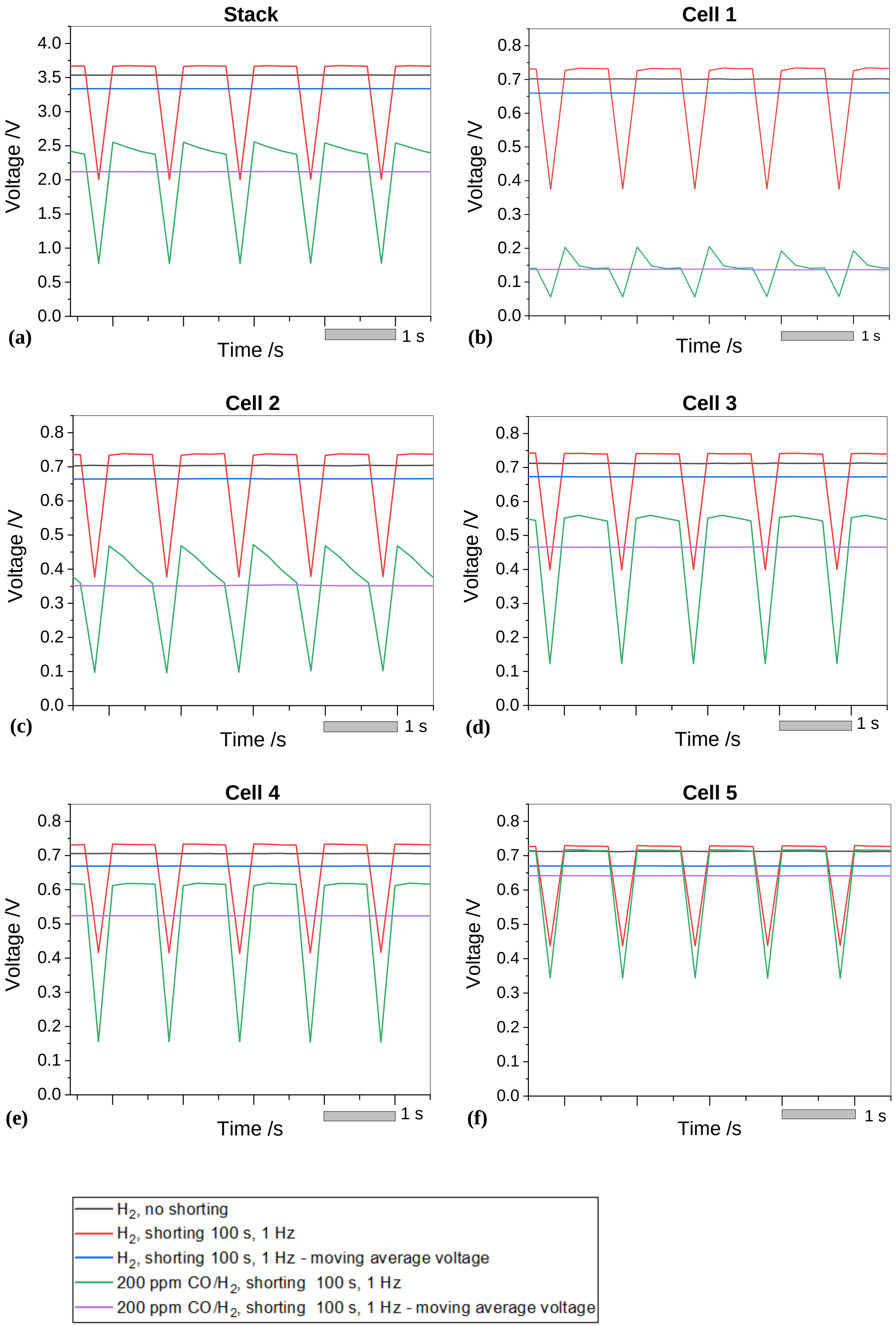

Figure 7.1 Evolution of the stack and individual cell voltages over time during the operation with pure H_2 and in the presence of 200 ppm CO/H_2 (steady-state), in the absence and the application of short-circuiting: (a) the stack, (b) Cell 1, (c) Cell 2, (d) Cell 3, (e) Cell 4 and (f) Cell 5. The shorting was applied simultaneously in all cells using a short length of 100 ms at a frequency of 0.1 Hz.

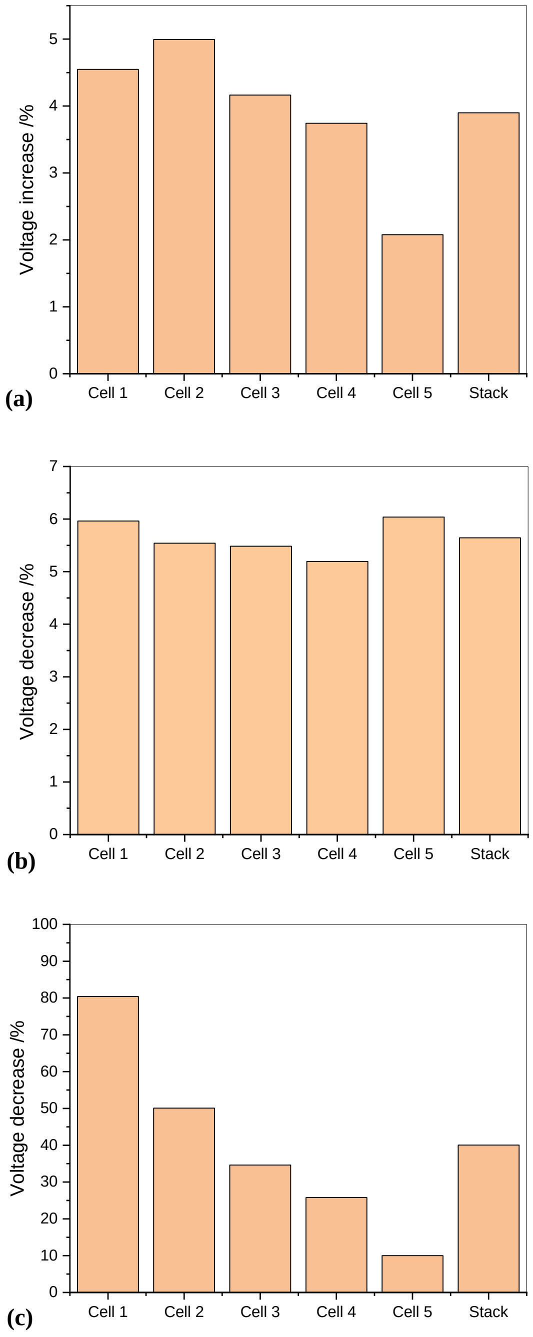

Figure 7.2 Voltage changes compared to the operation with H_2 without the application of shorting, (a) Voltage increase in between shorts during the operation with H_2; (b) Voltage decrease compared with the moving average voltage during the operation with H_2, and (c) voltage decrease compared with the moving average voltage during the operation with 200 ppm CO/H_2 at steady state. The shorting was applied simultaneously in all cells using a short length of 100 ms at a frequency of 0.1 Hz.

More studies are needed in order to examine the trend observed in Figure 7.2 (a) as different phenomena occur simultaneously; however, some hypothesis can be drawn in terms of the water production during the shorting. It is known that a counter-flow configuration results in higher humidification of the centre of the stack when hydrogen and air (or oxygen) are partially humidified [282]. In this study, it is assumed that the centre and the cells towards the cathode outlet (Cell 1) present higher humidification due to the injection of dry hydrogen. In these cells, water is also present on the anode due to back diffusion from the cathode. During the shorting, the current of the cells is increased and the production of water is intensified through electro-osmosis. The water contributes to higher conductivity of the membrane and to an increase in the performance, evidenced by a higher voltage. The increase in the humidification is dependent on the location of the cell, where the cells that presented higher humidification without shorting are also more humidified when the shorting is applied. The humidification gradient between the centre and the anode outlet is hence enlarged when the shorting takes place, and is reflected in the uneven increase of the cell voltages. The contribution of the removal of the oxide layers formed on the cathode catalyst during the shorting also needs to be evaluated; however, there is limited information about the conditions that enhance or inhibit their formation, and about the distribution of their accumulation in a cell.

Although the voltage of the cells in between the shorts is higher than under the normal operation with H_2, when the moving average voltage in the presence of shorts is compared with the initial operation with H_2 without shorts, it is observed that the moving average is lower, as shown in Figure 7.2 (b). The overall decrease is of 5.6%. The application of shorts at a frequency of 1 Hz is at the origin of this decrease, underlying the importance of the optimization of the length and the frequency for the improvement of the performance of the stack and the cells. Gupta *et al*. determined that both the optimal duration and the frequency of the shorts are both dependent on the operating conditions, contrary to the actual commercial controllers that impose invariable shorts of typical length and frequency of 100 ms and 0.1 Hz respectively [304].

The voltages curves in the presence of 200 ppm CO/H_2 in Figure 7.1 were captured after exposure of two hours. It is observed that despite the continuous shorting of the cells, these are affected by the presence of CO. Cell 1, located closer to the inlet, is the most affected by the higher concentration of CO, followed by Cell 2, 3, 4 and 5. Observing the evolution of the voltage of Cell 1 during the application of shorts in Figure 7.1 (b), an immediate increase in the voltage of the cells is present. As it occurs in the current pulsing technique (Section 2.3.3.10.1), during the short the cell is operated in the region where CO oxidation is favoured and the H_2 oxidation activity is reduced. The CO coverage is momentarily reduced, evidenced by the increase of the cell voltage. During this short period, the CO oxidation is also enhanced by the water production, due to the stronger presence of –OH species. After the cell voltage has reached a maximum, it decreases until it reaches a stable voltage due to the continuous flow of CO in the stack. In Cell 2 (Figure 7.1 (c)), due to the high frequency of the shorts it is not possible to observe the total decrease of the cell voltage after the peak.

In the rest of the cells, the peak is not present; however, it is presumed that the performance in-between shorts is higher than in their absence of shorts due to the lower concentration of CO entering the cells compared to Cells 1 and 2, the increase in the water production and the operation in the CO oxidation region. The combination of these factors causes the voltage of Cell 5 (Figure 7.1 (f)) in between shorts equals the voltage over the operation with H_2 in the absence of shorts. In the presence of 200 ppm CO/H_2 and the application of simultaneous shorts of 100 ms and 1 Hz, only Cell 5 is shown to be tolerant to CO.

The decrease in voltage (moving average voltage) compared to the voltage resultant from the operation with H_2 without shorting is presented in Figure 7.2 (c). The individual voltage reductions are of 80.4, 50.1, 34.6, 25.8 and 10% for Cells 1, 2, 3, 4 and 5 respectively, and the stack voltage decrease corresponds to 40.0%. The shorting under these conditions is consequently not effective for the mitigation of the poisoning by CO. Considering the uneven distribution of the poisoning, the length and the frequency of the shorts need to be evaluated for possible use of the shorting as a mitigation strategy.

7.2.2 Evaluation of the short length and frequency

The uneven distribution of CO poisoning in the stack entails the study of the short-circuiting in individual cells. For that purpose in a second experiment, a new stack was exposed to 100 ppm CO/H_2, and the effects of the length of the pulse and the frequency of the shorts were evaluated in the performance of the individual cells and the stack.

7.2.2.1 Short length variation

Table 7.1 presents the average voltage of the five individual cells during the operation of the stack under galvanostatic control (0.3 A cm^{-2}) with high purity H_2 and in the presence of 100 ppm CO/H_2 after one hour of exposure. The highest decrease in the cell voltage due to CO is presented in Cell 1, followed by Cells 2, 3, 4 and 5. This variation is due to the decreasing concentration of CO entering the cells, where the highest concentration enters Cell 1. These results are in agreement with the study presented in Chapter 6, and are taken as a reference for the analysis of the behaviour of the cells during the application of the short-circuiting.

Table 7.1 Voltage drop in the individual cells of a PEMFC stack after one hour of exposure to 100 ppm CO/H_2.

	Cell 1	**Cell 2**	**Cell 3**	**Cell 4**	**Cell 5**
H_2					
Average voltage (V)	0.6951	0.6955	0.7042	0.6743	0.6658
100 ppm CO/H_2					
Average voltage (V)	0.0492	0.1221	0.2631	0.4040	0.4745
Drop compared with H_2 (%)	92.9	82.5	62.6	40.1	28.7

Figure 7.3 presents the evolution of the individual cell voltages of Cells 1 to 4 in the presence of 100 ppm CO/H_2 after one hour of exposure, and the effects of different lengths of shorts. The frequency of the shorts in all cases is of 0.2 Hz. Comparing the evolution of the voltage in this experiment with the results presented in the previous section (Section 7.2.1), a peak after the application of the short is observed for all the short lengths in all the cells. The peaks are more prominent due to the lowest concentration of CO entering the stack. Table 7.2 presents the characteristics of these peaks according to the cell and the length of the short.

It is observed that for Cell 1, where the concentration of CO entering the cell is the highest, the variation of the length of shorts does not have a significant impact in the voltage increase in the peak. For shorts of 200, 500 and 1000 ms, the voltage drop compared with the behaviour with H_2 passes momentarily from 92.9% to 83.5, 81.3 and 82.3% respectively. Moreover, this increase is brief as the decrease from the peak voltage to the average voltage without shorting lasts between 0.6 and 0.8 s. The application of shorts is not a viable option to increase the CO tolerance of this cell.

The application of shorts is more efficient in the subsequent cells, where it was observed that as the short length is increased, the tolerance of the cells is also increased for a longer period due to higher removal of CO adsorbed. For instance, in Cell 2 a short of 200 ms provoked a momentary increase in the CO tolerance from 82.5% to 54.8% and a decreased time of 2.2 s, while a short of 1000 ms entailed an increase of the tolerance to 42.7% and a decreased time of 2.8 s. The maximum tolerance observed from Cells 1-4 is observed in Cell 4 when a short of 500 ms is applied, where a maximum tolerance of 30.5% is met. However, the decrease time from the voltage peak is difficult to quantify as it is suspected it is higher than the period in-between shorts. For this reason, the curves for the different short lengths are not completely overlapped. Although the tolerance of the cells increases with an increase of the short length, it is still insufficient for the continuous operation of the cells and the stack. For this reason, the frequency of the shorts needs to be evaluated and define whether the shorting is effective enough to be considered a mitigation strategy against CO poisoning.

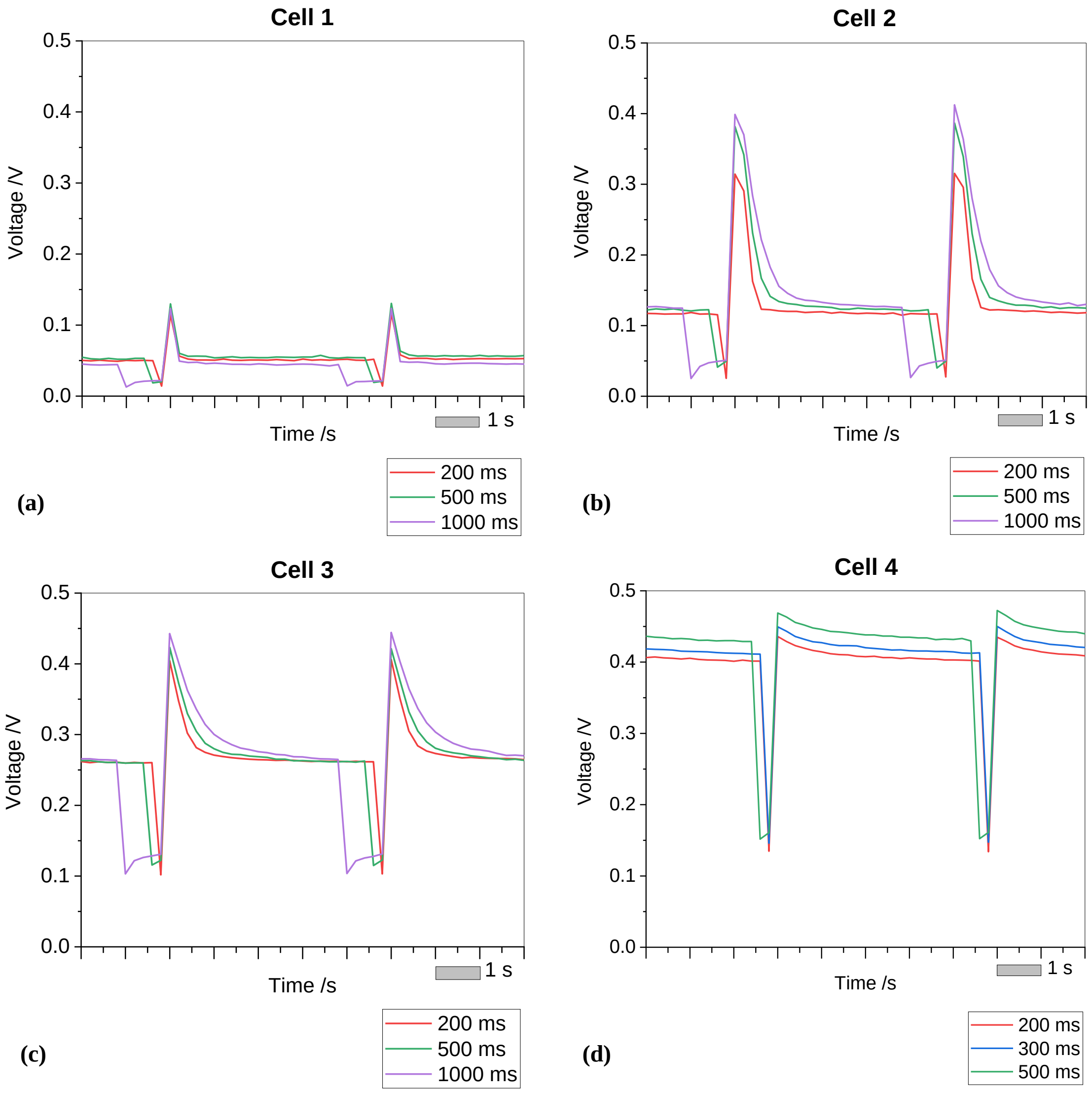

Figure 7.3 Effect of different lengths of shorts in the voltage of the individual cells of a stack exposed to 100 ppm CO/H_2 under galvanostatic control at 0.3 A cm^{-2}. (a) Cell 1, (b) Cell 2, (c) Cell 3 and (c) Cell 4.

Table 7.2 Characteristics of the peaks observed after the application of different short lengths in the cells of a PEMFC stack operating under galvanostatic control (0.3 A cm^{-2}) and after one hour of exposure to 100 ppm CO/H_2.

		Cell 1			**Cell 2**	
Short length (ms)	200	500	1000	200	500	1000
Peak after short (V)	0.1147	0.1298	0.1234	0.3145	0.3818	0.3989
Drop compared to H_2 (%)	83.5	81.3	82.3	54.8	45.1	42.7
Decrease time (s)	0.6	0.6	0.8	2.2	2.4	2.8
		Cell 3			**Cell 4**	
Short length (ms)	200	500	1000	200	300	500
Peak after short (V)	0.4044	0.4230	0.4427	0.4359	0.4495	0.4688
Drop compared to H_2 (%)	42.6	39.9	37.1	35.3	33.3	30.5
Decrease time (s)	3.0	3.2	3.4	>4.5	>4.5	>4.5

7.2.2.2 Variation of the shorts frequency

Figure 7.4 presents the voltage evolution for three different short frequencies for Cells 1, 2 and 3, and for two frequencies for Cell 5. The measurements were taken after approximately two hours of exposure to 100 ppm CO/H_2. Along with the voltage evolution, the one-second moving average voltage is graphed for a better comparison in between the different cases.

In the case of Cell 1 (Figure 7.4 (a)), the evolution of voltage during the application of 100 ms shorts at frequencies of 1, 2 and 3 Hz, is observed. At 1 Hz it is shown how the shorts provoke an increase in the cell voltage that promptly decreases and reaches a stable value before another short is applied. For 2 and 3 Hz, the shorts are applied before the mentioned steady state is reached. It is shown that for this degree of contamination, an increase in the frequency does not contribute to a rise in the average cell voltage due to the loss in power that the shorts entail. This is observed by comparing the one-second moving average in the three cases, as no significant rise is observed when the frequency of the shorts is increased.

Frequencies of 1, 2 and 3 Hz were similarly evaluated in Cell 2 using 100 ms shorts. As in Cell 1, at 1 Hz a steady state is reached after an increase of the voltage is observed. And, for the cases of 2 and 3 Hz the shorts were applied before the stable state is reached. The difference observed between the shorts at 2 and 3 Hz is the maximum voltage reached immediately after the shorts, where a higher value is reached when a frequency of 3 Hz is studied. It is inferred that at 3 Hz the high frequency of the shorts prevents the surface to be covered by the same amount of CO than for the cases of 1 and 2 Hz. In combination with a lower concentration of CO entering the cell compared to Cell 1, the surface is less saturated by CO and a higher voltage peak is reached. However, comparing the one-second moving average it is observed that the voltage loss that occurs at high frequencies impede to see a considerable increase in the performance of the cell.

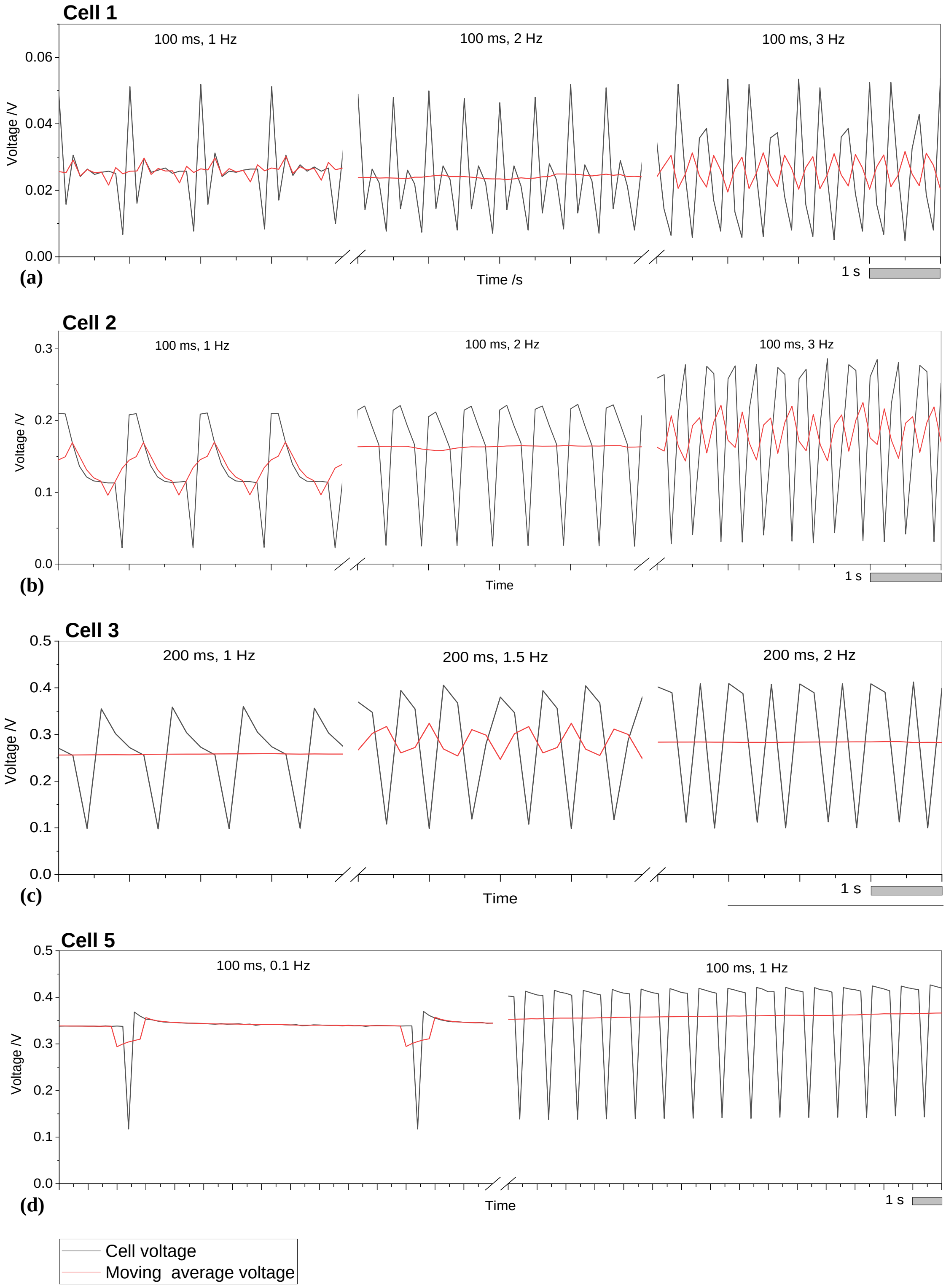

Figure 7.4 Effect of the frequency of the short-circuiting in the individual voltages of a stack exposed to 100 ppm CO/H_2 under galvanostatic control al 0.3 A cm^{-2}. (a) Cell 1, (b) Cell 2, (c) Cell 3 and (d) Cell 5.

The inefficiency of short-circuiting as a mitigation strategy against CO poisoning for the operating conditions of the stack was similarly confirmed in Cells 3 and 5, as the one-second moving average maintained the same values despite the increase of the frequency of the shorts. It is possibly the case that the concentration of CO used in this study is extremely high, and that other operating conditions such as temperature, humidity and current density have an effect of the degree of poisoning of the cells. Additionally, when compared to the current pulsing technique reported in the literature, most of the studies used PtRu as catalyst on the anode side.

7.3 Conclusions

Short-circuiting, which is extensively used for the improvement of the performance of PEMFC, was evaluated as a possible mitigation strategy against CO poisoning. The possibility of applying different short lengths at varying frequencies to the individual cells of a stack is of special interest due to the uneven distribution of the poisoning.

During the operation with high purity H_2, it was found that the shorts contributed to an increase in the voltage of the cells and the stack, as mentioned in the literature. The increase in the water production was pointed as the main cause for this improvement. Moreover, shorting simultaneously all the cells strengthened the uneven distribution of water production that provoked an irregular increase of the voltage in the cells. However, more information about the formation of oxide layers on the cathode side and their distribution is needed, as their removal through short-circuiting has also been pointed as a possible mechanism that contributes to the increase of the performance of the cells.

In the presence of CO, short-circuiting demonstrated a limited capability to act against the poisoning of concentrations of 100 ppm CO/H_2 or higher. Although increasing the short length provoked a higher removal of CO for a longer period of time, this approach was ineffective under these conditions. The same occurred when the frequency was varied, as the voltage losses that the shorts imply countered the gains obtained through the surface cleaning at high frequencies. However, due to the temporary operation in the CO oxidation potential and the increase of the water produced during the application of the short, it is hypothesised that the shorting contributes to an increase in the CO tolerance in the presence of lower concentrations of CO.

The inefficiency of short-circuiting as a mitigation strategy in this study could also be related to different operating parameters that need to be evaluated. Conditions of temperature, humidity and current density, for instance, have been identified to have a direct impact on the poisoning of the cells (Chapter 2). Varying these conditions in conjunction with short-circuiting should provide more information about the applicability of short-circuiting for the increase of the CO tolerance in PEMFC.

Chapter 8

Conclusions and Future Work

8.1 Conclusions

CO poisoning is an important area of research in PEM fuel cells, as their performance and durability are affected by it. A review of the mechanisms of poisoning as well as the effects on the performance of the cells was presented. In addition, the different mitigation strategies developed so far were introduced. A better understanding of the poisoning mechanisms is needed in order to develop more effective mitigation strategies. More efficient systems would make fuel cells more competitive. In this research, CO poisoning was experimentally examined. The studies presented focused on understanding the short-time effects of the poisoning of PEMFC by CO throughout the extent of a cell and throughout a larger industrial system. And, short-circuiting was evaluated as a possible mitigation strategy against this contaminant.

In previous research, a localised reference electrode was used in a HT-PEMFC in order to monitor the evolution of CO poisoning. Only one reference electrode was used and the measurements were done on the cathode side [24]. In this work, an array of localised reference electrodes was used to measure directly in the anode, the evolution of the overpotential in three different locations of a cell exposed to CO. An increase in the anodic overpotential was related to the rise of the coverage of CO that provoked the decrease in the cell voltage. These measurements contributed to depicting the uneven coverage by CO throughout the cell during the first minutes of the contamination until the cell reached a pseudo-steady state. It was found that the area closer to the anode inlet was covered by CO more rapidly and more severely than the rest of the cell. It was likewise possible to analyse the appearance of self-sustained oscillations, characteristic of the galvanostatic control in the presence of CO. The sustained potential oscillations were experimentally observed in three different points of the MEA for the first time. The information provided contributed to confirm predictions made by the model presented by Hanke-Rauschenbach *et al.* about the formation of different patterns during the self-sustained potential oscillations [62]. Moreover, it was possible to observe through the measurement of the concentration of CO_2 in the anode outlet, the variations in the CO oxidation rate. The distribution of the CO coverage and the characteristics of the oscillations were related to the varying concentration of CO throughout the cell and to the local conditions that enhanced or inhibited the oxidation of CO. The recovery of the cell with pure H_2 was also evaluated where the anodic overpotential in the distinct locations followed an exponential decay.

The study presented in Chapter 6 considered a larger system of five cells connected in series. The total area of the stack, typical of industrial applications, allowed the visualization of operating conditions closer to reality. Furthermore, the configuration of the system allowed the simultaneous use of distinct diagnostic tools. It was possible to measure the individual voltages of the cells and the effects in the following cells; to observe through thermal imaging the distribution of the waste energy dissipated in form of thermal mechanisms due to the presence of CO; to determine the variations of the ohmic resistance through current interrupt and, through the repetition of the experiment, to measure the concentration of gases in the anode outlet of each one of the cells. Also, due to the disposition of the cells in series, each cell can be considered a segment of a larger cell. Thermal imaging of the stack itself can be considered a diagnostic technique to evaluate the distribution of the poisoning.

The combined use of diagnostic techniques allowed the confirmation and elucidation of various mechanisms occurring during the CO poisoning from different perspectives. The more rapid and severe contamination in the area closer to the anode inlet shown in the single-cell experiment (Chapter 5) was confirmed in this study. Furthermore, the contamination of the cathode by CO had already been documented in the literature [93, 94]; however, this study showed the effects of CO in the local temperature, which increases and provokes a rise in the ohmic resistance. The crossover of species from the cathode to the anode and from the anode to the cathode increases, exacerbating the contamination of the cathode. These effects were observed under the operation of two distinct concentrations of CO, being able to confirm the more severe degradation of the performance when the concentration is increased.

The configurations of the single-cell setup in Chapter 5 and of the stack of five cells in series presented in Chapter 6 present fundamental differences, which are detailed in Chapter 3. Despite these divergences, the results highlight the utility and the need for new diagnostic techniques to elucidate the phenomena occurring throughout the cell in the presence of CO. The experiments carried out in both systems allowed the study of the CO poisoning taking account of spatial and temporal variations, and revealed the importance of studying the distribution of the poisoning in conjunction with local conditions for the design of more effective mitigation strategies. For example, a higher charge of CO tolerant catalyst can be applied to the area closer to the anode inlet, where the poisoning tends to be more severe.

Current pulsing and the application negative potential pulses have been presented as mitigation strategies against CO poisoning. In this work, short-circuiting was evaluated as a possible alternative. It was confirmed that short-circuiting enhances the performance of the cells when operating with H_2 as reported in the literature, most likely due to the increase of water production, although the production of oxide layers in the cathode side needs to be evaluated. When the cells were shorted simultaneously during the operation with H_2, the uneven distribution of water production was exacerbated provoking an irregular increase in the voltage cells. In the presence of CO, the mitigation of the pernicious effects of CO proved to be limited. Under the conditions evaluated in this study, the concentrations of 100 and 200 ppm CO/H_2 were too high, although the last cell proved to have a higher tolerance due to the lower concentration of CO reaching the cell. The variation of the short-length and the frequency were varied according to the location of the cell in the stack, which is one of the advantages of this technique, as the distribution of the poisoning is taking in consideration. However, no significant improvement in the performance was observed. Next studies should consider the evaluation of different operating conditions to determine if short-circuiting contributed to improving the tolerance of the cells. The temporary operation in the CO oxidation potential and the increase in production of water are indicative that this technique could be effective in the presence of lower concentrations of CO.

8.2 Future Work

The reach of the studies presented in this work is limited and lead to further work that could deepen our understanding of the mechanisms occurring during the CO poisoning in PEMFC systems, and to improve or develop new mitigation strategies against its pernicious effects.

The use of the localised reference electrodes was limited to the measurement of the anodic overpotential under galvanostatic control in the presence of CO. Future work should evaluate the poisoning under different conditions. For example, different flows and current densities where different patterns of self-sustained potential oscillations have been reported could be observed. More information about the oscillations could be disseminated from the measurements in the different locations in the MEA. Moreover, even though the operation of fuel cells under galvanostatic control is common, the potentiostatic operation is not exempt from use, in conditioning processes for example. It would be important to know the effects of CO in the cell under this type of operation. In the literature, both galvanostatic and potentiostatic control have been observed; however, no spatial information about the anodic overpotential has been reported under potentiostatic operation.

Additional studies using the reference electrodes would be to also monitor throughout the MEA the operating parameters that have a direct impact on the contamination, such as temperature and humidity. For example, the study presented in this work infers the humidity increases towards the end of the anode taking into consideration the partial counter-flow configuration of the cell. If the humidity is measured, this assumption could be confirmed and more importantly, quantified. The information could contribute to optimizing the design of the cell or the MEA. For instance, the area closer to the anode could be elaborated with a higher catalyst charge as it is expected this area is more severely contaminated. The array of localised reference electrodes could also be used to monitor the efficiency of these adjustments.

In the literature and this work, the adverse effects of CO have been reported in the anode, but also in the cathode and the membrane. The localised reference electrodes setup could be adapted for its use in the cathode side and evaluate the effects in this electrode of CO entering in the anode side. Different operating conditions could be examined, such as galvanostatic and potentiostatic controls, flows, temperature, humidity, among others.

In the case of the stacks, one of the main limitations is the measurement of the concentration of gases, as the experiment was repeated five times to obtain the measurement of each one of the cells. Repeating the experiment leads to uncertainty when the data is compared, as some degradation is prone to occur, in particular in the catalyst and the membrane. Future experiments should consider the simultaneous measurement of the concentration of the gases in all the cells. The data would contribute to accurately quantify the adsorption and oxidation of CO per cell.

As in the case of the localised reference electrodes, different operating conditions could be studied through the stacks. The occurrence of self-sustained potential oscillations, the potentiostatic control, a varying concentration of CO and fluctuating flows are among the parameters to be studied. Additionally, a different configuration of the stack would be useful. For example, an open-cathode stack would allow observing more clearly the phenomena occurring in the anode side. As the temperature and humidity variations existent in a closed-cathode configuration would not be present in the open-cathode case, the overall temperature distribution would be principally attributed to the dynamics occurring in the anode.

Thermal imaging was used in this study to determine the areas where waste energy due to the presence of CO is reflected by an increase in temperature. The use of this technique opens the possibility of integrating and optimizing a combined heat and power (CHP) system, taking into account the resultant distribution of the temperature. Moreover, thermal imaging could be used as a diagnostic tool of the contamination when combined with complementary techniques. It would be possible to optimize the operation of the cells and to develop and validate more accurate models.

The study of short-circuiting also requires further study. The characterisation techniques used in the segmented-in-series system confirmed the variability of the operating conditions in the cells according to their location in the stack during the operation with high purity H_2 and in the presence of CO. Temperature, current density, membrane humidification and CO content, for example, vary throughout the stack and constitute parameters to be taken into account for the optimization of the technique. Future work should determine the range of concentration of CO and the possible shorting patterns (short length and frequency) at which each one of the cells would present a sufficient tolerance to the contamination, without significant losses in the performance that the application of the shorts imply. Knowing these data would allow a direct comparison of this technique with the rest of the existent mitigation strategies, in particular with the current pulsing technique, which is similarly applied.

As the mitigation strategies developed against CO poisoning evolve, it is commonly observed the simultaneous use of several mitigation strategies. The combination of several techniques allows an increase of the overall CO tolerance. For instance, most of the studies reported on current pulsing have been carried out with MEAs containing PtRu as anode catalyst, reaching a tolerance of up to 3% CO/H_2 [239]. New studies on stacks should also consider the spatial and temporal variations for the incorporation of various mitigation strategies in one system. For instance, as in the case of the current pulsing technique, it is possible to apply the short-circuiting in combination with CO tolerant electro-catalysts. Considering the more rapid and severe contamination in the cell closer to the anode inlet, the design of the MEA could be prepared with a higher CO tolerant catalyst charge in this cell, while gradually reducing the amount of catalyst towards the outlet of the stack, where the cells are exposed to a lower content of CO. The higher content of CO tolerant electro-catalysts in the first cells could contribute to decrease the frequency of the short-circuiting, avoiding the performance loss and degradation of the cells that the shorts entail. It is consequently possible to decrease the consumption of valuable materials that impact the costs of fuel cells, avoid the rapid degradation of the MEA materials provoked by the short-circuiting, while increasing the CO tolerance of the stack.

Another plausible combination of mitigation strategies in the segmented-in-series system would be the use of the triode operation and the application of short-circuiting. While the triode operation could be used in the cell closer to the anode combined with the short-circuiting, the CO poisoning in the rest of the cells could be mitigated purely by short-circuiting. The triode cell could have the function of a scavenger cell. While the triode operation entails the use of less expensive materials, and the short-circuiting patterns could be adapted to each cell, there are other considerations to take into account that could affect negatively the performance of the cells in the short and long term, such as the corrosion mode at which the triode is operated and the degradation of the catalysts by the continuous shorts. It is important to evaluate the advantages and disadvantages of each mitigation strategy and determine the most appropriate combination for the fuel cell system in place.

Although the short-circuiting has been proved to be effective for the improvement of the performance of the cells during the operation with H_2 and under certain conditions in the presence of CO, the mechanisms involved are not fully understood. More information is needed about the formation of oxide layers that take part in the ORR mechanism, and the distribution of their accumulation in the cathode side. A deeper understanding of this phenomenon would contribute to the evaluation of the removal of these species through short-circuiting during the operation with H_2 and in the presence of CO. Moreover, understanding the effects of the water formation in the formation of oxide layers would also contribute to the optimization of the technique and the improvement of the performance of the cells.

Finally, although CO constitutes one of the most pernicious contaminants affecting the operation of PEMFCs, a variety of impurities are also present in hydrogen depending on the nature of the production process. For instance, the reformate obtained from steam reforming and partial oxidation or autothermal reforming, contains H_2, CO, CO_2, inert gases and sulphur contaminants [29]. Consequently, it is of great interest to understand the mechanisms occurring when a mixture of contaminants is introduced into a PEMFC system, as the operation is more representative of real situations. The two setups presented in this work, the array of localised reference electrodes and the segmented-in-series system would be useful to understand the phenomena occurring. And, the use of short-circuiting could also be examined to determine the efficacy to remove certain mixtures.

References

[1] EIA. International Energy Outlook 2016. In: USDOE, editor. Washington2016.

[2] IEA. Scenarios and Projections, https://www.iea.org/publications/scenariosandprojections; . 2016 [accessed 16.08.08].

[3] Besancon BM, Hasanov V, Imbault-Lastapis R, Benesch R, Barrio M, Mølnvik MJ. Hydrogen quality from decarbonized fossil fuels to fuel cells. International Journal of Hydrogen Energy. 2009;34:2350-60.

[4] Abdulkareem AS, Afolabi AS, Fungura N, Mokrani T, Mateescu C. The Realities and Economic Benefit of the Utilization of Fuel Cells as an Alternative Source of Energy: A Review. Energy Sources, Part B: Economics, Planning, and Policy. 2015;10:404-11.

[5] O'Hayre R, Cha S-W, Colella W, Prinz FB. Fuel Cell Fundamentals. Third Edition ed. New Jersey: John Wiley & Sons; 2016.

[6] FuelCellToday. Fuel Cell Electric Vehicles: The Road Ahead. Royston2013.

[7] USDOE. Types of Fuel Cells, http://energy.gov/eere/fuelcells/types-fuel-cells; . USDOE; 2020 [accessed 16.08.08].

[8] Hart D, Lewis J, Lehner F, Klippenstein M. The Fuel Cell Industry Review. E4tech; 2017.

[9] USDOE. Fuel Cells, http://energy.gov/eere/fuelcells/fuel-cells;. 2020 [accessed 20.08.10].

[10] USDOE. Fuel Cells. The Fuel Cell Technologies Office Multi-Year Research, Development, and Demonstration Plan: USDOE; 2016. p. 3.4-1 -3.4-32.

[11] Papadias DD, Ahmed S, Kumar R, Joseck F. Hydrogen quality for fuel cell vehicles – A modeling study of the sensitivity of impurity content in hydrogen to the process variables in the SMR–PSA pathway. International Journal of Hydrogen Energy. 2009;34:6021-35.

[12] BSI. ISO 14687-3 Hydrogen fuel. Product specification. Proton exchange membrane (PEM) fuel cell applications for stationary appliances. Switzerland: BSI Standards Limited; 2014.

[13] BSI. ISO 14687-2 Hydrogen fuel. Product specification. Proton exchange membrane (PEM) fuel cell applications for road vehicles. Switzerland: BSI Standards Institution; 2012.

[14] Sharaf OZ, Orhan MF. An overview of fuel cell technology: Fundamentals and applications. Renewable and Sustainable Energy Reviews. 2014;32:810-53.

[15] Pachauri RK, Chauhan YK. A study, analysis and power management schemes for fuel cells. Renewable and Sustainable Energy Reviews. 2015;43:1301-19.

[16] USDOE. Comparison of Fuel Cell Technologies, https://www.energy.gov/eere/fuelcells/comparison-fuel-cell-technologies; . In: Office FCT, editor.2020 [accessed 20.03.03].

[17] IEA. Energy Technology Perspective. Mobilising Innovation to Accelerate Climate Action. Paris2015.

[18] Spiegel C. PEM Fuel Cell Modeling and Simulation Using MATLAB. Elsevier; 2008.

[19] Li X. Principles of Fuel Cells. New York: Taylor & Francis; 2006.

[20] Eckstein L, Gnörich B. Design Criteria and Components for Fuel Cell Powertrains. Fuel Cell Science and Engineering: Wiley-VCH Verlag GmbH & Co. KGaA; 2012. p. 1045-73.

[21] Pu H. Introduction. Polymers for PEM Fuel Cells: John Wiley & Sons, Inc.; 2014. p. 1-49.

[22] Agaesse T. Simulations of one and two-phase flows in porous microstructures, from tomographic images of gas diffusion layers of proton exchange membrane fuel cells [PhD Thesis]. Toulouse: Université de Toulouse; 2016.

[23] Wang H, Yuan XZ, Li H. PEM Fuel Cell Diagnostic Tools: Taylor & Francis; 2011.

[24] Kaserer S, Rakousky C, Melke J, Roth C. Design of a reference electrode for high-temperature PEM fuel cells. J Appl Electrochem. 2013;43:1069-78.

[25] Mench MM. Fuel cell engines. Hoboken, N.J.: Hoboken, N.J. : John Wiley & Sons; 2008.

[26] USDRIVE. Fuel Cell Technical Team Roadmap. In: Energy USDo, editor. http://cms.doe.gov/eere/vehicles/downloads/us-drive-fuel-cell-technical-team-roadmap: U.S. Drive; 2013.

[27] Basile A, Dalena F, Tong J, Veziroğlu TN. Hydrogen Production, Separation and Purification for Energy. Institution of Engineering and Technology; 2017.

[28] Liu K, Song C, Subramani V. Hydrogen and syngas production and purification technologies. Hoboken, New Jersey: AIChE and John Wiley & Sons, Inc.; 2010.

[29] Cheng X, Shi Z, Glass N, Zhang L, Zhang J, Song D, et al. A review of PEM hydrogen fuel cell contamination: Impacts, mechanisms, and mitigation. Journal of Power Sources. 2007;165:739-56.

[30] Snytnikov PV, Zyryanova MM, Sobyanin VA. CO-Cleanup of Hydrogen-Rich Stream for LT PEM FC Feeding: Catalysts and Their Performance in Selective CO Methanation. Top Catal. 2016;59:1394-412.

[31] Lakshmanan B, Huang W, Weidner JW. Electrochemical Filtering of CO from Fuel-Cell Reformate. Electrochemical and Solid-State Letters. 2002;5:A267-A70.

[32] Nenoff TM, Spontak RJ, Aberg CM. Membranes for hydrogen purification: An important step toward a hydrogen-based economy. MRS Bull. 2006;31:735-41.

[33] Balasubramanian S, Weidner JW. Analysis of an Electrochemical Filter for Removing Carbon Monoxide from Reformate Hydrogen. Journal of The Electrochemical Society. 2015;162:E231-E6.

[34] Ha JW, Hyuck Jang J, Hyoung Gil J, Kim SH. The fabrication and performance of a poly(dimethylsiloxane) (PDMS)-based microreformer for application to electronics. International Journal of Hydrogen Energy. 2008;33:2059-63.

[35] Godula-Jopek A. Introduction. Hydrogen Production: Wiley-VCH Verlag GmbH & Co. KGaA; 2015. p. 1-32.

[36] Tafel J. The polarisation of cathodic hydrogen development. Zeitschrift Fur Physikalische Chemie-Stochiometrie Und Verwandtschaftslehre. 1905;50:641-712.

[37] Heyrovsky J. A theory of overpotential. Recueil Des Travaux Chimiques Des Pays-Bas. 1927;46:582-5.

[38] Erdey-Gruz T, Volmer M. The theory of hydrogen high tension. Z Phys Chem A-Chem Thermodyn Kinet Elektrochem Eigenschlehre. 1930;150:203-13.

[39] Kucernak AR, Zalitis C. General Models for the Electrochemical Hydrogen Oxidation and Hydrogen Evolution Reactions: Theoretical Derivation and Experimental Results under Near Mass-Transport Free Conditions. The Journal of Physical Chemistry C. 2016;120:10721-45.

[40] Vogel W, Lundquist L, Ross P, Stonehart P. Reaction pathways and poisons—II: The rate controlling step for electrochemical oxidation of hydrogen on Pt in acid and poisoning of the reaction by CO. Electrochimica Acta. 1975;20:79-93.

[41] Ye S, Kondo T, Hoshi N, Inukai J, Yoshimoto S, Osawa M, et al. Recent Progress in Electrochemical Surface Science with Atomic and Molecular Levels. Electrochemistry. 2009;77:2-20.

[42] Marković NM, Grgur BN, Ross PN. Temperature-dependent hydrogen electrochemistry on platinum low-index single-crystal surfaces in acid solutions. Journal of Physical Chemistry B. 1997;101:5405-13.

[43] Marković NM, Ross PN. Surface science studies of model fuel cell electrocatalysts. Surface Science Reports. 2002;45:117-229.

[44] Adams WA, Blair J, Bullock KR, Gardner CL. Enhancement of the performance and reliability of CO poisoned PEM fuel cells. Journal of Power Sources. 2005;145:55-61.

[45] Franco A. Polymer Electrolyte Fuel Cells: Science, Applications, and Challenges. Stanford: Pan Stanford Publishing; 2013.

[46] Zamel N, Li X. Effect of contaminants on polymer electrolyte membrane fuel cells. Progress in Energy and Combustion Science. 2011;37:292-329.

[47] Stonehart P, Ross PN. The Commonality of Surface Processes in Electrocatalysis and Gas-Phase Heterogeneous Catalysis. Catal Rev-Sci Eng. 1975;12:1-35.

[48] Gilman S. The Mechanism of Electrochemical Oxidation of Carbon Monoxide and Methanol on Platinum. II. The “Reactant-Pair” Mechanism for Electrochemical Oxidation of Carbon Monoxide and Methanol1. The Journal of Physical Chemistry. 1964;68:70-80.

[49] Bellows RJ, Marucchi-Soos EP, Buckley DT. Analysis of Reaction Kinetics for Carbon Monoxide and Carbon Dioxide on Polycrystalline Platinum Relative to Fuel Cell Operation. Industrial & Engineering Chemistry Research. 1996;35:1235-42.

[50] Igarashi H, Fujino T, Watanabe M. Hydrogen electro-oxidation on platinum catalysts in the presence of trace carbon monoxide. Journal of Electroanalytical Chemistry. 1995;391:119-23.

[51] Gasteiger HA, Markovic NM, Ross PN. H2 and CO Electrooxidation on Well-Characterized Pt, Ru, and Pt-Ru. 2. Rotating Disk Electrode Studies of CO/H2 Mixtures at 62 .degree.C. The Journal of Physical Chemistry. 1995;99:16757-67.

[52] Papageorgopoulos DC, de Bruijn FA. Examining a Potential Fuel Cell Poison: A Voltammetry Study of the Influence of Carbon Dioxide on the Hydrogen Oxidation Capability of Carbon-Supported Pt and PtRu Anodes. Journal of The Electrochemical Society. 2002;149:A140-A5.

[53] Murthy M, Esayian M, Hobson A, MacKenzie S, Lee WK, Van Zee JW. Performance of a Polymer Electrolyte Membrane Fuel Cell Exposed to Transient CO Concentrations. Journal of The Electrochemical Society. 2001;148:A1141-A7.

[54] Zhang J, Datta R. Sustained Potential Oscillations in Proton Exchange Membrane Fuel Cells with PtRu as Anode Catalyst. Journal of The Electrochemical Society. 2002;149:A1423-A31.

[55] Zhang J, Fehribach JD, Datta R. Mechanistic and Bifurcation Analysis of Anode Potential Oscillations in PEMFCs with CO in Anode Feed. Journal of The Electrochemical Society. 2004;151:A689-A97.

[56] Hanke-Rauschenbach R, Mangold M, Sundmacher K. Nonlinear dynamics of fuel cells: a review. Reviews in Chemical Engineering2011. p. 23.

[57] Thomason AH, Lalk TR, Appleby AJ. Effect of current pulsing and “self-oxidation” on the CO tolerance of a PEM fuel cell. Journal of Power Sources. 2004;135:204-11.

[58] Lopes PP, Ticianelli EA, Varela H. Potential oscillations in a proton exchange membrane fuel cell with a Pd–Pt/C anode. Journal of Power Sources. 2011;196:84-9.

[59] Kadyk T, Kirsch S, Hanke-Rauschenbach R, Sundmacher K. Autonomous potential oscillations at the Pt anode of a polymer electrolyte membrane fuel cell under CO poisoning. Electrochimica Acta. 2011;56:10593-602.

[60] Lu H, Rihko-Struckmann L, Hanke-Rauschenbach R, Sundmacher K. Spontaneous oscillations of cell voltage, power density, and anode exit CO concentration in a PEM fuel cell. Physical Chemistry Chemical Physics. 2011;13:18179-85.

[61] Mota A, Lopes PP, Ticianelli EA, Gonzalez ER, Varela H. Complex Oscillatory Response of a PEM Fuel Cell Fed with H2 / CO and Oxygen. Journal of The Electrochemical Society. 2010;157:B1301-B4.

[62] Hanke-Rauschenbach R, Kirsch S, Kelling R, Weinzierl C, Sundmacher K. Oscillations and Pattern Formation in a PEM Fuel Cell with Pt/Ru Anode Exposed to H2 / CO Mixtures. Journal of The Electrochemical Society. 2010;157:B1521-B8.

[63] Kirsch S, Hanke-Rauschenbach R, Sundmacher K. Analysis of Spatio-temporal Pattern Formation in a PEM Fuel Cell with Pt/Ru Anode Exposed to H2/CO Mixtures. Journal of The Electrochemical Society. 2011;158:B44-B53.

[64] Kirsch S, Hanke-Rauschenbach, R., Stein, B., Kraume, R., Sundmacher, K. The Electro-Oxidation of H2, CO in a Model PEM Fuel Cell: Oscillations, Chaos, Pulses. Journal of The Electrochemical Society. 2013;160:F436-F46.

[65] Lopes P, Batista B, Saglietti G, Varela H, Ticianelli E. Real-time determination of CO2 production and estimation of adsorbate coverage on a proton exchange membrane fuel cell under oscillatory operation. J Solid State Electrochem. 2013;17:1851-9.

[66] Oetjen HF, Schmidt VM, Stimming U, Trila F. Performance Data of a Proton Exchange Membrane Fuel Cell Using H 2 / CO as Fuel Gas. Journal of The Electrochemical Society. 1996;143:3838-42.

[67] Gottesfeld S, Pafford J. A New Approach to the Problem of Carbon Monoxide Poisoning in Fuel Cells Operating at Low Temperatures. Journal of The Electrochemical Society. 1988;135:2651-2.

[68] Schmidt VM, Bröckerhoff P, Höhlein B, Menzer R, Stimming U. Utilization of methanol for polymer electrolyte fuel cells in mobile systems. Journal of Power Sources. 1994;49:299-313.

[69] Rodrigues A, Amphlett JC, Mann RF, Peppley BA, Roberge PR. Carbon monoxide poisoning of proton-exchange membrane fuel cells. IECEC-97 Proceedings of the Thirty-Second Intersociety Energy Conversion Engineering Conference (Cat No97CH6203). Honolulu1997. p. 768-73 vol.2.

[70] Dhar HP, Christner LG, Kush AK. Nature of CO Adsorption during H 2 Oxidation in Relation to Modeling for CO Poisoning of a Fuel Cell Anode. Journal of The Electrochemical Society. 1987;134:3021-6.

[71] Zamel N, Li X. Transient analysis of carbon monoxide poisoning and oxygen bleeding in a PEM fuel cell anode catalyst layer. International Journal of Hydrogen Energy. 2008;33:1335-44.

[72] Zhang J, Thampan T, Datta R. Influence of Anode Flow Rate and Cathode Oxygen Pressure on CO Poisoning of Proton Exchange Membrane Fuel Cells. Journal of The Electrochemical Society. 2002;149:A765-A72.

[73] Murthy M, Esayian M, Lee WK, Van Zee JW. The Effect of Temperature and Pressure on the Performance of a PEMFC Exposed to Transient CO Concentrations. Journal of The Electrochemical Society. 2003;150:A29-A34.

[74] Ioroi T, Yasuda K, Miyazaki Y. Humidity dependence of the oxidation of carbon monoxide adsorbed on Pt/C and PtRu/C electrocatalysts. Physical Chemistry Chemical Physics. 2002;4:2337-40.

[75] Zhou F, Andreasen SJ, Kær SK, Park JO. Experimental investigation of carbon monoxide poisoning effect on a PBI/H3PO4 high temperature polymer electrolyte membrane fuel cell: Influence of anode humidification and carbon dioxide. International Journal of Hydrogen Energy. 2015;40:14932-41.

[76] Jiang R, Kunz HR, Fenton JM. Electrochemical Oxidation of H2 and H2∕CO Mixtures in Higher Temperature (T cell 100 ° C) Proton Exchange Membrane Fuel Cells: Electrochemical Impedance Spectroscopy. Journal of The Electrochemical Society. 2005;152:A1329-A40.

[77] Díaz MA, Iranzo A, Rosa F, Isorna F, López E, Bolivar JP. Effect of carbon dioxide on the contamination of low temperature and high temperature PEM (polymer electrolyte membrane) fuel cells. Influence of temperature, relative humidity and analysis of regeneration processes. Energy. 2015;90:299-309.

[78] Divisek J, Oetjen HF, Peinecke V, Schmidt VM, Stimming U. Components for PEM fuel cell systems using hydrogen and CO containing fuels. Electrochimica Acta. 1998;43:3811-5.

[79] de Bruijn FA, Papageorgopoulos DC, Sitters EF, Janssen GJM. The influence of carbon dioxide on PEM fuel cell anodes. Journal of Power Sources. 2002;110:117-24.

[80] Gu T, Lee W-K, Van Zee JW, Murthy M. Effect of Reformate Components on PEMFC Performance: Dilution and Reverse Water Gas Shift Reaction. Journal of The Electrochemical Society. 2004;151:A2100-A5.

[81] Baschuk JJ, Li X. Carbon monoxide poisoning of proton exchange membrane fuel cells. International Journal of Energy Research. 2001;25:695-713.

[82] Tingelöf T, Hedström L, Holmström N, Alvfors P, Lindbergh G. The influence of CO2, CO and air bleed on the current distribution of a polymer electrolyte fuel cell. International Journal of Hydrogen Energy. 2008;33:2064-72.

[83] Yan W-M, Chu H-S, Lu M-X, Weng F-B, Jung G-B, Lee C-Y. Degradation of proton exchange membrane fuel cells due to CO and CO2 poisoning. Journal of Power Sources. 2009;188:141-7.

[84] Rockward T, Urdampilleta I, Uribe F, Brosha EL, Pivovar B, Garzon FH. The Effects of Multiple Contaminants on Polymer Electrolyte Fuel Cells. ECS Transactions. 2007;11:821-9.

[85] Shi W, Yi B, Hou M, Jing F, Yu H, Ming P. The influence of hydrogen sulfide on proton exchange membrane fuel cell anodes. Journal of Power Sources. 2007;164:272-7.

[86] Wang X, Baker, P., Zhang, X., Garces, H. F., Bonville, L. J., Pasaogullari, U., Molter, T. M. An experimental overview of the effects of hydrogen impurities on polymer electrolyte membrane fuel cell performance. International Journal of Hydrogen Energy. 2014;39:19701-13.

[87] Borup R, Meyers J, Pivovar B, Kim YS, Mukundan R, Garland N, et al. Scientific aspects of polymer electrolyte fuel cell durability and degradation. Chemical Reviews. 2007;107:3904-51.

[88] Dorn S, Bender G, Bethune K, Angelo M, Rocheleau R. The Impact of Trace Carbon Monoxide / Toluene Mixtures on PEMFC Performance. ECS Transactions. 2008;16:659-67.

[89] Angelo M, Bethune K, Rocheleau R. The Impact of sub ppm Carbon Monoxide and ppm Level CO/Toluene and Methylcyclohexane/CO Mixtures on PEMFC Performance and Durability. ECS Transactions. 2010;28:169-81.

[90] Kortsdottir K, Lindström RW, Åkermark T, Lindbergh G. Influence of toluene contamination at the hydrogen Pt/C anode in a proton exchange membrane fuel cell. Electrochimica Acta. 2010;55:7643-51.

[91] Qi Z, He C, Kaufman A. Poisoning of Proton Exchange Membrane Fuel Cell Cathode by CO in the Anode Fuel. Electrochemical and Solid-State Letters. 2001;4:A204-A5.

[92] Qi Z, He C, Kaufman A. Effect of CO in the anode fuel on the performance of PEM fuel cell cathode. Journal of Power Sources. 2002;111:239-47.

[93] Reshetenko TV, Bethune K, Rocheleau R. Spatial proton exchange membrane fuel cell performance under carbon monoxide poisoning at a low concentration using a segmented cell system. Journal of Power Sources. 2012;218:412-23.

[94] Reshetenko TV, Bethune K, Rubio MA, Rocheleau R. Study of low concentration CO poisoning of Pt anode in a proton exchange membrane fuel cell using spatial electrochemical impedance spectroscopy. Journal of Power Sources. 2014;269:344-62.

[95] Angelo M, Bender G, Dorn S, Bethune K, Hossain T, Posey D, et al. The Impacts of Repetitive Carbon Monoxide Poisoning on Performance and Durability of a Proton Exchange Membrane Fuel Cell. ECS Transactions. 2008;16:669-76.

[96] Profatilova I, Jacques P-A, Escribano S. Evaluation of Parameters Accelerating the Aging of PEMFCs Operating under Reformate Containing Carbon Monoxide. Journal of The Electrochemical Society. 2018;165:F3251-F60.

[97] Wagner N, Gülzow E. Change of electrochemical impedance spectra (EIS) with time during CO-poisoning of the Pt-anode in a membrane fuel cell. Journal of Power Sources. 2004;127:341-7.

[98] Parry V, Berthomé G, Joud J-C, Lemaire O, Franco AA. XPS investigations of the proton exchange membrane fuel cell active layers aging: Characterization of the mitigating role of an anodic CO contamination on cathode degradation. Journal of Power Sources. 2011;196:2530-8.

[99] Søndergaard S, Cleemann LN, Jensen JO, Bjerrum NJ. Influence of carbon monoxide on the cathode in high-temperature polymer electrolyte membrane fuel cells. International Journal of Hydrogen Energy. 2017;42:3309-15.

[100] Franco AA, Guinard M, Barthe B, Lemaire O. Impact of carbon monoxide on PEFC catalyst carbon support degradation under current-cycled operating conditions. Electrochimica Acta. 2009;54:5267-79.

[101] Chandesris M, Guetaz L, Schott P, Scohy M, Escribano S. Investigation of Degradation Heterogeneities in PEMFC Stack Aged under Reformate Coupling In Situ Diagnosis, Post-Mortem Ex Situ Analyses and Multi-Physic Simulations. Journal of The Electrochemical Society. 2018;165:F3290-F306.

[102] Brett DJL, Atkins S, Brandon NP, Vesovic V, Vasileiadis N, Kucernak AR. Investigation of reactant transport within a polymer electrolyte fuel cell using localised CO stripping voltammetry and adsorption transients. Journal of Power Sources. 2004;133:205-13.

[103] Brett DJL, Aguiar P, Brandon NP, Kucernak AR. Measurement and modelling of carbon monoxide poisoning distribution within a polymer electrolyte fuel cell. International Journal of Hydrogen Energy. 2007;32:863-71.

[104] Murahashi T, Mitsumoto T, Nishiyama E. Current Distribution of a PEMFC under CO Poisoning. ECS Transactions. 2009;25:869-79.

[105] Boaventura M, Sander H, Friedrich KA, Mendes A. The influence of CO on the current density distribution of high temperature polymer electrolyte membrane fuel cells. Electrochimica Acta. 2011;56:9467-75.

[106] Rubio MA, Urquia A, Dormido S. Diagnosis of performance degradation phenomena in PEM fuel cells. International Journal of Hydrogen Energy. 2010;35:2586-90.

[107] Le Canut J-M, Abouatallah RM, Harrington DA. Detection of Membrane Drying, Fuel Cell Flooding, and Anode Catalyst Poisoning on PEMFC Stacks by Electrochemical Impedance Spectroscopy. Journal of The Electrochemical Society. 2006;153:A857-A64.

[108] Wagner N, Schulze M. Change of electrochemical impedance spectra during CO poisoning of the Pt and Pt–Ru anodes in a membrane fuel cell (PEFC). Electrochimica Acta. 2003;48:3899-907.

[109] Schiller CA, Richter F, Gulow E, Wagner N. Relaxation impedance as a model for the deactivation mechanism of fuel cells due to carbon monoxide poisoning. Physical Chemistry Chemical Physics. 2001;3:2113-6.

[110] Leng Y-J, Wang X, Hsing IM. Assessment of CO-tolerance for different Pt-alloy anode catalysts in a polymer electrolyte fuel cell using ac impedance spectroscopy. Journal of Electroanalytical Chemistry. 2002;528:145-52.

[111] Grashoff GJ, Pilkington CE, Corti CW. The Purification of Hydrogen. Platinum Metals Review. 1983;27:157-69.

[112] Al-Mufachi NA, Rees NV, Steinberger-Wilkens R. Hydrogen selective membranes: A review of palladium-based dense metal membranes. Renewable and Sustainable Energy Reviews. 2015;47:540-51.

[113] Uehara I. Separation and Purification of Hydrogen. In: Ohta T, editor. Energy Carriers and Conversion Systems with Emphasis on Hydrogen Oxford, United Kingdom: EOLSS Publications; 2009. p. 268-82.

[114] Zhang J, Datta R. Electrochemical Preferential Oxidation of CO in Reformate. Journal of The Electrochemical Society. 2005;152:A1180-A7.

[115] Park ED, Lee D, Lee HC. Recent progress in selective CO removal in a H2-rich stream. Catalysis Today. 2009;139:280-90.

[116] Conde JJ, Maroño M, Sánchez-Hervás JM. Pd-Based Membranes for Hydrogen Separation: Review of Alloying Elements and Their Influence on Membrane Properties. Separation & Purification Reviews. 2017;46:152-77.

[117] Chen X, Wei L, Deng L, Yang F, Zhang Z. A Review on the Metal Hydride Based Hydrogen Purification and Separation Technology. Applied Mechanics and Materials. 2013;448-453:3027-36.

[118] Zhu J, Hou J, Uliana A, Zhang Y, Tian M, Van der Bruggen B. The rapid emergence of two-dimensional nanomaterials for high-performance separation membranes. Journal of Materials Chemistry A. 2018;6:3773-92.

[119] Ma Z, Zhao X, Tang Q, Zhou Z. Computational prediction of experimentally possible g-C3N3 monolayer as hydrogen purification membrane. International Journal of Hydrogen Energy. 2014;39:5037-42.

[120] Modibane KD, Williams M, Lototskyy M, Davids MW, Klochko Y, Pollet BG. Poisoning-tolerant metal hydride materials and their application for hydrogen separation from CO2/CO containing gas mixtures. International Journal of Hydrogen Energy. 2013;38:9800-10.

[121] Majlan EH, Wan Daud WR, Iyuke SE, Mohamad AB, Kadhum AAH, Mohammad AW, et al. Hydrogen purification using compact pressure swing adsorption system for fuel cell. International Journal of Hydrogen Energy. 2009;34:2771-7.

[122] Bernardo P, Drioli E, Golemme G. Membrane Gas Separation: A Review/State of the Art. Industrial & Engineering Chemistry Research. 2009;48:4638-63.

[123] Adhikari S, Fernando S. Hydrogen Membrane Separation Techniques. Industrial & Engineering Chemistry Research. 2006;45:875-81.

[124] Liu G, Jin W, Xu N. Graphene-based membranes. Chemical Society Reviews. 2015;44:5016-30.

[125] Li Y, Zhou Z, Shen P, Chen Z. Two-dimensional polyphenylene: experimentally available porous graphene as a hydrogen purification membrane. Chemical Communications. 2010;46:3672-4.

[126] Tao Y, Xue Q, Liu Z, Shan M, Ling C, Wu T, et al. Tunable Hydrogen Separation in Porous Graphene Membrane: First-Principle and Molecular Dynamic Simulation. ACS Applied Materials & Interfaces. 2014;6:8048-58.

[127] Wei S, Zhou S, Wu Z, Wang M, Wang Z, Guo W, et al. Mechanistic insights into porous graphene membranes for helium separation and hydrogen purification. Applied Surface Science. 2018;441:631-8.

[128] Li G, Li Y, Liu H, Guo Y, Li Y, Zhu D. Architecture of graphdiyne nanoscale films. Chemical Communications. 2010;46:3256-8.

[129] Jiao Y, Du A, Hankel M, Zhu Z, Rudolph V, Smith SC. Graphdiyne: a versatile nanomaterial for electronics and hydrogen purification. Chemical Communications. 2011;47:11843-5.

[130] Cranford SW, Buehler MJ. Selective hydrogen purification through graphdiyne under ambient temperature and pressure. Nanoscale. 2012;4:4587-93.

[131] Zhao W-H, Yuan L-F, Yang J-L. Graphdiyne as Hydrogen Purification Membrane. Chinese Journal of Chemical Physics. 2012;25:434-40.

[132] Jiao Y, Du A, Smith SC, Zhu Z, Qiao SZ. H2 purification by functionalized graphdiyne – role of nitrogen doping. Journal of Materials Chemistry A. 2015;3:6767-71.

[133] Tan X, Kou L, Tahini HA, Smith SC. Charge-modulated permeability and selectivity in graphdiyne for hydrogen purification. Molecular Simulation. 2016;42:573-9.

[134] Zhang H, He X, Zhao M, Zhang M, Zhao L, Feng X, et al. Tunable Hydrogen Separation in sp–sp2 Hybridized Carbon Membranes: A First-Principles Prediction. The Journal of Physical Chemistry C. 2012;116:16634-8.

[135] Ji Y, Dong H, Lin H, Zhang L, Hou T, Li Y. Heptazine-based graphitic carbon nitride as an effective hydrogen purification membrane. RSC Adv. 2016;6:52377-83.

[136] Zhu L, Jin Y, Xue Q, Li X, Zheng H, Wu T, et al. Theoretical study of a tunable and strain-controlled nanoporous graphenylene membrane for multifunctional gas separation. Journal of Materials Chemistry A. 2016;4:15015-21.

[137] Xu J, Zhou S, Sang P, Li J, Zhao L. Inorganic graphenylene as a promising novel boron nitrogen membrane for hydrogen purification: a computational study. Journal of Materials Science. 2017;52:10285-93.

[138] Lototskyy MV, Tolj I, Pickering L, Sita C, Barbir F, Yartys V. The use of metal hydrides in fuel cell applications. Progress in Natural Science: Materials International. 2017;27:3-20.

[139] Miura S, Fujisawa A, Ishida M. A hydrogen purification and storage system using metal hydride. International Journal of Hydrogen Energy. 2012;37:2794-9.

[140] Miura S, Fujisawa A, Tomekawa S, Taniguchi Y, Hanada N, Ishida M. A hydrogen purification and storage system using CO adsorbent and metal hydride. Journal of Alloys and Compounds. 2013;580:S414-S7.

[141] Shenoy TA. Cryogenic process for separating synthesis gas. U.S. Patent 4,217,759, 1980.

[142] Balasubramanian S, Holland CE, Weidner JW. Electrochemical Filter Design for the Removal of CO Contaminant in Reformate Hydrogen. ECS Transactions. 2009;25:1873-80.

[143] Perry KA, Eisman GA, Benicewicz BC. Electrochemical hydrogen pumping using a high-temperature polybenzimidazole (PBI) membrane. Journal of Power Sources. 2008;177:478-84.

[144] Thomassen M, Sheridan E, Kvello J. Electrochemical hydrogen separation and compression using polybenzimidazole (PBI) fuel cell technology. Journal of Natural Gas Science and Engineering. 2010;2:229-34.

[145] Lee HK, Choi HY, Choi KH, Park JH, Lee TH. Hydrogen separation using electrochemical method. Journal of Power Sources. 2004;132:92-8.

[146] Oettel C, Rihko-Struckmann L, Sundmacher K. Characterisation of the electrochemical water gas shift reactor (EWGSR) operated with hydrogen and carbon monoxide rich feed gas. International Journal of Hydrogen Energy. 2012;37:11759-71.

[147] Oettel C, Rihko-Struckmann L, Sundmacher K. Combined generation and separation of hydrogen in an electrochemical water gas shift reactor (EWGSR). International Journal of Hydrogen Energy. 2012;37:6635-45.

[148] Gardner CL, Ternan M. Electrochemical separation of hydrogen from reformate using PEM fuel cell technology. Journal of Power Sources. 2007;171:835-41.

[149] Huang C, Jiang R, Elbaccouch M, Muradov N, Fenton JM. On-board removal of CO and other impurities in hydrogen for PEM fuel cell applications. Journal of Power Sources. 2006;162:563-71.

[150] Liu X, Christensen PA, Kelly SM, Rocher V, Scott K. Al2O3 disk supported Si3N4 hydrogen purification membrane for low temperature polymer electrolyte membrane fuel cells. Membranes. 2013;3:406-14.

[151] Hanke-Rauschenbach R, Weinzierl C, Krasnyk M, Rihko-Struckmann L, Lu H, Sundmacher K. Operating Behavior and Scale-Up of an ECPrOx Unit for CO Removal from Reformate for PEM Fuel Cell Application. Journal of The Electrochemical Society. 2009;156:B1267-B75.

[152] Lu H, Rihko-Struckmann L, Hanke-Rauschenbach R, Sundmacher K. Improved electrochemical CO removal via potential oscillations in serially connected PEM fuel cells with PtRu anodes. Electrochimica Acta. 2009;54:1184-91.

[153] Heidebrecht P, Hanke-Rauschenbach R, Jörke A, Sundmacher K. On the design of cascades of ECPrOx reactors for deep CO removal from reformate gas. Chemical Engineering Science. 2012;67:34-43.

[154] Balasubramanian S, Holland CE, Weidner JW. Electrochemical removal of carbon monoxide in reformate hydrogen for fueling proton exchange membrane fuel cells. Electrochemical and Solid-State Letters. 2010;13:B5-B7.

[155] Langer SH, Handelman RG. Electrolytic hydrogen purification and recovery of same. U.S. Patent 3,475,302, 1969.

[156] Maget HJR. Process for Gas Purification. U.S. Patent 3,489,670, 1970.

[157] Grigoriev SA, Shtatniy IG, Millet P, Porembsky VI, Fateev VN. Description and characterization of an electrochemical hydrogen compressor/concentrator based on solid polymer electrolyte technology. International Journal of Hydrogen Energy. 2011;36:4148-55.

[158] Sapountzi F, Tsampas MN, Vayenas CG. Electrocatalysis and electrochemical promotion of CO oxidation in PEM fuel cells: the role of oxygen crossover. Top Catal. 2007;44:461-8.

[159] Zhang J. Investigation of CO Tolerance in Proton Exchange Membrane Fuel Cells. PhD thesis. Worcester, Massachusetts: Worcester Polytechnic Institute; 2004.

[160] Ehteshami SMM, Chan SH. A review of electrocatalysts with enhanced CO tolerance and stability for polymer electrolyte membarane fuel cells. Electrochimica Acta. 2013;93:334-45.

[161] Ralph TR, Hogarth MP. Catalysis for Low Temperature Fuel Cells. Platinum Metals Review. 2002;46:117-35.

[162] Bellows RJ, Marucchi Soos E, Reynolds RP. The Mechanism of CO Mitigation in Proton Exchange Membrane Fuel Cells Using Dilute H 2 O 2 in the Anode Humidifier. Electrochemical and Solid-State Letters. 1998;1:69-70.

[163] Tolmachev YV, Petrii OA. Pt–Ru electrocatalysts for fuel cells: developments in the last decade. J Solid State Electrochem. 2017;21:613-39.

[164] Guo SM, Hasan ABM. Proton Exchange Membrane Fuel Cell High Carbon Monoxide Tolerance Operation Using Pulsed Heating and Pressure Swing. Journal of Fuel Cell Science and Technology. 2009;6:011022-1--6.

[165] Lopes PP, Ticianelli EA. The CO tolerance pathways on the Pt–Ru electrocatalytic system. Journal of Electroanalytical Chemistry. 2010;644:110-6.

[166] Narischat N, Takeguchi T, Mori T, Iwamura S, Ogino I, Mukai SR, et al. Effect of the mesopores of carbon supports on the CO tolerance of Pt2Ru3 polymer electrolyte fuel cell anode catalyst. International Journal of Hydrogen Energy. 2016;41:13697-704.

[167] McIntyre DR, Burstein GT, Vossen A. Effect of carbon monoxide on the electrooxidation of hydrogen by tungsten carbide. Journal of Power Sources. 2002;107:67-73.

[168] Li B, Higgins DC, Yang D, Lin R, Yu Z, Ma J. New non-platinum Ir–V–Mo electro-catalyst, catalytic activity and CO tolerance in hydrogen oxidation reaction. International Journal of Hydrogen Energy. 2012;37:18843-50.

[169] Lopes T, Paganin VA, Gonzalez ER. The effects of hydrogen sulfide on the polymer electrolyte membrane fuel cell anode catalyst: H2S–Pt/C interaction products. Journal of Power Sources. 2011;196:6256-63.

[170] Das SK, Reis A, Berry KJ. Experimental evaluation of CO poisoning on the performance of a high temperature proton exchange membrane fuel cell. Journal of Power Sources. 2009;193:691-8.

[171] Authayanun S, Im-orb K, Arpornwichanop A. A review of the development of high temperature proton exchange membrane fuel cells. Chinese Journal of Catalysis. 2015;36:473-83.

[172] Kallitsis JK, Geormezi M, Neophytides SG. Polymer electrolyte membranes for high-temperature fuel cells based on aromatic polyethers bearing pyridine units. Polymer International. 2009;58:1226-33.

[173] Geormezi M, Deimede V, Gourdoupi N, Triantafyllopoulos N, Neophytides S, Kallitsis JK. Novel Pyridine-Based Poly(ether sulfones) and their Study in High Temperature PEM Fuel Cells. Macromolecules. 2008;41:9051-6.

[174] Orfanidi A, Daletou MK, Neophytides SG. Mitigation strategy towards stabilizing the Electrochemical Interface under high CO and H2O containing reformate gas feed. Electrochimica Acta. 2017;233:218-28.

[175] Jiao K, Zhou Y, Du Q, Yin Y, Yu S, Li X. Numerical simulations of carbon monoxide poisoning in high temperature proton exchange membrane fuel cells with various flow channel designs. Applied Energy. 2013;104:21-41.

[176] Vassiliev A, Cleemann LN, Li Q, Jensen JO. Hydrogen Sulfide Tolerance in High Temperature Pemfcs. ECS Meeting Abstracts. 2016;MA2016-02:2813.

[177] Decoopman B, Vincent R, Rosini S, Paganelli G, Thivel PX. Proton exchange membrane fuel cell reversible performance loss induced by carbon monoxide produced during operation. Journal of Power Sources. 2016;324:492-8.

[178] Sung L-Y, Hwang B-J, Hsueh K-L, Su W-N, Yang C-C. Comprehensive study of an air bleeding technique on the performance of a proton-exchange membrane fuel cell subjected to CO poisoning. Journal of Power Sources. 2013;242:264-72.

[179] Narayanan H, Basu S. Regeneration of CO poisoned Pt black anode catalyst in PEMFC using break-in procedure and KMnO4 solution. International Journal of Hydrogen Energy. 2017;42:23814-20.

[180] Inaba M, Sugishita M, Wada J, Matsuzawa K, Yamada H, Tasaka A. Impacts of air bleeding on membrane degradation in polymer electrolyte fuel cells. Journal of Power Sources. 2008;178:699-705.

[181] Pérez LC, Rajala T, Ihonen J, Koski P, Sousa JM, Mendes A. Development of a methodology to optimize the air bleed in PEMFC systems operating with low quality hydrogen. International Journal of Hydrogen Energy. 2013;38:16286-99.

[182] Schmidt VM, Oetjen HF, Divisek J. Performance Improvement of a PEMFC Using Fuels with CO by Addition of Oxygen-Evolving Compounds. Journal of The Electrochemical Society. 1997;144:L237-L8.

[183] Wang W. The effect of internal air bleed on CO poisoning in a proton exchange membrane fuel cell. Journal of Power Sources. 2009;191:400-6.

[184] Yu H, Hou Z, Yi B, Lin Z. Composite anode for CO tolerance proton exchange membrane fuel cells. Journal of Power Sources. 2002;105:52-7.

[185] Haug AT, White RE, Weidner JW, Huang W. Development of a Novel CO Tolerant Proton Exchange Membrane Fuel Cell Anode. Journal of The Electrochemical Society. 2002;149:A862-A7.

[186] Haug AT, White RE, Weidner JW, Huang W, Shi S, Rana N, et al. Using Sputter Deposition to Increase CO Tolerance in a Proton-Exchange Membrane Fuel Cell. Journal of The Electrochemical Society. 2002;149:A868-A72.

[187] Janssen GJM, de Heer MP, Papageorgopoulos DC. Bilayer Anodes for Improved Reformate Tolerance of PEM Fuel Cells. Fuel Cells. 2004;4:169-74.

[188] Ball SC, Thompsett D. Ultra CO Tolerant PtMo/PtRu anodes for PEMFCs. MRS Proceedings. 2002;756:FF5.1.-FF5.1.12.

[189] Ball S, Theobald B, Thompsett D. PtMo Catalysts for Ultra High CO PEMFC Applications. ECS Proceedings Volumes. 2004;2004-21:206-12.

[190] Shi W, Hou M, Shao Z, Hu J, Hou Z, Ming P, et al. A novel proton exchange membrane fuel cell anode for enhancing CO tolerance. Journal of Power Sources. 2007;174:164-9.

[191] Santiago EI, Paganin VA, do Carmo M, Gonzalez ER, Ticianelli EA. Studies of CO tolerance on modified gas diffusion electrodes containing ruthenium dispersed on carbon. Journal of Electroanalytical Chemistry. 2005;575:53-60.

[192] Uribe FA, Valerio JA, Garzon FH, Zawodzinski TA. PEMFC Reconfigured Anodes for Enhancing CO Tolerance with Air Bleed. Electrochemical and Solid-State Letters. 2004;7:A376-A9.

[193] Adcock PA, Pacheco SV, Norman KM, Uribe FA. Transition Metal Oxides as Reconfigured Fuel Cell Anode Catalysts for Improved CO Tolerance: Polarization Data. Journal of The Electrochemical Society. 2005;152:A459-A66.

[194] Rohland B, Plzak V. The PEMFC-integrated CO oxidation — a novel method of simplifying the fuel cell plant. Journal of Power Sources. 1999;84:183-6.

[195] Balomenou SP, Sapountzi F, Presvytes D, Tsampas M, Vayenas CG. Triode fuel cells. Solid State Ionics. 2006;177:2023-7.

[196] Sapountzi FM, Divane SC, Tsampas MN, Vayenas CG. Enhanced performance of CO poisoned proton exchange membrane fuel cells via triode operation. Electrochimica Acta. 2011;56:6966-75.

[197] Tsampas MN, Sapountzi FM, Divane S, Papaioannou EI, Vayenas CG. Triode operation of CO poisoned PEM fuel cells: Fixed and cyclic potential triode operation. Solid State Ionics. 2012;225:272-6.

[198] Caliandro P, Diethelm S, Van herle J. Triode Solid Oxide Fuel Cell Operation Under Sulfur-Poisoning Conditions. Fuel Cells. 2017;17:457-63.

[199] Martino E, Koilias G, Athanasiou M, Katsaounis A, Dimakopoulos Y, Tsamopoulos J, et al. Experimental investigation and mathematical modeling of triode PEM fuel cells. Electrochimica Acta. 2017;248:518-33.

[200] Jiménez S, Soler J, Valenzuela RX, Daza L. Assessment of the performance of a PEMFC in the presence of CO. Journal of Power Sources. 2005;151:69-73.

[201] Wilkinson DP, Chow CYF, Allan DE, Allan PJ, Johannes EP, Roberts JA, et al. Method and apparatus for operating an electrochemical fuel cell with periodic fuel starvation at the anode. U.S. Patent 6,096,448, 2000.

[202] Carrette LPL, Friedrich KA, Huber M, Stimming U. Improvement of CO tolerance of proton exchange membrane (PEM) fuel cells by a pulsing technique. Physical Chemistry Chemical Physics. 2001;3:320-4.

[203] Choi W, Enjeti PN, Appleby AJ. An advanced power converter topology to significantly improve the CO tolerance of the PEM fuel cell power systems. Industry Applications Conference, 2004 39th IAS Annual Meeting Conference Record of the 2004 IEEE2004. p. 1185-91 vol.2.

[204] Palma L, Enjeti P. A cost effective power converter to improve CO tolerance in PEM fuel cell power systems. 2008 IEEE Power Electronics Specialists Conference. 2008:210-5.

[205] Farrell CG, Gardner CL, Ternan M. Experimental and modelling studies of CO poisoning in PEM fuel cells. Journal of Power Sources. 2007;171:282-93.

[206] Wingelaar PJH, Geers MPA, Duarte JL, Hendrix MAM. CO-tolerant operation of platinum-loaded PEM fuel cells. New York: Ieee; 2007.

[207] Mao ZQ, Zhen YJ, Liu LY, Lu WQ. The effect of pulsed voltage on the PEMFC. Hydrogen Energy Progress XIII. 2000;2:863-6.

[208] Lu H, Rihko-Struckmann L, Hanke-Rauschenbach R, Sundmacher K. Dynamic Behavior of a PEM Fuel Cell During Electrochemical CO Oxidation on a PtRu Anode. Top Catal. 2008;51:89-97.

[209] Lopes PP, Freitas KS, Ticianelli EA. CO Tolerance of PEMFC Anodes: Mechanisms and Electrode Designs. Electrocatal. 2010;1:200-12.

[210] Petrii OA. Pt–Ru electrocatalysts for fuel cells: a representative review. J Solid State Electrochem. 2008;12:609-42.

[211] Al-Ahmed A. 11. Components for PEM Fuel Cells: An Overview. Current Application of Polymers and Nano Materials: Trans Tech Publications Ltd; 2010.

[212] Nepel TCM, Lopes PP, Paganin VA, Ticianelli EA. CO tolerance of proton exchange membrane fuel cells with Pt/C and PtMo/C anodes operating at high temperatures: A mass spectrometry investigation. Electrochimica Acta. 2013;88:217-24.

[213] Watanabe M, Motoo S. Electrocatalysis by ad-atoms. Part II. Enhancement of the oxidation of methanol on platinum by ruthenium ad-atoms. Journal of electroanalytical chemistry and interfacial electrochemistry. 1975;60:267-73.

[214] Maiyalagan T, Pasupathi S. Components for PEM Fuel Cells: An Overview. Materials Science Forum. 2010;657:143-89.

[215] Wee J-H, Lee K-Y. Overview of the development of CO-tolerant anode electrocatalysts for proton-exchange membrane fuel cells. Journal of Power Sources. 2006;157:128-35.

[216] Shabani B, Hafttananian M, Khamani S, Ramiar A, Ranjbar AA. Poisoning of proton exchange membrane fuel cells by contaminants and impurities: Review of mechanisms, effects, and mitigation strategies. Journal of Power Sources. 2019;427:21-48.

[217] Ren X, Lv Q, Liu L, Liu B, Wang Y, Liu A, et al. Current progress of Pt and Pt-based electrocatalysts used for fuel cells. Sustainable Energy & Fuels. 2020.

[218] Ehteshami SMM, Jia Q, Halder A, Chan SH, Mukerjee S. The role of electronic properties of Pt and Pt alloys for enhanced reformate electro-oxidation in polymer electrolyte membrane fuel cells. Electrochimica Acta. 2013;107:155-63.

[219] Wang Q, Wang G, Tao H, Li Z, Han L. Highly CO tolerant PtRu/PtNi/C catalyst for polymer electrolyte membrane fuel cell. RSC Adv. 2017;7:8453-9.

[220] Isseroff R, Blackburn L, Kang J, Li H, Gentleman M, Rafailovich M. Incorporation of Platinum and Gold Partially Reduced Graphene Oxide into Polymer Electrolyte Membrane Fuel Cells for Increased Output Power and Carbon Monoxide Tolerance. MRS Advances. 2016;1:1477-86.

[221] Wang C, Wang S, Peng L, Zhang J, Shao Z, Huang J, et al. Recent Progress on the Key Materials and Components for Proton Exchange Membrane Fuel Cells in Vehicle Applications. Energies. 2016;9:603.

[222] Li Q, He R, Jensen JO, Bjerrum NJ. Approaches and Recent Development of Polymer Electrolyte Membranes for Fuel Cells Operating above 100 °C. Chemistry of Materials. 2003;15:4896-915.

[223] Liu Y, Lehnert, W., Janßen, H., Samsun, R. C., Stolten, D. A review of high-temperature polymer electrolyte membrane fuel-cell (HT-PEMFC)-based auxiliary power units for diesel-powered road vehicles. Journal of Power Sources. 2016;311:91-102.

[224] Sugiyama K, Sumiya Y, Takagi M, Saita K, Maeda S. Understanding CO oxidation on the Pt(111) surface based on a reaction route network. Physical Chemistry Chemical Physics. 2019;21:14366-75.

[225] Wan C-H, Zhuang Q-H. Novel layer wise anode structure with improved CO-tolerance capability for PEM fuel cell. Electrochimica Acta. 2007;52:4111-23.

[226] Zhang J. PEM Fuel Cell Electrocatalysts and Catalyst Layers: Fundamentals and Applications. Meppel: Springer; 2008.

[227] Rajala T. Enhancement of polymer electrolyte fuel cell tolerance to CO by combination of different mitigation methods. Helsinki: University of Helsinki; 2013.

[228] Hafttananian M, Ramiar A, Ranjbar AA. Novel techniques of oxygen bleeding for polymer electrolyte fuel cells under impure anode feeding and poisoning condition: A computational study using OpenFOAM®. Energy Conversion and Management. 2016;122:564-79.

[229] Scholta J, Pawlik J, Chmielewski N, Jörissen L. Longevity test results for reformate polymer electrolyte membrane fuel cell stacks. Journal of Power Sources. 2011;196:5264-71.

[230] Wilkinson D, Voss HH, Prater KB, Hards GA, Ralph TR, Thompsett D. Electrode. U.S. Patent 5,795,669, 1998.

[231] Zhigang S, Baolian Y, Ming H. Bifunctional electrodes with a thin catalyst layer for `unitized' proton exchange membrane regenerative fuel cell. Journal of Power Sources. 1999;79:82-5.

[232] Lindstrom RW. Electrocatalytic gas diffusion electrode employing thin carbon cloth later. U.S. Patent 4,647,359, 1987.

[233] Katsaounis A, Balomenou S, Tsiplakides D, Brosda S, Neophytides S, Vayenas CG. Proton tunneling-induced bistability, oscillations and enhanced performance of PEM fuel cells. Applied Catalysis B: Environmental. 2005;56:251-8.

[234] Katsaounis A, Balomenou SP, Tsiplakides D, Tsampas M, Vayenas CG. The role of potential-dependent electrolyte resistance in the performance, steady-state multiplicities and oscillations of PEM fuel cells: Experimental investigation and macroscopic modelling. Electrochimica Acta. 2005;50:5132-43.

[235] Zhang JZ, Liu Z, Goodwin JG. The effect of low concentrations of CO on H2 adsorption and activation on Pt/C. Part 1: In the absence of humidity. Journal of Power Sources. 2010;195:3060-8.

[236] Zhang JZ, Hongsirikarn K, Goodwin JG. The effect of low concentrations of CO on H2 adsorption and activation on Pt/C: Part 2—In the presence of H2O vapor. Journal of Power Sources. 2011;196:6186-95.

[237] Qin C, Wang J, Wang D, Li B, Zhang C. Proton Exchange Membrane Fuel Cell Reversal: A Review. Catalysts. 2016;6:197.

[238] Taniguchi A, Akita T, Yasuda K, Miyazaki Y. Analysis of electrocatalyst degradation in PEMFC caused by cell reversal during fuel starvation. Journal of Power Sources. 2004;130:42-9.

[239] Saunders J, Glenn B, Myers J, Cucksey C, Mukerjee S, Boggs C, et al. Pulsing for Enhanced CO Mitigation: Single Cell Performance. ECS Transactions. 2008;6:343-9.

[240] Ozdemir MO, Pasaogullari U. Modeling the oscillative behavior and carbon monoxide removal by current pulsing technique in H2/CO mixtures for Pt catalyst layer. International Journal of Hydrogen Energy. 2016;41:10854-69.

[241] Adams WA, Gardner CL. Fuel cell manager. U.S. Patent 6,339,313 B1, 2002.

[242] Adams W, Gardner CL, Dunn JH. Fuel cell manager. U.S. 6,541,941 B2, 2003.

[243] Palma L. Development of a power converter to improve CO tolerance in proton exchange membrane fuel cells. IET Renewable Power Generation. 2017;11:314-9.

[244] Hart D, Howes J, Lehner F, Dodds PE, Hughes N, Fais B, et al. Scenarios for deployment of hydrogen in contributing to meeting carbon budgets and the 2050 target. London: E4tech; 2015.

[245] Avgouropoulos G, Paxinou A, Neophytides S. In situ hydrogen utilization in an internal reforming methanol fuel cell. International Journal of Hydrogen Energy. 2014;39:18103-8.

[246] Lopes T, Paganin VA, Gonzalez ER. Hydrogen sulfide tolerance of palladium–copper catalysts for PEM fuel cell anode applications. International Journal of Hydrogen Energy. 2011;36:13703-7.

[247] Hinds G, Brightman E. In situ mapping of electrode potential in a PEM fuel cell. Electrochemistry Communications. 2012;17:26-9.

[248] Quesada C, Rockward T, Garzon F, Burleigh D, Mukundan R. Demonstration of Enhanced Sensitivity to CO in H2 Fuel Stream of an Electrochemical Analyzer. ECS Transactions. 2014;58:163-71.

[249] Noda Z, Hirata K, Hayashi A, Takahashi T, Nakazato N, Saigusa K, et al. Hydrogen pump-type impurity sensors for hydrogen fuels. International Journal of Hydrogen Energy. 2017;42:3281-93.

[250] Lee C-Y, Chang C-C, Lo Y-M. Fabrication of a Flexible Micro CO Sensor for Micro Reformer Applications. Sensors. 2010;10:10701-13.

[251] Lee CY, Hsu CW. Fabrication of Flexible Micro CO Sensor for Proton Exchange Membrane Fuel Cell Applications. Int J Electrochem Sci. 2016;11:2269-75.

[252] Caldwell KM, Kaserer S, Roth C, Ramaker DE. Following Adsorbate Coverage on Anodes of High-Temperature Polymer Electrolyte Membrane Fuel Cells in the Presence of CO and H2O by using In Operando X-ray Absorption Spectroscopy. ChemElectroChem. 2015;2:1502-9.

[253] Bender G, Angelo M, Bethune K, Rocheleau R. Quantitative analysis of the performance impact of low-level carbon monoxide exposure in proton exchange membrane fuel cells. Journal of Power Sources. 2013;228:159-69.

[254] Bacquart T, Murugan A, Carré M, Gozlan B, Auprêtre F, Haloua F, et al. Probability of occurrence of ISO 14687-2 contaminants in hydrogen: Principles and examples from

steam methane reforming and electrolysis (water and chlor-alkali) production processes model. International Journal of Hydrogen Energy. 2018;43:11872-83.

[255] Chung DY, Kim H-i, Chung Y-H, Lee MJ, Yoo SJ, Bokare AD, et al. Inhibition of CO poisoning on Pt catalyst coupled with the reduction of toxic hexavalent chromium in a dual-functional fuel cell. Scientific Reports. 2014;4:7450.

[256] Wu J, Yuan XZ, Wang H, Blanco M, Martin JJ, Zhang J. Diagnostic tools in PEM fuel cell research: Part I Electrochemical techniques. International Journal of Hydrogen Energy. 2008;33:1735-46.

[257] Kissinger PT, Heineman, W.R. Laboratory Techniques in Electroanalytical Chemistry. Second ed. New York: Marcel Dekker; 1996.

[258] Monk P. Analysis by Dynamic Measurement, A: Systems under Diffusion Control. Fundamentals of Electroanalytical Chemistry: John Wiley & Sons, Ltd.; 2007. p. 131-94.

[259] Cooper KR. In Situ PEM Fuel Cell Electrochemical Surface Area and Catalyst Utilization Measurement. Fuel Cell Magazine: Scribner Associates Incorporated; 2009.

[260] Brightman E, Hinds G, O'Malley R. In situ measurement of active catalyst surface area in fuel cell stacks. Journal of Power Sources. 2013;242:244-54.

[261] Pozio A, De Francesco, M., Cemmi, A., Cardellini, F., Giorgi, L. Comparison of high surface Pt/C catalysts by cyclic voltammetry. Journal of Power Sources. 2002;105:13-9.

[262] Yuan X, Wang H, Colin Sun J, Zhang J. AC impedance technique in PEM fuel cell diagnosis—A review. International Journal of Hydrogen Energy. 2007;32:4365-80.

[263] Stuart BH. Infrared Spectroscopy : Fundamentals and Applications. Hoboken, UNITED KINGDOM: John Wiley & Sons, Incorporated; 2004.

[264] Dinh T-V, Choi I-Y, Son Y-S, Kim J-C. A review on non-dispersive infrared gas sensors: Improvement of sensor detection limit and interference correction. Sensors and Actuators B: Chemical. 2016;231:529-38.

[265] Vaisala. How to measure carbon dioxide, https://www.vaisala.com/sites/default/files/documents/VIM-G-How-to-measure-CO2-Application-Note-B211228EN-C-LOW-v1.pdf; . Vaisala; 2020 [accessed 20.04.04].

[266] Brett DJL, Aguiar P, Clague R, Marquis AJ, Schöttl S, Simpson R, et al. Application of infrared thermal imaging to the study of pellet solid oxide fuel cells. Journal of Power Sources. 2007;166:112-9.

[267] Meola C. Infrared Thermography : Recent Advances And Future Trends. SAIF Zone, UNITED ARAB EMIRATES: Bentham Science Publishers; 2012.

[268] Vollmer M, Möllmann K-P. Infrared thermal imaging : fundamentals, research and applications. Second edition ed. Weinheim, Germany: Wiley-VCH; 2018.

[269] Minkina W, Dudzik S. Infrared thermography errors and uncertainties. Chippenham, UK: John Wiley & Sons, Ltd; 2009.

[270] Zhang J. PEM fuel cell testing and diagnosis. Amsterdam: Elsevier; 2013.

[271] Wruck WJ, Machado RM, Chapman TW. Current Interruption—Instrumentation and Applications. 1987;134:539-46.

[272] Barbir F. PEM Fuel Cells. 2nd edition ed: Academic Press; 2012.

[273] Mennola T, Mikkola M, Noponen M, Hottinen T, Lund P. Measurement of ohmic voltage losses in individual cells of a PEMFC stack. Journal of Power Sources. 2002;112:261-72.

[274] Dass C. Fundamentals of contemporary mass spectrometry. Hoboken, N.J.: Wiley-Interscience, John Wiley & Sons, Inc.; 2007.

[275] Ekman R, Silberring, J., Westman-Brinkmalm, A., Kraj, A. Mass spectrometry instrumentation, interpretation, and applications. Hoboken, N.J.: Hoboken, N.J. : John Wiley & Sons; 2009.

[276] Garrick TR, Moylan TE, Carpenter MK, Kongkanand A. Editors' Choice—Electrochemically Active Surface Area Measurement of Aged Pt Alloy Catalysts in PEM Fuel Cells by CO Stripping. Journal of The Electrochemical Society. 2017;164:F55-F9.

[277] Rudi S, Cui C, Gan L, Strasser P. Comparative Study of the Electrocatalytically Active Surface Areas (ECSAs) of Pt Alloy Nanoparticles Evaluated by Hupd and CO-stripping voltammetry. Electrocatal. 2014;5:408-18.

[278] Gamry. EIS300 Electrochemical Impedance Spectroscopy Software. Gamry Instruments; 2016.

[279] Heuer M, Bernstein PA, Wenske M, Styczynski ZA. Results of Current Density Distribution Mapping in PEM Fuel Cells Dependent on Operation Parameters. 2013;6:3841-58.

[280] Pei H, Liu Z, Zhang H, Yu Y, Tu Z, Wan Z, et al. In situ measurement of temperature distribution in proton exchange membrane fuel cell I a hydrogen–air stack. Journal of Power Sources. 2013;227:72-9.

[281] Schneider IA, Kramer D, Wokaun A, Scherer GG. Spatially resolved characterization of PEFCs using simultaneously neutron radiography and locally resolved impedance spectroscopy. Electrochemistry Communications. 2005;7:1393-7.

[282] Schneider IA, Kuhn H, Wokaun A, Scherer GG. Study of Water Balance in a Polymer Electrolyte Fuel Cell by Locally Resolved Impedance Spectroscopy. Journal of The Electrochemical Society. 2005;152:A2383.

[283] Kalyvas C, Kucernak A, Brett D, Hinds G, Atkins S, Brandon N. Spatially resolved diagnostic methods for polymer electrolyte fuel cells: a review. Wiley Interdisciplinary Reviews: Energy and Environment. 2014;3:254-75.

[284] Valdés-López VF, Mason T, Shearing PR, Brett DJL. Carbon monoxide poisoning and mitigation strategies for polymer electrolyte membrane fuel cells – A review. Progress in Energy and Combustion Science. 2020;79:100842.

[285] Lee Wk, Van Zee JW, Murthy M. A Method for Characterizing CO Transients in a PEMFC. Fuel Cells. 2003;3:52-8.

[286] Reed LJ, Berkson J. The Application of the Logistic Function to Experimental Data. The Journal of Physical Chemistry. 1928;33:760-79.

[287] Bian S, Du L-W, Gao Y-X, Huang J, Gou B-D, Li X, et al. Crystallization in Aggregates of Calcium Phosphate Nanocrystals: A Logistic Model for Kinetics of Fractal Structure Development. Crystal Growth & Design. 2012;12:3481-8.

[288] Taqvi ST, Almansoori A, Bassioni G. Modeling the Impact of Wettability Alterations on Calcium Carbonate System for Crude Oil and Asphaltenic Solutions. Industrial & Engineering Chemistry Research. 2014;53:4773-7.

[289] Arscott S. Dynamic Chemically Driven Dewetting, Spreading, and Self-Running of Sessile Droplets on Crystalline Silicon. Langmuir. 2016;32:12611-22.

[290] Hinds G, Stevens M, Wilkinson J, de Podesta M, Bell S. Novel in situ measurements of relative humidity in a polymer electrolyte membrane fuel cell. Journal of Power Sources. 2009;186:52-7.

[291] Garcia-Sanchez D, Morawietz T, da Rocha PG, Hiesgen R, Gazdzicki P, Friedrich KA. Local impact of load cycling on degradation in polymer electrolyte fuel cells. Applied Energy. 2020;259:114210.

[292] Robinson J, Shearing P, Brett D. Thermal Imaging of Electrochemical Power Systems: A Review. Journal of Imaging. 2016;2:2.

[293] Le Canut J-M, Latham R, Mérida W, Harrington DA. Impedance study of membrane dehydration and compression in proton exchange membrane fuel cells. Journal of Power Sources. 2009;192:457-66.

[294] Ous T, Arcoumanis C. Degradation aspects of water formation and transport in Proton Exchange Membrane Fuel Cell: A review. Journal of Power Sources. 2013;240:558-82.

[295] Baumgartner WRR, Baumgartner WRR, Wallnöfer E, Schaffer T, Hacker V, Peinecke V, et al. Electrocatalytic Corrosion of Carbon Support in PEMFC at Fuel Starvation. ECS Transactions. 2019;3:811-25.

[296] S. Cleghorn, Kolde J, Liu W. Catalyst coated composite membranes. In: Vielstich W, Gasteiger HA, Lamm A, Yokokawa H, editors. Handbook of fuel cells : fundamentals, technology and applications. Chichester: John Wiley & Sons; 2003. p. 566-75.

[297] Liu F, Yi B, Xing D, Yu J, Zhang H. Nafion/PTFE composite membranes for fuel cell applications. Journal of Membrane Science. 2003;212:213-23.

[298] Kilner J. Functional Materials for Sustainable Energy Applications. 1st edition ed: Woodhead Publishing; 2012.

[299] Schalenbach M, Hoefner T, Paciok P, Carmo M, Lueke W, Stolten D. Gas Permeation through Nafion. Part 1: Measurements. The Journal of Physical Chemistry C. 2015;119:25145-55.

[300] Broka K, Ekdunge P. Oxygen and hydrogen permeation properties and water uptake of Nafion® 117 membrane and recast film for PEM fuel cell. J Appl Electrochem. 1997;27:117-23.

[301] Kim J, Kim D-M, Kim S-Y, Nam SW, Kim T. Humidification of polymer electrolyte membrane fuel cell using short circuit control for unmanned aerial vehicle applications. International Journal of Hydrogen Energy. 2014;39:7925-30.

[302] Fuglevand WA, DeVries PD, Lloyd GA, Lott DR, Scartozzi JP. Fuel Cell and Method for Controlling Same. U.S. Patent 6,096,449, 2000.

[303] Zhan Y, Guo Y, Zhu J, Li L. Current short circuit implementation for performance improvement and lifetime extension of proton exchange membrane fuel cell. Journal of Power Sources. 2014;270:183-92.

[304] Gupta G, Wu B, Mylius S, Offer GJ. A systematic study on the use of short circuiting for the improvement of proton exchange membrane fuel cell performance. International Journal of Hydrogen Energy. 2017;42:4320-7.

[305] Pearson M. Method and apparatus for improving the performance of a fuel cell electric power system. U.S. Patent US 2010/0055514 A1, 2010.

[306] Panik MJ. Growth Curve Modeling: Theory and Applications. Hoboken, New Jersey: John Wiley & Sons, Inc.; 2014.

Appendices

A1. Calculation of the transition time through the logistic model

The logistic function used in Chapter 5 has the form:

$$\Delta\boldsymbol{\eta}(\boldsymbol{t}) = \frac{\boldsymbol{K}}{\mathbf{1}+\boldsymbol{\alpha}\boldsymbol{e}^{-\boldsymbol{\beta}\boldsymbol{t}}} \qquad \text{(A.1)}$$

Where *K*, refers to the $\Delta\eta$ upper limit, α is a constant and β is a growth rate [306]. From this equation the midpoint t_m, the point of inflection and where the highest increase in $\Delta\eta$ occurs is determined by

$$\boldsymbol{t_m} = \frac{\mathbf{1}}{\boldsymbol{\beta}}\boldsymbol{ln\alpha} \qquad \text{(A.2)}$$

The growth time, which corresponds to the time interval during which $\Delta\eta$ progresses from 10% to 90% of *K*, was likewise obtained [306]:

$$\Delta\boldsymbol{t} = \frac{\mathbf{4.39445}}{\boldsymbol{\beta}} + \frac{\boldsymbol{ln}(\mathbf{81})}{\boldsymbol{\beta}} \qquad \text{(A.3)}$$

Table A.1 Calculation of the transition time through the logistic function.

Reference electrode	**Range (min)**	**K (V)**	**α**	**β (min^{-1})**	**t_m (min)**	**Δt (min)**
RE1	0-50	0.33173	248.828	0.39328	14.0	22.3
RE2	0-100	0.10989	33.8089	0.17256	20.4	50.9
RE3	0-250	0.07002	101.034	0.0485	95.2	181.2

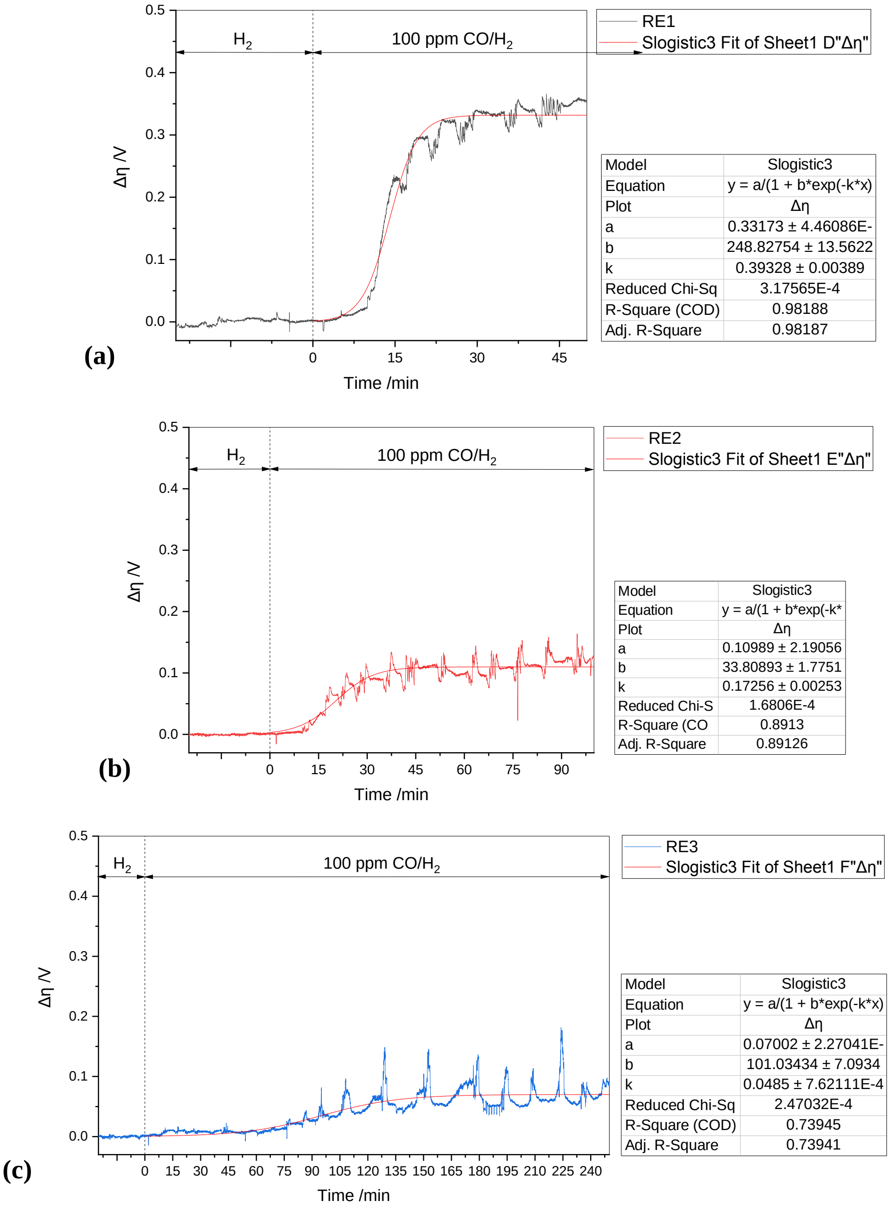

Model	Slogistic3
Equation	y = a/(1 + b*exp(-k*x)
Plot	Δη
a	0.33173 ± 4.46086E-
b	248.82754 ± 13.5622
k	0.39328 ± 0.00389
Reduced Chi-Sq	3.17565E-4
R-Square (COD)	0.98188
Adj. R-Square	0.98187

Model	Slogistic3
Equation	y = a/(1 + b*exp(-k*
Plot	Δη
a	0.10989 ± 2.19056
b	33.80893 ± 1.7751
k	0.17256 ± 0.00253
Reduced Chi-S	1.6806E-4
R-Square (CO	0.8913
Adj. R-Square	0.89126

Model	Slogistic3
Equation	y = a/(1 + b*exp(-k*x)
Plot	Δη
a	0.07002 ± 2.27041E-
b	101.03434 ± 7.0934
k	0.0485 ± 7.62111E-4
Reduced Chi-Sq	2.47032E-4
R-Square (COD)	0.73945
Adj. R-Square	0.73941

Figure A.1 Evolution of the anodic overpotential change ($\Delta\eta$) measured by (a) RE1, (b) RE2 and (c) RE3 and the respective fit of the logistic model during the transition phase in a PEMFC exposed to 100 ppm CO/H_2 under galvanostatic control (0.3 A cm^{-2}). The numeration follows the hydrogen path, where RE1 is closer to the anode inlet.

A2. Calculation of the recovery time through the exponential decay model

The exponential decay equation followed in Chapter 5 is

$$\boldsymbol{\Delta\eta = \Delta\eta_0 + A_1 e^{-t/t_1}} \qquad \text{(A.4)}$$

Where $\Delta\eta$ refers to the changes in the anodic overpotential at the time t; $\Delta\eta_0$ is the offset, A_1 is the amplitude and t_1 is a time constant. The equations to calculate the decay rate k and the half-life τ are given by

$$\boldsymbol{k = \frac{1}{t_1}} \qquad \text{(A.5)}$$

$$\boldsymbol{\tau = t_1 \cdot ln2} \qquad \text{(A.6)}$$

Figure A.2 presents the curves with the variations of $\Delta\eta$ over time for RE1, RE2 and RE3 during the recovery phase, when CO was removed from the stream and pure H2 was injected instead. Each graph shows the respective exponential decay fit. Table A.2 presents the calculations of the decay rate and half-life for each case.

Table A.2 Calculation of the decay rate and the half-life through the exponential decay model.

Reference electrode	**$\Delta\eta_0$ (V)**	**A_1 (V)**	**t_1 (min)**	**k (min^{-1})**	**τ (min)**
RE1	0.3213	0.3485	0.21783	4.5907	0.1510
RE2	8.36E-03	0.23163	0.14818	6.7485	0.1027
RE3	0.0123	0.16068	0.11615	8.6096	0.0805

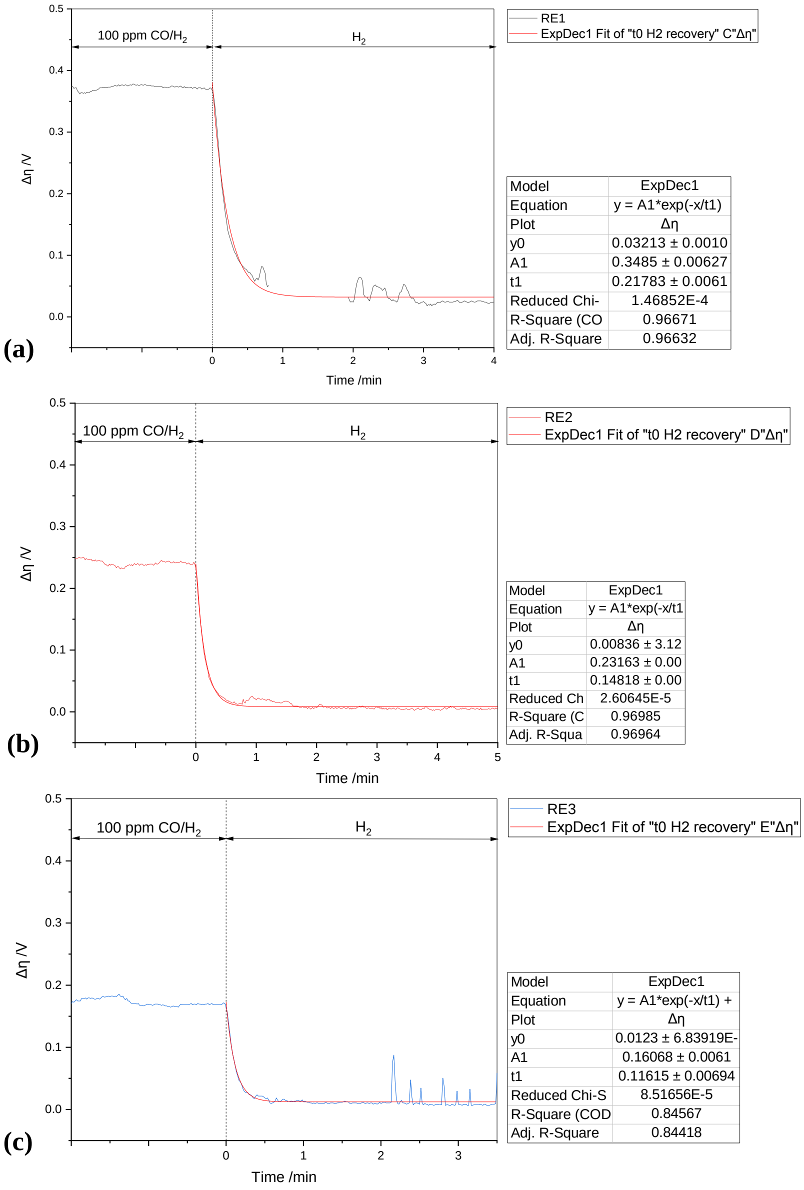

Figure A.2 Exponential decay of Δη during the recovery phase with pure H_2 measured by (a) RE1, (b) RE2 and (c) RE3 after the exposure to 100 ppm CO/H_2 during ~16 hours. The fit to the exponential decay function is presented in red. The operation of the cell is was galvanostatic (0.3 A cm^{-2}). *Note:* in RE1 some measured values between ~1-2 min after the injection of H_2 were not considered for the fit as these were considered noise.